Imaging the subthalamic nucleus in Parkinson's disease

Isaacs, B.R.

Publication date
2022
Document Version
Final published version

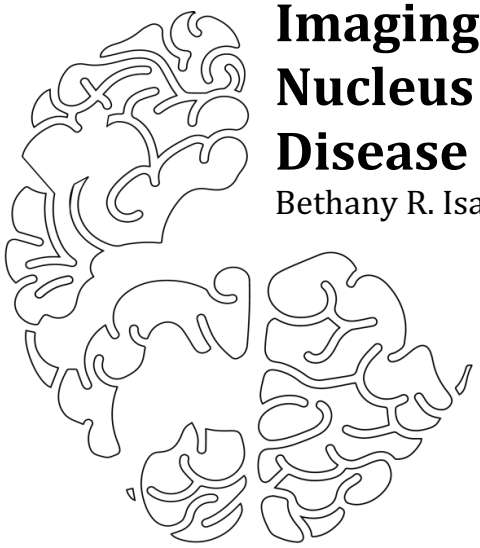

Imaging the Subthalamic Nucleus in Parkinson's Disease

Bethany R. Isaacs

Imaging the Subthalamic Nucleus in Parkinson's Disease

Bethany R. Isaacs

To my Dad

Imaging the Subthalamic Nucleus in Parkinson's Disease

ACADEMISCH PROEFSCHRIFT

ter verkrijging van de graad van doctor
aan de Universiteit van Amsterdam
op gezag van de Rector Magnificus
prof. dr. ir. P.P.C.C. Verbeek
ten overstaan van een door het College voor Promoties ingestelde commissie, in het openbaar te verdedigen op woensdag 26 oktober 2022, te 11.00 uur

door
Bethany Rose Isaacs
geboren te Plymouth

Promotiecommissie

***Promotores*:**	prof. dr. B. U. Forstmann	Universiteit van Amsterdam
	prof. dr. Y. Temel	Universiteit Maastricht
***Copromotores*:**	dr. P.L.E.A. Bazin	Universiteit van Amsterdam
	dr. J. M. Alkemade	Universiteit van Amsterdam
***Overige leden*:**	dr. ir. M. W. A. Caan	Universiteit van Amsterdam
	prof. dr. O. A. van den Heuvel	Vrije Universiteit Amsterdam
	prof. dr. S. A. Kotz	Universiteit Maastricht
	prof. dr. K. R. Ridderinkhof	Universiteit van Amsterdam
	dr. H. S. Scholte	Universiteit van Amsterdam
	dr. W. P. M. van den Wildenberg	Universiteit van Amsterdam

Faculteit der Maatschappij- en Gedragswetenschappen

Dit proefschrift is tot stand gekomen binnen een samenwerkingsverband tussen de Universiteit van Amsterdam en de Universiteit Maastricht met als doel het behalen van een gezamenlijk doctoraat. Het proefschrift is voorbereid aan de Faculteit der Maatschappij- en Gedragswetenschappen van de Universiteit van Amsterdam en aan de Faculteit Psychologie en Neurowetenschappen van de Universiteit Maastricht.

This thesis was prepared within the partnership between the University of Amsterdam and Maastricht University with the purpose of obtaining a joint doctorate degree. The thesis was prepared in the Faculty of Social and Behavioural Sciences of the University of Amsterdam and in the Faculty of Psychology and Neuroscience of Maastricht University.

When I had all the answers, the questions changed.

- Paulo Coelho

Contents

Author Contributions

Chapter 1. Max C. Keuken (MCK), Bethany R. Isaacs (BRI), Robert Trampel (RT), Wietske van der Zwaag (WZ), & Birte U. Forstmann (BUF). MCK and BRI designed and performed the literature review and contributed in equal amounts to the writing of the manuscript. MCK, BRI, and BUF formulated the research question. BUF formally supervised the project. RT, WZ, and BUF provided critical feedback, revised, and helped shape the manuscript.

Chapter 2. Birte U. Forstmann (BUF), Bethany R. Isaacs (BRI), & Yasin Temel (YT). BUF and BRI formulated and wrote the article together. YT provided critical feedback, revised, and helped shape the final paper. All authors were involved in the conceptualization of the paper.

Chapter 3. Jeroen Habets (JH), Bethany R. Isaacs (BRI), Saman R. Vinke (SRV), & Pieter Kubben (PK). JH and BRI conceptualized, researched, formulated, and wrote the chapter together. SRV and PK provided critical feedback, revised, and helped shape the final product. PK supervised the project.

Chapter 4. Bethany R. Isaacs (BRI), Margot Heijmans (MH), Yasin Temel (YT), Mark, Kuijf (MK), Linda Ackermans (LA), Pieter Kubben (PK), Max C. Keuken (MCK), & Birte U. Forstmann (BUF). BRI conceptualized and designed the study and performed the statistics. BRI and MH collected the MRI data, pre-processed and analyzed the results, and contributed equally to writing the manuscript. MH automated the tasks and organized the data. MH, YT, MK, LA, and PK contributed to the targeting data. MCK and BUF supervised the project. All co-authors provided critical feedback, revised, and helped shape the manuscript.

Chapter 5. Bethany R. Isaacs (BRI), Birte U. Forstmann (BUF), Yasin Temel (YT), & Max C. Keuken (MCK). BRI, BUF, and MCK were equally involved in the conceptualization and design of the study. BRI conducted the pre- and post-processing of MRI data, statistical analysis, and writing. MCK formally supervised all parts of the study. All co-authors provided critical feedback, revised, and helped shape the manuscript.

Chapter 6. Bethany R. Isaacs (BRI), Anne C. Trutti (ACT), Esther Pelzer (EP), Marc Tittgemeyer (MT), Yasin Temel (YT), Birte U. Forstmann (BUF), & Max C. Keuken (MCK). BRI prepared the manuscript, pre- and post-processed the MRI data, and conducted the statistical analysis. BRI, ACT, YT, BUF, and MCK conceptualized and formulated the study. EP and MT completed the organization and data collection. MCK formally supervised all parts of the study. All co-authors provided critical feedback, revised, and helped shape the manuscript.

Chapter 7. Bethany R. Isaacs (BRI), Martijn J. Mulder (MJM), Josephine M. Groot (JMG), Nikita van Berendonk (NB), Nicky Lute (NL), Pilou Bazin (PLB), Birte U. Forstmann (BUF), & Anneke Alkemade (AA). BRI, MJM, BUF, and AA conceptualized and formulated the study. BRI prepared the manuscript, pre- and post-processed the MRI data, conducted the statistical analysis, and optimized the automated parcellations. BRI and AA created the manual parcellations. MJM, JG, NB, and NL completed the data collection. PLB provided expert input regarding the physics and fundamentals of MRI. BUF and AA supervised the study. All co-authors provided critical feedback, revised, and helped shape the manuscript.

Chapter 8. Bethany R. Isaacs (BRI), Max C. Keuken (MCK), Anneke Alkemade (AA), Yasin Temel (YT), Pilou Bazin (PLB), & Birte U. Forstmann U (BUF). BRI and BUF conceptualized the paper. BRI conducted the research and wrote the paper. MCK assisted in the development of the manuscript. AA provided expertise on anatomy and biology. PLB provided expert input regarding the physics and fundamentals of MRI. All co-authors provided critical feedback, revised, and helped shape the manuscript

Financial Statement

The research of this doctoral thesis received financial assistance from Prof. Birte Forstmann and Prof. Yasin Temel. Specific funding per chapter is noted below.

Chapter 1. This research was supported by a Vidi grant from the Dutch Organization for Scientific Research (NWO, grant no. 452.Vidi.11.008) on behalf of Birte U. Forstmann (BUF) and a starter grant from the European Research Council (ERC, grant no. Stg:313481, BUF).

Chapter 2. This research was supported by an NWO Vidi grant (grant no. 452.Vidi.11.008, BUF), an ERC starter grant (grant no. Stg:313481) (BUF), and a Stichting Annadal NWO (grant no. 452-11-002) on behalf of Yasin Temel (YT).

Chapter 3. This research received no external funding.

Chapter 4. The research was funded by an NWO-STW grant (NOW-016.Vici.185.052), ERC-Stg (ERC-Stg 313481) and ERC-PoC obtained by BUF.

Chapter 5. This research was supported by an NWO Vidi grant (grant no. 452.Vidi.11.008, BUF), an ERC starter grant (grant no. Stg:313481) (BUF), and an ABC talent grant from the University of Amsterdam (2017) on behalf of Max C. Keuken (MCK).

Chapter 6. This research was supported by an NWO Vici grant (grant no. 016.Vici.185.052, BUF) and an ERC starter grant (grant no. Stg:313481) (BUF).

Chapter 7. This research was supported by an NWO Vidi grant (grant no. 452.Vidi.11.008, BUF), an NWO Vici grant (grant no. 016.Vici.185.052, BUF), and an NWO Applied and Engineering Sciences (AES/STW) grant (grant no. 14017) on behalf of BUF, Anneke Alkemade (AA) and Martijn J. Mulder (MJM). Data collection was funded by Boston Scientific Corporation (BUF, AA), which did not impose any restrictions on the performed research.

Chapter 8. This research received no external funding.

The funders had no role in study design, data collection, and analysis, decision to publish, or preparation of the manuscript.

List of Abbreviations

ACC	Anterior Cingulate Cortex
AD	Axial Diffusivity
B0	Main magnetic field
B1	Radiofrequency field
BET	Brain ExtracTed
BF	Bayes Factor
CIN	CINgulate Cortex
CNR	Contrast to Noise Ratio
DBS	Deep Brain Stimulation
DLPFC	DorsoLateral PreFrontal Cortex
dMRI	Diffusion MRI
DOF	Degrees of Freedom
DWI	Diffusion Weighted Imaging
EPI	Echo Planar Imaging
ES	Echo Spacing
FA	Fractional Anisotropy
FA	Flip Angle
FEF	Frontal Eye Fields
FFE	Fast Field Echo
fMRI	Functional MRI
FOV	Field Of View
FPA	FrontoPolar Area
GPe	Globus Pallidus Externa
GPi	Globus Pallidus Interna
GRE	GRadient Echo
H0	Null Hypothesis
H1	Alternative Hypothesis
HC	Healthy Controls
IFJ	Inferior Frontal Junction
IFS	Inferior Frontal Sulcus
M1	Primary Motor Cortex
MER	MicroElectrode Recording
MIST	Multimodal Image Segmentation Tool
MP2RAGE	Magnetization Prepared 2 Rapid GRE
MRI	Magnetic Resonance Imaging
NHP	Non-Human Primate
OFC	OrbitoFrontal Cortex
PD	Parkinson's Disease
PGA	PeriGenual Area
PI	Parallel Imaging
POP	Pars OPercularis
Pre-M1	Pre-Motor Area
Pre-SMA	Pre-Supplementary Motor Area
PTR	Pars TRiangularis
PVE	Partial Voluming Effects
qMRI	Quantitative MRI
QSM	Quantitative Susceptibility Mapping
RF	RadioFrequency
RN	Red Nucleus
ROI	Region Of Interest
rs-fMRI	Resting-State Functional MRI
SGA	SubGenual Area
SMA	Supplementary Motor Area
SN	Substantia Nigra
SNR	Signal to Noise Ratio
STN	SubThalamic Nucleus
STR	STRiatum
T	Tesla
TA	Acquisition Time
TE	Echo Time
Th	Thalamus
TI	Inversion Time
TR	Repetition Time
UHF	Ultra-High Field
UNI	UNIfied
VMPFC	VentroMedial PreFrontal Cortex

Summary

English

This thesis is comprised of a set of work that aims to visualize and quantify the anatomy, structural variability, and connectivity of the subthalamic nucleus (STN) with optimized neuroimaging methods. The study populations include both healthy cohorts and individuals living with Parkinson's disease (PD). PD was chosen specifically due to the involvement of the STN in the pathophysiology of the disease. Optimized neuroimaging methods were primarily obtained using ultra-high field (UHF) magnetic resonance imaging (MRI). An additional component of this thesis was to determine to what extent UHF-MRI can be used in a clinical setting, specifically for pre-operative planning of deep brain stimulation (DBS) of the STN for patients with advanced PD.

The thesis collectively demonstrates that i, MRI research, and clinical applications must account for the different anatomical and structural changes that occur in the STN with both age and PD. ii, Anatomical connections involved in preparatory motor control, response inhibition, and decision-making may be compromised in PD. iii. The accuracy of visualizing and quantifying the STN strongly depends on the type of MR contrast and voxel size. iv, MRI at a field strength of 3 Tesla (T) can under certain circumstances be optimized to produce results similar to that of 7 T at the expense of increased acquisition time.

Summary

Dutch

Dit proefschrift bestaat uit een reeks studies die tot doel hebben de anatomie, de structurele variabiliteit en de connectiviteit van de nucleus subthalamicus (STN) te visualiseren en te kwantificeren met behulp van geoptimaliseerde neuroimagingmethoden. De studiepopulaties omvatten zowel gezonde cohorten als patienten met de ziekte van Parkinson (PD). PD werd specifiek gekozen vanwege de betrokkenheid van de STN in de pathofysiologie van de ziekte. Geoptimaliseerde neuroimagingmethoden werden voornamelijk verkregen met behulp van ultra-high field (UHF) magnetic resonance imaging (MRI). Daarom was een aanvullend onderdeel van dit proefschrift het bepalen van in hoeverre UHF MRI gebruikt kan worden voor klinische toepassingen, specifiek voor pre-operatieve planning van diepe hersenstimulatie (DBS) van de STN voor patiënten met gevorderde PD.

Het proefschrift toont aan dat i. MRI-onderzoek en klinische toepassingen rekening moeten houden met de verschillende anatomische en structurele veranderingen die optreden in de STN met zowel leeftijd als PD. ii. Anatomische verbindingen die betrokken zijn bij de controle van het motorische systeem, responsinhibitie en keuzegedrag kunnen aangetast zijn bij PD. iii. De nauwkeurigheid van het zichtbaar maken en kwantificeren van de STN is sterk afhankelijk van het type MR-contrast en de voxelgrootte. iv. MRI bij een veldsterkte van 3 Tesla (T) kan onder bepaalde omstandigheden worden geoptimaliseerd om resultaten te verkrijgen die vergelijkbaar zijn met die van 7 T, maar dit gaat ten koste van een langere acquisitietijd.

Synopsis

The following section provides a brief explanation of each chapter and the corresponding reference. For chapters 1, 4, 5, 6 and 7, the data, analysis code, and scripts are available for other researchers via the Open Science Framework (OSF) under the Creative Commons License and comply with the rules and anonymization procedures of the General Data Protection Regulation (EU) 2016/679. The OSF project page ID is provided below and can be accessed via www.osf.io. In some instances, access will require a direct request.

> Chapter 1. Keuken, M. C*., **Isaacs, B. R***., Trampel, R., van der Zwaag, W., & Forstmann, B. U. (2018). Visualizing the human subcortex using ultra-high field magnetic resonance imaging. *Brain Topography, 31*(4), 513-545.

The first chapter is an extensive literature review that forms the basis of the thesis. The article introduces the progression and current state of Ultra-high field Magnetic resonance imaging (UHF, MRI) in visualizing subcortical structures. The review includes a total of 169 papers, investigating field strengths of 7.0 Tesla (T), 8.0T, 9.4T, and 9.4T+, examining in-vivo and post-mortem samples, healthy controls and disease groups, including various forms of dementia and neurodegenerative diseases including Parkinson's disease (PD). The most commonly investigated structures include the amygdala, caudate, dentate nucleus, globus pallidus external and internal components (GPe and GPi), the inferior and superior colliculi, mamillary body, periaqueductal grey, pons, pulvinar, putamen, red nucleus (RN), substantia nigra (SN), subthalamic nucleus (STN) and the thalamus (THA). The SN, STN, and THA were chosen for further investigation due to their involvement in PD. Various sequences are discussed, whereby T2* based and Susceptibility Weighted Imaging (SWI) are reported as the most common methods for visualizing all three structures. The paper discusses observed methodological discrepancies between identification and parcellation, inconsistencies in anatomical and structural definition, voxel volume and isotropic voxel sizes, and the distinct lack of objective measures. Further, most studies utilized weighted imaging rather than quantitative maps, which is unfortunate given the advantages of UHF-MRI in developing bias-free imaging with biologically and spatially specific

information. This paper was awarded first prize for Best Publication Award of the journal Brain Topography in 2018.

OSF ID: *fwc2p*

Chapter 2. Forstmann, B. U., **Isaacs, B. R**., & Temel, Y. (2017). Ultra-high field MRI-guided deep brain stimulation. *Trends in Biotechnology, 35*(10), 904-907.

The second chapter is a short trends paper discussing the theoretical benefit of UHF-MRI for deep brain stimulation (DBS), specifically for the STN in PD. The paper focuses on highlighting the global accessibility of 7T MRI scanners and examines concepts such as spatial resolution, contrast, and signal to noise ratios (SNR) and acquisition times with field strength and clinical applicability. We further explain the potential benefits of adopting a patient-specific approach to DBS targeting with UHF-MRI.

Chapter 3. Habets, J*., **Isaacs, B***., Vinke, S., & Kubben, P. (2019). Controversies in Deep Brain Stimulation Surgery: Micro-Electrode Recordings. *In Evidence for Neurosurgery* (pp. 97-109). Springer, Cham.

An additional literature review forms the third chapter, which investigates the use of microelectrode recordings (MER) and MRI for intra-operative DBS targeting and post-operative electrode placement verification. Target identification and verification can be achieved by both or either pre-operative MRI and intra-operative MER. MER has several shortcomings, whereby it requires the patient to be awake, undergo macrostimulation, and rigorous, time-consuming intra-operative behavioral testing. Furthermore, MER has been associated with an increased likelihood of post-operative infection, intra- or post-operative hemorrhagic events, and intra-operative brain shift with subsequent lead displacement. Additionally, the DBS target can be targeted pre-operatively and or verified intra-operatively with MRI or computerized tomography (CT). In this chapter, we conducted a structured literature review including 20 articles that assessed the application of MER and or MRI for DBS targeting and verification. While a consensus on a favored method is missing, optimized MRI techniques do not appear to be commonly applied within a clinical setting, and current clinical MRI remains insensitive to the

intricacies of deep brain imaging. More often, both MER and MRI are combined for DBS. The development of optimized and UHF-MRI as well as directional leads could revolutionize current planning and verification procedures for DBS and other functional neurosurgeries.

Chapter 4. **Isaacs, B. R***., Heijmans, M*., Temel. Y., Kuijf, M., Ackermans, L., Kubben, P., Keuken, M. C., & Forstmann, B. U. (2021). Variability in Subthalamic Nucleus Targeting for Deep Brain Stimulation with 3 and 7 Tesla Magnetic Resonance Imaging. *Under review. Neuroimage Clinical.*

The study in chapter 4 aims to test whether optimized 7T imaging protocols result in less variable targeting of the STN for DBS compared to clinically utilized 3T images. Three DBS-experienced neurosurgeons determined the optimal STN DBS target site on three repetitions of 3T-T2, 7T-T2*, 7T-R2* and 7T-QSM images for five PD patients. The distance in millimetres between the three repetitive coordinates was used as an index of targeting variability and was compared between field strength, MRI contrast and repetition in both native and MNI space. The results indicate that the neurosurgeons are stable in selecting the DBS target site across MRI field strength, MRI contrast and repetitions. The analysis of the coordinates in MNI space however revealed that the actual selected location of the electrode is seemingly more ventral when using the 3T scan compared to the 7T scans.

OSF ID: *dw2fr*

Chapter 5. **Isaacs, B. R**., Forstmann, B. U., Temel, Y., & Keuken, M. C. (2018). The connectivity fingerprint of the human frontal cortex, subthalamic nucleus, and striatum. *Frontiers in neuroanatomy, 12*, 60.

Chapter 5 is an empirical piece investigating the differences in connectivity between the STN and STR with a-priori defined cortical areas. The STN and STR were chosen as they are both considered crucial input structures to the basal ganglia, and are essential for optimal and adaptive control of action selection and motor responses, involved in the direct, indirect, and hyperdirect pathways. Traditionally, animal literature has formed the basis of cortico-basal pathway

hypotheses and suggests that while STN connections do exist, they are generally sparser than STR. We utilized 7T diffusion-weighted MRI (dMRI) and resting-state functional (rs-f) MRI to assess whether the STN and STR showed different connectivity profiles to the same cortical areas. A total of 17 functionally distinct cortical structures were chosen based on their comparative similarity to non-human primate models and tracer studies of basal ganglia functioning and connectivity. We report that the STN is more sparsely connected than the STR, in line with traditional models of primate based cortico-basal models, and that functional and structural connectivity are predictive of one another. However, we do report some novel findings. The STN showed higher structural connections to the orbitofrontal (OFC) and the ventromedial prefrontal (VMPFC) cortex compared to the STR, which are assumed to be essential for reward processing, choice bias, and mood which are conventionally processed via limbic loops. However, the aforementioned processes are also strongly influenced by memory, decision-making, and motivation which are all essential for optimal action and movement. Moreover, these cortico–subcortical connections are assumed to be predictive for the efficacy of STN DBS in PD

OSF ID: *s46hr*

Chapter 6. **Isaacs, B. R**., Trutti, A. C., Pelzer, E., Tittgemeyer, M., Temel, Y., Forstmann, B. U., & Keuken, M. C. (2019). Cortico-basal white matter alterations occurring in Parkinson's disease. *PloS one, 14*(8).

In chapter 6 we utilized 3T dMRI and probabilistic tractography to investigate cortico-basal connections in a PD population. Connections between the STN and cortical areas including the pars operculiaris (POp), anterior cingulate cortex (ACC), dorsolateral prefrontal cortex (DLPFC), primary motor area (M1), supplementary motor area (SMA), and pre-supplementary motor (pre-SMA) area were assessed. These areas were chosen due to their connectivity with the STN, which we hypothesized may exhibit disease-specific alterations given their functional involvement in limbic, cognitive, and motor processes that are known to be affected in PD. While tract strengths remained structurally unaffected by disease, fractional anisotropy (FA) decreased in PD between the STN and areas collectively involved in preparatory motor control, response inhibition, decision-making, and task monitoring, namely the POp, DLPFC, and pre-SMA. FA has been used as an index for white matter integrity and microstructural changes. A decrease in FA in the

PD in these tracts could reflect impaired connectivity and function and may be used as a biomarker for disease status and progression. Further, we incorporated PD and age-specific atlases of the STN. Anatomical atlases have largely consisted of data from healthy male groups, which is not representative of elderly or diseased populations. We highlight the importance of using disease- and age-specific anatomical atlases by establishing that results vary depending on whether or not known structural differences in these groups are accounted for.

OSF ID: *4uxxs*

Chapter 7. **Isaacs, B. R.**, Mulder, M. J., Groot, J., van Berendonk, N., Lute, N., Bazin, P-L., Forstmann, B. U., & Alkemade, A. (2020). 3 versus 7 Tesla MRI for parcellations of subcortical brain structures in clinical settings. *PloS one, 15*(11), e0236208.

Chapter 7 assesses whether 7T is superior regarding localization procedures of small brain structures, we compared manual parcellations of the red nucleus, subthalamic nucleus, substantia nigra, globus pallidus interna and externa. These parcellations were created on a commonly used clinical anisotropic clinical 3T with an optimized isotropic (*o*)3T and standard 7T scan. The clinical 3T MRI scans did not allow delineation of an anatomically plausible structure due to its limited spatial resolution. *o*3T and 7T parcellations were directly compared. We found that 7T outperformed the *o*3T MRI as reflected by higher Dice scores, which were used as a measurement of the interrater agreement for manual parcellations on quantitative susceptibility maps. This increase in the agreement was associated with higher contrast to noise ratios for smaller structures, but not for the larger globus pallidus segments. Additionally, control-analyses were performed to account for potential biases in manual parcellations by assessing semi-automatic parcellations. These results showed a higher consistency for structure volumes for 7T compared to optimized 3T which illustrates the importance of the use of isotropic voxels for 3D visualization of the surgical target area. Together these results indicate that 7T outperforms *c*3T as well as *o*3T given the constraints of a clinical setting.

OSF ID: *4nrku*

Chapter 8. **Isaacs, B. R**., Keuken, M. C., Alkemade, A., Temel. Y., Bazin, P-L., & Forstmann, B. U. (2020). Methodological considerations for neuroimaging in Deep Brain Stimulation of the Subthalamic Nucleus in Parkinson's Disease patients. *Journal of Clinical Medicine,* 9(10), 3124.

Chapter 8 offers a discussion and concluding remarks with regards to the application of UHF-MRI in clinical settings. A small fraction of patients will fail to respond to DBS, develop psychiatric and cognitive side-effects, or incur surgery-related complications such as infections and hemorrhagic events. In these cases, DBS may require recalibration, reimplantation, or removal. These negative responses to treatment can partly be attributed to suboptimal pre-operative planning procedures via direct targeting through low-field and low-resolution MRI. One solution for increasing the success and efficacy of DBS is to optimize pre-operative planning procedures via sophisticated neuroimaging techniques such as high-resolution MRI and higher field strengths to improve visualization of DBS targets and vasculature. We discuss targeting approaches, MRI acquisition, parameters, and post-acquisition analyses. Additionally, we highlight several approaches including the use of UHF-MRI to overcome limitations of standard settings. There is a trade-off between spatial resolution, motion artifacts, and acquisition time, which could potentially be dissolved through the use of UHF-MRI. Image registration, correction, and post-processing techniques may require the combined expertise of traditional radiologists, clinicians, and fundamental researchers. The optimization of pre-operative planning with MRI can therefore be best achieved through direct collaboration between researchers and clinicians.

* first authorship

Introduction

Movement, Cortico-Basal Pathways and the Subthalamic Nucleus

Movement requires the selection of the most appropriate action according to both external cues from the environment and from internally generated goals, which can occur intentionally or habitually and without thought or effort. Movement control entails a variety of functions such as attention, coordination, speed perception, time calculations, spatial awareness, and working memory, which are performed by distributed and interconnected networks across the entire brain. Movement is a dynamic process that requires activation and communication between regions that work in tandem and continuously update to enact the most suitable action response while suppressing alternative and competing plans. It is thought that motor control and action selection are facilitated by white matter connections between the cortex and the basal ganglia (BG), known as cortico-basal pathways (Alexander, DeLong, & Strick, 1986; Parent & Hazrati, 1995). These pathways can be divided into the direct, indirect and hyperdirect pathways, which each recruit the BG in a different way to either initiate or suppress movement (Mathai & Smith, 2011; Nambu, Takada, Inase, & Tokuno, 2018; Nambu, Tokuno, & Takada, 2002). The main components of the BG are the caudate, nucleus accumbens, and putamen (collectively referred to as the striatum (STR), the external and internal segments of the globus pallidus (GPe and GPi, respectively), the subthalamic nucleus (STN), and substantia nigra pars compacta and reticulata (SNc and SNr, respectively). See figure 1 for a representation of BG nuclei and figure 2 for an illustration of the BG pathways.

The direct pathway facilitates the initiation and execution of voluntary movements which begins with excitatory projections from motor-related areas of the frontal cortex to the STR that occur in response to goal-directed action. Striatal neurons have gamma-aminobutyric acid (GABAergic) projections with the GPi and SNr, which elicits an inhibitory effect on to the thalamus (THA). Since the THA is excitatory, inhibitory effects of the GPi and SNr release the THA from inhibition (a process known as double inhibition) and result excitation of cortical motor areas through excitatory glutaminergic connections, that are responsible for movement.

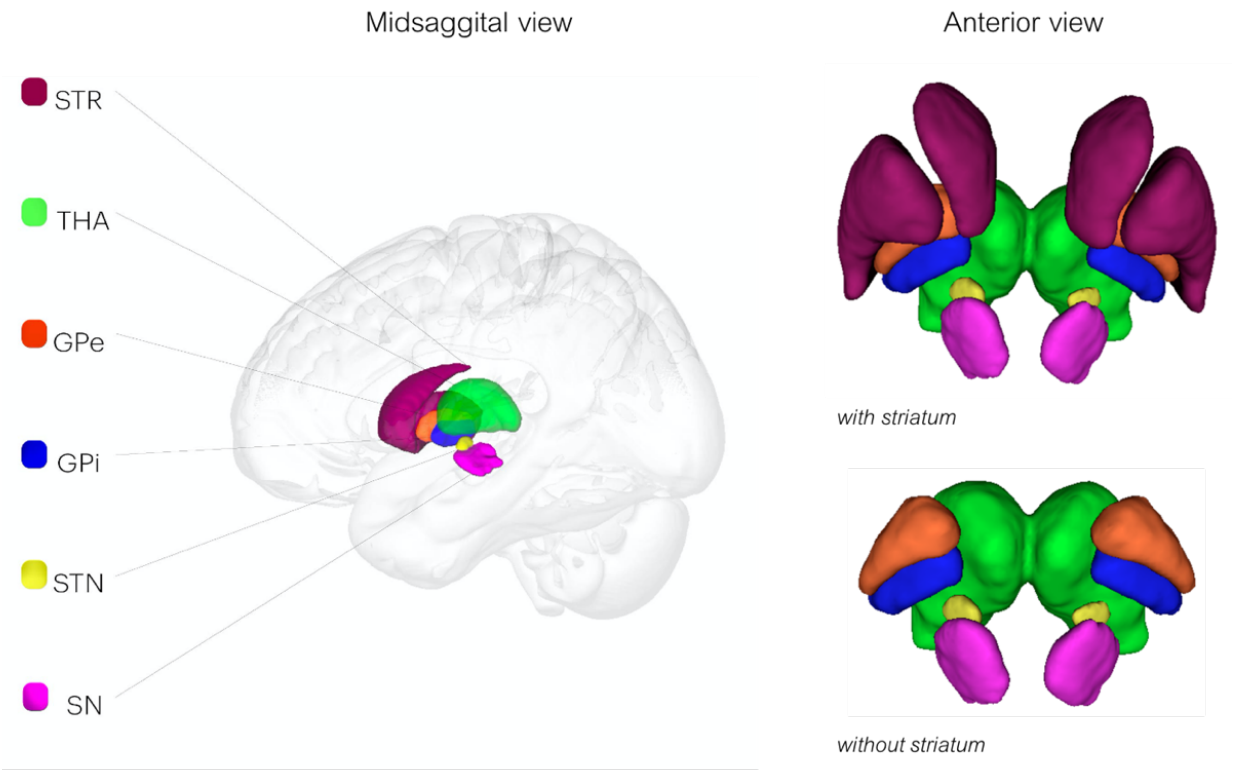

Figure 1: Basal ganglia nuclei. On the left is a midsagittal view (left to right) of the left hemisphere including subcortical areas involved in the direct, indirect and hyperdirect pathways. Striatum (STR) in maroon, thalamus (THA) in green, globus pallidus external segment (GPe) in orange, globus pallidus internal segment (GPi) in blue, subthalamic nucleus (STN) in yellow and the substantia nigra (SN) in pink. On the right are two sets of close ups of the nuclei in the anterior view (also slightly inferior) with and without the striatum present to better show the GPe/i.

The indirect pathway functions in parallel with the direct pathway to suppress competing motor responses. As with the direct pathway, it begins with excitation of the STR via input from the cortex. However, the inhibitory striatal neurons then synapse onto and the GPe, which projects additional inhibitory fibers towards the STN. This double inhibition again results in a disinhibition of the STN, resulting in activation of the GPi and SNr. Since the GPi and SNR are inhibitory, activation will result in suppression of THA excitation.

In the absence of cortical excitation and when in a neutral state, the BG will exert

an inhibitory effect over motor activity (so we can stay still). These basal pathways intrinsically modulated by additional nigrostriatal connections between the SN and the STR. These nigrostriatal pathways function to excite the direct pathway and inhibit the indirect pathway which relies on activation via specific dopamine receptors (D1 and D2, respectively) projected from the SNc (Kwak & Jung, 2019; Obeso et al., 2008). See figure 2 for an illustration of these pathways.

An additional hyperdirect pathway exists to process information and feedback to the cortex at a much faster rate than either the direct or indirect pathway. The hyperdirect pathway exhibits a persistent tonic activation that overrides the inhibitory effects of the BG and acts as a threshold adjuster for movement initiation, as well as a phasic mode that initiates quicker stopping responses. Together, this pathway functions to optimize behavioral outcomes, suppress potential competing, unwanted motor programs already in motion or erroneous movements, switch tasks and monitor conflict (Brunenberg et al., 2012). This is achieved by bypassing the STR and connecting the cortex directly with the STN, sending excitatory projections to the GPi, and SNr, which subsequently inhibit the THA. It may be that within the hyperdirect pathway, the role of the STN is to integrate information and perform as a decisional threshold, ultimately permitting whether or not an action may be performed (Frank, 2006).

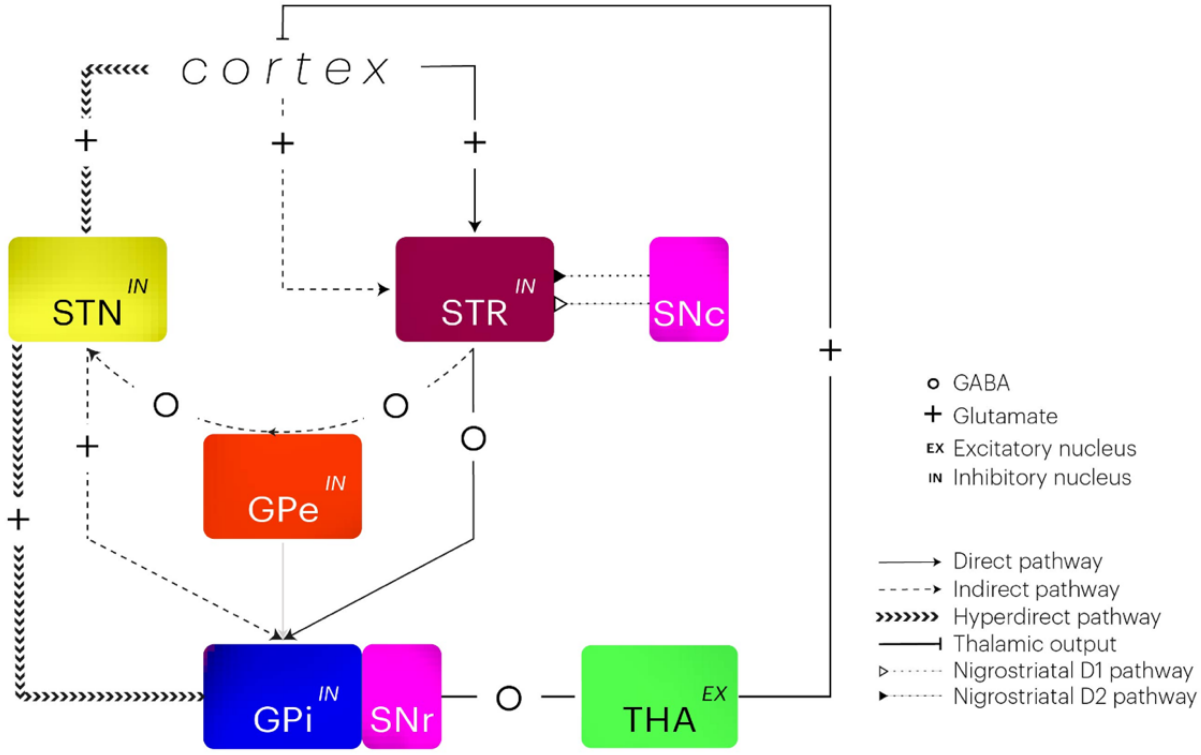

Figure 2: A schematic of the direct, indirect, and hyperdirect pathways. The direct pathway (solid thin line) involves double inhibition of projections from the cortex to the striatum (STR), and the globus pallidus internal segment (GPi) and substantia nigra pars reticulata (SNr), and then to the thalamus (THA) which projects excitatory output back to the cortex via glutamate, which functions to initiate voluntary motor output. The indirect pathway (dashed thin line) also sends excitatory projections from the cortex to the striatum, which subsequently inhibits the globus pallidus external segment (GPe) and then the subthalamic nucleus (STN). Double inhibition results in disinhibition of the STN, which results in excitation of GPi and SNr via glutamate, which inhibits the THA and functions to suppress movement. The hyperdirect pathway (thick dashed arrows) inputs excitatory projects from the cortex directly to the STN, which projects to the GPi and SNr, and functions to override slower responses from the direct and indirect pathways, as well as acting as a decisional threshold for appropriate action selection (Frank, Samanta, Moustafa, & Sherman, 2007). These pathways are modulated by GABA (circle), which has an inhibitory effect on neurons, and glutamate (cross) which is an excitatory neurotransmitter. While the indirect and hyperdirect pathway possess different functions, note that anatomically they most likely arise from the same portion of white matter fibers. Note that there is also an excitatory connection between the GPe and GPi/SNr which is shown with a greyed out arrow (Aron & Poldrack, 2006). Further, nuclei may be excitatory (EX) or inhibitory (IN). If GABA inhibits an excitatory nucleus then it results in inhibition, if GABA inhibits an inhibitory nucleus then it results in excitation. If glutamate excites an excitatory nucleus then it results in excitation, and if it excites an inhibitory nucleus it results in inhibition. The STR receives separate dopaminergic input from the SN pars compacta (SNc) for the direct (D1) and indirect (D2) pathways.

Further, the STN is hypothesized to possess functional subdivisions; known as the tripartite model. To oversimplify matters, the dorsolateral portion of the STN is thought to connect with cortical motor-related areas such as the primary and pre-motor cortex and supplementary motor areas, and is therefore involved in movement, motor control, and action; the central portion of the STN connects with cortical cognitive and associative areas within the frontal, temporal and parietal lobes which are involved in executive functions such as decision-making; and the ventromedial tip of the STN constitutes the limbic portion, which connects to the medial temporal lobe, insula and cingulate areas which process emotion, long term memory and olfaction (Lambert et al., 2012; Temel, Blokland, Steinbusch, & Visser-Vandewalle, 2005). This tripartite model has been used to explain the effects of deep brain stimulation (DBS, discussed in the next section) in Parkinson's disease (PD) where direct stimulation of the motor portion of the STN should restore normal communication within the motor pathways that are pathologically disrupted. While the tripartite model can be used to explain the intended effects such as suppression of involuntary motor movements, it can also be used to explain occurrence of side effects which may occur whenever the associative and limbic portions of the STN are stimulated. However, there is no consensus in the literature on the exact topographic organization of the STN (Keuken et al., 2012).

An Introduction to Parkinson's Disease

PD is a progressive and chronic neurodegenerative disease, characterized by motor-related disturbances including bradykinesia, tremor, rigidity, and postural instability (Lang & Lozano, 1998). These symptoms are related to both abnormal voluntary and involuntary movements, which are controlled by the direct, indirect, and hyperdirect pathways explained in the above section (Braak & Del Tredici, 2008). The disease typically affects people of 50 years of age and older, with a higher occurrence in persons born with an XY than XX phenotype (Mayeux et al., 1992). Later stages of the disease include several secondary symptoms such as anxiety, confusion, chronic depression and stress, changes in speech, difficulty swallowing, and dementia. At present, PD is not curable or preventable.

In PD, dopaminergic denervation occurring in the SNc results in an overall reduction of dopamine available for neurotransmission within the basal ganglia (Calabresi, Centonze, & Bernardi, 2000). Therefore, a disruption in striatal output occurs, which is thought to cause an imbalance in the cortico-basal pathways and abnormal activity of downstream BG nuclei (Rubin, Mcintyre, Turner, & Wichmann, 2012). For instance, the loss of available dopamine also causes reduced activation of D1 receptors within the direct pathway and increased inhibition of D2 receptors in the indirect pathway, similarly resulting in excessive inhibitory effects on the THA (Wichmann & DeLong, 2006). Other occur in the BG in PD, such as abnormal spontaneous activity and hyperactivity of inhibitory GPi and STN neurons to the THA, which results in excessive inhibition of the motor cortex, represented by PD symptoms such as involuntary and hypokinetic movements (Hamani, Saint-Cyr, Fraser, Kaplitt, & Lozano, 2004; Jahanshahi, Obeso, Baunez, Alegre, & Krack, 2015). Furthermore, neurons within the different BG nuclei start to synchronize, which is thought to index a loss of functional specificity and impair the excitation-inhibition balance, reflected behaviorally by tics and tremors (Bronfeld & Bar-Gad, 2011). These are just a few examples of the reported physiological alterations observed in PD and reflect the complexity of the disease and the interconnected nature of the BG.

Like many neurodegenerative disorders, the primary symptoms of PD only occur once significant damage has already transpired. The brain initially exhibits dynamic,

compensatory mechanisms that mask symptoms of the disease, and in the case of PD, only tend to appear after patients have already lost 60 to 90% of their dopaminergic cells within the SN (Giguère, Nanni, & Trudeau, 2018). These compensatory mechanisms make it substantially more difficult to study disease progression in real-time, and attempt to halt pathological processes.

While we know what causes the symptoms of PD, at present we can only speculate as to the direct origin of the disease. For some patients, PD will arise due to mutations in specific genes which (e.g. the LRRK2, PARK7, PINK1, PRKN or SNCA genes) may or may not be hereditary, while other risk factors include exposure to certain chemicals and toxins or head trauma (Bartels & Leenders, 2009). More recent advancements have suggested that PD begins in the peripheral nervous system through the gut and nose, and its development is largely influenced by diet and the microbiome (Houser & Tansey, 2017). The diagnosis of PD is determined by clinical features and based upon several behavioral tests and symptomatic criteria. This makes for a somewhat subjective approach, with limited diagnostic accuracy. Confirmation for a diagnosis of PD can only be facilitated through ante- or post mortem neuropathology. While PD itself is not generally fatal, it can severely affect patients' quality of life, poses a great strain on their overall mental and physical health, and make them more vulnerable to certain types of infections (which can become fatal, e.g., recurrent and treatment resistant pneumonia due to inhalation caused by swallow problems). However, with appropriate treatment, PD patients can greatly reduce their symptomatic profile and expect a near to normal life expectancy.

Treatments for PD typically begin with dopamine replacement therapy by administration of Levodopa (L-DOPA), a type of dopamine agonist that works to increase dopamine concentrations, effectively restoring the normal functioning of the cortico-BG networks (Bastide, Meissner, & Picconi, 2015). However, dopamine replacement therapies do not alleviate pathological alterations in alternative neurotransmitter systems (e.g. cholinergic, noradrenergic, and serotonergic systems) (Klingelhoefer & Reichmann, 2017). The disease will continue to progress, and up to 45% of patients exhibit dyskinesias with L-DOPA. Additionally, more than half of patients will display wearing-off effects whereby the usual dosages no longer optimally control the symptoms of PD from as early as 2 years after

their initial treatment (Holloway et al., 2000).

DBS is a viable alternative for a subset of patients no longer responding to pharmacological intervention (Benabid et al., 2009). DBS is a neurosurgical procedure that involves the chronic implantation of bilateral electrodes into specific brain areas, that deliver high frequency-stimulation (constant or intermittent) and can improve motor function in PD by up to 60% (Limousin et al., 2002). At present the most common target is the STN, partly due to its position as a primary modulator of cortico-BG pathways and receiving direct connections from cortical motor areas. As previously discussed, the STN exhibits distinct pathophysiological activity associated with PD that can be modulated with electrical stimulation (Frank et al., 2007; Herz et al., 2015). While the exact mechanisms of DBS are not well understood, it is generally accepted that DBS may override pathological activity and restore 'normal' functioning (Romanelli, Esposito, Schaal, & Heit, 2005; Stefani et al., 2019). Identification of the STN for DBS in PD often relies on pre-operative magnetic resonance imaging (MRI) (O'Gorman et al., 2011) which will be discussed extensively throughout the rest of this thesis.

Basic MRI Concepts and Contrasts

Introduction

Magnetic Resonance Imaging (MRI) refers to a non-invasive method of neuroimaging that uses strong magnetic fields, radiofrequency (RF) waves, and gradient coils to visualize structural and functional anatomy. The basis of MRI relies on the notion that elements within our body (specifically protons) have magnetic properties and therefore can be modulated by large magnets. Protons (or hydrogen nuclei) are abundantly present in bodily water and fat. Each proton within your body possesses an intrinsic quantum property known as a nuclear spin; think of it as a small, rotating magnet that creates its own magnetic field. A spin results in two additional properties; angular momentum (A_M) and the magnetic moment (M_M). An M_M is the vector quantity used to determine a protons intrinsic magnetic field, and at which point it will respond to an external magnetic field (i.e., B0). Whereas A_M refers to the rate of rotation and rotational velocity, which usually remains constant but will also change in response to B0. When the body is placed into a strong magnetic field, such as an MRI scanner, a proportion of protons M_M will change and align with the main magnetic field (B0). When this happen across a large group of protons (in a vector), it creates a net magnetization, which refers to the aggregate magnetization of this large group of protons which now produces distinguishable amount of signal. However, the rotational force of a proton is resistant to change and the properties of A_M mean that the spins to not align precisely with B0, but rather at an angle to the field. Magnetic fields cause a twisting force, or a torque, which can alter the original direction of rotation of the spin vector, a process known as precession.

To create an MR image, we have to generate a measurable difference in signal of the spin vector, which is achieved via disruption of B0. Intentional disruption of the B0 field is achieved with RF pulses emitted via transmit coil(s) elements. These generate another magnetic field, known as B1, which forces (or flips) some of the protons' spin into a superposition of 'up' (parallel to B0, low-energy state) and 'down' (antiparallel B0, high-energy state) in the z-direction. Collectively, this results in tipping the net magnetization out of alignment with B0 and causes a phase coherence in a small proportion of the protons'

spins. Once the B1 field is removed, the net magnetization moves back towards B0 (relaxation, or more specifically, T1 relaxation) and additionally the phase coherence in the transverse plane is lost (dephasing, forming the basis of T2 and T2* relaxation) which collectively produces a net magnetization flux that is captured by the receive elements of the coil. This signal is amplified, digitized, and extracted into phase (location information of raw signal and inhomogeneities) and magnitude (amplitude information in greyscale representation of tissue magnetization) images, and recombined to form an MRI (McRobbie, Moore, Graves, & Prince, 2006). See figure 3.

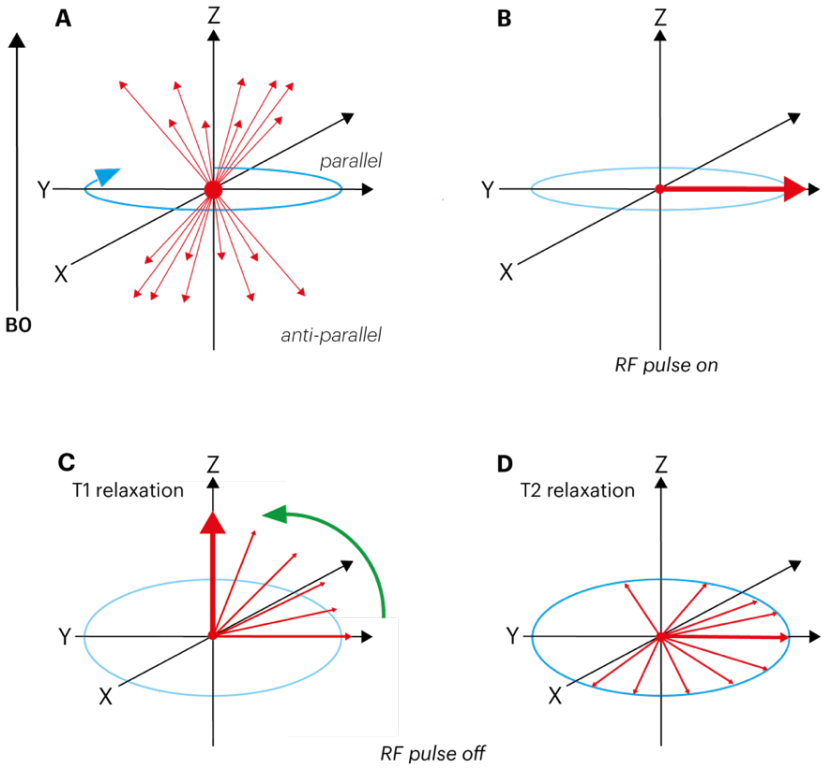

Figure 3: Mechanisms of MRI. (A) When the body enters the MRI scanner, a proportion of protons precess around the main magnetic field (B0), which can be parallel or anti-parallel. (B) When a radiofrequency pulse (RF) pulse is applied, the magnetic field flips and is now perpendicular to B0 (B1), and protons then align to the new B1 field and are locked in phase, precessing coherently in the transverse plane. Once the RF pulse is turned off (removing the B1 field), protons will undergo two changes. (C) The net magnetization vector will move back from the y to the z axis, which is known as longitudinal or T1 relaxation. As the protons move from y to z, (D) they will begin to lose their phase coherence in the x-y plane, which is known as T2 relaxation or dephasing.

Contrasts

Groups of protons within different tissues will realign to B0 at different rates due to their specific biochemical compositions. These different rates provide tissue contrast, via a visible or quantifiable difference in signal between anatomical structures (Hashemi, Bradley, & Lisanti, 2010; Plewes & Kucharczyk, 2012). Broadly speaking, there are three main forms of structural MRI contrast; T1, T2 and T2*, where the T1 signal relies on the speed at which the net magnetization vector realigns with B0, and T2, and T2* rely on the speed of dephasing[1].

T1

T1, also known as longitudinal relaxation, relies on the longitudinal relaxation of the net magnetization vector from the transverse plane back to its original maximum value (Mo), and can be described by the following calculation:

$$M_t = M_{max}(1\text{-}e^{-t/T1})$$

Where Mt refers to the magnetization at time *t* after application of the initial RF pulse at time t and Mmax refers to the fully recovered maximum magnetization. Specifically, T1 relaxation is modeled as an exponential growth curve with T1 as a first-order time constant where T1 refers to the time it takes to reach 63% of the Mo (Figure 4). As T1 relaxation occurs, the energy of the spins collectively decreases. This dissipation of energy is transferred into the surrounding environment and can influence the relaxation of neighboring spins and is therefore sometimes referred to as spin-spin relaxation. Generating T1 contrast is achieved through specific pulse sequences, comprised of a set of RF and gradient manipulations of the magnetic field, which typically consist of a short repetition time (TR) and echo time (TE). TR refers to the time between each RF pulse and TE to the time between the RF pulse and signal measurement. T1 sequences have a short TR to prevent the net magnetization from

[1] T1 and T2 relaxation begin to occur at the same time, however in some cases T2 can also occur without T1 relaxation, which is known as a 'flip-flop', referring to when one spinning proton has gained energy and another has lost, in the absence of net energy changes or transference

reaching the Mo (which would mean that all tissues produce a uniform intensity in the image) and incorporate a short TE to reduce the effect of T2(*) (discussed in the next section). T1 further depends on the flip angle (FA) which refers to the amount of rotation the net magnetization experiences in response to the RF pulse. Some tissues will relax within a single TR, while others may retain a portion of their FA across RF pulses, which allows for signal differentiation between tissues with varying T1 relaxation rates such as white matter (WM), grey matter (GM), and cerebral spinal fluid (CSF). Typically, in T1 images, GM will have intermediate signal intensity and appear, WM will be hyperintense compared to GM and appear white, and CSF will have a low signal intensity and appear black.

*T2 and T2**

T2, also known as transverse relaxation, refers to the process of dephasing along the *x-y* plane. After the application of the initial RF pulse, protons that initially showed a preference to the *x*-direction will be rotated into the transverse plane and start to spin in phase. These protons then subsequently decay from their aligned precession back to their original state. Transverse relaxation also occurs along a first-order exponential decay, whereby T2 is observed when the transverse magnetization reduces to 37% of its initial value (Figure 4). T2 occurs much faster than T1 relaxation, and is collected using both long TE and TR times. As protons within different tissues dephase at different rates, the TR and TEs can be manipulated to obtain contrast between structures. T2 relaxation specifically refers to the speed of dephasing that occurs in absence of any local field inhomogeneities. However, the decay of phase coherence is influenced by both local field inhomogeneities and interactions between neighboring spins. These local field inhomogeneities influence the local precession rates, which increases the rate of dephasing and therefore decreases the *effective* T2, which is known as T2*, forming the basis for an additional contrast mechanism (Chavhan et al., 2009). T2* occurs at a much faster rate than T2, and is typically obtained using longer and or multiple TEs to account for the influence of surrounding tissue types. The relationship between T2 and T2* can be expressed as:

$$1/T2^* = 1/T2 + \gamma \Delta Binhom$$

Here, γ is the gyromagnetic ratio of a proton, which is defined by the ratio of the magnetic moment to the angular momentum, and ΔBinhom refers to the magnetic field inhomogeneity across a voxel. T2* relaxation is especially useful for brain structures with higher paramagnetic compounds such as iron and diamagnetic components such as lipids within myelin and visualizes highly magnetic structures, such as subcortical nuclei, darker than surrounding grey and white matter, and fluids or fat show as intermediate-bright.

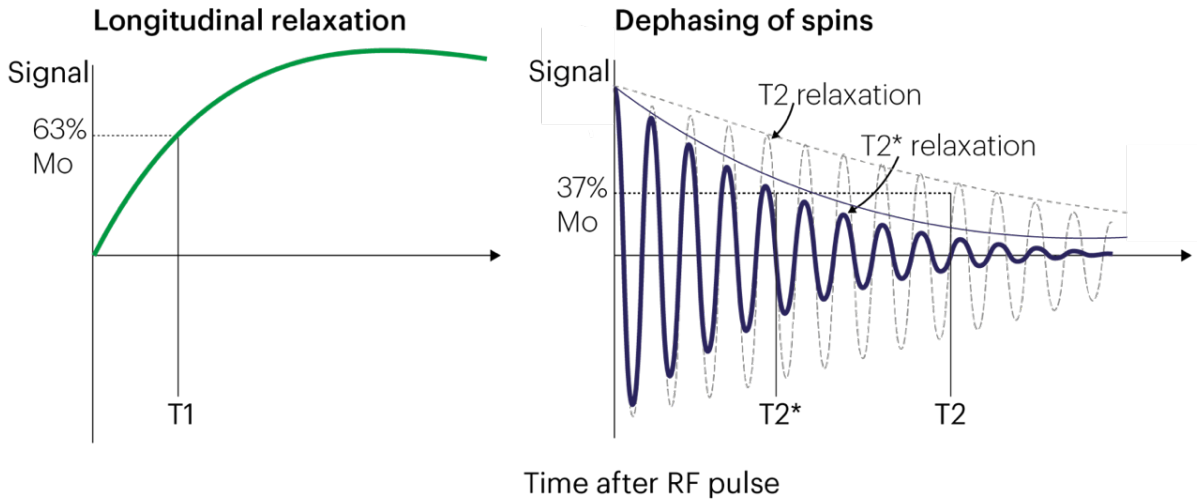

Figure 4: Relaxation times. The *y*-axis represents the signal from the net magnetization vector and the *x*-axis represents the time following the removal of an initial radiofrequency (RF) pulse. On the left, the green line shows the recovery of T1 relaxation time, where T1 is observed at 63% of the original net magnetization (Mo). The graph on the right shows the loss of phase coherence (dephasing) of protons that occurs upon removal of an RF pulse, simultaneously with T1 relaxation. Both T2 and T2* occur at 37% of Mo, though the T2* (thick blue line) is earlier than the T2 signal (dashed grey line). The amplitudes decrease as the spins move out of phase. Though the amplitude of the T2* signal decreases faster than T2 due to local field inhomogeneities where the magnetic fields of neighboring protons interfere with each other's rate of decay.

Structural and functional connectivity

In addition to imaging gross structural anatomy with T1, T2, and T2* contrasts, MRI can be used to image connectivity and function. Complex behaviors such as those driving motor action require communication between multiple brain areas (Rubinov & Sporns, 2010). Brain

areas may communicate through myelinated nerve fibers which are also known as white matter tracts that provide a physical, structural connection. Alternatively, brain areas can be functionally connected or form integrated networks which can be identified by temporal similarities, coupling or correlated signals, and coherence across structurally distinct cell groups. Structure and function can be imaged with diffusion MRI (dMRI) with subsequent tractography and task-based or resting-state functional MRI (rs-fMRI), respectively.

dMRI is based on the principles of Brownian motion of water molecules which refers to the random movement of small molecules like water that occurs due to thermal agitation (Brown, 1828). Intracellular molecules are highly constrained by the cell membrane whereas extracellular molecules can diffuse more freely, though are still constrained by multiple physical obstacles such as cell walls, organelles, macromolecules, and fibers (Bammer, 2003). Asymmetric white matter fibers are abundantly present throughout the brain and form the basis of structural connections between functionally distinct and distant brain regions. Extracellular water molecules are also present within these white matter fibers. Their movement within these fibers will exhibit highly restricted diffusion and the trajectory of molecules will show a preference for certain directions based on the orientation of the fiber which is mainly characterized by anisotropic diffusivity (Figure 5).

Diffusion is characterized in an MRI per voxel with a diffusion ellipsoid, represented as a three-order tensor. The tensor includes three eigenvalues ($\lambda 1, \lambda 2, \lambda 3$) and three principal eigenvectors ($\varepsilon 1, \varepsilon 2, \varepsilon 3$) which represent the displacement and diffusion. To simplify matters, the eigenvalue can be considered as a measure of stretch and shape, and the eigenvector as a measure of direction and orientation which together allow us to calculate four main measures of diffusion; fractional anisotropy (the degree of anisotropy or directional coherence), mean diffusivity (total diffusion or compactness), axial diffusivity and radial diffusivity (parallel and perpendicular diffusivity). dMRI uses T2 or T2* based sequences to image white matter fibers whereby water molecules showing little diffusion due to highly constrained boundaries exhibit very fast transverse relaxation rates (Basser, Mattiello, & LeBihan, 1994). Entire fibers are then tracked with post-processing techniques (chapters 5 and 6 discuss this in more detail).

rs-fMRI images the functional organization of the brain at rest by detecting changes

in blood flow with a contrast known as BOLD, or Blood-Oxygen-Level-Dependent imaging (Figure 6) (Khanna, Altmeyer, Zhuo, & Steven, 2015). BOLD is also commonly based on the T2* signal and image changes in the hemodynamic response that are controlled by the vascular arterial system. When brain areas become active, they require oxygen and glucose due to the increased neuronal energy demands. Oxygen and glucose are transported via fresh blood (oxygenated hemoglobin, oHb) to smaller brain regions via a network of interconnected capillary beds. The increase in oHb causes a subsequent net decrease in deoxygenated hemoglobin (dHb) within the arterial blood and is transported out through the venules to the venous blood system. oHb is diamagnetic and dHb is paramagnetic, therefore the changing ratio of oHb/dHb caused by increased blood flow results in quantifiable changes in magnetic susceptibility, specifically by an increase in T2*. Additional changes such as a higher rate of blood flow and expansion of the blood vessels also occur which contribute to the change in magnetic susceptibility due to brain activation. This allows us to localize the space and time at which specific brain areas are activated and link them to certain behaviors (Glover, 2011).

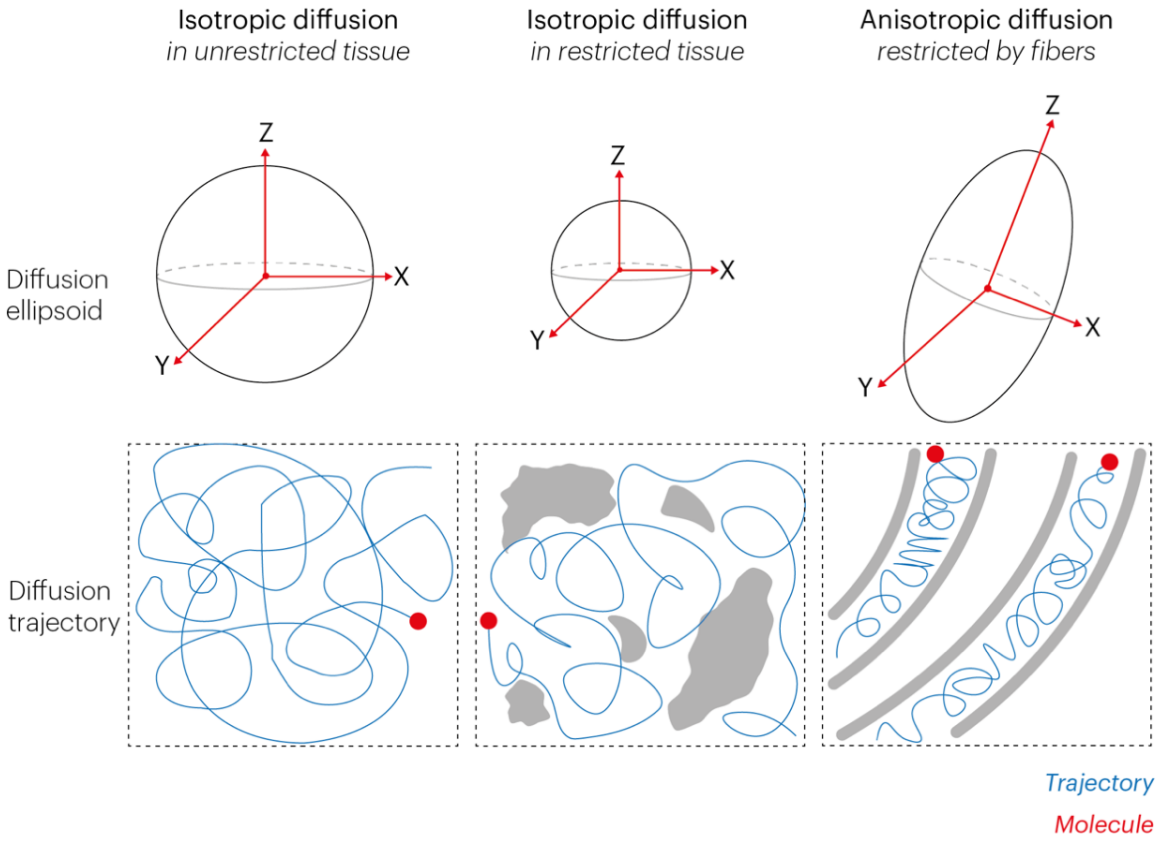

Figure 5: Diffusion ellipsoids and trajectory. On the far left, the diffusion ellipsoid reflects complete isotropic diffusion, where movement is restricted equally along each axis in 3D space. Below is an example of the diffusion trajectory of a molecule moving through unrestricted tissue. In the middle is an ellipsoid representing diffusion within randomly restricted tissue, but still isotropic as it is not following any coherent trajectory. On the far right is an ellipsoid representing highly anisotropic diffusion, which occurs when molecules move through restricted tissues such as white matter fibers as shown in the box below.

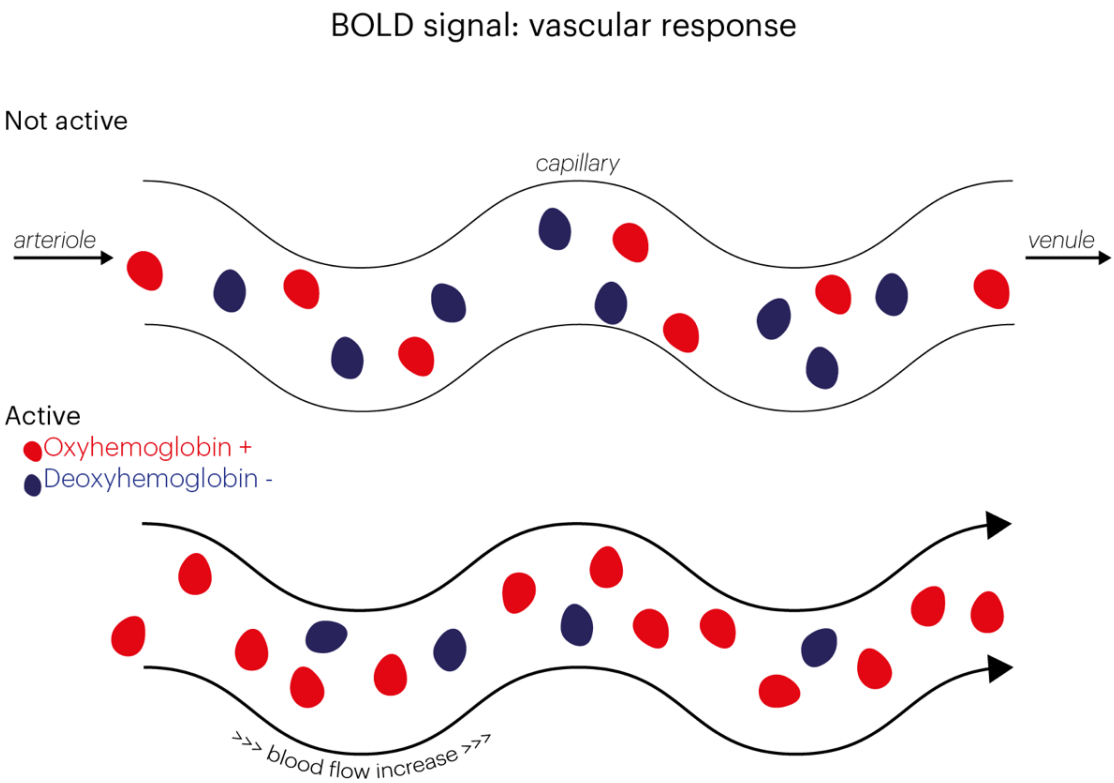

Figure 6: Blood-oxygen-level-dependent (BOLD) contrast mechanism. The BOLD signal refers to changes in spatially selective hemodynamic responses (i.e., blood flow) that occur in response to the increased demand in cellular energy that occurs when specific brain regions become activated. Increased energy demands require an increase in oxygenated blood (oxyhemoglobin, shown in red) compared to unoxygenated blood (deoxyhemoglobin, shown in blue), which leads to increased tissue susceptibility and therefore increased T2* signal. Moreover, blood flow and volume may also increase as shown in the bottom image. In fMRI, the signal commonly arises from signal changes that occur through blood flow from the arterioles, through to capillaries within the capillary bed, and out through venules as shown in this image; however, the fMRI signal may also arise from venous blood flow changes. Please note that a living brain is never totally inactive and that blood flow is a continuous mechanism, and in the absence of overt tasks the brain continues to exist in a default mode or resting-state.

Field strength

Only a small proportion of protons are manipulated by the magnetic field (B0). However, the number of protons that respond to B0 increase with the strength of the magnetic field, which is indexed by Tesla (or T). Increasing B0 produces a greater spin excess whereby spins in a low energy state exceed the number of spins in a high energy state. Subsequently, the precessional frequency of the spin vectors increase, which results in a larger net magnetization and therefore stronger signal. Moreover, MRI is inherently noisy, and the observed signals do not only arise from the tissue of interest but thermal motion within the rest of the body and electrical resistance within the MRI system itself (e.g., receiver coils). As higher strength MRI systems (7T +) manipulate more protons than lower field strengths (typically 1.5 and 3T), they can obtain stronger signal and contrast to noise ratios (SNR and CNR respectively) leading to better image quality (Kraff, Fischer, Nagel, Mönninghoff, & Ladd, 2014; Marques, Simonis, & Webb, 2019; Springer et al., 2016). However, lower field MRI systems are more common, particularly in healthcare settings, than 7 T+ due to several factors, not limited to cost, expertise, and safety factors. The concept of field strength is extensively discussed throughout this thesis; specifically, in chapters 1, 7, and 8.

Statistical Methods and Bayesian Interpretation

The majority of the statistics conducted in this thesis incorporated a Bayesian approach. Among the benefits of using Bayesian statistics is that it allows for the quantification of the strength of evidence in favor of the null hypothesis (H_0) versus the alternative hypothesis (H_1). The output of Bayesian statistics results in Bayes factors, which represents the likelihood of one particular hypothesis relative to another. Bayes factors noted as BF_{10} indicate favor for H_1 over H_0, and BF_{01} indicate favor for H_0 over H_1. For interpretation, we will use the Bayes Factors labels as proposed by (Jeffreys, 1961) and adjusted by (Wetzels and Wagenmakers, 2012) which are shown in table i. This table will be referred to throughout the thesis. Whereas frequentist approaches using a p-value as the significance criterion will lead to a dichotomous decision as to whether the data is probable under a null hypothesis or not. Further, Bayesian approaches determine the probability of an event depending on the observed data distribution, and can better handle biased population distributions. Therefore, Bayesian approaches are more suited to datasets that are small, with unequal groups, or drawn from non-normal distributions, such as clinical populations (Akaike, 1998; Rouder, Morey, Speckman, & Province, 2012).

Table i. Suggested categories for interpreting the Bayes factors.

Bayes factor BF_{10}			Interpretation
	>	100	Decisive evidence for H_1
30	-	100	Very strong evidence for H_1
10	-	30	Strong evidence for H_1
3	-	10	Substantial evidence for H_1
1	-	3	Anecdotal evidence for H_1
	1		No evidence
1/3	-	1	Anecdotal evidence for H_0
1/10	-	1/3	Substantial evidence for H_0
1/30	-	1/10	Strong evidence for H_0
1/100	-	1/30	Very strong evidence for H_0
	<	1/00	Decisive evidence for H_0

One

Visualizing the Human Subcortex using Ultra-High Field Magnetic Resonance Imaging

Introduction

In the last 25 years, the number of ultra-high field (UHF) (7.0 Tesla and higher) Magnetic Resonance Imaging (MRI) scanner sites has steadily increased globally (>70 UHF-MRI scanners worldwide at the time of writing). Previous reviews have highlighted the benefits of UHF-MRI in the clinical domain (Beisteiner et al., 2011; Benjamin, Viessmann, MacKinnon, Jezzard, & Markus, 2015; Van Der Kolk, Hendrikse, Zwanenburg, Visser, & Luijten, 2013) in functional (f)MRI (Barth & Poser, 2011; Francis & Panchuelo, 2014), and in the visualization of specific subcortical structures such as the basal ganglia (BG) (Plantinga et al., 2014). For the subcortex as a whole, ultra-high field imaging is especially important, because of the possibility of identification and parcellation of subcortical structures per individual. The use of atlases is more common for larger cortical and subcortical regions, but atlases only exist for a relatively low number of the smaller subcortical structures (Alkemade, Keuken, & Forstmann, 2013). In addition, the size and location of subcortical regions vary substantially between individuals (Keuken et al., 2014; Tona et al., 2017), necessitating visualization of these areas in individual space. The subcortex is approximately five times smaller than the neocortex but consists of a large number of unique subcortical structures (approximately 455 structures (Alkemade et al., 2013; Dirckx, 1998; Dunbar, 1992; Forstmann, de Hollander, Van Maanen, Alkemade, & Keuken, 2016)). See figure 1 for several subcortical structures.

Recent empirical studies on human cognition seem to neglect this part of the brain (Johansen-Berg, 2013). To understand how cognitive functions are implemented in the brain, it is, however, vital to study the entire network of structures that might be functionally involved. The so-called cortical-basal ganglia-thalamic loops exemplify how studying both cortical and subcortical areas is essential for fully understanding cognitive function (Alexander & Crutcher, 1990; Alexander, Crutcher, & DeLong, 1991; Ding & Gold, 2013; Haber & Calzavara, 2009). These structural loops have a general topographic organization, whereby distinct cortical areas project to both the striatum (STR) and subthalamic nucleus (STN). The STR and STN are strongly connected to other BG nuclei, which via thalamic sub-nuclei project back to the cortex. It is thought that as a result of these distinct structural

connections, the cortical-BG-thalamic loops are involved in motor, limbic, and cognitive functions (Alexander & Crutcher, 1990; Haber & Calzavara, 2009; Middleton, 2000). For instance, within the thalamus, the motor loop projects from the cortical motor areas to the ventral lateral nucleus pars oralis, whereas the cognitive loops, involving cortical areas such as the DLPFC, are thought to involve the directly adjacent ventral anterior nucleus pars parvocellularis (Middleton & Strick, 2000). To be able to study these functional domains it is therefore crucial to separate the distinct areas in the subcortex just as it is essential to identify the structural and functional distinct cortical areas (Forstmann et al., 2016; Turner, 2013; Turner & Geyer, 2014).

With the increase of field strength, substantial progress has been made in visualizing the human brain in extraordinary detail (Budinger et al., 2016; Cho, 2016; Dumoulin, Fracasso, van der Zwaag, Siero, & Petridou, 2018; Duyn, 2010; Federau & Gallichan, 2016; Gallichan, 2018; Giuliano et al., 2017; Kemper, de Martino, Emmerling, Yacoub, & Goebel, 2018; Marques, Khabipova, & Gruetter, 2017; Marrakchi-Kacem et al., 2016; Robitaille, 2007; Sclocco, Beissner, Bianciardi, Polimeni, & Napadow, 2017; Setsompop, Feinberg, & Polimeni, 2016; Turner & Haan, 2017; van der Zwaag, Schäfer, Marques, Turner, & Trampel, 2015). Using UHF-MRI, it has become possible to visualize intracortical anatomical structures, such as the bands of Baillarger, in vivo where before they could only be identified using post mortem myelin stains (Fracasso et al., 2016; Turner, 2011).

However, imaging the human subcortex with MRI has been particularly challenging for a number of reasons (Forstmann et al., 2016). The subcortex consists of a large number of small, directly adjunct structures of which a large number have anatomical properties that makes them very hard to distinguish with standard anatomical T1-weighted MRI and require tailored MRI contrasts (Priovoulos et al., 2018; Tourdias, Saranathan, Levesque, Su, & Rutt, 2014; Visser, Douaud, et al., 2016). Other general MRI factors that hinder the visualization of the subcortex include the substantially lower absolute SNR in the middle of the brain than in the cortex due to the increased distance from the elements of the modern head coils (de Hollander, Keuken, van der Zwaag, Forstmann, & Trampel, 2017; Wiggins et al., 2009). In addition, g-factor penalties associated with parallel imaging, are larger in the middle of the brain (Larkman, 2007; Pohmann, Speck, & Scheffler, 2015; Vaughan & Griffiths, 2012).

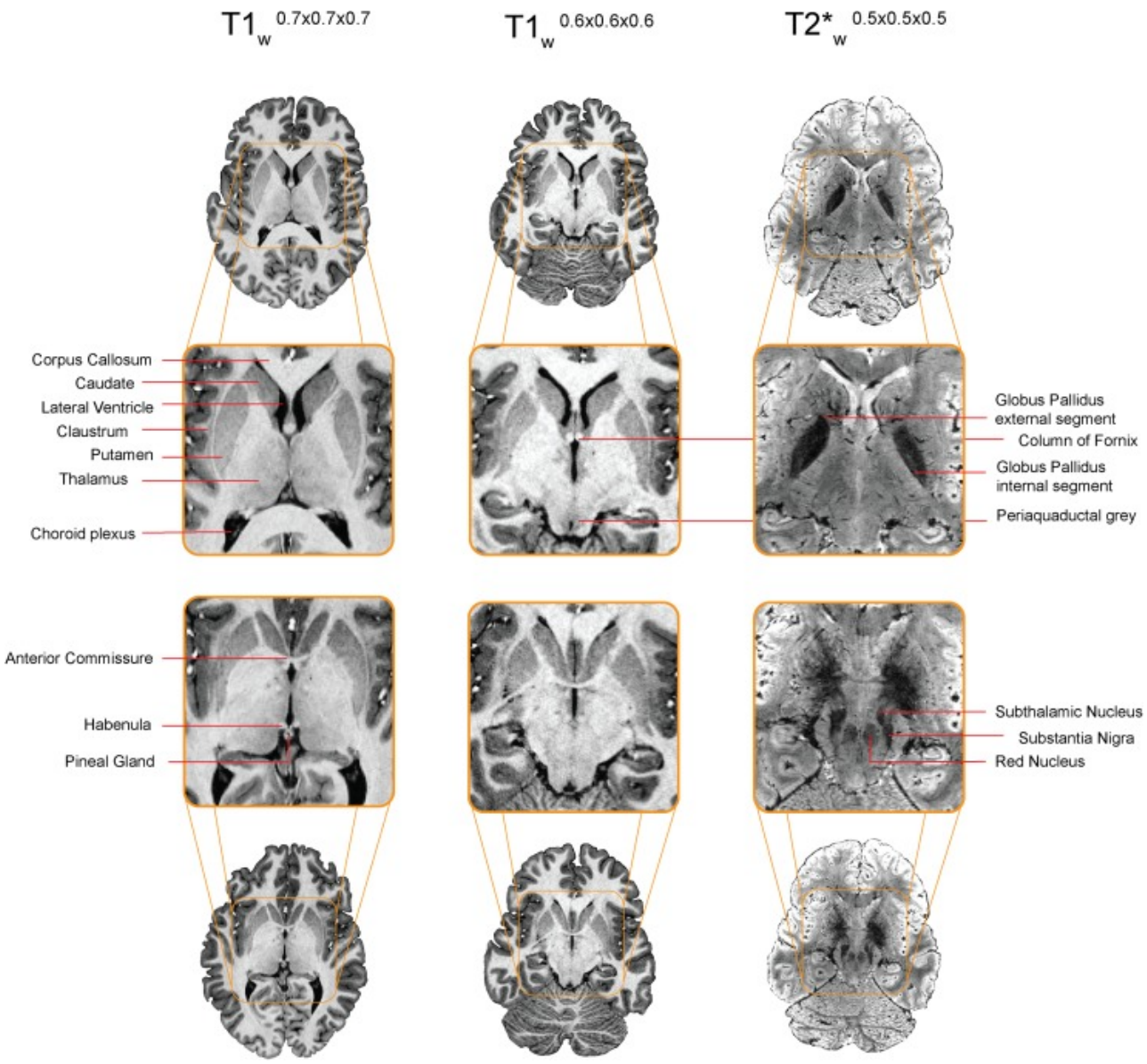

Figure 1: A visualization of several subcortical nuclei. Note that a number of nuclei, such as the STN, barely show any contrast on the T1-weighted scans but are clearly visible on the T2*-weighted scans. Image is adapted from (Forstmann et al., 2016).

The visualization of small subcortical structures benefits from UHF for many reasons. The first is the linear increase of signal-to-noise ratio (SNR) with field strength (Duyn, 2012; McRobbie, Moore, Graves, & Prince, 2006; Pohmann et al., 2015; Robitaille & Berliner, 2007; van der Zwaag et al., 2015). This increased SNR can be used to improve the spatial resolution and visualize fine-grained details due to reduced partial volume effects (PVE) (Federau & Gallichan, 2016; Lüsebrink, Wollrab, & Speck, 2013). Further, UHF-MRI can provide increased T1-contrast between grey and white matter (van der Zwaag et al., 2015). Similarly, T2* differences tend to be larger at 7T than at lower fields, leading to larger contrasts which have been used for the identification of anatomical borders between the substantia nigra (SN) and STN which were previously challenging to visualize (Abosch, Yacoub, Ugurbil, & Harel, 2010; Cho, Oh, et al., 2011; Dula et al., 2010). Finally, the g-factor penalties in the middle of the brain are lower on 7T than on 3T, which means that higher acceleration factors can be achieved on 7T with a smaller SNR loss than on 3T (Wen, Cross, & Yablonskiy, 2015). These advantages of UHF-MRI make it a powerful tool for visualizing small nuclei in vivo.

Using UHF-MRI several of the thalamic subnuclei can now be visualized in individual space without the need to refer to standardized atlases (Kanowski et al., 2014; Saranathan, Tourdias, Bayram, Ghanouni, & Rutt, 2014; Tourdias et al., 2014). However, a large and growing number of subcortical structures can be visualized using UHF-MRI, many of which have been demonstrated in a single publication. This paper provides an overview of the 163 subcortical structures which have so far been visualized in the human brain using UHF-MRI and the methods used to achieve this. The review will focus on the type of MRI sequence, participant demographics, and methods used to parcellate the structure of interest.

Materials and Methods

Search strategy

A comprehensive literature search was conducted using the Entrez search tools implemented in the Biopython's Bio.Entrez module (Cock et al., 2009). This is a python application programming interface (API) tool that queries the PubMed database (www.pubmed.org).

The query date was the 1st of December 2017 and used the following inclusion criteria: publication date was before the 1st of December 2017, focused on humans, used an MRI scanner with a static B0 field strength >= 7.0 Tesla, and report the visualization of a subcortical (either in the cerebrum, cerebellum or brainstem) nucleus or region. The search terms that were used were for example "ultra-high field magnetic resonance imaging", "7 Tesla structural MRI", "7T neuroimaging", and "7.0 Tesla magnetic resonance imaging". All search terms were used with the different common B0 field strengths for UHF-MRI (7.0, 8.0, 9.4, 10.5, and 11.7).

Inclusion procedure

All 5818 resulting abstracts were read by two raters (MCK & BRI) and based on the inclusion criteria detailed above, a decision was made to read the full-text paper or not. The abstracts that both raters did not agree on were checked again. The potential 388 full-text papers were read by a single rater (MCK) and were separated into reviews and empirical papers. The 299 empirical papers were checked for all inclusion criteria and if there was a match, the paper was included in the final list. The 58 review papers were cross-referenced, which entailed that the 5252 abstracts of all cited papers were read and checked for additional potential full-text papers. Finally, to test whether the employed search strategy resulted in a comprehensive set of papers, the included papers were compared to the publications of the authors of this review. The included papers were compared to the list of publications that were a priori known to fit the inclusion criteria. This comparison indicated that 2 out of the 27 papers by our own group were not found via the PubMed search, implying that approximately 7% of the empirical papers that would fit the inclusion criteria were not identified. The literature search resulted in the inclusion of 169 papers (see Figure 2 for an overview of the article selection procedure). The information extracted from the papers was as follows: which subcortical structures were visualized or parcellated, whether the measurements were from in vivo or post mortem samples, whether the population consisted of healthy or clinical subjects, which MRI contrast was used to visualize the subcortical structures and the accompanying MRI parameters.

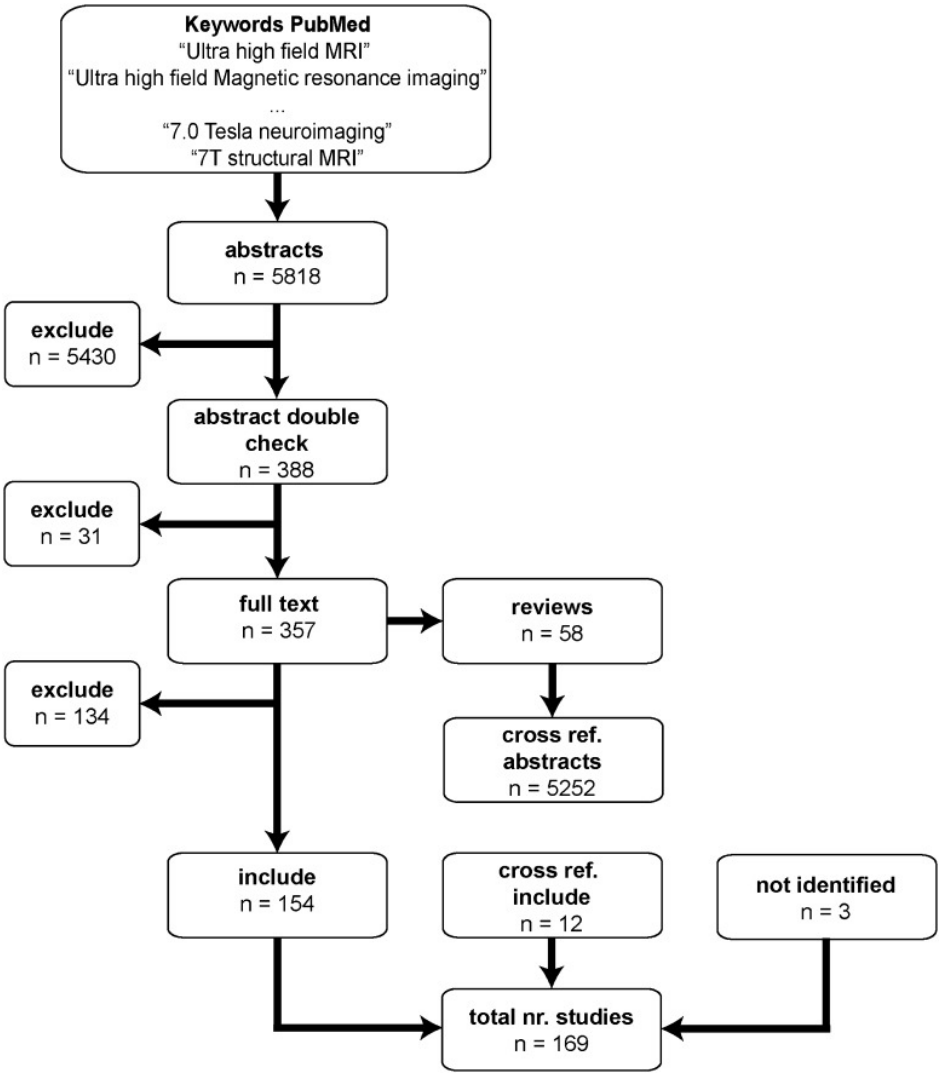

Figure 2: Search strategy. Using the Entrez search tools implemented in the Biopython's Bio.Entrez module the PubMed database was queried for several search terms. This resulted in a number of abstracts that were read and double-checked by two independent readers. The resulting full texts were then downloaded and separated into empirical studies and reviews. The empirical papers were read to check if they matched the inclusion criteria, resulting in the inclusion of 131 papers. The reviews were cross-referenced and resulting abstracts were read by one rater. The resulting full-text empirical papers were read, and an additional 9 papers were added. Finally, the 140 papers from the PubMed search were compared to the publications by the authors of this review. This resulted in 2 papers that were not identified by our search strategy

Identification versus parcellation

The subcortical structure(s) in each paper was classified as being either 'identified' or 'parcellated'. Identification was defined as the placement of abbreviations, arrows, or other visual markers that corresponded to an anatomical label in an image of a structural MRI scan. Parcellation was defined as the manual, automatic, or semi-automatic delineation of the entire or partial structure. Manual parcellation is defined as the process where an expert delineates and labels the borders of a region of interest (ROI) manually (e.g., (Kwon et al., 2012; Lenglet et al., 2012)). Automatic parcellation is defined as the process where the ROI is parcellated using a software package without any manual editing (e.g., (Visser, Douaud, et al., 2016; Zhang, Brady, & Smith, 2001)). Semi-automatic parcellation is defined as automatic parcellation whereby the resulting parcellation is manually edited if needed (e.g.(Mestres-Missé, Bazin, Trampel, Turner, & Kotz, 2014)). The parcellation method had to employ the actual contrast of the nuclei and the surrounding tissue. Single atlas label propagations, where an individual anatomical MRI scan is registered to a pre-labeled standard structural template, were excluded. The reason for this exclusion is that label propagation is a registration problem between the template and the entire individual anatomical MRI volume and is unable to capture large anatomical variation (Cabezas, Oliver, Lladó, Freixenet, & Cuadra, 2011; Doan, de Xivry, & Macq, 2010).

MRI sequence classes

The MRI contrast which was used to visualize the structures of interest were grouped according to the main classes of contrasts: T1, T2, T2*, functional (regardless of underlying mechanism), Diffusion-Weighted Imaging (DWI), Susceptibility Weighted Imaging (SWI), including Phase Imaging and Quantitative Susceptibility Mapping (QSM), Magnetization Transfer (MT), Proton Density (PD), multiple, and other. The multiple MRI sequence category entails those studies that visualized the structure of interest in a number of MRI sequences. Inclusion in the 'other' category was either a single MRI sequence that was not specific to a given contrast mechanism (e.g., both PD and T2 weighted) or did not fit the

above classification scheme (e.g., magnetic resonance spectroscopy). It is beyond the scope of this review to go into a detailed description of the separate contrast mechanisms and we refer to the following literature (McRobbie et al., 2006; Robitaille & Berliner, 2007).

Very briefly, a T1 contrast is based on the recovery time of the longitudinal component of the magnetization following the application of a radiofrequency excitation pulse, while T2 refers to the decay of the transverse magnetization component as a result of proton interactions (McRobbie et al., 2006). The T2* contrast is based on the decay of the transverse magnetization component as a result of proton interactions and the magnetic field inhomogeneity (Chavhan et al., 2009; McRobbie et al., 2006). The DWI contrast is based on the dephasing of the protons due to the diffusion of water molecules (Chilla, Tan, Xu, & Poh, 2015; Jones, Knösche, & Turner, 2013). SWI and QSM contrasts are based on a combination of T2*-weighted magnitude and filtered phase images (Haacke, Mittal, Wu, Neelavalli, & Cheng, 2008; Liu, Li, Tong, Yeom, & Kuzminski, 2014). The MT contrast is based on the effect of off-resonance RF pulses on bound and free moving protons (Grossman, Gomori, Ramer, Lexa, & Schnall, 1994; McRobbie et al., 2006). Finally, the PD contrast reflects the density of the protons (McRobbie et al., 2006). To be able to summarize across a large number of sequence categories no distinction was made between quantitative or qualitative MRI scans (e.g., T1 maps versus T1 weighted scans or QSM versus SWI).

(Near) Isotropic voxel size

Isotropic voxels are essential when visualizing small structures, as they have equal biases in all directions when determining the borders. Using anisotropic voxels has the advantage of high in-plane resolution, but determining the border in the z-direction becomes problematic as PVE are increased and can result in measurement biases of subcortical structures (Wonderlick et al., 2009). We determined whether a study acquired isotropic or near isotropic voxels by first calculating the reported voxel volume. For a given volume, the corresponding isotropic voxel dimension was calculated and compared to the actual acquired voxel size. If the acquired voxel dimensions were within a 10% margin of the isotropic dimensions, the acquired voxel was deemed (near) isotropic, all other voxels were classified as anisotropic.

Open access and interactive use

All data and code used to analyze and generate the summary figures can be found online (https://osf.io/fwc2p/). In addition, a condensed R script is provided which can be used to generate the list of subcortical structures identified with UHF as well to create a summary figure (figures 6,7, 8) for a given structure of interest. The R code contains a description of software requirements and instructions for use.

Results

A total of 169 papers were published between 1993 and 2018 that together report the visualization of 163 subcortical structures using 7 Tesla or higher, including both in vivo and post mortem studies. The most frequently employed field strength was 7.0T (7.0T: 147 studies; 8.0T: 7 studies; 9.4T: 11 studies; 11.7T: 2 study; 21.1T: 2 studies; see Figure 3a). This was expected as the number of 7.0T MRI scanner sites is much larger than that of the higher field strengths (Plantinga et al., 2014). The most frequently employed MRI contrast across the different field strengths and structures were T2* based scans, followed by T1, SWI, and T2 contrasts (see Figure 3b for the frequency of using a given MRI contrast).

Demographics

The overall sample size ranged between 1 and 152 participants, with a mean sample size of 18.99 (SD 21.81) and a median of 11 participants across the 169 papers. The in vivo sample size was on average 19.09 (SD 17.93) with a median of 13 participants. The post mortem sample size was on average 15.67 (SD 31.90) with a median of 3.5 specimens. 108 studies included only healthy controls, 13 studies included only patients, 43 studies included both patient and healthy participants, and for 5 studies the participants' status was not disclosed. The most frequently measured patient groups with UHF-MRI were people suffering from Parkinson's Disease (PD) and Multiple Sclerosis followed by studies that focused on fetal development and or fetal abnormalities. Two out of the six studies that included fetal samples

used a wide-bore UHF-MRI scanner (see table 1).

Subcortical structures

The frequency with which a structure was reported ranged between 1 and 51, with a mean reported frequency of 4.62 (SD 8.88) and a median of 1. There are 55 UHF-MRI studies that only reported a single structure, whereas for 83 structures there was only a single UHF-MRI study that visualized that specific structure (e.g., for the locus coeruleus (Keren et al., 2015); the field of Forel (Massey et al., 2012); and a number of thalamic sub-nuclei such as the magno- and parvocellular part of the lateral geniculate nucleus (Denison et al. 2014)). The SN was reported most frequently (51 reports), closely followed by the red nucleus (50 reports) and putamen (48 reports; see Figure 3d for the seventeen most frequently reported structures).

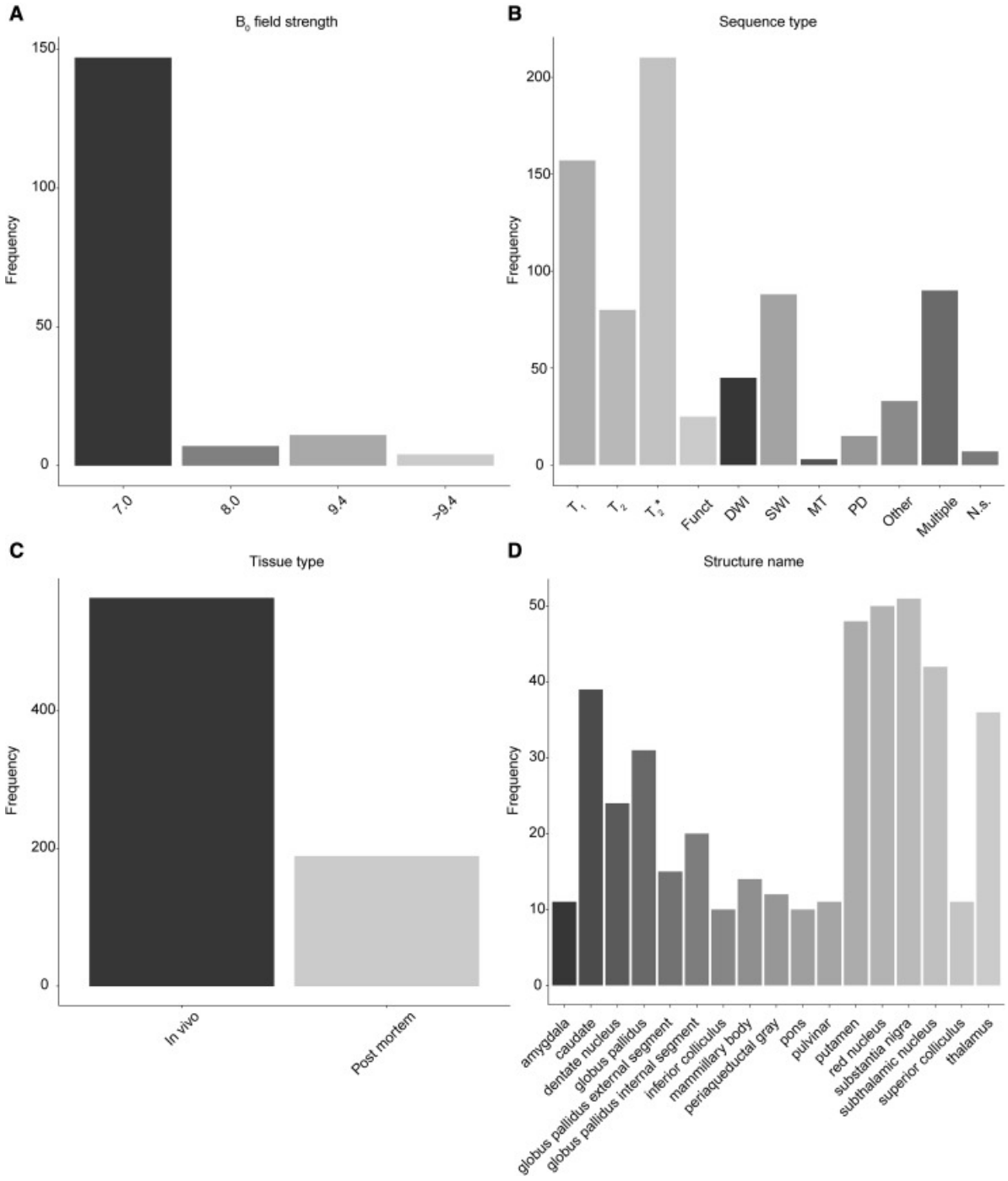

Figure 3: Overview results. **a**) The frequency that an MRI scanner with a given B_0 field strength was used in the 142 studies. **b**) The frequency of using a certain MRI sequence type to visualize a subcortical area. **c**) Of the 658 cases of identifying a subcortical area, most were done using in vivo samples. **d**) The thirteen most frequently reported structures. Funct functional MRI sequences that employed functional localizer stimuli, DWI diffusion-weighted imaging; SWI susceptibility-weighted imaging, MT magnetization transfer; PD proton density, N.s. not stated

Table 1. The publications that identified a subcortical structure with the use of UHF-MRI.

Publication	Tesla	Vendor	Structure	In vivo /Post mortem	Control /Patient	Type of Patient	N	F/M	age (sd)
Abduljalil et al., 2003	8.0	Brucker	cau, gp, put, rn, tha, other	In vivo	Control	-	20	n.s.	n.s.
Abosch et al., 2010	7.0	Siemens	gp, gpe, gpi, pul, rn, sn, stn, tha, other	In vivo	Control	-	6	n.s.	n.s.
Aggarwal et al., 2013	11.7	Brucker Biospin	other	PM	Control	-	1	1/0	n.s.
Al-Helli et al., 2015	9.4	Varian	stn	PM	Patient	Idiopathic PD	1	0/1	73
Al-Radaideh et al., 2013	7.0	Phillips	cau, gp, pul, put, other	In vivo	Control	-	20	7/13	34.6 (9.4)
					Patient	Clinically Isolated Syndrome	19	10/9	26.63 (8.9)
Alarcon et al., 2014	7.0	Brucker Biospin	cau, gpe, gpi, put, rn, sn, stn, other	PM	Control	-	5	n.s.	n.s.
Alkemade et al., 2017	7.0	Siemens	stn	In vivo	Control	-	12	6/6	65 (7.9)
					Patient	PD	12	6/6	68 (9,6)
Augustinack et al., 2014	7.0	Siemens	mam, rn, sn	PM	Patient	Medically intractable epilepsy	1	0/1	82
Bao et al., 2017	7.0	Siemens	cau, gp, put, sn, rn	In vivo	Control	-	5	0/5	30-36
Barry et al., 2013	7.0	Phillips	sn, other	In vivo	Control	-	26	3/23	30.7
Batson et al., 2015	7.0	Phillips	den, other	In vivo	Control	-	7	¾	31 (n.s.)
Betts et al., 2016	7.0	Siemens	amy, cau, den, gp, gpe, gpi, put, rn, stn, sn, tha	In vivo	Control	-	40	22/18	47
Beulset al.,1993	9.4	Varian	other	PM	n.s.	-	5	n.s.	n.s.
Beuls et al., 2003	9.4	Varian	pns, other	PM	Patient	Fetal specimen Arnold-Chiari type 2 malformation	1	n.s.	20 weeks of GA
					Control	Fetal specimen	1	n.s.	21 weeks of GA
Bianciardi et al., 2015	7.0	Siemens	stn, other	In vivo	Control	-	12	6/6	28 (1)

Bianciardi et al., 2017	7.0	Siemens	other	In vivo	Control	-	12	6/6	28 (1)
Blazejewska et al., 2013	7.0	Philips	sn	In vivo	Control	-	2	n.s.	39
				PM	Control	-	2	n.s.	56
				PM	Patient	PD	1	n.s.	75
Blazejewska et al., 2014	7.0	Philips	rn, sn	In vivo	Control	-	27	n.s.	36.4 (8.8)
				In vivo	Patient	Relapsing-remitting MS	14	n.s.	42.4 (11.3)
				In vivo	Patient	Clinically Isolated Syndrome	21	n.s.	37.2 (8.8
Bourekas et al., 1999	8.0	Brucker	cau, gp, gpi, ic, mam, pag, pns,put, rn, sc, sn, tha	In vivo	Control	-	1	1/0	30
Bouvy et al., 2014	7.0	Philips	put	In vivo	Control	-	13	n.s.	18 - 80
Bouvy et al., 2016	7.0	Philips	other	In vivo	Control	-	50	30/20	63 (8.5)
Budde et al., 2010	9.4	Siemens	cau, gp, put, other	In vivo	Control	-	5	n.s.	n.s.
Budde et al., 2014	9.4	Siemens	put	In vivo	Control	-	5	1/4	33 (n.s.)
Calamante et al., 2013	7.0	Siemens	cau, mam, pul, rn, sn, other	In vivo	Control	-	4	2/2	27-31
Chalifoux et al., 2013	7.0	Siemens	cau, other	In vivo	Patient	Tuberous Sclerosis complex	4	2/2	21.75 (4.35)
Chen et al., 2010	7.0	Siemens	cau, sn	In vivo	Control	-	1	n.s.	n.s.
Cho et al., 2008	7.0	Siemens	mam, pns, rn, sn, stn, tha, other	In vivo	Control	-	n.s.	n.s.	early twenties
Cho, Min et al., 2010	7.0	Siemens	gpe, gpi, put, sn, stn	In vivo	Control	-	11	n.s.	21-30
				In vivo	Patient	PD	1	1/0	48
Cho, Han et al., 2010	7.0	Siemens	amy	In vivo	Control	-	13	7/9	42.5 (n.s.)
Cho, Choi et al., 2011	7.0	Siemens	ic, mam, sc, tha, other	In vivo	Control	-	34	12/22	24.29 (n.s.)
Cho et al., 2008	7.0	Siemens	rn, sn	In vivo	Control	-	9	8/1	67.7 (7.4)
				In vivo	Patient	Early PD	8	7/1	58.3 (8.5)
				In vivo	Patient	Late PD	2	1/1	59 (11.3
Cho, Son et al., 2011	7.0	Siemens	pul, other	In vivo	Control	-	5	n.s.	n.s.

Christoforidis et al., 1999	8.0	Brucker	cau, gp, mam, pul, put, sc, tha, other	In vivo	Control	-	n.s.	n.s.	n.s.
Cosottini et al., 2015	7.0	GE	rn, other	In vivo	Control	-	13	4/9	54.8 (n.s.)
				In vivo	Patient	PD	14	6/8	57.4 (n.s.)
Cosottini et al., 2014	7.0	GE	other	In vivo	Control	-	13	4/9	54.7
				PM	Control	-	1	1/0	67
				In vivo	Patient	PD	17	9/8	52.2
Costagli et al., 2015	7.0	GE	amy, other	In vivo	Control	-	10	3/7	51.7 (n.s.)
de Hollander et al., 2014	7.0	Siemens	stn	In vivo	Control	-	13	6/7	24.38 (2.36)
				PM	Control	-	5	3/2	82.4
de Hollander et al., 2017	7.0	Siemens	stn	In vivo	Control	-	20	10/10	26 (2.6)
de Martino et al., 2013	7.0	Siemens	ic, other	In vivo	Control	-	9	4/5	n.s.
De Reuck, Deramecourt et al., 2014	7.0	Brucker BioSpin	cau, den, gp, mam, put, rn, sn, stn, tha, other	PM	Control	-	15	2/13	65
				PM	Patient	AD	46	24/22	78
				PM	Patient	Frontotemporal lobar degeneration	37	17/20	68
				PM	Patient	Amyotrophic lateral sclerosis	11	8/3	66
				PM	Patient	Lewy body disease	13	2/11	80
				PM	Patient	PSP	14	10/4	74
				PM	Patient	Vascular dementia	16	9/7	80
De Reuck et al., 2014	7.0	Brucker BioSpin	den, pns, rn, sn, tha, other	PM	Control	-	11	n.s.	n.s.
				PM	Patient	PSP	14	n.s.	n.s.
De Reuck et al., 2015	7.0	Brucker BioSpin	den	PM	Control	-	16	8/8	68
				PM	Patient	AD	38	17/21	71.82
				PM	Patient	Frontotemporal lobar degeneration	10	4/6	68

				PM	Patient	Amyotrophic lateral sclerosis	9	4/5	65
				PM	Patient	Lewy body disease	10	3/7	82.4
				PM	Patient	PSP	12	8/4	75
				PM	Patient	Vascular dementia	9	6/3	68
De Reuck et al., 2017	7.0	Brucker BioSpin	put	PM	Control	-	11	3/8	71 (9)
				PM	Patient	Vascular dementia	14	3/11	75 (10)
				PM	Patient	Mixed dementia	24	5/19	76 (11)
Deistung et al., 2013	7.0	Siemens	ic, mam, rn, sc, sn, other	In vivo	Control	-	6	2/4	27.3 (3)
Deistunget al., 2013	7.0	Siemens	gpe, gpi, mam, pul, put, rn, sc, sn, stn, tha, other	In vivo	Control	-	9	5/9	25.3 (2.8)
Denison et al., 2014	7.0	Siemens	other	In vivo	Control	-	6	5/1	25-27
Derix et al., 2014	7.0	Siemens	amy	In vivo	Control	-	6	n.s.	24-28
Dezortova et al., 2012	7.0	Siemens	cau, gp, put	In vivo	Control	-	5	2/3	42 (13.76)
				In vivo	Patient	Panthothenate-kinase associated neurodegeneration	6	4/2	20.47 (7.46)
Di Ieva et al., 2011	7.0	Siemens	den	In vivo	Control	-	2	n.s.	n.s.
Diedrichsen et al., 2011	7.0	Siemens	den, other	In vivo	Control	-	23	14/9	35.1 (13.1)
Dortch et al., 2013	7.0	Philips	put, tha, other	In vivo	Control	-	13	3/10	22-37
Eapen et al., 2011	7.0	Philips	mam, rn, sn, other	In vivo	Control	-	10	3/7	20-40
	7.0	Siemens	pns, put, sn	In vivo	Control	-	12	7/5	54 (8)
				In vivo	Patient	PD	13	6/7	56 (10)
Faull et al., 2015	7.0	Siemens	amy, cau, gp, put, sn, stn, other	In vivo	Control	-	16	6/10	28(7)
Federau & Gallichan, 2016	7.0	Siemens	amy, cau, gpe, gpi, ic, mam, pag, pul, put, stn, rn, sc, other	In vivo	Control	-	1	0/1	34
Foroutan et al., 2013	21.1	Brucker BioSpin	gpi, gpe, put, rn, sn	PM	Control	-	3	3/0	70 (4)

				PM	Patient	PSP	6	6/0	76 (6)
Forstmann et al., 2010	7.0	Siemens	stn	In vivo	Control	-	9	6/3	24.5 (2.1)
Forstmann et al., 2012	7.0	Siemens	stn	In vivo	Control	-	13	6/7	24.38 (2.36)
Forstmann et al., 2014	7.0	Siemens	cau, gpe, gpi, put, rn, sn, stn, tha, other	In vivo	Control	-	54	25/29	39.72 (n.s.)
(Forstmann et al., 2017)	7.0	n.s.	gp, stn, other	In vivo	Patien	PD	1	0/1	57
Fritzsch et al., 2014	7.0	Siemens	gp, put, rn, sn, other	In vivo	Control	-	10	5/5	44 (n.s.)
				In vivo	Patient	Wilson's Disease	11	6/5	41 (n.s.)
Frosini et al., 2017	7.0	GE	other	In vivo	Control	-	10	3/7	65.2 (5.1)
				In vivo	Patient	MSA	6	n.s	64.5 (7.64)
				In vivo	Patient	PSP	5	n.s	71.4 (8.82)
				In vivo	Patient	CBD	4	n.s	69.8 (4.57)
Fujioka et al., 2011	21.1	Brucker BioSpin	gpe, gpi, put	PM	Control	-	1	0/1	87
				PM	Patient	Diffuse Lewy body disease	1	0/1	81
Ghaznawi et al., 2017	7.0	Philips	cau	In vivo	Patient	Systematic atherosclerotic disease	90	17/73	68 (8)
Gizewski et al., 2007	7.0	Siemens	tha	In vivo	Control	-	9	2/7	31 (n.s.)
Gizewski et al., 2013	7.0	Siemens	pag, other	In vivo	Control	-	8	5/3	31 (n.s.)
Gorka et al., 2018	7.0	Siemens	other	In vivo	Control	-	27	14/13	27.3 (6)
Grabner et al., 2014	7.0	Siemens	den	In vivo	Control	-	8	n.s.	n.s.
Hammond, Lupo, et al., 2008	7.0	GE	cau, gpe, gpi, pag, pns, put, rn, sn, tha	In vivo	Control	-	12	5/7	36.9 (n.s.)
				In vivo	Patient	MS	10	3/3	43.6 (n.s.)
				In vivo	Patient	Brain tumors	25	10/15	48.6 (n.s.)
Hammond, Metcalf, et al., 2008	7.0	GE	cau, gp, put, tha	In vivo	Control	-	13	8/5	40.15 (14.19)
				In vivo	Patient	Relapse remitting MS	19	16/6	42.32 (12.9)

Kanowski et al., 2014	7.0	Siemens	other	In vivo	Control	-	5	3/2	21-28
Keren et al., 2015	7.0	Brucker	other	PM	Patient	AD	7	4/3	76.4 (9.5)
Kerl et al., 2012	7.0	Siemens	rn, sn, stn, other	In vivo	Control	-	9	4/5	25 (n.s.)
Kerl, 2013	7.0	Siemens	gp, rn, sn, other	In vivo	Control	-	9	4/5	25 (n.s.)
Keuken et al., 2013	7.0	Siemens	stn	In vivo	Control	-	31	15/16	45.93 (n.s.)
Keuken et al., 2014	7.0	Siemens	stn	In vivo	Control	-	30	14/16	24.2 (2.4)
Keuken & Forstmann, 2015	7.0	Siemens	gpe, gpi, rn, sn, stn, other	In vivo	Control	-	15	9/6	23.7 (1.58)
Keuken et al., 2017	7.0	Siemens	gpe, gpi, pag, rn, sn, stn, other	In vivo	Control	-	53	21/31	39.72 (n.s.)
Khabipova et al., 2015	7.0	Siemens	cau, gp, put, rn, sn	In vivo	Control	-	3	1/2	30 (6)
				In vivo	Patient	MS	1	n.s.	n.s.
Kim et al., 2011	7.0	n.s.	other	In vivo	Control	-	20	6/14	22-30
Kim et al., 2014	7.0	n.s.	cau, gpe, gpi, put, sn, stn, tha	In vivo	n.s.	-	5	n.s.	n.s.
Kim, Son et al., 2015	7.0	n.s.	ic, pns, sc, tha, other	In vivo	Control	-	16	4/12	30 (7.9
Kim, Son, Kim, et al., 2015	7.0	n.s.	pul, other	In vivo	Control	-	15	5/10	30.5
				In vivo	Patient	Schizophrenia	12	3/9	29.7
Kim et al., 2016	7.0	Siemens	sn	In vivo	Control	-	26	15/11	49.5 (12.6)
				In vivo	Patient	PD	30	15/15	51.0 (9.6)
				In vivo	Patient	MSA	7	6/1	55.3 (6.1)
				In vivo	Patient	PSP	3	0/3	71.0 (4.6)
Kim et al., 2017	7.0	n.s.	other	In vivo	Control	-	18	5/13	32.6 (12)
				In vivo	Patient	Schizophrenia	19	7/12	30.7 (7.9)
Kim et al., 2018	7.0	Siemens	cau, put, sn, stn, other	In vivo	Control	-	n.s.	n.s	n.s.
Kirov et al., 2013	7.0	Siemens	rn	In vivo	Control	-	15	7/8	35.6 (9.4)
	7.0			In vivo	Patient	Schizophrenia	16	6/10	40.7 (10.6)
Kollia et al., 2009	7.0	Siemens	den	In vivo	Patient	MS	12	8/4	32 (n.s.)

Küper, Dimitrova, et al., 2011	7.0	Siemens	den	In vivo	Control	-	23	0/23	28.1 (6.3)
Küper, Thürling, et al., 2011	7.0	Siemens	den	In vivo	Control	-	23	0/23	28.1 (6.3)
Küper et al., 2013	7.0	Siemens	den	In vivo	Control	-	19	7/12	26.6 (3.8)
Kwon et al., 2012	7.0	Siemens	rn, sn, stn	In vivo	Control	-	10	9/1	59.7 (5.1)
				In vivo	Patient	PD	10	7/3	60 (7.2)
Lee et al., 2014	7.0	Siemens	other	In vivo	Control	-	18	10/8	45.2 (10.9)
				In vivo	Patient	Primary open-angle glaucoma	18	10/8	47.6 (13.3)
Lenglet et al., 2012	7.0	Siemens	cau, gpe, gpi, put, sn, stn, tha	In vivo	Control	-	4	n.s.	23-57
Liem et al., 2012	7.0	Philips	gp, put, tha, other	In vivo	Control	-	18	8/10	45.8 (12.8)
				In vivo	Patient	NOTCH3 mutation carriers	25	13/12	46.5 (12.2)
				PM	Patient	NOTCH3 mutation carriers	3	2/1	60.67 (3.06)
Liu et al., 2011	7.0	Brucker	den	PM	Control	Fetal specimen	40	n.s.	14-22 weeks GA
Lotfipour et al., 2011	7.0	Philips	rn, sn, other	In vivo	Control	-	11	7/4	59.13 (8.59)
				In vivo	Patient	PD	9	5/4	64.67 (13.28)
Makris et al., 2013	7.0	n.s.	other	PM	Control	-	2	0/2	40 (15.57)
Marques et al., 2010	7.0	Siemens	den	In vivo	Control	-	3	1/2	30 (n.s.)
Marques & Gruetter, 2013	7.0	Siemens	cau, put, other	In vivo	control	-	7	n.s.	26.29 (n.s.)
Massey et al., 2012	9.4	Varian	gp, gpi, mam, pul, rn, sc, sn, stn, tha, other	PM	Control	-	8	4/4	77.34 (17.64)
Meijer et al., 2016	11.7	Brucker	rn, other	PM	Control	-	2	2/0	80 (5.66)
					Patient	PD	2	1/1	78.5 (3.53)
Meng et al., 2012	7.0	Brucker	cau, other	PM	Control	Fetal specimen	69	n.s.	12-22 weeks GA

Mestres-Missé et al., 2014	7.0	Siemens	other	In vivo	Control	-	23	11/12	26 (3)
Miller et al., 2015	7.0	Philips	amy	In vivo	Control	-	1	0/1	42
Mitsumori et al., 2011	7.0	Siemens	cau, gp, put, tha	In vivo	Control	-	6	0/6	49.3 (8)
Moenninghoff et al., 2010	7.0	Siemens	den	In vivo	Patient	Lhermitte-Duclos disease	1	0/1	46
Moerel et al., 2015	7.0	Siemens	other	In vivo	Control	-	6	5/1	25 (1.7)
Mollink et al., 2015	7.0	Siemens	den, tha	PM	Control	-	1	1/0	87
Novak et al., 2001	8.0	Brucker	ic, pag, pns, rn, sc, sn, other	In vivo	Control	-	5	2/3	34-46
Novak et al., 2001	8.0	Brucker	cau, gp	In vivo	Control	-	11	n.s.	37-59
				In vivo	Patient	Hypertensive	6	n.s.	37-59
O'Brien et al., 2014	7.0	Siemens	other	In vivo	Control	-	8	2/6	29 (4.1)
				In vivo	Patient	Epilepsy	2	n.s.	n.s.
Plantinga et al., 2016	7.0	Siemens	gpe, gpi, stn, other	PM	Control	-	1	n.s.	70-95
Plantinga et al., 2018	7.0	Siemens	stn	In vivo	Patient	PD	17	5/12	62
Peters et al., 2007	7.0	Philips	cau, put	In vivo	Control	-	6	n.s.	37 (11)
Rijkers et al., 2007	9.4	Varian unity	pag, pul, rn, sc, sn, stn, other	PM	n.s.	-	1	n.s.	n.s.
Robitaille et al., 1999	8.0	Brucker	mam, rn, other	In vivo	n.s.		n.s.	n.s.	n.s.
Romanzetti et al., 2014	9.4	Siemens	tha	In vivo	Control	-	19	3/16	36 (4)
Rooney et al., 2007	7.0	n.s.	cau, gp, put, tha	In vivo	Control	-	3	0/3	32-59
de Rotte et al., 2014	7.0	Philips	other	In vivo	Control	-	10	6/4	25 (n.s.)
				In vivo	Patient	Micro adenoma	5	n.s.	35.2 (12.40)
de Rotte et al., 2015	7.0	Philips	other	In vivo	Patient	Cushing disease	16	n.s.	n.s.
Rudko et al., 2014	7.0	Agilent	cau, gp, put, tha	In vivo	Control	-	15	12/3	36.4 (6.42)
				In vivo	Patient	MS	25	18/7	37.3 (6.1)
Satpute et al., 2013	7.0	Siemens	pag	In vivo	Control	-	11	6/5	20-35
Schäfer et al., 2009	7.0	Philips	rn, sn, stn	In vivo	Control	-	n.s.	n.s.	n.s.
Schäfer et al., 2012	7.0	Siemens	rn, sn	In vivo	Control	-	8	3/5	22-28

Schindler et al., 2013	7.0	Siemens	gpi, mam, sn, stn, tha, other	In vivo	Control	-	10	8/2	38.5 (13.6)
Schindler et al., 2017	7.0	Siemens	other	In vivo	Control	-	84	51/33	39 (13)
Schmidt, Schindler et al., 2017	7.0	Siemens	other	In vivo	Control	-	20	12/8	36.45 (13.16)
				In vivo	Patient	Unmedicated MDD	20	12/8	36.20 (12.83)
				In vivo	Patient	Medicated MDD	20	13/7	40.60 (12.11)
Schmidt, Engelhorn et al., 2017	7.0	Siemens	other	In vivo	Control	-	13	5/8	46.7 (12.5)
Schreiner et al., 2014	7.0	Philips	amy, cau, gp, put, tha, other	In vivo	Control	-	14	6/8	68.43 (5.3)
Shmueli et al., 2009	7.0	GE	put, rn, sn	In vivo	Control	-	1	n.s.	n.s.
Sladky et al., 2013	7.0	Siemens	amy	In vivo	Control	-	15	6/9	29.54 (6.65)
Solano-Castiella et al., 2011	7.0	Siemens	amy, other	In vivo	Control	-	9	n.s.	21-29
Solbach et al., 2014	7.0	Siemens	den	In vivo	Control	-	14	7/7	38.1 (7.7)
				In vivo	Patient	Friedreich's ataxia	14	8/6	38.1 (8.5)
Soria et al., 2011	7.0	Brucker	ic, pag, rn, other	PM	Control		3	n.s.	n.s.
Stefanescu et al., 2013	7.0	Siemens	den	In vivo	Control	-	19	9/10	26.5 (3.5)
Stefanescu et al., 2015	7.0	Siemens	den	In vivo	Control	-	23	10/13	46.39 (15.82)
				In vivo	Patient	SCA6	12	5/7	57.75 (12.06)
				In vivo	Patient	Friedreich's ataxia	12	7/5	39.08 (12.87)
				In vivo	Patient	SCA3	10	3/7	47.2 (10.58)
Strotmann, Kögler, et al., 2013	7.0	Siemens	other	PM	Control	-	1	1/0	65
Strotmann, Heidemann, et al., 2013	7.0	Siemens	other	In vivo	Control	-	3	n.s.	n.s.
				PM	Control	-	1	1/0	65
Stüber et al., 2014	7.0	Siemens	sn, stn	PM	n.s.	-	1	n.s.	n.s.
Tang et al., 2014	7.0	Philips	other	In vivo	Control	-	1	0/1	42

Thayyil et al., 2009	9.4	Varian	tha	PM	Patient	Fetal specimen	17	n.s.	less than 22 weeks of GA
Thomas et al., 2008	7.0	Philips	amy	In vivo	Control	-	6	0/6	32 (n.s.)
Thulborn et al., 2015	9.4	GE	tha, other	In vivo	Control	-	49	26/23	48 (19)
Thürling et al., 2012	7.0	Siemens	den	In vivo	Control	-	17	0/17	27.4 (6.4)
Thürling et al., 2011	7.0	Siemens	den	In vivo	Control	-	21	10/11	25.5 (3.9)
				In vivo	Control	-	23	8/15	27 (3.8)
Thurling et al., 2015	7.0	Siemens	den, other	In vivo	Control	-	24	11/13	31.8 (6.4)
Tourdias et al., 2014	7.0	GE	pul, rn, stn, other	In vivo	Control	-	6	1/5	31.2 (n.s.)
Trampel et al., 2013	7.0	Siemens	other	In vivo	n.s.	-	n.s.	n.s.	n.s.
Truong et al., 2006	8.0	Brucker	gp, put, rn, sn	In vivo	Control	-	2	2/0	34 (0)
				PM	Patient	Various neuropathologies	4	2/2	72-81
van Bergen et al., 2015	7.0	Philips	sn, rn	In vivo	Control	-	16	8/8	43.3 (11.7)
				In vivo	Patient	Premanifest Huntington Disease	15	5/10	42.4 (8.7)
van den Bogaard et al., 2011	7.0	Philips	cau, put, tha, other	In vivo	Control	-	18	9/9	47.7 (7.4)
				In vivo	Patient	Premanifest Huntington Disease	14	8/6	42.9 (11)
				In vivo	Patient	Manifest Huntington Disease	12	7/5	48.6 (7)
Verma et al., 2013	7.0	Siemens	other	In vivo	Control	-	2	n.s.	38.5 (10.61)
Visser, Douaud, et al., 2016	7.0	Siemens	cau, gp, put	In vivo	Control	-	54	25/29	39.72 (n.s.)
Visser, Keuken et al., 2016	7.0	Siemens	sn, stn, rn	In vivo	Control	-	54	25/29	39.72 (n.s.)
Wang et al., 2016	7.0	Siemens	other	In vivo	Control	-	53	21/31	39.72 (n.s.)

Wargo & Gore, 2013	7.0	Philips	pns, put, rn, tha	In vivo	Control	-	8	4/4	20-54
Weiss et al., 2014	7.0	Siemens	stn	PM	Control	-	4	3/1	66.75 (19.48)
Wharton, Schäfer, & Bowtell, 2010	7.0	Philips	rn, sn	In vivo	Control	-	3	n.s.	n.s.
Wharton & Bowtell, 2010	7.0	Philips	cau, gp, put, rn, sn, tha	In vivo	Control	-	5	0/5	25-30
Wright et al., 2008	7.0	Philips	cau, put	In vivo	Control	-	4	1//3	36.5 (8.5)
Yang et al., 2013	7.0	Siemens	den	PM	Control	-	2	2/0	74.5 (2.12)
Yao et al., 2009	7.0	GE	cau, gp, put, tha	In vivo	Control	-	9	4/5	31 (5)
				PM	Control	-	2	0/2	68 (2)
Zeineh et al., 2014	7.0	GE	rn, sn, stn	In vivo	Control	-	6	n.s.	n.s.
Zhang et al., 2011	7.0	Brucker	cau, other	PM	Control	Fetal specimen	20	10/10	20 weeks of GA
Zielman et al., 2014	7.0	Philips	pns, other	In vivo	Control	-	19	12/7	38.5 (12.1)
				In vivo	Patient	Hemiplegic migraine	18	11/7	38.1 (14.4)
Zrinzo et al., 2011	9.4	Varian	pag	PM	Control	-	1	0/1	68
Zwanenburg et al., 2008	7.0	Philips	gp, put, tha, other	In vivo	Control	-	7	1/6	26 (10)
Zwanenburg et al., 2009	7.0	Philips	stn	In vivo	Control	-	5	1/5	24 (4)

n.s. : not stated, PM: post mortem, PD: Parkinson's Disease, AD: Alzheimer Disease, MDD. Major Depressive Disorder, MS: Multiple sclerosis, PSP: Progressive supranuclear palsy, GA: gestation, MSA: multiple system atrophy, CBD: corticobasal degeneration, The seventeen most frequently reported structures were: amy: amygdala, cau: caudate, den: dentate nucleus, gp: globus pallidus, gpe: globus pallidus external segment, gpi: globus pallidus internal segment, ic: inferior collicus, mam: mammillary body, pag: periagueductal gray, pns: pons, pul: pulvinar, put: putamen, rn: red nucleus, sn: substantia nigra, stn: subthalamic nucleus, sc: superior colliculus, tha: thalamus. The remaining structures are indicated with the label other.

Identification versus parcellation

Of the 753 reports across the 169 papers, there were 344 reports where the authors (partially) parcellated a subcortical structure. This was either done by manual parcellation (208 reports), placing an ROI in a visually identified area (51 reports), semi-automatic procedures (22 reports), fully automatic procedures (26 reports), using a functional localizer (5 reports), or otherwise parcellated in a way that was unclear from the manuscript (32 reports). Overall, regardless of method, the most frequently parcellated structure was the putamen (31 reports) whereas the STN was the most frequently manually parcellated structure (21 reports). Of the 344 parcellated reports there were 75 structures parcellated in vivo, and 36 structures parcellated using post mortem samples. There is an overlap of 17 structures that are parcellated in both in vivo and post mortem data (see Figure 4 for a comparison between the image quality achievable with in vivo versus post mortem scanning).

Structures that were only parcellated using post mortem data include a number of small structures in the lower brainstem such as the abducens nucleus, primary olivary nucleus, cuneate nucleus, a number of sub-nuclei of the hypothalamus, and the claustrum. That the claustrum has never been parcellated in vivo was somewhat surprising as it is a relatively large structure, medial to the striatum. A potential explanation why such small structures in the brainstem are only parcellated using post mortem data is the employed voxel volume (see Figure 5 for an overview of voxel volumes used per MRI sequence and sample type). One of the benefits of post mortem scanning is the possibility to employ longer scan times in the absence of motion, which allows for the acquisition of smaller voxels, and/or the possibility of scanning a smaller sample at higher fields than available in vivo (e.g., 0.05mm isotropic voxels with an acquisition time of 4.3 hours using 21.1T (Foroutan et al., 2013) or 0.09mm isotropic voxels with an acquisition time of 10.5 hours using 7.0T (Makris et al., 2013)).

Voxel volume and Isotropic voxels

The voxel volume across the different structural MRI contrasts including the DWI scans for the in vivo scans ranged between 0.0144 mm3 and 42.875 mm3, with a mean volume of 1.09 mm3 (SD 3.71 mm3) and a median of 0.245 mm3. The voxel volume for the functional MRI contrasts for the in vivo scans ranged between 0.422 mm3 and 39.051 mm3, with a mean volume of 4.50 mm3 (SD 7.72 mm3) and a median of 1.33 mm3. For the post mortem scans the volume varied between 0.000125 mm3 and 1.47 mm3 with a mean voxel volume of 0.075 mm3 (SD 0.23 mm3) and a median of 0.01 mm3. See Figure 5 for an overview of voxel volumes used per MRI sequence.

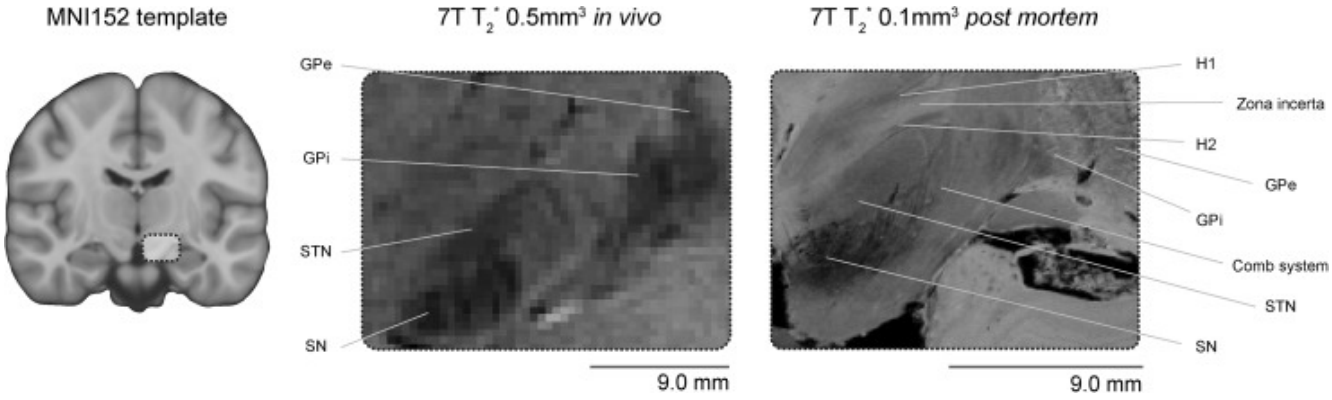

Figure 4: In vivo versus post mortem comparison. The left panel shows the MNI152 template with a highlighted subcortical region. The middle panel highlights this subcortical region using a 7T in vivo 0.5 mm isotropic resolution T2*-weighted structural scan where the globus pallidus externa (GPe), globus pallidus interna (GPi), STN and SN can be visualized. The right panel illustrates a similar region in a post mortem sample scanned with a 0.1 mm isotropic resolution T2*-weighted scan where a number of subcortical areas can be identified which are not clearly visible in the in vivo scans such as the fields of Forel (H1, H2), zona incerta and the comb system. Image is adapted from (Forstmann, Isaacs, & Temel, 2017).

Of all the structures that were identified using a T1 based contrast, 128 reports of structures were achieved using isotropic or near isotropic voxels, and 83 reports were based on anisotropic voxels. For the T2 based contrasts sequences, 26 reports were based on isotropic voxels, and 90 reports were based on anisotropic voxels. Using a T2* sequence, 114 reports were based on isotropic voxels, whereas 138 reports were not. For the functional sequences,

all 25 reports were based on isotropic voxels. The DWI sequence resulted in 60 reports using isotropic voxels and 27 reports using anisotropic voxels. SWI sequences that were used to identify structures were isotropic in 82 cases and in 21 cases anisotropic. All three reports that identified a structure using an MT-based sequence were based on anisotropic voxels. The PD sequences that were used to identify structures were isotropic for 6 reports and 18 reports were based on anisotropic voxels.

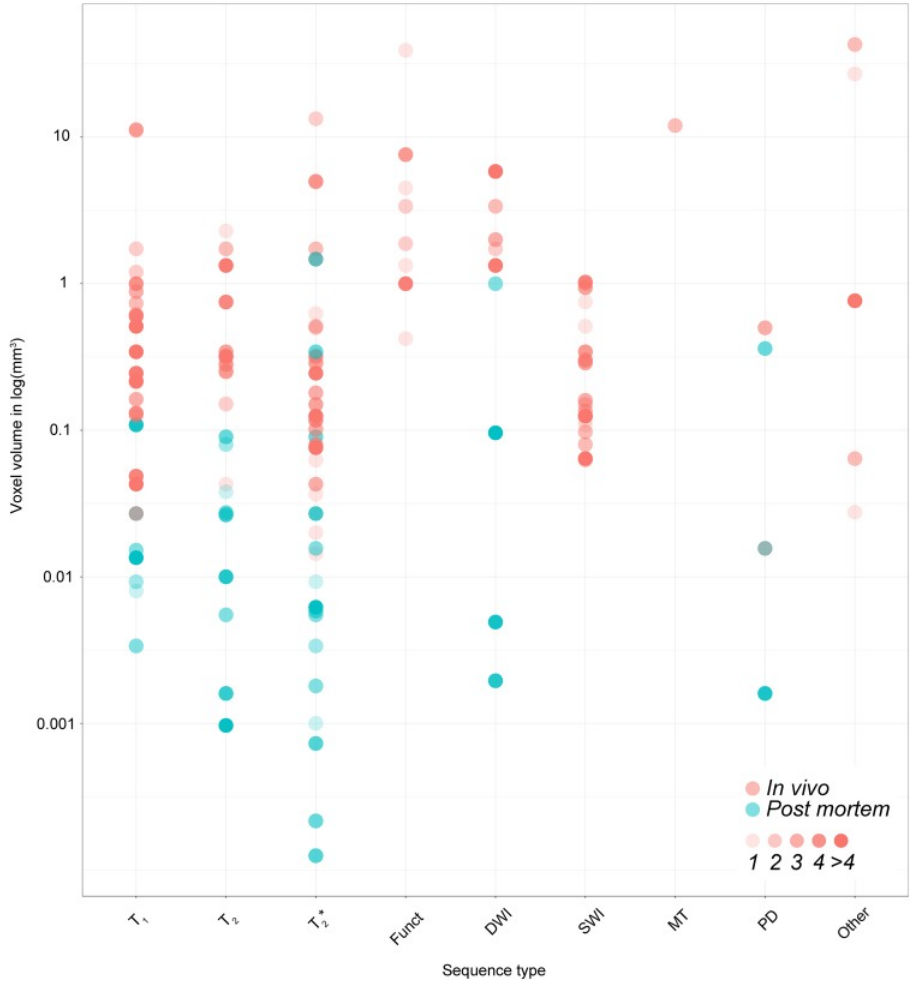

Figure 5: Voxel volume for the different MRI sequences. Each dot represents the voxel volume used to visualize a subcortical structure across the 169 studies. The in vivo samples are displayed in red, whereas the post mortem samples are shown in blue. The color intensity corresponds to the number of studies using the same voxel volume. Funct functional MRI sequences that employed functional localizer stimuli, DWI diffusion-weighted imaging, SWI susceptibility-weighted imaging, MT magnetization transfer, PD proton density, N.s. not stated, PD (patient type) Parkinson's disease, MS multiple sclerosis

Volumetric reports

With a total of 51 reports, the SN is the most frequently visualized structure, of which only 9 papers provide an explicit volume estimate (see Table 2). For the STN, directly adjacent to the SN, there are 42 reports, of which there are 12 reports that provide a volume estimate. There is substantial variability in volume estimates for both structures. For the SN, volumes range between 224.75 mm3 to 1300 mm3. For the STN the volumes range between 37.32 mm3 and 223 mm3. The volumes are based on a range of different MRI contrasts and parcellation methods, such as automatic segmentations or the conjunction of two manual raters. This variability in methods makes it problematic to provide a summary of volume estimates and whether there is a systematic difference due to the acquisition technique.

Table 2. SN and STN volume estimates.

Publication	Structure	Volume estimate	Population	Segmentation method	MRI contrast	Voxel dimension
Bianciardi et al., 2015	SN	490 mm^3	Control	Semi-automatic	FA & T_2	1.1x1.1x1.1
Chen et al., 2010	SN	79 mm^{2a}	Control	Manual	T_2*	0.25x0.25x2.0
Eapen et al., 2011	SN	725.7 mm^3	Control	Automatic	T_2 (Hybrid Echo)	0.4x0.4x2.0
	SN	753.1 mm^3	Control	Automatic	T_2*	0.4x0.4x2.0
Keuken et al., 2014	SN	224.75 mm^3	Control	Conj. masks of two manual raters	T_2*	0.5x0.5x0.5
Keuken et al., 2017	SN	270.36 mm^3	Control	Conj. masks of two manual raters	T_2*	0.5x0.5x0.5
Kwon et al., 2012	SN	270.63 mm^3	Control	Masks of two manual raters	T_2*	0.35x0.35x0.35
	SN	310.68 mm^3	PD	Masks of two manual raters	T_2*	0.35x0.35x0.35
Plantinga et al., 2016	SN	281.4 mm^{3b}	PM Control	Manual	T_2*	0.3x0.3x0.3
Lenglet et al., 2012	SN	586 mm^{3c}	Control	Manual masks	T_2+SWI	0.4x0.4x2.0
van Bergen et al., 2015)	SN	1300 mm^3	Control	Semi-automatic	SWI	1.0x1.0x1.0

	SN	1300 mm^3	Premanifest HD	Semi-automatic	SWI	1.0x1.0x1.0
Alkemade et al., 2017	STN	82.34 mm^3	Control	Conj. masks of two manual raters	QSM	0.5x0.5x0.6
	STN	76.8 mm^3	PD	Conj. masks of two manual raters	QSM	0.6x0.6x0.8
Bianciardi et al., 2015	STN	163.5 mm^3	Control	Semi-automatic	FA & T_2	1.1x1.1x1.1
Keuken et al., 2013	STN	63.13 mm^3	Control	Conj. masks of two manual raters	T_2*	0.5x0.5x0.6
Keuken et al., 2014	STN	56.17 mm^3	Control	Conj. masks of two manual raters	T_2*	0.5x0.5x0.5
Keuken et al., 2015	STN	62.25 mm^3	Control	Conj. masks of two manual raters	T_2*	0.5x0.5x0.5
Keuken et al., 2017	STN	37.32 mm^3	Control	Conj. masks of two manual raters	T_2*	0.5x0.5x0.5
Lenglet et al., 2012	STN	223.5 mm^{3c}	Control	Manual mask	T_2+SWI	0.4x0.4x2.0
Massey et al., 2012	STN	198 mm^3	PM Control	Manual mask	T_2*	0.18x0.18x0.18
Plantinga et al., 2016	STN	100.5 mm^3	PM Control	Manual mask	T_2*	0.3x0.3x0.3
Plantinga et al., 2018	STN	125.4 mm^3	PD	Manual mask	T_2	0.39x1.0x0.39
Schäfer et al., 2012	STN	48 mm^3	Control	Masks of two manual raters	T_2*	0.5x0.5x0.6
Weiss et al., 2014	STN	109 mm^3	PM Control	Conj. masks of two manual raters	T_2*	0.1x0.1x0.1

a: single slice; b: SNc and SNr combined; c: extracted using webplot digitizer; PD: Parkinson Disease; PM: post mortem; FA: Fractional Anisotropy; n.s. not stated; SWI: susceptibility-weighted imaging; Conj: conjunction. Voxel dimension is in mm.

MRI contrasts for visualizing the SN, STN, and thalamus.

It is interesting to note the variability in MRI contrasts used to visualize several subcortical structures. For the SN by far the most commonly used contrast is a T2* based sequence followed by SWI contrasts (Figure 6d). Given that the SN contains relatively large amounts of iron, which increases the magnetic susceptibility, it is not surprising that T2* and SWI seem to be the contrasts of choice (Chavhan et al., 2009; Hallgren & Sourander, 1958). In

terms of demographics, the SN is regularly visualized in PD patients, which is expected due to the underlying pathology occurring in the SN in PD (Figure 6c). Another structure that is implicated in the pathophysiology of PD is the STN, a structure also high in iron content and located directly adjacent to the SN. As with the SN, the most frequently used contrast mechanism to visualize the STN is T2* (Figure 7d). The ratio for identification versus parcellation of the STN is larger than for the SN. Additionally, the STN is more commonly visualized in the healthy population, compared to the SN which included relatively more clinical groups (Figure 6c versus Figure 7c). The thalamus (Th), a structure that contains roughly 4 times less iron than the SN (Hallgren & Sourander, 1958) is visualized with a much wider range of MRI sequences (fig. 8d). A T2* based contrast is used most frequently which is surprising given the lower iron concentrations in the Th, but is closely followed by T1 based sequences.

Optimal MRI contrast

There are a number of studies that explicitly state that one MRI contrast is superior to other sequences for the identification or parcellation of the SN, STN, or Th. There were 7 papers for the SN (Abduljalil et al., 2003; Abosch et al., 2010; Deistung, Schäfer, Schweser, Biedermann, Güllmar, et al., 2013; Deistung, Schäfer, Schweser, Biedermann, Turner, et al., 2013; Eapen et al., 2011; Kerl et al., 2012b; Khabipova et al., 2015; Schäfer et al., 2012; Shmueli et al., 2009), 6 papers for the STN (Abosch et al., 2010; Alkemade et al., 2017; Deistung, Schäfer, Schweser, Biedermann, Güllmar, et al., 2013; Kerl et al., 2012b; Schäfer et al., 2012; Zeineh et al., 2014) and 6 papers that compared sequences for the Th (Abduljalil et al., 2003; Abosch et al., 2010; Deistung, Schäfer, Schweser, Biedermann, Turner, et al., 2013; Hammond, Metcalf, et al., 2008; Kanowski et al., 2014; Tourdias et al., 2014). For the SN, the consensus for visualization seems to be that either a T2* or SWI based sequence is optimal, which are highly similar contrasts. For the STN, this is not as clear as there are roughly an equal number of studies that prefer T2*, SWI or T2 based images. The Th was preferentially visualized using a T2* contrast (see Table 3).

Table 3. Preferred MRI sequence for the visualization of the SN, STN and Th

Structure	T_1	T_2	T_2*	SWI	Other
SN	-	-	6	4	-
STN	-	-	2	4	1
Th	2	-	3	2	-

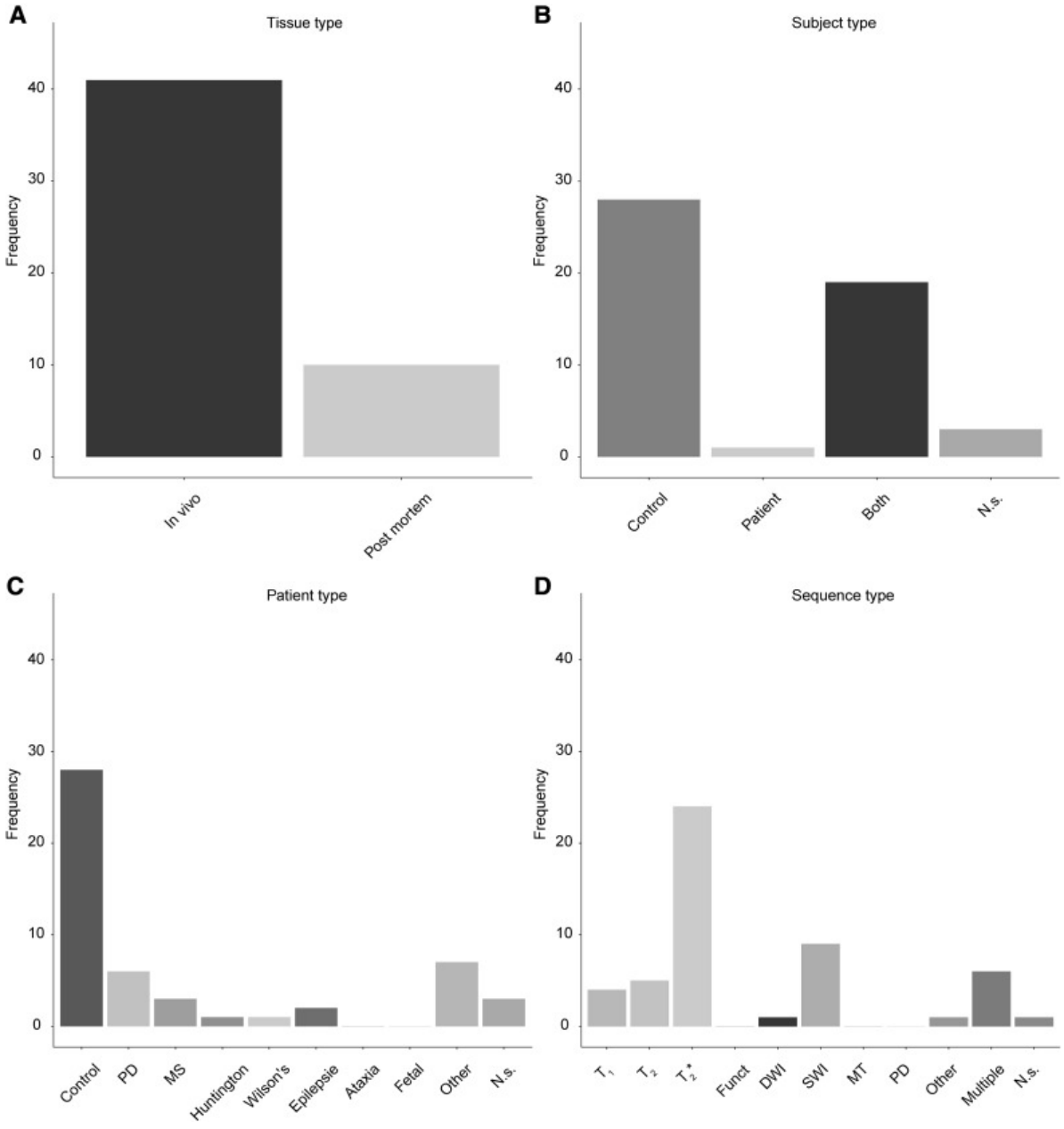

Figure 6: Overview of the use of UHF-MRI for visualizing the substantia nigra. a) Of the 51 studies that identified the SN, most were done using in vivo samples. b) Most studies only used healthy controls, whereas a substantial number also included patients. c) The studies that included a clinical group mainly focused on Parkinson's Disease patients or abnormal fetal developments. d) The frequency of using a certain MRI sequence type to visualize the SN. The most frequently used contrast was a T2* type of sequence. Funct functional MRI sequences that employed functional localizer stimuli, DWI diffusion-weighted imaging, SWI susceptibility-weighted imaging, MT magnetization transfer, PD proton density, N.s. not stated, PD (patient type) Parkinson's Disease, MS multiple sclerosis.

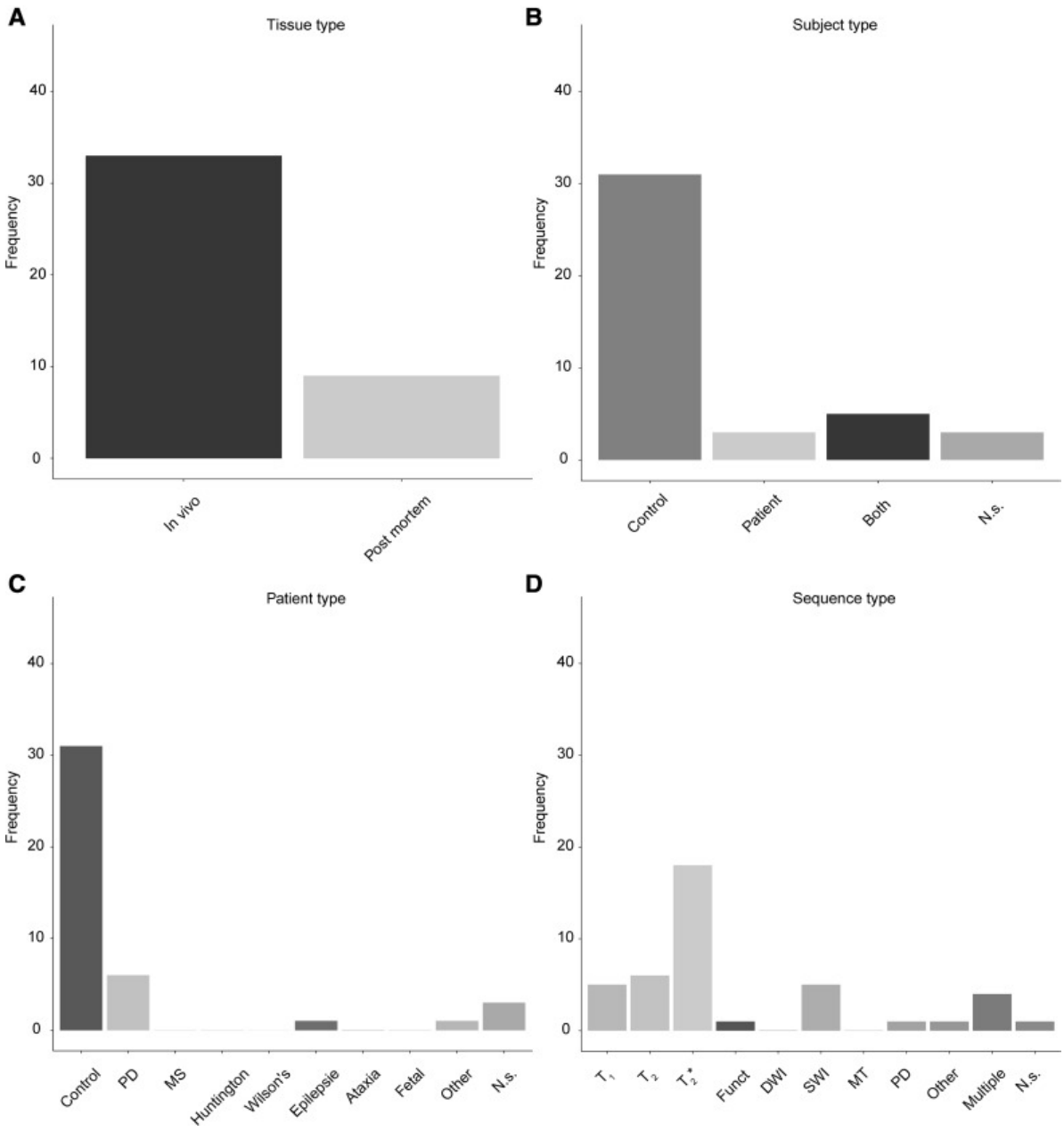

Figure 7: Overview of the use of UHF-MRI for visualizing the subthalamic nucleus. a) Of the 42 studies that identified the STN, most were done using in vivo samples. b) Most studies only used healthy controls. Compared to the SN there were substantially fewer studies that also included patients. c) The studies that included a clinical group mainly focused on Parkinson's Disease patients or abnormal fetal developments. d) The frequency of using a certain MRI sequence type to visualize the STN. The most frequently used contrast was a T2* type of sequence. Funct functional MRI sequences that employed functional localizer stimuli, DWI diffusion-weighted imaging, SWI susceptibility-weighted imaging, MT magnetization transfer, PD proton density, N.s. not stated, PD (patient type) Parkinson's Disease, MS multiple sclerosis

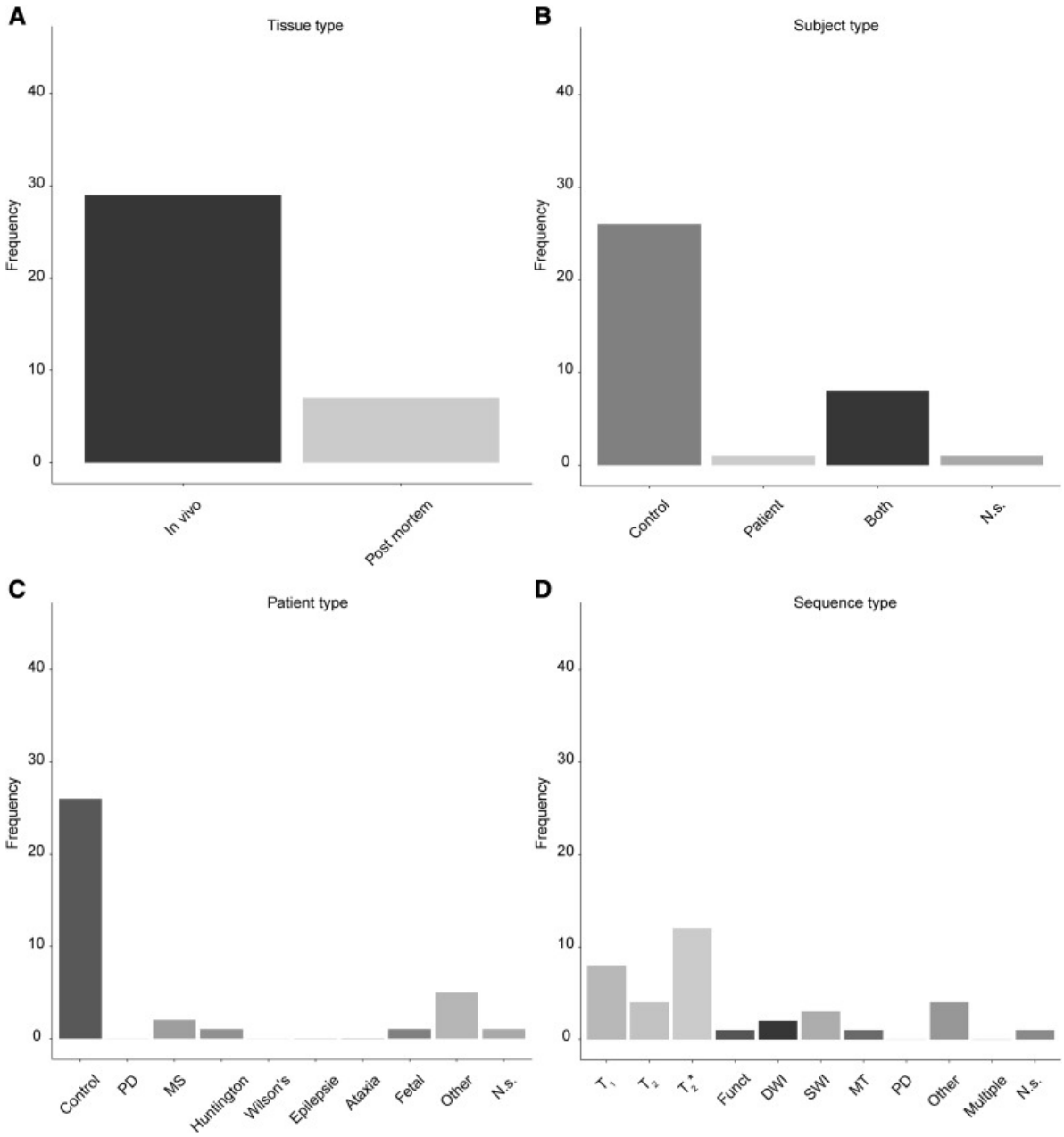

Figure 8: Overview of the use of UHF-MRI for visualizing the thalamus. a) Of the 36 studies that identified the Th, most were done using in vivo samples. b) Most studies only used healthy controls. Compared to the SN, there were substantially fewer studies that also included patients. c) The studies that included a clinical group mainly focused on abnormal fetal developments. d) The frequency of using a certain MRI sequence type to visualize the Th. The most frequently used contrast was a T2* type of sequence, followed closely by T1 sequences. Funct functional MRI sequences that employed functional localizer stimuli, DWI diffusion weighted imaging, SWI susceptibility-weighted imaging, MT magnetization transfer, PD proton density, N.s. not stated, PD (patient type) Parkinson's disease, MS multiple sclerosis.

Discussion

The subcortex can be parcellated into a large number of anatomically distinct structures (Dirckx, 1998). Only approximately 7% of these known structures are incorporated in standard anatomical MRI atlases (Alkemade et al., 2013). However, by reviewing the literature that utilized UHF-MRI to visualize the subcortex, it became apparent that the number of observed subcortical structures is considerably larger. Specifically, at least 163 unique subcortical structures are identifiable in individual space using UHF-MRI. We have provided R code to enable the reader to explore the use of UHF-MRI for a given structure. A reader interested in structure 'A' can now obtain a list of the papers identifying this structure and the resolutions and methods used to do so. The ability of UHF-MRI to identify a large number of subcortical nuclei in individual space is of the utmost importance given the anatomical variability that exists across individuals (Amunts et al., 1999; Daniluk, Davies, Ellias, Novak, & Nazzaro, 2009; Forstmann et al., 2014; Keuken et al., 2017; Mazziotta, Toga, Evans, Fox, & Lancaster, 1995; Uylings, Rajkowska, Sanz-Arigita, Amunts, & Zilles, 2005). This anatomical variability is far from static as several factors including gene-environment interactions, healthy aging, and disease all influence individual anatomy over time (Daniluk et al., 2009; Keuken et al., 2013; Lenroot & Giedd, 2008; Raz et al., 2005; Thompson et al., 2001). These factors question the validity of using anatomical atlases that fail to incorporate anatomical variability or are not specific for an age group or clinical population (Alho, Grinberg, Heinsen, & Talamoni, 2011; Devlin & Poldrack, 2007).

The clinical use of UHF-MRI

Numerous recent reviews are highlighting the substantial benefits of UHF-MRI in a clinical setting (Beisteiner et al., 2011; Cho et al., 2010; Duchin, Abosch, Yacoub, Sapiro, & Harel, 2012; Gizewski, Mönninghoff, & Forsting, 2015; Kraff et al., 2014; Plantinga et al., 2014; Springer et al., 2016; Trattnig et al., 2015). A number of studies have directly compared clinically utilized 1.5 and 3.0T field strengths to UHF-MRI, showing UHF-MRI results in an improved visualization across various patient groups and structures (Abosch et al., 2010;

Blazejewska et al., 2013; Chalifoux et al., 2013; Cho, Choi, et al., 2011; Cho, Han, et al., 2010; Cho et al., 2008; Cho, Min, et al., 2010; Cosottini et al., 2015; Derix et al., 2014; Hammond, Metcalf, et al., 2008; Kollia et al., 2009; Peters et al., 2007; Saranathan et al., 2014; Yao et al., 2009; Zwanenburg et al., 2009). Based on our review, it is clear that UHF-MRI is already frequently used to visualize subcortical structures in a clinical setting for populations such as Parkinson's Disease, Alzheimer's Disease, and Multiple Sclerosis. The benefit of UHF-MRI in a clinical setting can be illustrated by its use with regards to pre-operative planning for Deep Brain Stimulation (DBS) procedures as a treatment for PD patients. DBS is a surgical procedure where an electrode is inserted into the STN to reduce the motor symptoms of the disease, while simultaneously minimizing the occurrence of cognitive and limbic side-effects known to affect some patients (Limousin et al., 1995; Temel, Blokland, Steinbusch, & Visser-Vandewalle, 2005). The development of these side-effects can partially be attributed to the suboptimal placement of the electrode in the STN (Cakmakli, Oruckaptan, Saka, & Elibol, 2009; Kleiner-Fisman et al., 2006; Paek et al., 2011). Given that the location of the STN changes with both age and disease (den Dunnen & Staal, 2005; Keuken et al., 2017, 2013; Kitajima et al., 2008; Mavridis, Boviatsis, & Anagnostopoulou, 2013; Pereira et al., 2016) it is crucial to visualize such a structure as accurately as possible per individual, which is why the superior visualization of UHF-MRI is so valuable to DBS. The same logic can be passed to alternative neurosurgical interventions such as tumor delineation and removal, proton beam, gamma knife, and radiation therapies which all require precise anatomical visualization, best afforded by UHF-MRI (Forstmann et al., 2017).

Optimal MRI sequence per structure

Optimal MRI sequences providing sufficient contrast-to-noise ratio (CNR) are essential for clinical research. It is crucial to visualize the structure of interest while maintaining a clinically feasible scanning time. Therefore, given that different tissues require different MR sequences and parameters, it is important to experimentally determine the optimal sequence for each structure of interest (Marques & Norris, 2017). To highlight the variability of preferred sequences, the studies that used multiple MRI sequences to visualize the SN, STN, and Th

were compared. Based on the literature review, the preferred contrast to visualize any of these three structures, even the Th is a T2* sequence (Abduljalil et al., 2003; Abosch et al., 2010; Deistung, Schäfer, Schweser, Biedermann, Güllmar, et al., 2013; Deistung, Schäfer, Schweser, Biedermann, Turner, et al., 2013; Eapen et al., 2011; Gizewski et al., 2013; Hammond, Metcalf, et al., 2008; Kanowski et al., 2014; Kerl, 2013; Kerl et al., 2012b; Khabipova et al., 2015; Saranathan et al., 2014; Schäfer et al., 2012; Shmueli et al., 2009; Tourdias et al., 2014; Zeineh et al., 2014). Such T2* sequences have been used in PD patients to investigate pathological alterations occurring in the SN dopaminergic system (e.g., (Cho, Min, et al., 2010; Cho, Oh, et al., 2011; Kwon et al., 2012)). Particularly at UHF-MRI the use of a T2* weighted sequence for a volumetric study is however not trivial. Pronounced B0 inhomogeneities lead to additional dephasing which may result in signal dropouts especially in regions with high iron content. Additionally, a major difficulty in interpreting T2*-weighted gradient-echo data is that the dependence of the signal on the tissue susceptibility is a non-local effect, i.e., the signal within a voxel is not only affected by sources within but also from neighboring sources outside that voxel. Therefore, T2* hypointensity and phase contrast in gradient-echo techniques are not directly reflective of local tissue properties (Schäfer et al., 2009) which can affect volumetric measurements (Chandran, Bynevelt, & Lind, 2015). Shorter TE acquisition is preferable for volumetric measurements in terms of edge fidelity, but do not have the high contrast associated with midrange TE's. What the optimal sequence is for the other subcortical structures is unclear from the currently available publications and will probably differ from the SN, STN, and Th due to differences in tissue properties, most notably the lower concentrations of iron.

It should also be noted that these comparison studies should be viewed with the ongoing development of MRI contrasts such as QSM in mind (Marques & Norris, 2017). QSM is a novel post-acquisition processing technique where the susceptibility of the tissue is quantified by estimating the magnetic field distribution and solves the inverse problem from field perturbation to magnetic susceptibility while removing the background field contribution (Schweser, Deistung, Lehr, & Reichenbach, 2011; Schweser, Deistung, & Reichenbach, 2016). As such the QSM suffers less from non-local effects as described above which makes it an interesting contrast for volumetric studies of iron-rich nuclei (e.g.

(Alkemade et al., 2017; Liu et al., 2013)).

Quantitative maps

Most of the included UHF-MRI studies use standard MRI sequences that are (mainly) weighted for a certain contrast mechanism as opposed to a quantitative map, of, e.g., T1 or T2* relaxation. This is unfortunate as there are several clear advantages to quantitative MRI (qMRI) over standard weighted sequences (Weiskopf, Mohammadi, Lutti, & Callaghan, 2015b). One of the benefits of qMRI is that the quantitative maps can be used to generate bias-free weighted images (e.g. (Renvall, Witzel, Wald, & Polimeni, 2016)). Another benefit of quantitative maps is the possibility of assigning a physical meaning to the intensity value of the image and therefore being able to provide biologically and spatially specific information (Ropele & Langkammer, 2016; Weiskopf et al., 2015b). For instance, T1, the parameter describing the spin-lattice relaxation, has been used as a proxy for myelin content (Dinse et al., 2015; Koenig, 1991; Lutti, Dick, Sereno, & Weiskopf, 2014; Stüber et al., 2014), whereas T2*, the parameter describing the spin-spin relaxation in combination with field inhomogeneity, and especially QSM are thought to be informative for iron concentration (Cohen-Adad et al., 2012; Fukunaga et al., 2010; Lee et al., 2010; Stüber et al., 2014). One of the downsides of qMRI is that the acquisition time of a quantitative map is usually longer than standard weighted MRI. However, this can be solved by combining different contrast mechanisms into one data acquisition enabling quantification of multiple MRI parameters within a clinically acceptable time (Weiskopf et al., 2015b). The advantage of having multiple contrasts is that each contrast contains complementary anatomical information that can be used to inform segmentation algorithms, such as the Multimodal Image Segmentation Tool (MIST, (Visser, Douaud, et al., 2016; Visser, Keuken, et al., 2016)).

Reporting the demographic and MRI protocol values

A critical note needs to be made regarding the lack of details reported in the included papers. A substantial number of studies fail to report basic demographic information of the measured

subjects. At times information regarding the exact age, gender ratio, and whether the participant is healthy is missing. This is problematic as age and disease can have substantial effects on the biological properties of the brain (Aquino et al., 2009; Fritzsch et al., 2014; Lorio et al., 2014; Minati et al., 2007; Visser, Keuken, et al., 2016). In other cases, essential information regarding the MRI protocol such as field of view, matrix size, or voxel size is missing or incomplete. This hinders the reproducibility of these studies and makes it challenging to implement their sequences and protocols. As such it should be recommended that groups adhere to the guidelines on reporting neuroimaging studies (Nichols et al., 2017; Poldrack et al., 2008).

Challenges of UHF-MRI

An obvious limitation of UHF-MRI is the limited accessibility. Of the approximately 36,000 MRI scanners available worldwide, only +/- 0.2% are UHF-MRI scanners (Rinck, 2016). Given the advantages of visualizing clinically relevant subcortical nuclei, this calls for an increase of UHF-MRI scanner sites but we acknowledge the substantial higher purchasing and running costs of a UHF-MRI scanner. A more technical challenge with UHF-MRI is the B0 and B1 field inhomogeneities which increase with field strength resulting in local signal intensity variations and signal dropout (Truong et al., 2006; van der Zwaag et al., 2015). While B0 and B1 field inhomogeneity remains an active field of research, substantial progress has already been made in overcoming these problems (Sclocco et al., 2017; van der Zwaag et al., 2015; Yarach et al., 2016). For the subcortex, the absence of nearby air-water interfaces for most of the subcortical structures means that B0 inhomogeneities are a relatively minor problem. B1 inhomogeneities are more problematic. While the standard single-channel transmit / 32-channel receive coils have a relatively favorable transmit B1 pattern with the highest achieved flip angles in the middle of the brain, the received profile of the array coils means that SNR is lower in the midbrain than in the cortex.

While the spatial resolutions achieved by in vivo UHF-MRI are impressive, on its own, it is not able to deliver the anatomical resolution needed to visualize all structures known to be present in the human brain. At present, the combination of neuroimaging and post

mortem staining's are still needed to create a complete and comprehensive picture of the human brain in its entirety (Amunts et al., 2013; Yang et al., 2013). An example of such a combination has been given by Ding and colleagues (Ding et al., 2016). Here they used a single post mortem brain, which was structurally scanned with 7.0T and subsequently further processed using various staining techniques. A staggering 862 cortical and subcortical areas were manually segmented and aligned to the structural MRI scans. Given that it is not yet possible to fully automatize such a pipeline nor translate it directly to the individual in vivo brain, these efforts will not quickly result in a tool to identify the structures per individual brain. However, what such a multi-modal atlas could do is to provide shape, intensity, and spatial relationship priors for automatic segmentation methods (Bogovic, Prince, & Bazin, 2013; Kim et al., 2014; Visser, Douaud, et al., 2016; Visser, Keuken, et al., 2016).

A final limitation of UHF-MRI utility is that the standard FDA approval for clinical scanning only goes up to 3.0T (van Osch and Webb 2014). This restriction does not seem to be based on safety concerns, as the risks associated with UHF-MRI up to 8.0T are similar to 1.5 and 3.0T (FDA, 2003; van Osch & Webb, 2014). This limitation has hindered the use of UHF-MRI in standard clinical practice which, given the clear clinical advantages, is unfortunate (Kraff et al., 2014; Trattnig et al., 2015). It is expected that this will be solved with the newest generation of 7.0T systems as they will have both CE and FDA clinical approval. This might result in more institutes having a larger interest in investing in UHF-MRI scanners, increasing the accessibility for clinical and non-clinical research.

Future development

As the voxel sizes continue to decrease, involuntary subject motion becomes an increasing challenge, to the extent that muscle relaxation, cardiac pulsation, respiratory motion, and swallowing have a measurable effect on the image quality (Herbst et al., 2013; Stucht et al., 2015). A possible solution for this would be prospective motion correction (PMC), where the MR gradient system is adjusted in real-time to ensure that the brain remains in the same location in the imaged volume (Maclaren, Herbst, Speck, & Zaitsev, 2012). PMC has been used in combination with UHF-MRI and results of whole brain MP2RAGE scans with an

isotropic resolution of 0.44 mm have been presented (Stucht et al., 2015). One of the downsides of PMC is that for the currently commercially available systems additional hardware is necessary to track the motion of the brain (Maclaren, Herbst, et al., 2012). Another possibility would be to use MR-based motion measures such as fat image navigators (fat-navs) (Federau & Gallichan, 2016; Gallichan, Marques, & Gruetter, 2016). Fat-navs are interleaved acquired high contrast images of the sub-cutaneous fat and bone marrow of the skull and can be used to estimate and correct head motion. Using these fat-navs, whole-brain MP2RAGE scans with an isotropic resolution of 0.35 mm have been acquired at 7T (Stucht et al., 2015). The advantage of such high spatial resolution is that certain anatomical details such as the grey matter islands between the putamen and caudate become much more visible (see Figure 8 for a visual comparison between two whole-brain MP2RAGE datasets of which one used fat-Navs and higher spatial resolution. Data is provided by (Federau & Gallichan, 2016; Forstmann et al., 2014; Stucht et al., 2015).

Conclusion

The number of UHF-MRI sites is steadily increasing as there are several advantages over lower field MRI such as intrinsic higher SNR and increased CNR. With the increase of field strength, it becomes possible to visualize small subcortical structures and their subnuclei which are challenging to localize. This is illustrated in this review by the fact that UHF-MRI, with a wide range of imaging approaches, has been able to identify 163 subcortical structures in the individual brain. Some of these concern subdivisions in structures that were only identifiable as a whole at lower fields. It should however be noted that most of these structures were only identified in a single publication. This is substantial progress, but also emphasizes the amount of work yet to be done to find a comprehensive imaging approach to parcellate the subcortex per individual. With the large efforts currently directed at UHF sequence development (Marques & Norris, 2017) it seems especially likely that the number of identifiable structures will increase further.

Acknowledgments
The work was supported by a Vidi grant by the Dutch Organization for Scientific Research (NWO) (BUF) and a starter grant from the European Research Council (ERC) (BUF). We would like to thank Bob Turner, Andreas Schäfer, and Pierre-Louis Bazin for helpful discussions on the use of UHF-MRI and Rosie Mulray for proofreading the manuscript.

Two

Ultra-High Field MRI-Guided Deep Brain Stimulation

Deep brain stimulation in Parkinson' disease

"My neurologist has advised me to think about DBS-surgery, and when I see the reports on TV I would do it immediately, but reading the negative stories on this forum, I get doubts…".

A deep brain stimulation (DBS) candidate posted the above quote on a web-based forum for patients suffering from Parkinson's disease (PD) (forum.parkinson-vereniging.nl). The quote illustrates that although the effectiveness of DBS of the subthalamic nucleus (STN) as a treatment for PD has been extensively established, it does not necessarily equate to an increased quality of life as perceived by patients who have either undergone or are candidates for DBS surgery (Odekerken et al., 2015; Wichmann & DeLong, 2006). Such negative perceptions stem from the fact that STN DBS is not as equally effective in all patients. For instance, a fraction of patients will exhibit little to no change in their motor symptoms while others may develop psychiatric side-effects such as cognitive decline, associative disturbances, and emotional disorders, all of which may be attributed to the suboptimal placement of DBS leads (Temel, Blokland, Steinbusch, & Visser-Vandewalle, 2005).

Benefits and accessibility of ultra-high field MRI

In this paper, we discuss how utilizing ultra-high field (UHF) magnetic resonance imaging (MRI) in pre-operative planning for DBS can improve both the clinical outcome and the public perception of the treatment. The main advantages of UHF-MRI are the increased spatial resolution, contrast, and signal which can be achieved in a clinically acceptable timeframe. We explain that by adopting a patient-specific approach to DBS targeting with UHF-MRI, we can maximize the clinical efficacy of the treatment for each patient while simultaneously eliminating the development of associated side-effects.

In the Netherlands, there are six active DBS centers (www.nfu.nl). Each center is located near a UHF-MRI site, offering the opportunity to apply and advance its use for clinical purposes including DBS, with the added benefit of potential direct collaborations with specialized neuroimaging departments associated with these UHF-MRI sites. With this

multidisciplinary set-up, UHF-MRI can become a standard clinical tool for DBS surgeries in the Netherlands, and eventually worldwide (Figure 1).

MR technology has advanced greatly over the past three decades through higher field strengths and specialized sequences (Figure 2). However, subcortical imaging remains more challenging as these nuclei are scarcely represented in standardized anatomical atlases, are lacking in post-mortem validation, and, at present, require labor-intensive and expert analysis for accurate identification. This is problematic given that the majority of DBS targets are small and deeply situated subcortical nuclei which cannot be reliably nor reproducibly imaged with clinically utilized 1.5T and 3T MRI (Figure 2) (Cho et al., 2010; Patel, Khan, & Gill, 2008). However, efforts to create automated parcellation procedures with multimodal contrasts are being made with UHF-MRI which would be of great benefit to DBS targeting (Visser et al., 2016; Yang et al., 2013). For a more detailed review on UHF-MRI advancements in data acquisition and analyses see (Alkemade et al., 2017; Forstmann, de Hollander, Van Maanen, Alkemade, & Keuken, 2016).

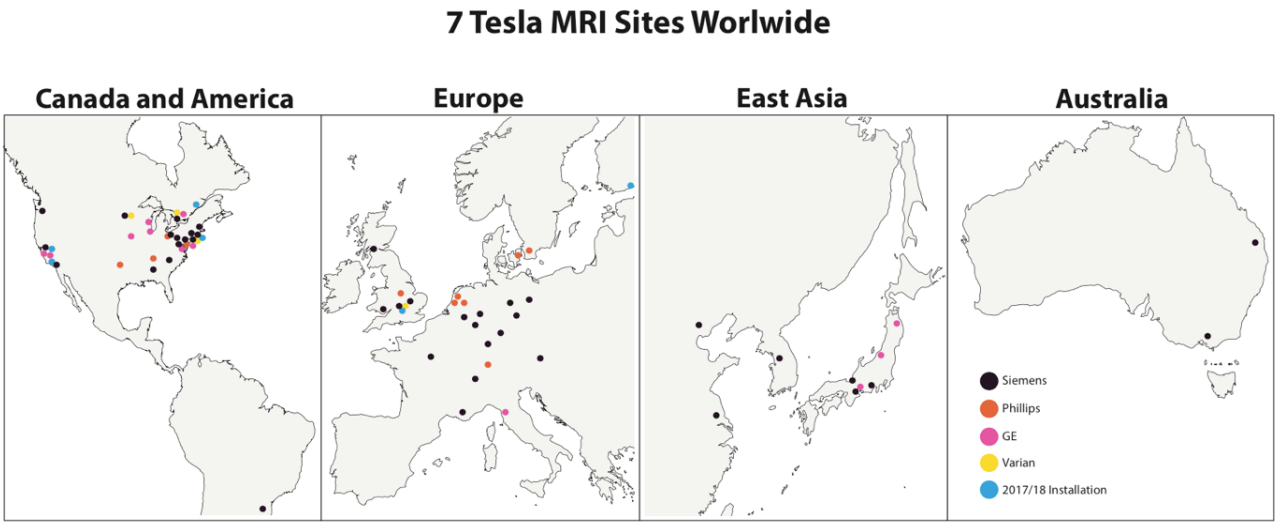

Figure 1: Depicts the locations of all known 7T MRI sites worldwide. The MR sites are color-coded regarding the vendor, where purple represents Siemens MR scanner location, orange represents Phillips scanner location, pink represents GE scanner location, yellow represents Varian scanner location and blue for locations that are planning to install a 7T MRI system between 2017 and 2018. To date, there are a total of 42 7T Siemens scanners, 12 Phillips scanners, 11 GE scanners, and 4 Varian, totaling at least 71 whole body 7T MR sites worldwide, each either near or within a DBS center.

Ultra-high field MRI guided deep brain stimulation

Successful application of DBS requires precise localization of the optimal target structure which is achieved by either pre-operative patient-specific MRI or standardized atlases as well as intra-operative microelectrode recordings (MER). However, there are two crucial yet unmet requirements for optimal DBS which are high-precision individualized targeting and reduced operation-time.

DBS targets are typically visualized with either 1.5T or 3T MRI. However, these lower field strengths are often suboptimal when compared to 7T MRI in imaging both entire nuclei such as the STN or nucleus accumbens (NC) as well as subcomponents of thalamic and pallidal structures, such as the anterior thalamic nucleus (ANT), ventral intermediate nucleus (VIM), globus pallidus interna (GPi) and externa (GPe) (Calamante et al., 2013; Cho et al., 2010). Additionally, clinical scans obtained via routine practice are often shorter than those used for research purposes due to limitations in scanning time, and therefore differ in quality. While an optimized 3T sequence may allow for reasonable visualization of subcortical nuclei, they require a longer acquisition time than an analogous 7T sequence (Figure 2). Even when low field MRI is optimized for specific nuclei such as the STN, we often fail to produce consistent volumetric measures. Similarly, with low field MRI it is difficult to identify the supposed cognitive, limbic, and motor subcomponents which have been more consistently observed with UHF-MRI, which additionally differ both functionally and structurally across individuals (Cho et al., 2010; Lenglet et al., 2012; Patel et al., 2008; Temel et al., 2005; Verhagen et al., 2016). Such findings strongly support the use of patient-specific UHF-MRI for optimal DBS lead placement, for which the same logic may be passed to other stereotaxic neurosurgeries (Lenglet et al., 2012; Plantinga et al., 2018).

Clinical identification of subcortical DBS targets is largely facilitated via anatomical landmarks and a-priori defined assumptions especially when a nucleus such as the VIM or ANT is not directly observable. Such an approach to identification likely varies from surgeon to surgeon. Therefore, to avoid subjectivity, it is important to accurately image not only the target nucleus but also its surrounding structures such as the internal capsule and mammillothalamic tracts, which are best achieved by the increased signal and contrast afforded by UHF-MRI.

Furthermore, the viability of the DBS target must be either confirmed or modified

with time-consuming and invasive intraoperative electrophysiological methods taken during implantation such as microelectrode recordings, macrostimulation, and behavioral feedback in the awake patient (Patel et al., 2008). If surgeries were planned using UHF-MRI, target nuclei could be more reliably and objectively identified, limiting the chance of the removal and/or re-implantation of suboptimally placed DBS leads. Further, high-precision imaging would reduce operation time and allow the patient to be placed under general sedation where behavioral assessments can be conducted post-operatively, ultimately maximizing patient comfort.

An additional factor to consider is whether stimulation of the targeted nucleus will result in the optimal clinical outcome. The choice of DBS target depends on the clinical presentation of symptoms which can vary within the same disease across patients and is highly dependent on individual differences in neuroanatomy. This is exemplified by the number of different DBS targets that exist for the same disorder. For PD and related movement disorders, DBS targets include not only the STN but the substantia nigra, GPi and VIM. In Epilepsy, the hippocampus, ANT, or centromedian thalamic nucleus and seizure foci are possible neurostimulation targets, and for Obsessive Compulsive Disorder (OCD) one may choose from the medial thalamus, the anterior limb or ventral part of the internal capsule, and NC (Wichmann & DeLong, 2006). Such findings call into question the accuracy and reproducibility of low field MRI and raise several questions such as: How do we chose the target nucleus for each disorder and is this target different for each patient?

We believe each issue described here can be overcome by applying patient-specific UHF-MRI. UHF-MRI allows for more anatomically correct imaging that also accounts for subtle individual differences in neuroanatomy that cannot be captured with lower field strengths. Specialized sequences already exist for complex structures such as intra-thalamic subnuclei, which could greatly aid pre-operative planning for DBS in OCD, Tremor, Tourette's, and Epilepsy (Cho et al., 2010). UHF functional MRI and diffusion-weighted imaging may be used to determine the nature of structural and functional connectivity for subcomponents of target nuclei, facilitating for example identification of the motor portion of the STN for PD patients, which would maximize the efficacy of the treatment while minimizing the occurrence of psychiatric side effects (Lenglet et al., 2012; Plantinga et al.,

2018). High precision imaging should result the elimination of intra-operative testing, permitting surgeries to be performed under general anesthesia which maximizes patient comfort as well as minimizing the related anxiety often reported by potential candidates.

Remaining challenges

Despite the advantages previously discussed, the application of UHF-MRI in neurosurgical targeting is not yet FDA approved and is very much an experimental technique, requiring a more advanced knowledge than is typical in the field of clinical radiology. Moreover, the aforementioned practices have yet to be standardized or implemented on conventional scanners. Several challenges exist regarding increased geometric distortions, specific absorption rate, power deposition and artifacts, inhomogeneity of the B1 field, incompatible coils, and contraindicative metal implants (Lehericy et al., 2017). Ongoing technical developments to harmonize the B1 field with specially designed coils as well as developing UHF coils that are compatible with stereotaxic coordinate frames along with corresponding fusion protocols, optimization of sequences, radiofrequency shimming, post-processing, and multi-modal methods are underway to counter such challenges (Dammann et al., 2011; Lehericy et al., 2017).

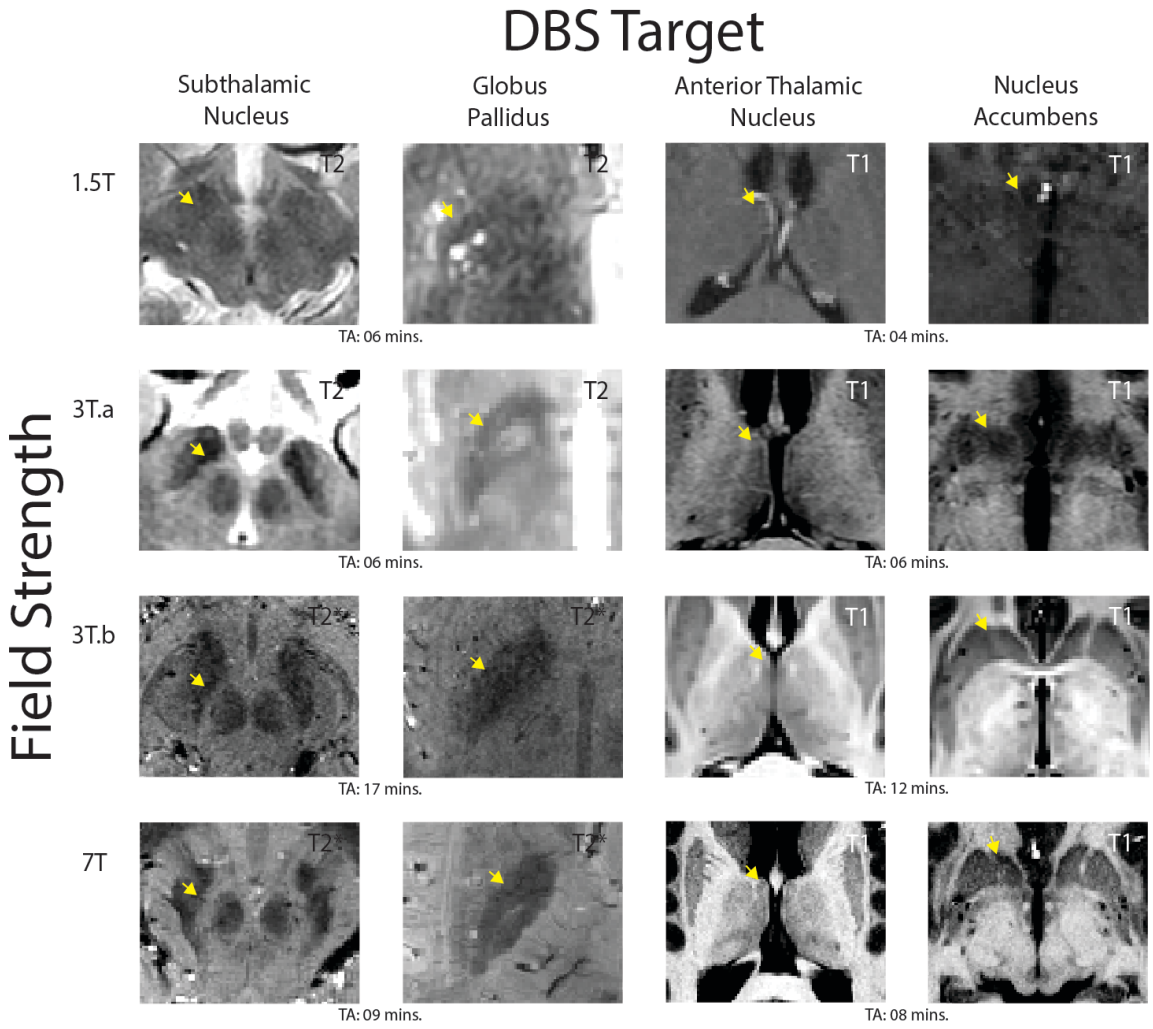

Figure 2: Visualizing DBS targets with different MRI field strengths. 1.5T images were obtained from a 52-year-old male Parkinson's disease patient at the Maastricht University Medical Centre (MUMC). Clinical 3T and 7T images were obtained from a 57-year-old male Parkinson's disease patient at the Maastricht University Medical Centre (MUMC). The optimized 3T images were obtained from a healthy male age-matched subject at the Spinoza Centre for Neuroimaging, Amsterdam. All images are shown in the axial plane, in their native space with no post-processing to replicate visualization as performed on neurosurgical planning software. The T1 contrasts show the anterior thalamic nucleus and nucleus accumbens at all field strengths. The subthalamic nucleus and globus pallidus (GP) are shown with a T2 contrast at 1.5T and clinical 3T scan. Note that in the 7T contrast, the medial medullary lamina is visible, and allows to distinguish between the internal and external segment of the GP. For optimized 3T and 7T the STN and GP are shown with a T2* contrast. The acquisition times (TA) for each scan are included to highlight the fact that optimized 3T can provide high-quality images similar to those at 7T, but take nearly twice as long to obtain. While the STN and GP are visible in both 3T images, the contrast and sharpness of borders increases at 7T.

Conclusions

UHF-MRI could be the new golden standard for stereotaxic neurosurgeries such as DBS. Before this can become reality, UHF-MRI must be confirmed as a superior method for localizing surgical targets. For this, MR researchers and neuroscientists must collaborate with neurosurgeons and clinics to start consistently utilizing UHF-MRI for DBS pre-operative planning. Then we can begin to assess post-operative lead placement and behavioral outcome to determine whether targeting at UHF does indeed significantly increase the efficacy of the treatment as well as reduce the occurrence of associated side-effects when compared to targeting with clinical MR. Promoting such a vision will further require a systematic and updated review of the various stereotactic methods, targeting techniques, MR parameters utilized for pre-operative planning, intra-operative CT verification as well post-operative confirmation of DBS lead location.

Acknowledgments
We would like to thank Max C. Keuken and Frédéric Schaper for their helpful discussions. This research was supported by an ERC grant from the European Research Council (B.U.F.), a Vidi grant from the Dutch Organization for Scientific Research (B.U.F.). Y.T received financial support from Stichting Annadal and Dutch Organization for Scientific Research (NWO, Grant no. 452-11-002) for the ultra-high field MR research.

Three

Controversies in Deep Brain Stimulation Surgery: Microelectrode Recordings and Magnetic Resonance Imaging

Introduction

Deep brain stimulation (DBS) of the subthalamic nucleus (STN) was first applied as a neurosurgical intervention technique for Parkinson's disease (PD) in the 1990s and has since become a widely accepted practice. DBS is generally considered in patients only when pharmacological treatment no longer provides sufficient alleviation of symptoms or results in adverse effects. Stimulation of the subthalamic nucleus (STN) is the most common practice since it allows for more time in well-treated 'ON-condition', though the internal segment of the globus pallidus (GPi) is also a possibility (Bronstein et al., 2011; Odekerken et al., 2013). While DBS of the STN specifically is effective for the majority of patients in relieving the motor-related symptoms of PD, a fraction of patients will fail to witness such beneficial effects. Moreover, DBS patients may develop several side effects spanning a range of domains, from speech and gait impairments to cognitive decline and impulse control disorders, as well as psychiatric and emotional disturbances. The first two concepts here are a product of accurate target identification and verification, which can be achieved via pre-operative magnetic resonance imaging (MRI) and or intra-operative microelectrode recordings (MER). This chapter will attempt to determine whether MRI with or without additional intra-operative MER-guidance is the most effective method for target identification and verification in DBS via a structured literature review. Additionally, we will discuss some advantages, caveats, and outstanding complications for both methods, with a focus on STN-DBS for PD.

Originally, MER was seen as the golden standard for anatomical verification of a DBS target. In this method, the leads are placed in the brain based on standard atlas coordinate systems applied on a pre-operative MRI of the patient. Through macrostimulation of functionally distinct portions of the STN along with behavioral and clinical tests, MER can spatially map out the optimal location for DBS lead placement (Bot et al., 2018). However, the verification via MER requires that the patient be awake and tested during DBS implantation. The patient's awake response on the intra-operative stimulation regarding motor symptoms and adverse effects can influence the final lead placement. Moreover, MER signals will be influenced by general anesthesia. This is time consuming, stressful, and causes

a lot of anxiety for patients. Originally controversial, but steadily gaining popularity is the use of pre-operative MRI for targeting and intra-operative MRI or CT for identifying the lead location, rather than MER. This approach allows the patient to be under general anesthesia and is potentially equally as effective as MER (Follett et al., 2010; Nakajima et al., 2011; Williams et al., 2010). Despite many studies, some contradictions still exist. For example, supporters of MER suggest optimal final lead placement can deviate from the (MRI or atlas-based) planned target by using intra-operative MER (Bour et al., 2010). While, on the other hand, opponents of MER suggest image-guided and verified surgery can reduce intra-operative brain-shift and accompanying lead inaccuracy, especially in the second placed lead (Petersen et al., 2010). Relatedly, the overall success of traditional target identification and implantation still will depend on several factors; namely, the existing knowledge of the anatomy of the STN and surrounding structures, counteracting intra-operative brain shift, and the use of multiple leads for MER. Furthermore, modern technical advances offer new possibilities that might positively influence the outcome of lead placement and clinical outcome, however, they are bringing their considerations. Some of them are pre-operative ultra-high field MRI, multimodal image techniques such as diffusion and functional MRI, personalized stimulation parameters, and calculation of surrounding tissue activated outside of the target by stimulating with directional steering leads. The following chapter, therefore, consists of a literature review of DBS of the STN in PD patients using both, or either MRI and MER, as well as papers discussing the aforementioned factors which are deemed essential for successful DBS, though remain subject to personal preference.

Methods

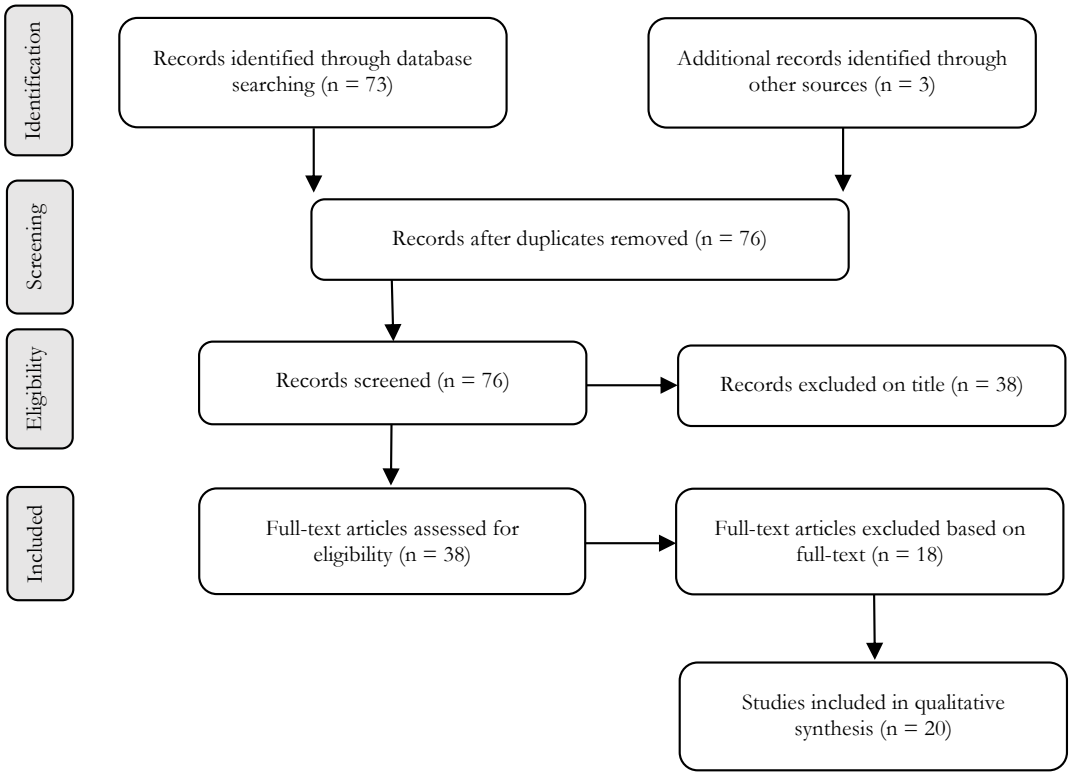

To collect relevant and recent literature we performed a literature search in the Pubmed database with the search string: "((microelectrode recording) OR (microelectrode recording) OR MER) AND (MRI OR MR OR (magnetic resonance imag*)) AND (DBS OR (deep brain stimulation)) AND (STN OR (sub thalamic nucleus) OR (subthalamic nucleus))" on 18-07-2018, with a limitation of publication date within 10 years, which gave us 73 potential articles. We included 3 papers from cross-references. We excluded 38 papers based on the title. From the 38 full-articles, we excluded 18 articles because they had non-human subjects, described alternative methods besides conventional MRI-guided or MER-guided stereotactical DBS surgery, used non-STN targets, or were non-original articles. We included 20 articles for the qualitative evaluation we describe in this paper. Included articles are rated following the GRADE criteria for quality of evidence (BMJ, 2010). Since this literature is very heterogenic, we did not perform a quantitative meta-analysis on clinical outcome, e.g.

UPDRS or quality of life scores, or on the anatomical outcome, e.g. millimeters deviation per MR-field strength or percentage of central MER-recordings used for final lead-implantation.

Results

We formatted the results section as three tables, 1. including literature in favor of MER, 2. in favor of MRI, and 3. studies using alternative MRI techniques. Since different endpoints are used as outcome parameters in the literature, and most studies use different methodologies, we give a comprehensive, overview of the current opinions and evidence on this topic. We tried to summarize the concluding decisive of the authors in comparable arguments to enable quick comparison of the actual opinions.

Table 1. In favor of MER-guided targeting, using 1.5- or 3-Tesla MRI

Reference	Study design	Arguments	GRADE certainty rating
Amirnovin et al., 2006	Comparing 1.5T-MRI coordinates with final placement based on MER and intra-operative testing	- 58% of locations changed based on MER and testing	Low
Temel et al., 2007	STN DBS with single (n=32) vs. multiple (n=23) intra-operative MER electrode recordings	- Multiple MER trajectories lead to better post-operative rigidity and tremor without more complications - Multiple MER trajectories induced mild declines in memory function	Low
Bour et al., 2010	Comparing central MER trajectory (based on 1.5T-MRI) with final electrode trajectory	- Final trajectory was accurate according MRI in 50%, final depth was within 1 mm range of MRI-target in 57% - 64% of final placement was the channel with best MER activity	Low
Schlaier et al., 2011	Comparing posterior STN-border based on 1.5T-MRI vs. MER	- 44% of MER STN volumes were larger than the MRI STN volumes - 46% of MER STN being incompatible with the MRI STN	Low
Reck et al., 2012	Comparing DBS STN surgeries with 1.5T-MRI targeting and MER-guidance with (n=32) vs. without (n=10) intra-operative stimulation	- Significantly better UPDRS III outcome in MER vs. non-MER - In 27% MER-guidance lead to trajectory adjustment	Low
Juergen et al., 2013	Comparing 1.5T-MRI defined STN vs. location defined as STN based on MER	- 38% of active contact points beyond MRI defined STN borders	Low
Longhi et al., 2015	Comparison of accuracy of 1.5T- vs. 3T-MRI in predicting final electrode location	- 1.5T: 2/12; 3T: 21/28 - Better clinical performance in 3T group - MER to determine lead deepness and prevent adverse effects	Low

Rabie, Metman, & Slavin, 2016	Direct targeting based on 3T-MRI vs. indirect targeting based on stereotaxic atlases and comparing MRI-coordinates with final implantations	- Significant difference in Euclidian distances between 3T-MRI coordinates and final coordinates based on MER and intra-operative testing - MER has increased spatial resolution	Low
Nowacki et al., 2017	Comparing targeting accuracy of 3T-MRI in 78 MER-verified implanted DBS electrodes	- Average difference between STN crossing lengths: 0.28 mm - In 43% the deviation was more than 1mm	Low
Lozano et al., 2019	Evaluation of 100 consecutive DBS STN surgeries: comparing direct and in-direct targeting (1.5T-MRI) and MER-guided target adjustments	- 18% corrected based on MER in first side, 20% corrected in second side - Intra-operative electrophysiology or MRI is needed next to MRI-targeting	Moderate

Table 2. In favor of MRI-guided targeting, without additional MER, using 1.5- or 3-Tesla MRI

Reference	**Study design**	**Arguments**	**GRADE certainty rating**
Foltynie et al., 2010	Description of cohort one-year after 1.5T-MRI-guided STN DBS, without additional MER (n=79)	- Mean UPDRS improvement during off-medication of 52% (28 points) - Dyskinesia severity from 3.2 to 1.6 points (UPDRS IV) - Mean levodopa reduction of 39% - Mean DBS: 3.0 V, 60 microseconds, 139 Hz	Low
Nakajima et al., 2011	Comparison of 2 cohorts: local anaesthesia with MER and clinical testing (n=68) vs. general anaesthesia without MER or intra-operative stimulation (n=14)	- Comparable improvement of UPDRS-III (general: 52.8% vs. local: 50.8%) and LED reduction (general: 50.8%, local: 60,2%) - No comparison on DBS settings	Moderate
Aviles-Olmos et al., 2014	Same cohort as Foltynie 2011; five-year follow-up (n=41) and eight-year follow-up (n=12)	- Off-medication UPDRS improvement remained 70% for tremor, 50% for rigidity and bradykinesia improvement decreased from 46% to 23%	Low
Liu et al., 2017	Comparison of two retrospective cohorts: implantation without MER based on 1.5T T2 MRI (n=61) vs. implantation with MER guidance (n=76)	- Similar improvement after one year in off-medication UPDRS (resp. 65% vs. 66%) and quality of life (resp. 44% vs. 50%); similar levodopa reductions	Moderate
Brodsky et al., 2017	Comparison of two cohorts (STN subgroups): asleep implantation without MER (n=7) vs. awake implantation with MER (n=18)	- No significant difference in UPDRS II and III improvement (no sub scores for STN/GPi separately) - Asleep cohort was superior on quality-of-life, cognition and communication/speech outcomes	Low
Lee et al., 2018	Evaluation of 45 consecutive DBS STN surgeries: either asleep without MER and intra-operative testing, or MER-guided DBS with intra-operative testing	- Side effect thresholds during initial programming were slightly lower in the MER group - No significant difference in the reduction of clinical symptoms or medication dosage was observed	Moderate

Table 3. Studies using alternative MRI techniques as ultra-high field MRI and susceptibility-weighted sequences

Reference	Study design	Arguments and conclusions	GRADE certainty rating
Polanski et al., 2015	Comparing 182 MER trajectories from 42 STN's vs. T2, FLAIR and SWI 3T-MRI	- Recommendation for SWI MRI based on sensitivity, specificity and negative pred. value - Reserved to advise DBS without MER	Low
McEvoy et al., 2015	Comparing 3T MRI SWI STN-SN border on coronal plane with MER activity in 7 DBS STN surgeries	- SWI MRI demonstrates reliable STN delineation	Low
Verhagen et al., 2016	Comparing dorsal and lateral STN borders on 1.5T, 3T and 7T T2 MRI vs. computational MER-STN model	- 7T decreased variance between dorsal + lateral MRI and MER borders - 3T and 7T STN borders more dorsal than MER - 7T SWI should be explored besides 7T T2	Low
Keuken, Schäfer, & Forstmann, 2016	Comparing STN targeting based on T2 and SWI 1.5T and T2 3T with MER STN activity	- MER STN activity in 84% of MRI target trajectories - 1.5T SWI inferior to 1.5T T2	Low
Bus et al., 2018	Compare STN activity in MER trajectories (visualized with intra-operative CT) vs. 3T T2 and SWI MRI	- Low correspondence of ventral and dorsal MRI STN borders with MER STN activity - 3T SWI MRI decreases false-positive MRI-based STN targets - Only 42% of central SWI-based trajectories targeted final electrode placement	Low

Discussion

While advancements in MRI acquisition and analysis techniques such as ultra-high field and diffusion tractography have greatly advanced and have the potential to be used for neurosurgical purposes like DBS, their application within the clinics has been severely limited (Brunenberg et al., 2012; Hariz et al., 2002; Zrinzo, Hariz, Hyam, Foltynie, & Limousin, 2016). The combined literature fails to provide a single favorable approach for DBS targeting. This is in part due to the differences in both the method and the outcome determinant. For instance, some studies report differences in the planned target with the actual location as determined on CT, or by the deviation identified with MER. Others determine treatment efficacy by differences in pre and post-operative levodopa equivalent dose (LED) response and UPDRS scores. The manufacturers of both software and hardware used for surgical planning (e.g. Medtronic, Abbott, Boston Scientific) differs across DBS centers, as do the number of MER test electrodes used, types of MRI (e.g. 1.5T, 3T, 7T), vendors (e.g. Siemens, Phillips, GE), sequences and scan parameters (e.g. contrasts, voxel size). The number of

patients also differs greatly across studies, which is a threat to statistical power in group-based analyses. Different surgeons can even be a confounder in such cross-comparisons. Some studies suggest that intra-operative MER can significantly improve the outcome of DBS of the STN (Chen et al., 2006). Whereas others will argue that while targeting through standardized atlases are unreliable, the addition of MER fails to significantly improve STN DBS (Patel, Heywood, O'Sullivan, Love, & Gill, 2002). Following the trend of individualized and personalized medicine, direct targeting is certainly preferred over indirect targeting in MRI, though this does not necessitate that MER is no longer required. Instead, the increasing success of DBS will most likely depend on the implementation of advanced MRI techniques within the clinics. Relatedly, advancements in lead and electrode hardware, such as the use of directional steering might play a role in the elimination of MER in DBS surgeries (Contarino et al., 2014).

Regardless, the clinical relevance attributed to MER by many authors cannot be neglected. MER enables us to measure nucleus-specific neuronal activity, for example, the beta activity of the STN which can help identify the dorsolateral borders, reflecting the motor portion of the target. Additionally, MER allows for direct behavioral testing, optimization of stimulation parameters, and assessment of potential side effects, which in theory collectively result in minimizing the occurrence of post-operative side effects and maximizing clinical benefit (Ho et al., 2018). The latter is however no insurance for the absence of adverse effects. Identification of specific nuclei and their subcomponents through MER was only necessary due to the limitations of conventional MRI techniques, which traditionally lacked the contrast and spatial resolution required for the desired level of anatomical accuracy (Alterman & Weisz, 2012; Chandran, Bynevelt, & Lind, 2015; Polanski et al., 2015). Moreover, DBS surgeries still heavily rely on the application of standardized coordinates and atlases, referred to as indirect targeting. Such an approach is erroneous given the well-documented heterogeneity of deep brain structures. For instance, the STN is known to shift in the lateral direction with age as well as a decrease in volume with the disease; such alterations are not captured with stereotaxic atlases which can lead to suboptimal placement of electrodes.

The application of ultra-high field MRI and advanced multi-modal approaches has the potential to revolutionize current practices. The increased signal and contrast offered by

UHF-MRI allows for sharper and more accurate visualization of deep brain structures within a clinically feasible time frame (Federau & Gallichan, 2016; Keuken et al., 2016; Lüsebrink, Wollrab, & Speck, 2013; McRobbie, Moore, Graves, & Prince, 2006). The combination of diffusion MRI and functional MRI allows for the identification of both functional and structural networks which can provide additional information concerning optimal DBS placement, which can additionally be used to inform on the potential volume of tissue activated and with connected networks, which is useful for predicting clinical outcomes. Relatedly, novel contrasts that exploit the paramagnetic properties of iron-rich basal nuclei such as susceptibility-based contrasts and quantitative maps can be used to better visualize such DBS targets on 7T compared to 3T (Abosch et al., 2010; Alkemade et al., 2017; Alkemade, Schnitzler, & Forstmann, 2015; Cho, Oh, et al., 2011; Dula et al., 2010; Duyn, 2012; Keuken et al., 2017; Liu et al., 2017).

Moreover, low field strength intra-operative MRI (iMRI) can be used to monitor in real-time the location of DBS leads. Although that low field strength MRI is notorious for suboptimal visibility of the STN, there are positive reports on the use of iMRI during DBS. Improved motor symptoms comparable to MER-guided DBS are reported for DBS using 1.5-T-iMRI techniques (Ostrem et al., 2013). Reliance purely on radiological and neuroimaging techniques, in theory, leads to a reduction in the additive surgical risks of MER usage, decreased operation time, and increased peri-operative patient wellbeing since surgery can be performed under general sedation and pre-operative dopamine-withdrawal can be excluded (Ben-Haim, Asaad, Gale, & Eskandar, 2009; Xiaowu et al., 2010). The statement whether major surgical risks such as bleeding will decrease is debatable since the use of multiple MER trajectories did not increase surgical risks compared to the use of a single MER trajectory (Temel et al., 2007). However, leads placed in a single penetration, in a faster time frame, when based on MRI, can potentially limit the occurrence of brain shift by reducing CSF loss (Lee et al., 2018). Further, a cost analysis showed MER more than doubles the price of a bilateral STN DBS surgery in the United States (McClelland, 2011).

The use of UHF-MRI in DBS should be applied with caution. Firstly, the deep brain structures like the STN are located in the middle of the brain, which means that the signal to noise ratio is substantially lowered compared to the cortex (de Hollander, Keuken, van der

Zwaag, Forstmann, & Trampel, 2017; Larkman & Nunes, 2007; Pohmann, Speck, & Scheffler, 2015; Vaughan & Griffiths, 2012). This is important when considering the requirement of acquiring scans in a clinically feasible window, especially for PD patients, given the potential for accumulative movement artifacts, though methods do exist for motion correction (Maclaren et al., 2012). Secondly is the requirement of post-processing techniques and expertise outside of a standard clinical setting, which is especially true for tractography and functional MRI (Forstmann et al., 2017). And thirdly, the absolute requirement of an accurate co-registration between pre, intra- and post-operative MRI-MRI and or MRI-CT. Therefore, error can occur during the initial targeting on MRI and transformation to a stereotaxic coordinate system on CT, and during the intra- and post-operative MRI and or CTs acquired for lead localization. This argument exists still for 1.5 and 3T clinical scans though appears to be more difficult to account for at 7T. Suboptimal fusion can lead to geometrical errors of up to 3mm (O'Gorman et al., 2009). If we rely purely on neuroimaging, these errors cannot be accounted for.

A reasonable conclusion would be that when MRI based targeting does not result in an intra-operative deviation significantly more than when based on targets are based on MER, MRI should be preferred (Kochanski & Sani, 2018). This doesn't suggest that MRI is significantly better than MER but rather it is a viable and attractive alternative given MRI guided DBS allows the patient to be fully anesthetized and eliminating the need for behavioural feedback and intra-operative testing (Burchiel, McCartney, Lee, & Raslan, 2013; Chen et al., 2016; Chen, Mirzadeh, & Ponce, 2017; Martin, Starr, Ostrem, & Larson, 2017; Mirzadeh et al., 2016; Mirzadeh & Ponce, 2015; Ostrem et al., 2013, 2016; Sidiropoulos et al., 2016; Slavin, Thulborn, Wess, & Nersesyan, 2006). What remains unanswered is whether direct targeting via MRI-guided DBS reduces the risk of reimplantation compared to DBS performed with MRI and-or only MER. The patient preference can be a heavy argument in the decision-making on DBS surgery strategy. This preference can be influenced by for example disease severity and the impact of the withdrawal of dopaminergic medication, psychological reasons, and psychiatric comorbidities which might be part of the Parkinsonian non-motor symptoms or can be independent of the disease.

Conclusions

Literature is inconclusive regarding the added value of intra-operative MER during DBS surgery. Studies in favor of this technique use different endpoints than studies that do not find added value. This chapter provided an overview of these various arguments. For the near future, we expect decision-making regarding "awake MER" versus "asleep MRI-guided" DBS to be made on an individual patient level, taking into account the clinical presentation, MR imaging characteristics, experience with directional steering, and patient preference. Clinical trials comparing both methods will be needed to address this issue further.

Four

Variability in Subthalamic Nucleus Targeting for Deep Brain Stimulation with 3 and 7 Tesla Magnetic Resonance Imaging

Introduction

Since its introduction in the 1990s, deep brain stimulation (DBS) of the subthalamic nucleus (STN) has proven to be an effective surgical treatment for advanced Parkinson's disease (PD) (Benabid et al., 2009; Limousin et al., 1995). STN DBS for PD is especially efficacious in treating otherwise refractory tremor, motor fluctuations, and dyskinesias (Deuschl et al., 2006; Limousin & Foltynie, 2019). However, in despite these positive outcomes, STN DBS has the potential to induce several side-effects including behavioral changes, cognitive impairments, and speech, balance, or gait problems (Frank et al., 2007; Parsons et al., 2006; Temel et al., 2006; Zarzycki & Domitrz, 2020). These side-effects may be a product of suboptimal placement of the DBS lead (Gilmore et al., 2017; Kloc et al., 2017; Petry-Schmelzer et al., 2019). Here we focus on the first of many procedural steps that can contribute to such suboptimal placement; stereotactic planning of the electrode site (Giller & Jenkins, 2015).

Targeting the STN can either be done using a constant coordinate relative to a given anatomical landmark or by visualizing the STN per individual and determining the target per patient. These two approaches are respectively called indirect and direct targeting, where direct targeting typically results in a better patient outcome as individual anatomical variability is taken into account (Lahtinen et al., 2020). Common clinical practices for direct targeting of the STN for DBS is achieved using T2-weighted (-w) magnetic resonance imaging (MRI) (Bus et al., 2018; Verhagen et al., 2016). T2-w MRI is sensitive to iron content, and the STN is rich in iron, which causes it to appear hypointense compared to the surrounding grey matter structures (Deistung et al., 2013; Hollander et al., 2014). Additionally or alternatively, some centers incorporate intraoperative microelectrode recordings (MER) for target verification, while others rely exclusively on indirect targeting approaches with MER and standardized coordinate systems (Habets et al., 2019). Notably, most centers perform the DBS surgery in awake settings with local anaesthesia, thereby enabling the clinician to assess stimulation related side-effects during test stimulation and adjustment of the final electrode targeting. STN surgeries are increasingly being performed under general anaesthesia and therefore the precision of the stereotactic planning with MRI is becoming even more

important.

Direct targeting for DBS traditionally relies on lower field MRI (1.5 and 3T MRI) which are prone to low contrast and signal to noise ratios (CNR and SNR, respectively), and result in images that lack sharp and clear borders of small deep brain structures (Forstmann et al., 2017; Isaacs, Keuken, et al., 2020). Ultra-high-field MRI systems (7T and above) can obtain submillimeter anatomical information with increased contrast (Inglese et al., 2018; Keuken et al., 2018). Whether the benefits of ultra-high-field MRI result in better targeting for DBS remains unclear (Bot et al., 2018, 2019; Duchin et al., 2018; Hartmann et al., 2019; Isaacs, Mulder, et al., 2020; Springer et al., 2016).

In addition to higher field strengths, quantitative imaging methods may contribute to the vizualisation of DBS targets as they convey microstructural properties of the area of interest. For example, while T2* contrasts visualize the STN as a hypointense structure, they can provide additional quantitative maps that provide information in relation to iron content and load (Chavhan et al., 2009; Elolf et al., 2007; Plantinga, 2016). Further, effective transverse relaxation rate, or R2*, maps (R2*=1/T2*) derived from T2* contrasts are even more sensitive to iron load and visualize the STN as a hyperintense structure (Ulla et al., 2013). T2* contrasts can be processed into Quantitative Susceptibility Maps (QSM) which are also sensitive to iron. However, contrary to T2* and R2* based modalities, QSM accounts for local susceptibility inhomogeneities by incorporating both magnitude and phase image information as well as incorporating methods to remove background fields such as a dipole convolution (Schäfer et al., 2012; Zhou et al., 2014). This has led some groups to suggest that QSM is the superior contrast for imaging subcortical structures that are high in iron content (Alkemade et al., 2017; Isaacs, Mulder, et al., 2020).

Once the STN is visualized the question still remains where to place the electrode. While the exact optimal site of stimulation within the STN is still under debate (e.g., Hamel et al., 2017) and seems to vary per patient (Horn et al., 2017; Vanegas-Arroyave et al., 2016), DBS is thought to be most effective in treating PD when the lead is placed in the dorsolateral (sensorimotor) portion of the nucleus (Duchin et al., 2018; Hamel et al., 2017; Starr, 2002; Welter et al., 2014). When targeting the ventral (limbic) portion of the STN, cognitive and psychiatric side-effects are more likely to occur (Machado et al., 2006). Or in the words of

lead-DBS core-developer Andreas Horn 'Millimetres matter' when it comes to DBS (Horn et al., 2019). The importance of precision is highlighted by the recent work of (Schrock et al., 2021) where within-patient repositioning of the lead location in the STN resulted in marked improvement of motor symptoms and reduction of associative and cognitive side-effects. The precision of electrode target selection is therefore considered to be one of the first of many important factors that determine DBS outcome but the reproducibility, to the best of our knowledge, has not been formally investigated.

This study aims to test whether optimized 7T imaging protocols including T2*, R2* and QSM contrasts result in less variable targeting for STN DBS than clinically utilized 3T T2 scans. Three neurosurgeons targeted, what they considered the optimal STN DBS site, on 3 repetitions of 3T-T2, 7T-T2*, 7T-R2* and 7T-QSM images for five PD patients (Benabid et al., 2009). A low degree of variability across repetitions would indicate that the MR image allows for a consensus view as to the optimal target location, whereas a high degree of variability would indicate that the image lacks the required visibility to reach a unanimous agreement. We do not focus on the performance of the individual neurosurgeons, but we specifically focus on the amount of variability in the targeted coordinates of the various MR image modalities. We hypothesize that the test-retest reliability of STN targeting will be higher for the optimized 7T contrasts than for the clinically utilized 3T images. Further, we hypothesize that the test-retest reliability of STN targeting on 7T-QSM contrasts will be higher compared to 7T-T2* or R2* as previous literature has suggested that QSM is superior in imaging the STN at 7T. A second aim is to test whether different MRI contrasts can result in different target locations as each MRI contrast contains complimentary anatomical information (Bazin et al., 2020; Visser, Keuken, Douaud, et al., 2016; Visser, Keuken, Forstmann, et al., 2016).

Materials and Methods

Participants

A total of five PD patients participated in the study (M=4; F=1) with a mean age of 62.2 years (SD=7.9 years) and a mean number of 8.4 years since the official diagnoses (SD=3.6 years). The number of patients in this study was limited due to the availability of patients meeting all the inclusion criteria and on the feasibility for the neurosurgeons to perform the stereotactic planning. PD patients were recruited as candidates for DBS surgery at the Neurology department within the Maastricht University Medical Centre (The Netherlands). The study was approved by the local Medical Ethical Committee at the Maastricht University Medical Centre (NL60342.068.17/METC172010). All data was collected and is held in accordance with the EU General Data Protection Regulation (GDPR) and the Dutch Act on Implementation of the GDPR, good clinical practice and relevant data protection laws. PD patients had no diagnosed neurological comorbidities and provided written informed consent prior to the scanning.

Data acquisition

3 Tesla MRI

Each PD patient underwent a preoperative clinical 3T scan as part of the standard clinical practice with a Phillips Ingenia scanner using a 32-channel head coil at the Maastricht University Medical Center. The 3T data that was obtained consisted of the standard clinical sequences used for DBS planning at the Maastricht University Medical Center. A whole brain 3D turbo field echo (TFE) T1-w scan was obtained with 1mm isotropic voxel sizes, with the following parameters: Repetition Time (TR) = 8.1ms, Echo Time (TE) = 3.7ms, Inversion Recovery (IR) delay = 776ms, Flip Angle (FA) = 8°, Bandwidths (BW) = 191.5Hz/px, Echo Spacing (ES) = 13.6ms, TFE factor = 183, transverse orientation acquisition in the anterior-posterior direction, with SENSE factor of 1.4 and total acquisition time (TA) of 05:51mins.

A whole brain T2-w scan was obtained with spin echo sequence with 0.45 x 0.45 x 2mm voxel sizes, with the following parameters: 65 slices, TR = 8264ms, TE 80ms, FA = 90°, BW = 193.6Hz/px, TFE factor = 15, transverse orientation acquisition in the anterior-posterior direction, with SENSE factor of 1.5 and TA of 06:20mins.

7 Tesla MRI

In addition to the standard clinical 3T acquisition, a 7T scan was acquired with a Siemens Magnetom scanner using a 32-channel head coil at the Scannexus Centre for Neuroimaging in Maastricht. Whole brain T1-w 3D images were obtained with an adapted version of the multi echo MP2RAGE (magnetization-prepared rapid gradient echo multi-echo) sequence (Caan et al., 2018; Marques et al., 2010) with 0.8mm isotropic voxel sizes and the following parameters: 208 slices, TR = 6000ms, $TE_{1,2}$ = [2.74ms, 8.71ms], Inversion Time (TI) $_{1,2}$ = [750ms, 29000ms], $FA_{1,2}$ = [4°, 6°], $BW_{1,2}$ = [350Hz/Px, 150Hz/Px], ES = 13.6ms, interleaved and single shot multi slice mode and interleaved, sagittal orientation acquisition in the anterior-posterior direction, phase partial Fourier 6/8, parallel acquisition with GRAPPA and acceleration factor of 3 and TA of 10:56mins. Where possible, dielectric pads were placed between the side of the participants head and the receiver coil to reduce B_1 inhomogeneity artefacts. The T2*-w 3D scan was acquired with a partial volume GRE (gradient echo) ASPIRE (multi-channel phase data from multi-echo acquisitions) sequence covering the subcortex with 0.5mm isotropic voxel sizes and the following parameters: 90 slices, 16.7% slice oversampling, TR = 33ms, TE_{1-4} = [2.49ms, 6.75ms, 13.50ms, 20.75ms], FA = 12°, BW_{1-4} = [300Hz/px, 300Hz/px, 200Hz/px, 100Hz/px], interleaved multi slice mode, sagittal orientation acquisition in the anterior-posterior direction, slice partial Fourier 7/8, parallel acquisition with GRAPPA and acceleration factor of 2 and TA 07.42mins (Eckstein et al., 2018).

Calculation of Quantitative MRI Maps

All quantitative maps were created in native space. First, skull information was removed using the Brain Extraction Tool as implemented in FSL 5.0 (Jenkinson et al., 2012; Smith, 2002). The 3T T2-w MRI sequence did not allow the calculation of quantitative maps due to the

acquisition parameters. The maps for 7T MRI scans were created using the following procedure: T2*-maps were computed by least-squares fitting of the exponential signal decay over the four echoes of magnitude image from the GRE ASPIRE sequence (Whittall et al., 1997). R2* maps were then calculated by taking the reciprocal of the T2* map. For QSM, phase maps of the fourth echo were pre-processed using iHARPERELLA (integrated phase unwrapping and background phase removal using the Laplacian) and used to calculate QSM with LSQR (sparse linear equation and least-squares method) (Li et al., 2014, 2015; van Bergen et al., 2016).

Targeting the STN

Identification of the STN was conducted by a total of three neurosurgeons with a mean experience of 13.7 years (SD = 5.7 years) in STN DBS planning and surgery. Each neurosurgeon targeted separate left and right STNs per participant on the following image modalities: 3T-T2, 7T-T2*, 7T-R2* and 7T-QSM. All scans used to target the STN were in native acquisition space. The targeting procedure was repeated three times for every image and was assigned a novel identifier, so the neurosurgeons were unaware of the identification of each patient and repetition. The targeting procedure of the STN is shown in Figure 1. Order of presentation of the images was fixed and the same for all three neurosurgeons. There were no images of the same participant following each other. Images were automatically loaded and presented in FSLeyes with pre-set intensity levels using an in-house Bash script. The masks were marked with the anonymized patient identifier, hemisphere and initial of the targeting neurosurgeon. The neurosurgeons then identified the coordinate in which they would place the DBS electrode, and a screenshot of this coordinate was saved. A total of 120 STN targets were obtained per neurosurgeon, and targeting was achieved in multiple sessions depending on the availability of the neurosurgeons. The first neurosurgeon was able to complete all targets in three sessions, with respectively 49 and 6 days between sessions. The second neurosurgeon completed the targeting in four different sessions that were spaced 67, 36, and 36 days apart. Finally, the third neurosurgeon finalized all STN targets in two sessions 13 days apart. This resulted in an average interval of 35 days between rating sessions, with a minimum of 6 days and a maximum of 67 days.

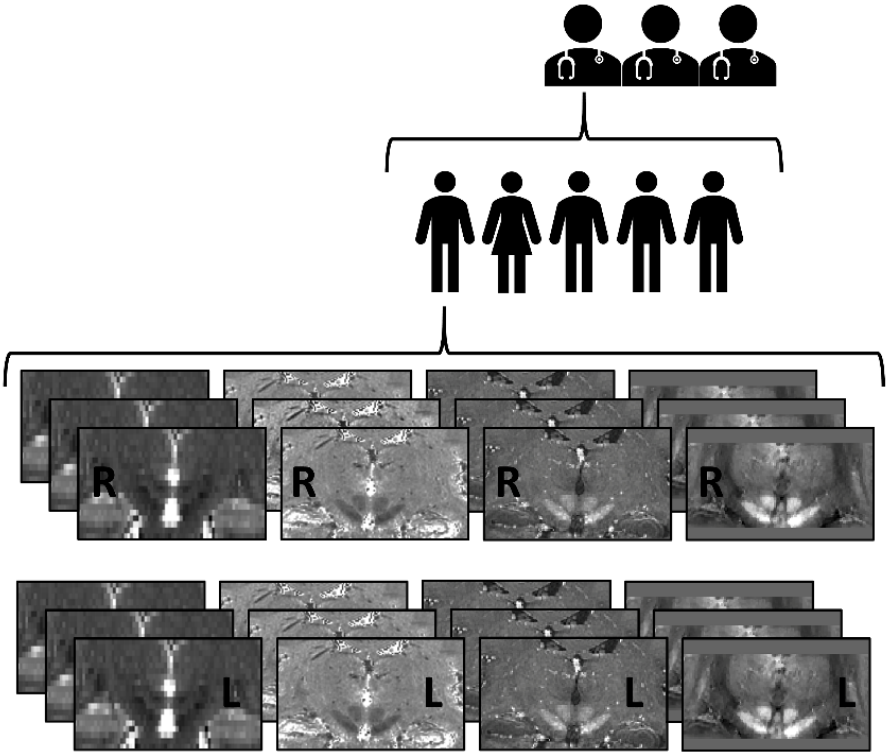

Figure 1: Targeting procedure of the subthalamic nucleus (STN). Identification was conducted by three neurosurgeons. Each neurosurgeon targeted the STN for five deep brain stimulation (DBS) candidates suffering from Parkinson's Disease (PD), on four image modalities, with three repetitions, for both left and right STN. The image modalities included (from left to right) a 3T-T2 weighted MRI, 7T-T2* map, 7T-R2* map and 7T Quantitative Susceptibility Map (QSM). This resulted in a total of 120 STN targets per neurosurgeon, with 24 targets per patient.

As the neurosurgeons were more used to planning on 3T, instructions and examples were provided to explain the 7T images with the following: i. 'T2* images provide an indirect measure of iron content. Iron rich regions like the STN show a higher magnetic field perturbation compared to adjacent regions with lower iron content. The STN appears as a hypointense structure'. ii. 'R2* maps offer a direct measure of magnetism. The STN appears as a hyperintense structure'. iii. 'QSM (quantitative susceptibility maps) are post processed images based on the fourth echo of the T2* sequence, and invert the image contrast, also allowing for a direct measure of magnetism per voxel. The STN appears as a hyperintense structure'. The neurosurgeons were asked to define the position where they would place the electrode tip without taking the corresponding trajectory into account. An example of the intended electrode tip location for a patient by a single neurosurgeon is given in Figure 2.

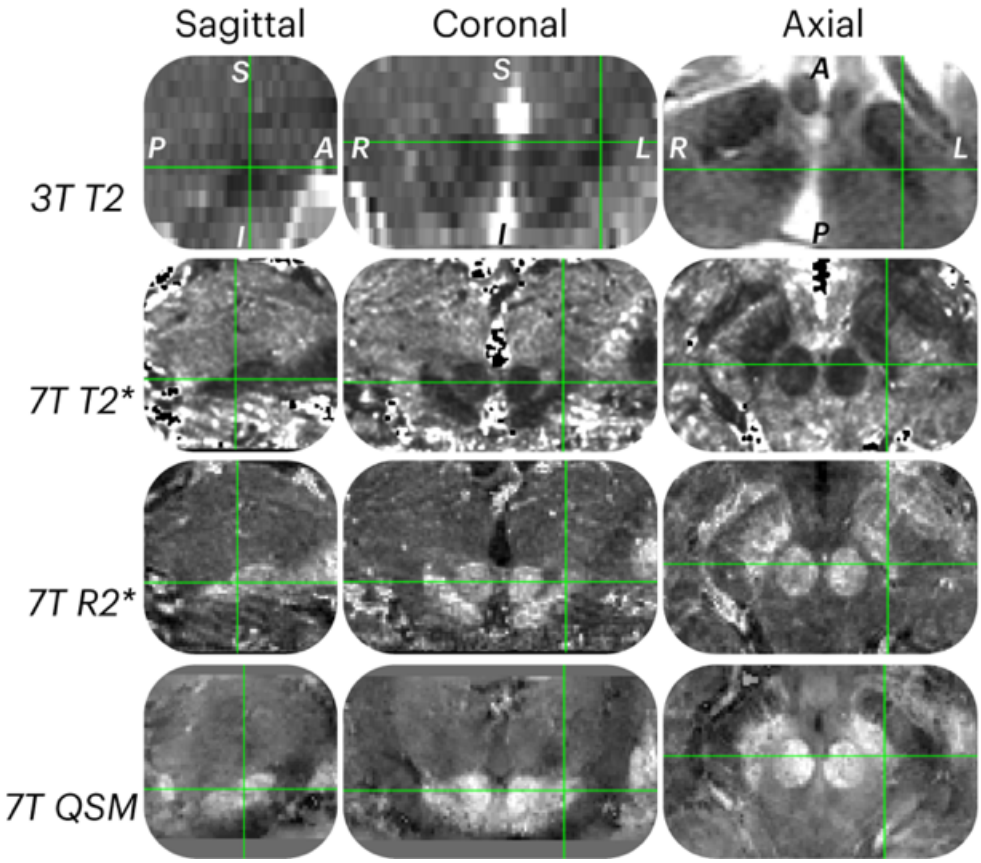

Figure 2: MRI image modalities. An example of each MRI image modality used for targeting for a single patient, including from top to bottom, a 3T-T2 weighted MRI, 7T-T2* map, 7T-R2* map and 7T Quantitative Susceptibility Map (QSM). The image shows a zoomed section of the subthalamic nucleus (STN) in the sagittal, coronal and axial planes. The STN is highlighted by the green intersection.

Euclidean Distance

The Euclidean distance (from here onwards called distance) between the repetitive coordinates was used as an index of variability, where smaller distances indicate better test-retest reliability (Liberti et al., 2014). The distance was calculated between the first and second repetition, second and third repetition, and first and third repetition. This resulted in three distance pairs per hemisphere for each contrast, subject, and neurosurgeon, or 90 distance pairs in total per MRI contrast. Due to technical errors six target coordinates were not saved correctly and are therefore missing from the dataset (resp. two 3T coordinates and four 7T coordinates), resulting in 348 distance pairs in total. To account for differences in voxel

geometry between the 3T and 7T contrasts, the voxel coordinate of the target was transformed to millimetres by multiplying the x and y voxel coordinate values with, respectively, 0.44921875 or 0.53125 for the 3T and 7T coordinates and the z voxel coordinate values with, respectively, 2.0 or 0.5300006. This ensured that a direct comparison between the 3T and 7T derived distances was possible.

Target coordinates in standard stereotactic MNI-space

To be able to compare the location of the target coordinate across subjects and MRI contrasts it was necessary to estimate the 3T and 7T slab transformations to standard MNI space. All individual scans were skull stripped using BET as implemented in FSL 5.0. The 3T T2-w and the average of the four 7T T2* volumes were registered to the 7T whole brain T1-w scan using a rigid transformation 'DenseRigid' as implemented in ANTsPy. As the different sequences and field strengths have different levels of geometric distortions (Dammann et al., 2011; Duchin et al., 2012; Lau et al., 2018; Peerlings et al., 2019) the within-registration was also done using the non-linear symmetric normalization registration method 'SyN' as implemented in ANTsPy. This extra registration step was done to ensure that the results in MNI space were not driven by within-subject misalignment. The 7T whole brain T1-w scan was registered to the icbm_avg_152_t1_tal_nlin_symmetric_VI 1mm isotropic MNI template using the Symmetric normalization as implement in ANTsPy. This is a combination of affine and deformable transformations using mutual information as the optimization metric. All registration steps were visually inspected using the following landmarks: lateral ventricles, striatum, top indentation of the pons, corpus callosum and global outline of the brains. The landmarks were chosen for clear visibility between the different sequences and the location relative to the STN. Based on the alignment of the different landmarks, all registrations were considered to be reasonable. Note that all resulting registrations are visualized in the annotated Jupyter notebook. Using fslmaths a NifTi file was created for every single target coordinate in native space. The different transformation matrices were then combined with the deformation field and applied to the respective target coordinates using a bSpline interpolation. Finally, the X, Y and Z MNI coordinates of the Center of Gravity (COG) were extracted for every single target coordinate and used for further

analyses. In line with our previous work (Keuken et al., 2017) we reduced the number of statistical tests by computing a principal component analysis (PCA) on the resulting X, Y, and Z COG coordinates.

As we had no a-priori hypothesis regarding effects of lateralization and targeting precision, the negative X coordinates (corresponding to the left hemisphere) were converted to positive values before the PCA was calculated. The resulting first principal component corresponds to a new latent variable which captures the maximal amount of variance in the X, Y, and Z coordinates across the different target locations.

Manual parcellation of the STN

The STN was manually parcellated by two independent anatomical experts (BRI and MCK) and verified by a third independent rater (MH), per patient, for both 3T and 7T images. The left and right hemispheres were parcellated separately. The 7T parcellations were achieved by overlaying the 7T-T2*, 7T-R2* and 7T-QSM contrasts together, to create a single 7T parcellation based on the three image modalities. Parcellations were achieved in native space and were created to assess whether any differences in test-retest or MNI location could be explained by differences in STN visibility. This was quantified by calculating the Dice coefficient.

$$Dice\ coefficient\ = \frac{2 * |m_1 \cap m_2|}{|m_1| + |m_2|}$$

Where $|m_i|$ is the volume of the mask for rater $_i$ and $|m_1 \cap m_2|$ is the volume of the conjunct mask for rater 1 and 2. The conjunct mask therefore only includes the voxels in the STN that were included by both raters (Dice, 1945).

Data analysis

Statistical methods

All statistical analyses were conducted using ANOVAs within a Bayesian framework using

the JASP software package (V.0.14.1; (JASP Team, 2020)). The ANOVAs used a uniform prior model probability, and the assumption of normality were visualized using a Q-Q plot of the residuals. For both the test-retest reliability and the spatial location analyses patient ID and neurosurgeon ID were included as nuisance variables. For the Dice coefficient and volumetric analysis, the patient ID was included as a nuisance variable. The implementation of the Bayesian ANOVA in JASP relies on the R package BayesFactor (V.0.9.10-2; (Morey & Rouder, 2015; Rouder et al., 2012)). The resulting Bayes Factors (BF) are interpreted in light of assumptions proposed by (Jeffreys, 1998) and adapted by (Wetzels et al., 2011). Note that the analyses regarding the test-retest reliability, Dice coefficient and volume are based on values calculated in native space whereas the spatial location analysis is based on values in MNI space.

Outlier analysis

Outliers were identified with the 1.5xIQR rule whereby any data point 1.5*IQR above the third quartile or below the first quartile was rejected from further analysis and was done per MRI contrast or field strength. For the distance pairs, 14 data points were identified as outliers across the MRI contrasts. The final sample for the test-retest ANOVA was 84 pairs for the 3T-T2 contrast, 77 pairs for the 7T-T2* contrast, 86 pairs for the 7T-R2* contrast and 87 pairs for the 7T-QSM contrast. For the coordinates in MNI space, there were two 7T-T2* coordinates that were identified as outliers. There was a single 3T Dice coefficient value and a single 7T conjunction volume that were identified as outliers.

Open science

All target coordinates and STN parcellation masks are made available (DOI 10.17605/OSF.IO/DW2FR). In addition, an annotated Python notebook that was used to pre-process all the data and all resulting JASP files used to conduct the statistical analysis are provided.

Results

Test-retest reliability of the target coordinates

On average the neurosurgeons deviated 1.35mm (SD=0.78) between sessions. In Table 1 the mean distances between the three targeting sessions are provided per MRI field strength and contrast whereas in Figure 3 the distance between the pairs are visualized per hemisphere and MRI contrast.

Table 1. Targeting distance between the repetition pairs over MRI field strengths and contrasts.

						95% Credible Interval	
MRI field strength	**MRI Contrast**	**Repetition pairs**	**Mean (mm)**	**SD (mm)**	**N**	**Lower**	**Upper**
3T	T2	1 - 2	1.197	0.780	28	0.895	1.499
		1 - 3	1.554	0.934	29	1.198	1.909
		2 - 3	1.433	0.940	27	1.061	1.804
7T	T2*	1 - 2	1.560	0.902	26	1.196	1.924
		1 - 3	1.178	0.661	24	0.899	1.457
		2 - 3	1.339	0.814	27	1.017	1.661
	R2*	1 - 2	1.170	0.715	28	0.893	1.447
		1 - 3	1.608	0.605	28	1.373	1.842
		2 - 3	1.370	0.623	30	1.138	1.603
	QSM	1 - 2	1.266	0.987	30	0.898	1.635
		1 - 3	1.061	0.623	28	0.819	1.302
		2 - 3	1.467	0.734	29	1.188	1.746

Note. The mean distance between sessions in millimetres and calculated over surgeon, patient and hemisphere.

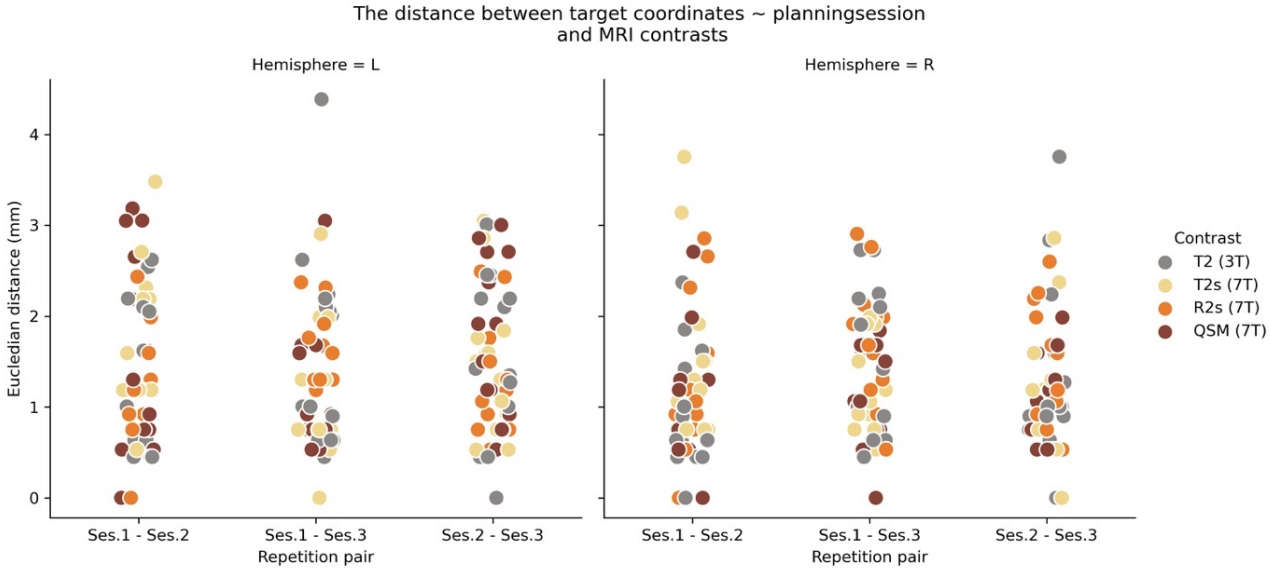

Figure 3: The Euclidean distance between the target coordinates over sessions and MRI contrasts. Note that we visualize the coordinates per hemisphere but as we had no a-priori hypothesis on lateralization, hemisphere was not included as a factor in the statistical testing.

Model comparison.

To test whether MRI field strength, MRI contrast or planning session had an influence on the distance between target locations a Bayesian ANOVA was conducted. The primary output from the ANOVA is presented in Table 2, which shows the amount of support that the data offer for each model under consideration. The left-most column lists all models at hand: 18 alternative models and a single null model. The models are ordered by their predictive performance relative to the best model; this is indicated in the BF_{10} column, which shows the Bayes factor relative to the best model which, in this case is the Null model. For example, the data are 5.88 times more likely under the Null model than under the second-best model where MRI field strength (Tesla) is included as a predictor. This means that there is substantial evidence that there is no effect of field strength, MRI contrast or planning session on the test-retest reliability of the STN targeting.

Table 2. Model Comparison test-retest reliability of the target coordinates

Models	P(M)	P(M | data)	BF_M	BF_{10}	error %
Null model (incl. PatientNr, Surgeon)	0.053	0.781	64.011	1.000	
T	0.053	0.133	2.751	0.170	4.842
RP	0.053	0.046	0.876	0.059	3.877
C	0.053	0.019	0.355	0.025	3.393
T + RP	0.053	0.007	0.133	0.009	1.875
T + C	0.053	0.007	0.124	0.009	2.249
T + C + T✻C	0.053	0.003	0.046	0.003	7.390
T + RP + T✻RP	0.053	0.002	0.029	0.002	4.812
C + RP	0.053	0.001	0.019	0.001	2.113
C + RP + C✻RP	0.053	6.776e -4	0.012	8.681e -4	1.771
T + C + RP	0.053	3.902e -4	0.007	5.000e -4	2.594
T + C + RP + C✻RP	0.053	2.620e -4	0.005	3.357e -4	3.145
T + C + RP + T✻C	0.053	1.329e -4	0.002	1.703e -4	2.846
T + C + RP + T✻C + C✻RP	0.053	9.083e -5	0.002	1.164e -4	2.988
T + C + RP + T✻RP	0.053	7.860e -5	0.001	1.007e -4	3.188
T + C + RP + T✻RP + C✻RP	0.053	5.930e -5	0.001	7.597e -5	2.295
T + C + RP + T✻C + T✻RP	0.053	2.653e -5	4.775e -4	3.398e -5	2.433
T + C + RP + T✻C + T✻RP + C✻RP	0.053	2.356e -5	4.241e -4	3.019e -5	6.678
T + C + RP + T✻C + T✻RP + C✻RP + R✻C✻RP	0.053	6.359e -6	1.145e -4	8.147e -6	2.739

Note. All models include PatientNr, Surgeon.T: MRI field strength (Tesla); C: MRI Contrast; RP: Repetition pair; P(M): Prior model probability; P(M | data): posterior model probability; BF_M: the change from prior odds to posterior odds; BF_{10}: the Bayes factor relative to the best model; error %: indicates the precision of the numerical approximation and it is thought that in many situations an error percentage below 20.0% is acceptable (Bergh et al., 2020).

Spatial location of targets in MNI space

While we can conclude that the neurosurgeons are stable in selecting the electrode target over planning sessions it is unknown whether the neurosurgeons select similar targets across MRI field strengths and MRI contrasts. For that the individual electrode target locations were registered to MNI space and visualized in Figure 4.

Model comparison.

To test whether MRI field strength, MRI contrast or session had an influence on the DBS electrode location in MNI space a Bayesian ANOVA was conducted. The primary output from the ANOVA is presented in Table 3, which shows the amount of support that the data offer for each model under consideration. There is anecdotal evidence that the data is 1.74 times more likely under the model where MRI field strength is included than under the second-best model where MRI field strength and MRI contrast are included. There is however conclusive evidence that the data is more likely under the model including MRI field strength than under the Null model.

As the amount of evidence to prefer the winning model over the second-best model was anecdotal, an analysis of effects was conducted (the results are given in Table 4). The BFincl indicates that the data is 7.24 times more likely under the models that include MRI field strength than models without this predictor. Whereas the BFincl indicates that the data is 2.98 times more likely under models that do not include MRI contrast as a predictor (1/0.336). This means that the target of the DBS electrode as quantified by the first component of the PCA differs between 3T and 7T MRI scans, where based on Figure 4, this difference seems to be mainly along the Y-axis or in dorsal-ventral (brainstem orientation) | anterior-posterior (cerebrum orientation) direction. In the remainder we will use the brainstem orientation when referring to the MNI coordinate system.

Note that the results presented in section 3.2 and 3.2.1 are conceptually similar when a non-linear within-subject registration method is used (see Supplementary Figure 1 and Supplementary Table 1 and 2).

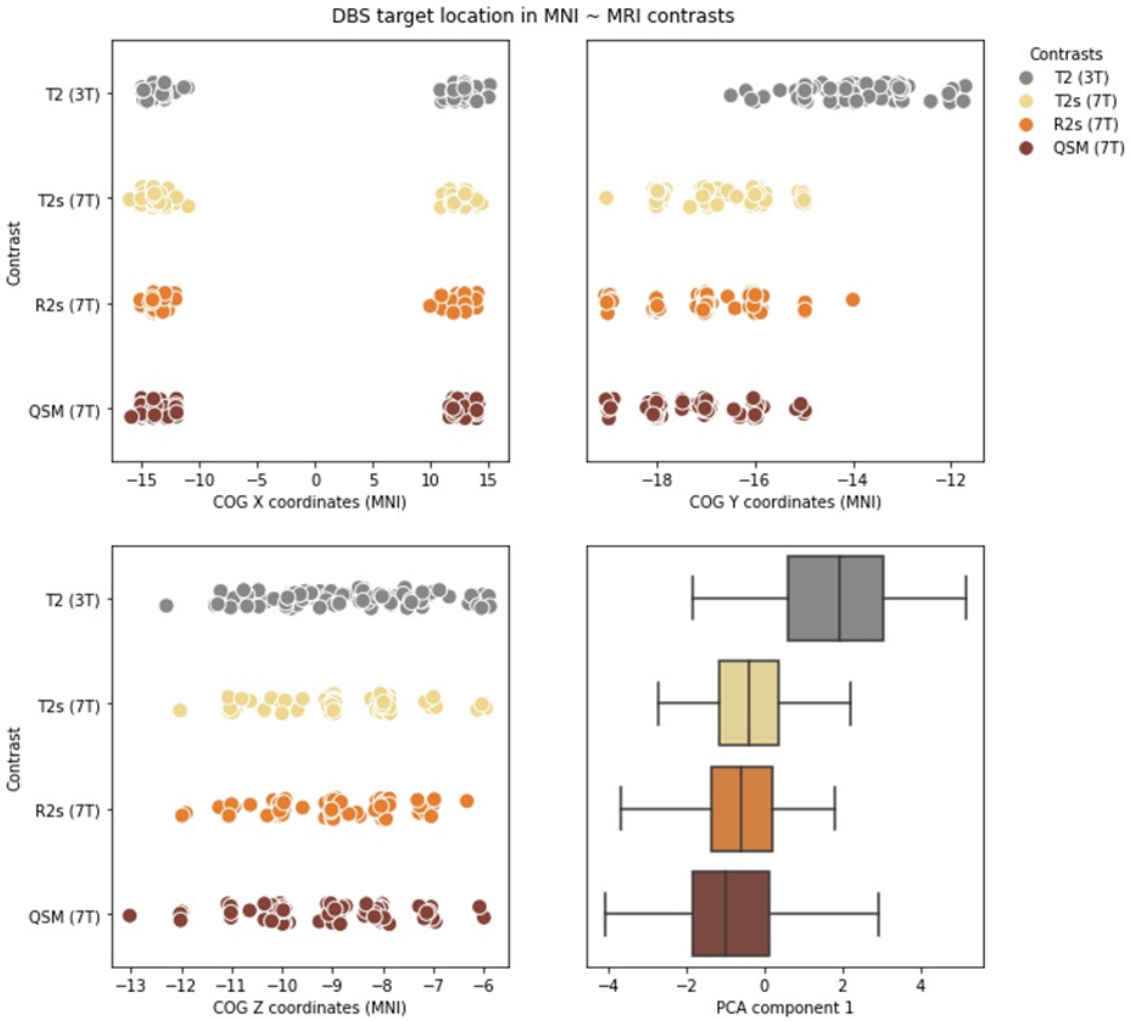

Figure 4: The intended DBS electrode location in MNI space over MRI contrasts. The left upper panel shows the X MNI coordinates of the planned electrode's Centre of Gravity (COG) per MRI contrast, patient, surgeon and planning session registered from native to MNI space. Note that we visualize the X coordinates per hemisphere but as we had no a-priori hypothesis on lateralization, hemisphere was not included as a factor in the statistical testing. The right upper panel shows the Y MNI coordinates. The left lower panel shows the Z MNI coordinates. The right lower panel shows the boxplot of first PCA component per MRI contrast which were used for the statistical testing.

Table 3. Model comparison of the spatial location of the DBS electrode targets.

Models	P(M)	P(M|data)	BF_M	BF_{10}	error %
T	0.053	0.478	16.501	1.000	
T + C	0.053	0.274	6.804	0.574	5.736
T + C + T∗C	0.053	0.130	2.682	0.271	4.329
C	0.053	0.044	0.823	0.091	2.914
T + R	0.053	0.035	0.645	0.072	3.366
T + C + R	0.053	0.022	0.400	0.045	8.444
T + C + R + T∗C	0.053	0.009	0.170	0.020	4.263
C + R	0.053	0.003	0.059	0.007	3.861
T + R + T∗R	0.053	0.002	0.045	0.005	3.162
T + C + R + T∗R	0.053	0.001	0.026	0.003	4.968
T + C + R + T∗C + T∗R	0.053	7.006e -4	0.013	0.001	6.743
T + C + R + C∗R	0.053	1.817e -4	0.003	3.798e -4	3.657
T + C + R + T∗C + C∗R	0.053	1.009e -4	0.002	2.111e -4	7.923
T + C + R + T∗R + C∗R	0.053	3.938e -5	7.089e -4	8.234e -5	21.787
C + R + C∗R	0.053	3.166e -5	5.700e -4	6.620e -5	3.088
T + C + R + T∗C + T∗R + C∗R	0.053	1.859e -5	3.346e -4	3.886e -5	21.086
T + C + R + T∗C + T∗R + C∗R + T∗C∗R	0.053	2.288e -6	4.118e -5	4.784e -6	4.272
Null model (incl. PatientNr, Surgeon)	0.053	1.506e -41	2.711e -40	3.149e -41	2.182
R	0.053	6.767e -43	1.218e -41	1.415e -42	2.807

Note. All models include PatientNr, Surgeon.T: MRI field strength (Tesla); C: MRI Contrast; R: Repetition; P(M): Prior model probability; P(M|data): posterior model probability; BF_M: the change from prior odds to posterior odds; BF_{10}: the Bayes factor relative to the best model; error %: indicates the precision of the numerical approximation and it is thought that in many situations an error percentage below 20.0% is acceptable (Bergh et al., 2020).

Table 4. Analysis of Effects – spatial location of the DBS electrode targets

Effects	P(incl)	P(excl)	P(incl|data)	P(excl|data)	BF_{inc}
					1
T	0.737	0.263	0.953	0.047	7.236
C	0.737	0.263	0.485	0.515	0.336
R	0.737	0.263	0.074	0.926	0.029
T∗C	0.316	0.684	0.140	0.860	0.352
T∗R	0.316	0.684	0.005	0.995	0.010
C∗R	0.316	0.684	3.745e -4	1.000	8.117e -4
T∗C∗R	0.053	0.947	2.288e -6	1.000	4.118e -5

Note. T: MRI field strength (Tesla); C: MRI Contrast; R: Repetition; P(incl): prior inclusion probability; P(excl): prior exclusion probability; P(Incl|data): posterior inclusion probability; P(excl|data): posterior exclusion probability; BFincl: the inclusion Bayes facto

Visibility of the STN

To test whether the observed differences in MNI space might be explained by differences in STN visibility, the STN was parcellated by two raters and the Dice coefficient was calculated to quantify the interrater reliability. The mean Dice coefficient was 0.70 (SD=0.05) for 3T and 0.61 (SD=0.09) for the 7T based masks. The Dice coefficient indicated moderate to substantial agreement between the two raters and were similar to our previous work (Keuken et al., 2017; Landis & Koch, 1977). The data was 4.95 (1/0.202) times more likely under the model with MRI field strength as a predictor compared to the Null model. In addition, we tested whether there were any differences in volume as quantified by the conjunction masks. The mean conjunction volume was 20.70mm^3 (SD=7.16) for the 3T and 15.09mm^3 (SD=2.47) for the 7T based masks. Note that the conjunction masks are considered extremely conservative volumetric estimates as only voxels that both raters agree on are included. The volumetric data was 2.93 (1/0.341) times more likely under the model with MRI field strength as a predictor than under the Null model.

Discussion

Direct targeting of the STN for DBS is shown to result in improved clinical outcome and has resulted in surgical centres to prefer it over an indirect targeting approach (Lahtinen et al., 2020; Machado et al., 2006; Tonge et al., 2016). However, the feasibility and accuracy of direct targeting is dependent on the quality of the MRI image (Hartmann et al., 2019; Machado et al., 2006). The current study assessed whether theoretical benefits of 7T MRI translate into more reliable targeting of the STN for DBS. We did so by comparing neurosurgical targets across field strength, image modality and across repetition using a test-retest approach. Target accuracy was assessed by calculating the distance in millimetres between the repetitive target locations. We hypothesized that optimized 7T image modalities would result in less variable target locations. Further, and in line with previous literature, we hypothesized that 7T-QSM images would result in the least variability in targeting compared to any other 7T images due to its superior ability in visualizing the STN.

The results, however, indicate that within these five patients there was substantial evidence that the test-retest reliability of neurosurgeons is not influenced by MRI field strength, contrast or targeting session. This indicates that the neurosurgeons selected the same target site within a given MRI contrast across sessions. It can therefore be argued that variability based on direct targeting methods probably is not a factor on itself in suboptimal placement of the DBS lead, since the same target site would have been selected if targeting was performed repetitively. Furthermore, it is interesting to note the anatomical variability between patients as shown in Figure 4. This illustrates the importance of an individualized targeting approach which accounts for substantial anatomical variability as opposed to using indirect methods such as STN templates or standard coordinates (Alkemade et al., 2017; Cho et al., 2010; Duchin et al., 2018; Keuken et al., 2013)

Next to the variability in stereotactic planning, the exact anatomical location of the electrode target may potentially on itself be a factor in suboptimal placement of the DBS lead. The general consensus is that the effectiveness of DBS depends on the portion of the STN in which the DBS lead is placed, with the dorsolateral portion of the STN being most effective in treating PD (Duchin et al., 2018; Hamel et al., 2017; Starr, 2002; Welter et al., 2014). A second question that was addressed is whether the neurosurgeons select the similar target sites between MRI contrasts and field strengths, considering that different contrasts and resolutions might convey different anatomical information (Bazin et al., 2020; McRobbie, 2006; Visser, Keuken, Douaud, et al., 2016). While the neurosurgeons were stable in selecting the electrode location, the location itself seemed to differ between field strengths whereby the selected electrode location appeared (mainly) more ventral when using a 3T MRI image versus a 7T MRI image. This shift in location is unlikely to have occurred due to a difference in STN visibility as both 3T and 7T resulted in moderate to substantial interrater agreement. Note, however, that in the current study the visibility of the STN was not quantified by the neurosurgeons themselves, but by two independent anatomical experts and a third independent rater. As such it does not seem that neurosurgeons are hampered by reduced visibility of the STN but it might be the case that they use different image features, such as landmarks, to determine the electrode location. Our results are conceptually in line with the recent work by (Bot et al., 2019) where it was shown that the intended DBS electrode sites

were more posterior and inferior to the midcommissural point when using 1.5T and 3T compared to 7T MRI images. Note, however, that another study failed to find differences in target location between the 3T and 7T MRI images (van Laar et al., 2016).

Whether the electrode is placed more ventral has clear clinical relevance as previous work has indicated that more ventral stimulation seems to be associated with reduced cognitive outcome (Machado et al., 2006; McNeely et al., 2011; Zarzycki & Domitrz, 2020). For example, it was shown that stimulation of specifically the ventral STN led to an impaired performance on the Go-No-Go task, which requires higher cognitive functions (Hershey et al., 2010). Our results showed that the selected electrode location using a 3T MRI image is more ventral compared to using a 7T MRI image. Future work should focus on whether this theoretical difference in STN targeting based on MRI strength actually leads to less cognitive and psychiatric side-effects. It should further be studied what differences in imaging features causes the difference in electrode location when targeting on 7T versus 3T MRI images.

There are a number of limitations to the present study. The number of patients that were included in the study was limited, but we feel that this is a minor issue as the main metric of interest was the test-retest reliability within a patient and that direct pre-operative planning approaches always employ individualized targeting (Isaacs, Mulder, et al., 2020). Although the number of patients was limited, the main results were all supported by substantial or more evidence, inspiring reasonable confidence in our conclusions (Rosenfeld & Olson, 2021; Schönbrodt & Wagenmakers, 2018). Another limitation is that the selection of MRI contrasts included a standard clinical 3T protocol and an optimized 7T protocol, adapted for anatomical changes with both age and disease. We did not however include either a 7T-T2 or an optimized/quantitative 3T-T2* based sequence which would have allowed for a direct comparison between field strengths while directly accounting for difference in MRI contrasts mechanism. As such, it remains challenging to disentangle the contributions of MRI contrast and MRI field strength in the difference in MNI target location. We attempted to quantify the different factors by conducting an analysis of effects where the results indicated that the data is 6.62 times more likely to occur in models that include MRI field strength than not, and that the data is 2.93 times more likely to occur under models that did not include MRI contrast as a predictor. Together with the findings reported by (Bot et al., 2019) we would

tentatively interpret our results as evidence in favour of an effect of MRI field strength on the intended electrode position and not so much due to a difference in MRI contrast mechanisms. A final limitation that complicates the interpretability of the results in standard MNI space are the potential biases in MNI registrations for the 3T data compared to the 7T scans due to the difference in voxel geometry and volume (Mulder et al., 2019; Zhao et al., 2016).

In light of these limitations, the present study provides substantial evidence that regardless of the MRI field strength and MRI contrast, neurosurgeons are stable in selecting the intended DBS electrode location. In addition, we conclude that the intended electrode location differs between MRI field strengths, where the 3T scans resulted in a more ventral location. Future research should focus on what image features drive the neurosurgeons to select a slightly different location across the images.

Acknowledgments
We would like to acknowledge Pierre-Louis Bazin for helpful discussions.

Supplementary Material

Figure 1:

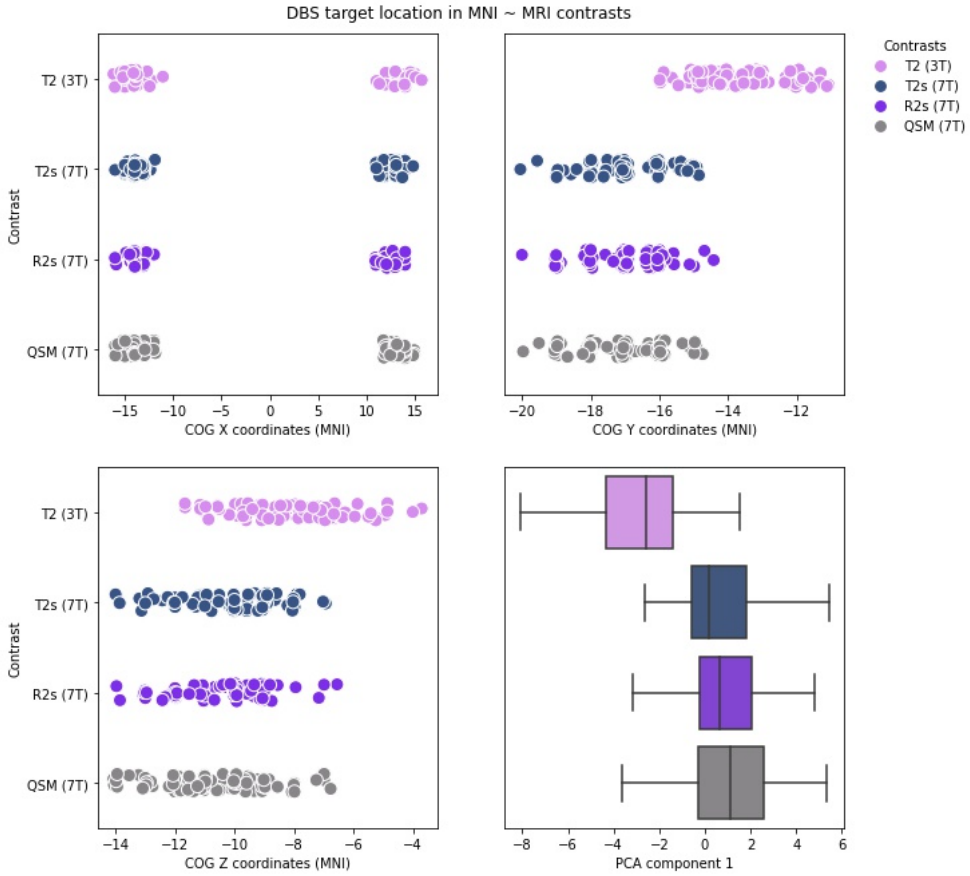

Supplementary Figure 1. The intended DBS electrode location MNI space over MRI contrast when using a fully non-linear registration pipeline. Similar to figure 4 in the main document, the three scatterplot panels shows the X, Y, and Z MNI coordinate of the planned electrode's Centre of Gravity (COG) per MRI contrast, patient, surgeon and planning session registered from native to MNI space. The difference with figure 4 is that the individual slab to individual whole brain registration was done using a non-linear symmetric normalization function as opposed to a purely rigid transformation. As a result, not only does the COG clearly differ on the Y axis but now also on the Z axis for the 3T T2 contrast relative to the 7T contrasts.

Supplementary Table 1:

Supplementary table 1. Model comparison of the spatial location of the DBS electrode target, non-linear registration pipeline.

Models	P(M)	P(M|data)	BF_M	BF_{10}	error %
T	0.053	0.577	24.524	1.000	
T + C	0.053	0.230	5.377	0.399	8.262
T + C + T ✻ C	0.053	0.105	2.103	0.181	5.662
T + R	0.053	0.036	0.671	0.062	4.000
C	0.053	0.026	0.487	0.046	3.859
T + C + R	0.053	0.013	0.241	0.023	4.015
T + C + R + T ✻ C	0.053	0.007	0.128	0.012	7.690
T + R + T ✻ R	0.053	0.003	0.049	0.005	5.196
C + R	0.053	0.002	0.029	0.003	3.429
T + C + R + T ✻ R	0.053	9.530e -4	0.017	0.002	4.180
T + C + R + T ✻ C + T ✻ R	0.053	4.264e -4	0.008	7.394e -4	4.437
T + C + R + C ✻ R	0.053	1.979e -4	0.004	3.431e -4	4.342
T + C + R + T ✻ C + C ✻ R	0.053	9.010e -5	0.002	1.562e -4	4.209
T + C + R + T ✻ R + C ✻ R	0.053	3.510e -5	6.318e -4	6.086e -5	7.064
C + R + C ✻ R	0.053	2.430e -5	4.374e -4	4.214e -5	4.400
T + C + R + T ✻ C + T ✻ R + C ✻ R	0.053	1.509e -5	2.716e -4	2.617e -5	5.723
T + C + R + T ✻ C + T ✻ R + C ✻ R + T ✻ C ✻ R	0.053	2.918e -6	5.253e -5	5.060e -6	11.018
Null model (incl. PatientNr, Surgeon)	0.053	1.940e -52	3.492e -51	3.363e -52	2.722
R	0.053	7.849e -54	1.413e -52	1.361e -53	3.696

Note. All models include PatientNr, Surgeon. T: MRI field strength (Tesla); C: MRI Contrast; R: Repetition; P(M): Prior model probability; P(M|data): posterior model probability; BFM: the change from prior odds to posterior odds; BF10: the Bayes factor relative to the best model; error %: indicates the precision of the numerical approximation and it is thought that in many situations an error percentage below 20.0% is acceptable (Bergh et al., 2020).

Supplementary Table 2:

Supplementary table 2. Analysis of Effects – Spatial location of the DBS electrode targets, non-linear registration pipeline.

Effects	P(incl)	P(excl)	P(incl|data)	P(excl|data)	BF_{incl}
T	0.737	0.263	0.972	0.028	12.414
C	0.737	0.263	0.385	0.615	0.223
R	0.737	0.263	0.062	0.938	0.024
T✻C	0.316	0.684	0.112	0.888	0.274
T✻R	0.316	0.684	0.004	0.996	0.009
C✻R	0.316	0.684	3.654e -4	1.000	7.920e -4
T✻C✻R	0.053	0.947	2.918e -6	1.000	5.253e -5

Note. T: MRI field strength (Tesla); C: MRI C; R: Repetition; P(incl): prior inclusion probability; P(excl): prior exclusion probability; P(Incl|data): posterior inclusion probability; P(excl|data): posterior exclusion probability; BFincl: the inclusion Bayes factor.

Five

The Connectivity Fingerprint of the Human Frontal Cortex, Subthalamic Nucleus and Striatum

Introduction

The basal ganglia (BG) collectively refer to a group of interconnected subcortical nuclei. The main BG components are the caudate and putamen, which together form the striatum (STR), the internal and external segments of the globus pallidus (GPi and GPe, respectively), the substantia nigra, and the subthalamic nucleus (STN) (Parent and Hazrati, 1995a). Together with the cortex and the thalamus, these BG nuclei form an integrative network consisting of several loops involved in a wide range of cognitive, limbic, and motor functions (Alexander and Crutcher, 1990; Alexander et al., 1990; Albin et al., 1989; Haber and Calzavara, 2009; Temel et al., 2005). Each circuit is characterized by three functionally distinct pathways: direct, indirect, and hyperdirect. Anatomically, the direct and indirect pathways entail projections from the cortex to the STR, while the hyperdirect pathway bypasses the STR and projects from the cortex, directly to the STN (Jahanshahi et al., 2015; Nambu et al., 2002b).

Therefore, both the STN and STR are considered as crucial input structures to the BG and are essential for both optimal and flexible adaptive motor control and action selection which may arise from many scenarios, from goal-directed behaviors to habitual responses (Alexander and Crutcher, 1990; Bogacz and Gurney, 2007; Ding and Gold, 2013; Nambu et al., 2002b). Animal literature indicates that the majority of the cortical input to BG arises from prefrontal and primary motor cortices (Parent and Hazrati, 1995b; 1995a). However, it is generally accepted that frontal connections monosynaptically connecting to the STN are more sparse in comparison to those connecting directly to the STR (Frankle et al., 2006).

To the best of our knowledge, a quantitative comparison of the connectivity profiles between the frontal cortex and the STN and STR in humans has yet to be conducted. There have been numerous studies quantifying the diffusion-weighted (DWI) and resting-state functional (rs-f) MRI connectivity patterns of the cortex, STN, and STR separately (Anteraper et al., 2017; Brunenberg et al., 2012; Cacciola et al., 2017; Di Martino et al., 2008; Draganski et al., 2008; Lambert et al., 2012; Morris et al., 2016). Though many studies use lower MRI field strengths, where the STN is notoriously difficult to visualize due to its small size and high iron content (Cho et al., 2010; de Hollander et al., 2015; 2017; Forstmann et al.,

2017). To complement the previous connectivity studies, we set out to characterize the connectivity fingerprint of the frontal cortex with the STN and STR in healthy young subjects using ultra-high field (UHF) 7 Tesla (T) DWI and rs-fMRI data.

Material and Methods

Participants

Sixteen healthy participants (9 female, age range= 19-28, mean age = 23.13, SD= 2.47) were scanned. All participants reported normal or corrected to normal vision and were right-handed, as confirmed by the Edinburgh Inventory (Oldfield, 1971). None of the participants had a history of neurological disorder or currently suffered from psychiatric disorders as indicated by self-report and structured clinical interview. The study was approved by the local ethical committee at the Max Planck Institute for Human Brain and Cognitive Sciences in Leipzig, Germany. Written informed consent was acquired and participants received a monetary reward for participation.

MRI Sequences

Structural scans

The structural data was obtained from a 7T whole-body Siemens MAGNETOM using a 24 channel Nova head coil (NOVA Medical Inc., Wilmington MA) during two sessions. The first session consisted of a whole-brain MP2RAGE (Marques et al., 2010), an MP2RAGE covering a smaller slab, and a multi-echo 3D FLASH slab (Haase et al., 1986). Whole-brain MP2RAGE scans were collected with the following parameters: 240 sagittal slices, acquisition time (TA) of 10:57 min, repetition time (TR) = 5000 ms, echo time (TE) = 2.45 ms, inversion times $(TI)_{1,2}$ = 900 ms/ 2750 ms, flip angle $(FA)_{1,2}$ = 5°/3°, bandwidth (BW) = 250 Hz/Px and a voxel size of 0.7 mm isotropic. Zoomed MP2RAGE slab images were acquired to facilitate the registration of FLASH images to whole-brain MP2RAGE images which consisted of 128 sagittal slices, with a TA of 9:07 min, TR = 5000 ms, TE=3.71 ms, $TI_{1,2}$ =

900 ms / 2750 ms, $FA_{1,2}$ = 5°/3°, BW = 240 Hz/Px and 0.6 mm isotropic voxel size. Zoomed FLASH slab images consisted of 128 axial slices covering the midbrain, TA =17:18 min, TR = 41 ms, TE_{1-3} = 11.22 ms / 20.39 ms / 29.57 ms, FA = 14°, BW = 160 Hz/Px and 0.5 mm isotropic voxel size. For the exact acquisition parameters and the raw data see (Forstmann et al., 2014).

Diffusion-weighted imaging

In a second structural scan session, DWI was acquired with a spin echo planar imaging sequence (Heidemann et al., 2010). A total of 100 axial slices were acquired with a TA of 54:16min, TR = 11.3 sec, TE = 67 ms, voxel size = 1.0 mm isotropic, and GRAPPA acceleration factor 3. Diffusion weighting was isotropically distributed along 60 directions with a *b* value of 1000s/mm^2, AV = 4, and 7 diffusion-weighted images to every B_0 image.

Resting-state functional MRI

Finally, in a third MRI session, rs-fMRI was acquired using a 2D EPI sequence. A total of 76 slices were acquired interleaved in transversal direction, with a TA of 5:16 min, TR = 3330 ms, TE = 18 ms, voxel size = 1.5 mm isotropic, phase encoding A > P, GRAPPA acceleration factor 3, BW = 1086 Hz/Px, echo spacing = 1.03 ms. To correct for distortions, a GRE field map with 57 slices was acquired in transversal direction with a TA of 4:53 min, TR = 1500, TE1= 6.00 ms, TE2= 7.02 ms, voxel size = 2.0 mm isotropic, FA = 68°, phase encoding A > P, BW = 259 Hz/Px.

Region of Interest (ROI) definition

Subcortical masks

The STN and STR masks have been previously described in (Keuken et al., 2014). The STN was parcellated using the multi-echo FLASH, whereas the STR was parcellated using the MP2RAGE slab. In short, both the STN and STR as a whole were manually parcellated by two independent researchers using FSLview (version 4.1.4. (Jenkinson et al., 2012)). The STR was not subdivided into its anatomical subdivisions due to the challenges associated with

identifying the border between the caudate nucleus, the putamen, and the fundus striati (Keuken et al., 2014; Neto et al., 2008). Only voxels identified by both raters as belonging to the structure were included for further analyses. Given the size of the STN in relation to the resolution of the DWI and rs-fMRI we decided to only focus on the connectivity profile of the two subcortical structures as a whole and not investigate any topographical organization within the given structures. For more information regarding the parcellation protocol see (Keuken et al., 2014; 2017).

Cortical masks

Instead of testing the connectivity of the STN and STR with the entire cortex, we selected several cortical areas that have been identified in non-human primate tracer studies as connecting to both the STN and STR. These connections were selected by conducting an empirical literature search using the PubMed database (www.pubmed.org). The employed keywords included: "subthalamic nucleus", "striatum", "macaque", "monkey", "histological", "tracer(s)", and "connection(s)" and was published in English. All abstracts and resulting in full-text articles were read by two researchers (BRI and MCK).

Since a large number of studies used different nomenclature to refer to the same or similar brain regions (e.g., Brodmann, Walkers, Vogts, 'own labeling system') we summarized these studies into a single cortical area using the anatomical description of the original study. The human homolog of each cortical area was then identified in standard MNI-space using a number of comparative anatomical atlases that are based on both human and non-human primates (Neubert et al., 2014; 2015; Sallet et al., 2013) as implemented in FSL. See table 1 for the cortical areas identified in the literature search and figure 1 for a visualization of the cortical ROI's in MNI-space.

Table 1. Cortical areas that connect both to the STR and STN based on tracer studies in non-human primates. The separate cortical masks from (Neubert et al., 2014; 2015; Sallet et al., 2013) were extracted from FSL, combined in a single region if relevant, binarized, and used as a cortical ROI.

Cortical ROIs	**Tracer studies**	**Cortical masks and corresponding atlas**
1) Primary motor cortex (M1)	(Hartmann Von Monakow et al., 1979; Haynes and Haber, 2013; Kemp and Powell, 1970; Künzle, 1975; 1977; Liles and Updyke, 1985; McFarland and Haber, 2000; Miyachi et al., 2006; Nambu et al., 1996; 1997; Petras, 1968; Selemon and Goldman-Rakic, 1985; Takada et al., 1998b; 2001; Tokuno et al., 1999)	M1 (Neubert et al., 2015)
2) Pre-motor cortex (pre-M1)	(Akert and Künzle, 1978; Akkal et al., 2007; Calzavara et al., 2007; Hartmann Von Monakow et al., 1979; Haynes and Haber, 2013; Kemp and Powell, 1970; Liles and Updyke, 1985; McFarland and Haber, 2000; Miyata and Sasaki, 1984; Nambu et al., 1997; 2002a; Petras, 1968; Selemon and Goldman-Rakic, 1985; Tachibana et al., 2004; Takada et al., 1998a)	6v, 6r (Neubert et al., 2014) and PMd, PMv (Sallet et al., 2013)
3) Supplementary motor area (SMA) **4) Pre-supplementary motor area (pre-SMA)**	(Inase et al., 1999; Kemp and Powell, 1971; McFarland and Haber, 2000; Nambu et al., 1996; 1997; Parthasarathy et al., 1992; Petras, 1968; Takada et al., 1996; 1998a; 2001)	SMA, pre-SMA (Neubert et al., 2015)
5) Frontal eye fields (FEF)	(Borra et al., 2013; Calzavara et al., 2007; Ferry et al., 2000; Hartmann Von Monakow et al., 1979; Künzle and Akert, 1977; Parthasarathy et al., 1992; Stanton et al., 1988)	8A, 8B (Sallet et al., 2013)
6) Dorsolateral prefrontal cortex (DLPFC)	(Akert and Künzle, 1978; Borra et al., 2013; Calzavara et al., 2007; Ferry et al., 2000; Frankle et al., 2006; Goldman and Nauta, 1977; Haynes and Haber, 2013; Kemp and Powell, 1970; Parthasarathy et al., 1992; Selemon and Goldman-Rakic, 1985; 1988; Uylings and Van Eden, 1990)	46, 9, 9/46d, 9/46v (Sallet et al., 2013)

Cortical ROIs	Tracer studies	Cortical masks and corresponding atlas
7) Frontopolar area (FPA)	(Ferry et al., 2000; Haynes and Haber, 2013; Kemp and Powell, 1970; Selemon and Goldman-Rakic, 1985; 1988; Yeterian and Van Hoesen, 1978)	10 (Sallet et al., 2013) and FPm, FPl (Neubert et al., 2014)
8) Ventromedial and lateral prefrontal cortex (VMPFC)	(Ferry et al., 2000; Frankle et al., 2006; Haber et al., 1995; Haynes and Haber, 2013)	47o, 47m, 14m (Neubert et al., 2015)
9) Orbitofrontal cortex (OFC)	(Ferry et al., 2000; Frankle et al., 2006; Haber et al., 1995; Haynes and Haber, 2013; Kemp and Powell, 1970; Selemon and Goldman-Rakic, 1985)	11, 11m (Neubert et al., 2015)
10) Inferior frontal sulcus (IFS) **11) Inferior frontal junction (IFJ)**	(Borra et al., 2013; Ferry et al., 2000; Yeterian and Van Hoesen, 1978)	IFS, IFJ (Neubert et al., 2014)
12) Inferior frontal gyrus pars opercularis (POP) **13) Inferior frontal gyrus pars triangularis (PTR)**	(Borra et al., 2013; Ferry et al., 2000; Yeterian and Van Hoesen, 1978)	POP: 44d, 44v PTR: 45 (Neubert et al., 2014)
14) Cingulate cortex (CIN)	(Calzavara et al., 2007; Ferry et al., 2000; Frankle et al., 2006; Haynes and Haber, 2013; McFarland and Haber, 2000; Selemon and Goldman-Rakic, 1985; Yeterian and Van Hoesen, 1978)	23ab, 24 (Neubert et al., 2015)
15) Cingulate motor area (CMA)	(Ferry et al., 2000; McFarland and Haber, 2000; Takada et al., 2001)	CCZ, RCZa, RCZp (Neubert et al., 2015)
16) Perigenual area (PGA) **17) Subgenual area (SGA)**	(Ferry et al., 2000; Frankle et al., 2006; Freedman et al., 2000)	PGA: 32pl, 32d SGA: 25 (Neubert et al., 2015)

MRI registration

Subcortical masks

The average FLASH volume of the three TE's was linearly registered to the MP2RAGE whole-brain second inversion volume using a mutual information function, trilinear interpolation, and 6 degrees of freedom (DoF) in FLIRT (FSL 5.0.9). The MP2RAGE slab image was linearly registered to the MP2RAGE whole-brain UNI volume using a correlation cost function, trilinear interpolation, and 6 DoF in FLIRT. The MP2RAGE whole brain was registered to the average rs-fMRI volume using a mutual information cost function, trilinear interpolation, and 6 DoF. The MP2RAGE whole brain was registered to the B0 volume using a correlation cost function, trilinear interpolation, and 7 DoF (6 DoF did not result in a reasonable registration). All images were skull stripped before registration using BET (Smith, 2002). All registrations were visually inspected. The resulting transformation matrices from the slab to the whole brain and whole brain to either the B0 or average rs-fMRI were concatenated and used to transform the STN and STR masks to the either DWI or rs-fMRI space using nearest-neighbor interpolation.

Cortical masks

The skull stripped 1mm MNI template was linearly registered to the MP2RAGE whole-brain UNI volume using a correlation cost function, trilinear interpolation, and 12 DoF in FLIRT. The resulting transformation matrix was concatenated with the transformation matrix of the whole-brain to either the B0 or average rs-fMRI and used to transform the cortical masks to the either DWI or rs-fMRI space using nearest-neighbor interpolation.

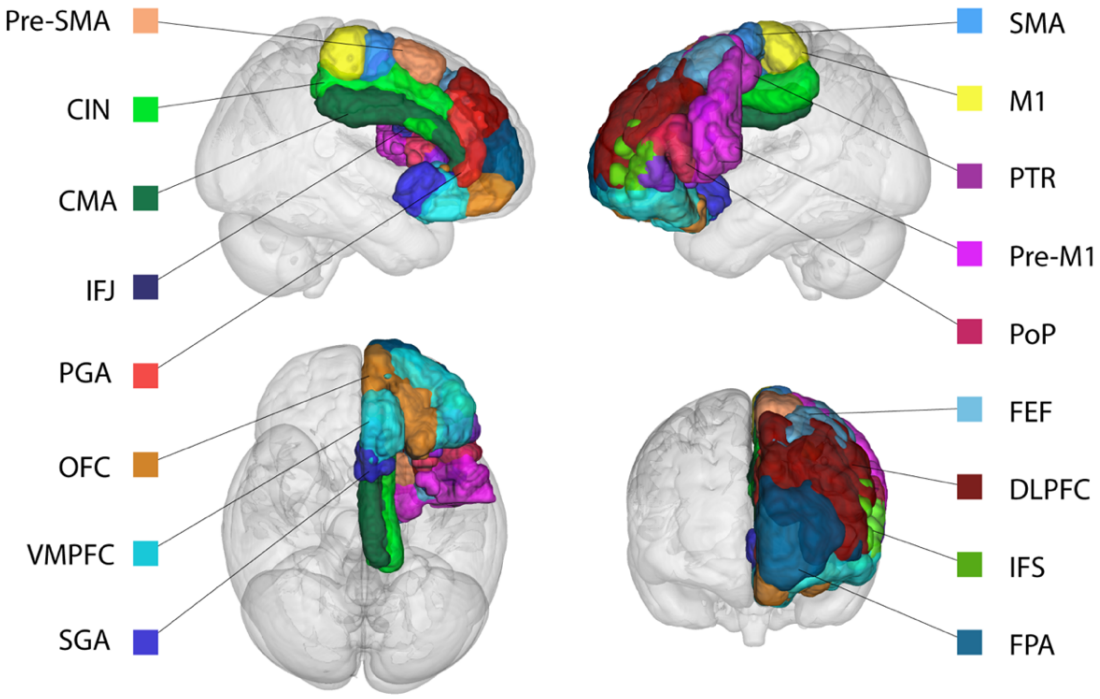

Figure 1: Cortical ROIs. Based on the literature search, all areas have a non-human primate homolog and structurally connect to both the STN and STR in non-human primates. For visualization purposes, only the ROIs in the left hemispheres are displayed. See table 1 for abbreviations.

DWI processing

Diffusion-weighted image pre-processing and all subsequent analyses were conducted using FSL (version 5.0.10). The four runs were concatenated and the data was corrected for eddy currents and motion. A single volume without diffusion weighting (B_0) was extracted from the DWI volume and used to create a brain-mask using BET (Smith, 2002). BedpostX (Behrens et al., 2003) was then run on the pre-processed data to estimate the voxel-wise diffusion parameter distributions. Then probabilistic tractography was used to estimate the tract strength between the cortical and subcortical regions. This was done in both directions using a midline exclusion mask, 5000 samples, a curvature threshold of 0.2, and a distance correction was used to correct for differences in the cortical-subcortical distances (Azadbakht

et al., 2015). See table 2 for the average path cortical-subcortical length for the STN and STR separately. The tractography analysis resulted in an image which, for each voxel in the seed mask, contains the number of samples reaching the target mask.

Table 2. Summary statistics of the tract lengths between the cortical areas and the STN and STR averaged over hemispheres. The BF_{10} is the resulting Bayes factors from the paired t-tests between the STN and STR tracts.

	STN		**STR**		
	Mean	***SD***	***Mean***	***SD***	***BF_{10}***
1) Primary motor cortex (M1)	104.3	22.76	107.3	20.88	0.85
2) Pre-motor cortex (pre-M1)	92.62	7.23	100.32	9.18	781.37
3) Supplementary motor area (SMA)	96.96	6.36	102.37	5.98	14.82
4) Pre-supplementary motor area (pre-SMA)	93.45	6.17	107.22	11.29	≥1000
5) Frontal eye fields (FEF)	95.56	7.51	104.21	10.84	≥1000
6) Dorsolateral prefrontal cortex (DLPFC)	94.36	9.59	97.92	12.6	1.44
7) Frontopolar area (FPA)	95.48	11.61	86.59	11.47	≥1000
8) Ventromedial & lateral prefrontal cortex (VMPFC)	70.62	20.28	45.08	14.02	≥1000
9) Orbitofrontal cortex (OFC)	61.28	14.68	37.0	11.39	≥1000
10) Inferior frontal sulcus (IFS)	99.85	8.46	107.13	11.78	45.70
11) Inferior frontal junction (IFJ)	103.38	10.8	104.81	14.09	0.25
12) Pars opercularis (POP)	76.97	18.53	95.07	13.55	≥1000
13) Pars triangularis (PTR)	79.25	17.55	94.35	14.07	≥1000
14) Cingulate cortex (CIN)	93.77	15.25	92.25	12.15	0.24
15) Cingulate motor area (CMA)	86.47	6.85	91.14	4.82	33.16
16) Perigenual area (PGA)	88.86	11.5	87.12	15.47	0.26
17) Subgenual area (SGA)	44.63	25.48	48.36	11.59	0.30

Calculations of tract seed ratio

To remove any spurious connections, the resulting seed images were thresholded so that only voxels that had at least 50 samples were kept. The resulting thresholded masks were divided by the number of samples (n=5000). This creates a ratio between the number of samples that

reached the target versus the total number of samples used per voxel. Finally, an average ratio was calculated for a given seed mask which indicates, on average, how many samples ended in the target region. Tract seed ratio was defined here as the average of the two seed-ratios that resulted from the seed-to-target tractography and target-to-seed tractography.

Calculation of tract strength

Tract seed ratio can be informative to show differences in connectivity between regions it does not take differences in volume into account. Therefore, in addition to the tract seed ratio, we also calculate tract strength. To remove any spurious connections, the resulting seed image was thresholded so that only voxels that had at least 50 samples were kept. The number of non-zero voxels was then divided by the total number of voxels in the seed mask, resulting in a ratio indicating the proportion of seed mask voxels that was probabilistically connected to the target mask. This ratio is relative to the volume of the seed mask and compensates for the volumetric differences between the STN and STR. Tract strength was defined as the average of the two ratios that resulted from the seed-to-target tractography and target-to-seed tractography (Boekel et al., 2017; Forstmann et al., 2010). Tract strength differs from tract seed ratio in two ways: the absolute number of samples is not taken into account but the volumes of the seed masks are. Note that the term tract strength here is used to index a probability density function (PDF), quantifying the ratio of how many streamlines directly and continuously commence from a seed region and terminate at a target area. This PDF is a commonly used measure for inferring the strength of structural white matter tracts (Behrens et al., 2007; Khalsa et al., 2014; van den Bos et al., 2014). While the PDF is a commonly used measure for inferring the strength of white matter tracts, it is not without its limitations. For instance, the 'amount' of probability or confidence we have in a tract can be influenced by the distance between two areas. As errors and noise accumulate over time, shorter connections would result in higher tract strengths (Jbabdi and Johansen-Berg, 2011). Therefore we used a distance correction. While the tract strength ratio is normalized for volume and a distance correction was applied, the direct statistical comparisons between the STN and STR should be interpreted with caution.

rs-fMRI processing

The rs-fMRI data was corrected for B_0 field inhomogeneities using fsl_prepare_fieldmap and FUGUE as implemented in FSL (version 5.0.9). Subsequently, the rs-fMRI data was motion-corrected using MCFLIRT. The average time series of each cortical and subcortical ROI were correlated using a Pearson correlation, and the correlation coefficient was used for further analyses.

Statistics

The outlier criteria was 3 times the interquartile range. All statistics were done using the Bayesian tests implemented in the BayesFactor toolbox (Morey et al., 2014) in R (R Core Team, 2016). The benefit of using Bayesian statistics is that it allows the quantification of evidence for the null hypothesis (H_0: the STN and STR do not differ in tract strength or rs-fMRI correlation) versus the alternative hypothesis (H_1: the STN and STR do differ in tract strength or rs-fMR correlation). We will use the labels as proposed by (Jeffreys, 1961) and adjusted by (Wetzels and Wagenmakers, 2012) and are shown in table i (Introduction). Bayes factors that are larger or equal to 1000 will be noted as ≥1000. The tract strengths and correlation coefficients were compared using a JZS Bayesian mixed-effect model with the subcortical region and cortical region as independent variables, and participant and hemisphere as random factors with default prior scales as implemented in the BayesFactor toolbox.

Open science

All corresponding analysis scripts can be found on https://osf.io/s46hr/

Results

Seed ratio differences between the STN & STR

The outlier analysis indicated that for a single tract (STN – orbitofrontal cortex) there were four outliers. These data points were removed from any further analysis. The JZS Bayesian mixed-effect model revealed that the model with main effects for subcortical structure and cortical structures, as well as an interaction between these two variables, is preferred over the model without the interaction, by a Bayes factor of >1000. Therefore, the data provides decisive evidence that the average number of samples reaching the target is generally higher for the tracts between the STN and cortex than for the STR. Pairwise post-hoc comparisons between the STN and STR are given in table 3.

Table 3. Summary statistics of the average seed ratios for the STN and STR to cortex Averaged across hemisphere. The BF_{10} are the resulting Bayes factors from the paired t-tests between the STN and STR tracts. For illustrative purposes, the average seed ratio values in this table are multiplied by 10.

	STN		**STR**		
	Mean	***SD***	***Mean***	***SD***	BF_{10}
1) Primary motor cortex (M1)	0.21	0.02	0.18	0.01	≥1000
2) Pre-motor cortex (pre-M1)	0.18	0.01	0.16	0.01	≥1000
3) Supplementary motor area (SMA)	0.19	0.01	0.16	0.01	≥1000
4) Pre-supplementary motor area (pre-SMA)	0.18	0.01	0.16	0.01	≥1000
5) Frontal eye fields (FEF)	0.19	0.02	0.17	0.02	≥1000
6) Dorsolateral prefrontal cortex (DLPFC)	0.18	0.01	0.16	0.01	≥1000
7) Frontopolar area (FPA)	0.18	0.02	0.15	0.01	≥1000
8) Ventromedial & lateral PFC (VMPFC)	0.15	0.02	0.14	0.01	17.56
9) Orbitofrontal cortex (OFC)	0.15	0.01	0.15	0.01	0.24
10) Inferior frontal sulcus (IFS)	0.19	0.02	0.17	0.02	≥1000
11) Inferior frontal junction (IFJ)	0.20	0.02	0.17	0.02	≥1000
12) Pars opercularis (POP)	0.17	0.02	0.17	0.02	0.19
13) Pars triangularis (PTR)	0.17	0.02	0.17	0.02	0.19
14) Cingulate cortex (CIN)	0.19	0.02	0.17	0.01	≥1000
15) Cingulate motor area (CMA)	0.17	0.01	0.16	0.01	≥1000
16) Perigenual area (PGA)	0.17	0.02	0.16	0.01	909.18
17) Subgenual area (SGA)	0.13	0.04	0.14	0.02	0.52

Tract strength differences between the STN & STR

The outlier analysis indicated that for a single tract (STR – perigenual area) there was a single outlier. This data point was removed from any further analysis. The JZS Bayesian mixed-effect model revealed that the model with main effects for subcortical structure and cortical structures, as well as an interaction between these two variables, is preferred to the model without the interaction with a Bayes factor of >1000. Therefore, the data provides decisive evidence that the tract strength between the STN and cortex is generally lower than for the STR and the cortex. Note that this was the case even though the absolute number of samples reaching the target was higher for the STN. The post-hoc comparisons indicated a few exceptions, namely that there was decisive evidence for the STN for higher tract strengths towards the ventromedial and lateral prefrontal cortex (VMPFC) and orbitofrontal cortex (OFC). There was substantial evidence for the STN and the STR showing similar tract strengths to the pre-supplementary motor area (pre-SMA). There was only anecdotal evidence that tract strengths for the perigenual area (PGA) and subgenual area (SGA) were similar between the STN and STR (see table 4 for the paired t-tests between the STN and STR per tract and figure 2). The main effect of cortical areas and the interaction indicated that various cortical areas have different tract strengths to the subcortex and that this tract strength varied per cortical area and subcortical structure.

As illustrated in figure 1, the cortical masks used in this study are rather large. It might therefore be the case that the cortical areas projecting to the STN did not overlap with the cortical areas projecting to the STR. We illustrated this by back projecting the thresholded cortical masks from individual B_0 to MNI standard space where a probabilistic map was created across participants (see figure 3). It seemed that the cortical region projecting to the STR that had the highest overlap across participants is the same region that also projects to the STN.

Table 4. Summary statistics of the tract strengths for the STN and STR to cortex averaged over hemispheres. The BF_{10} are the resulting Bayes factors from the paired t-tests between the STN and STR tracts.

	STN		**STR**		
	Mean	***SD***	***Mean***	***SD***	***BF_{10}***
1) Primary motor cortex (M1)	0.71	0.1	0.84	0.09	≥1000
2) Pre-motor cortex (pre-M1)	0.64	0.06	0.69	0.07	139.30
3) Supplementary motor area (SMA)	0.77	0.08	0.83	0.07	132.52
4) Pre-supplementary motor area (pre-SMA)	0.74	0.06	0.73	0.09	0.27
5) Frontal eye fields (FEF)	0.43	0.2	0.65	0.12	≥1000
6) Dorsolateral prefrontal cortex (DLPFC)	0.67	0.07	0.76	0.09	≥1000
7) Frontopolar area (FPA)	0.7	0.09	0.79	0.11	131.73
8) Ventromedial & lateral PFC (VMPFC)	0.57	0.2	0.39	0.12	≥1000
9) Orbitofrontal cortex (OFC)	0.45	0.18	0.3	0.08	≥1000
10) Inferior frontal sulcus (IFS)	0.7	0.09	0.76	0.1	10.87
11) Inferior frontal junction (IFJ)	0.61	0.12	0.73	0.07	≥1000
12) Pars opercularis (POP)	0.48	0.15	0.7	0.07	≥1000
13) Pars triangularis (PTR)	0.63	0.18	0.71	0.08	7.0
14) Cingulate cortex (CIN)	0.64	0.08	0.78	0.08	≥1000
15) Cingulate motor area (CMA)	0.76	0.07	0.84	0.06	721.13
16) Perigenual area (PGA)	0.75	0.11	0.78	0.11	0.37
17) Subgenual area (SGA)	0.22	0.2	0.27	0.11	0.55

For illustrative purposes, the average seed ratio values in this table are multiplied by 10.

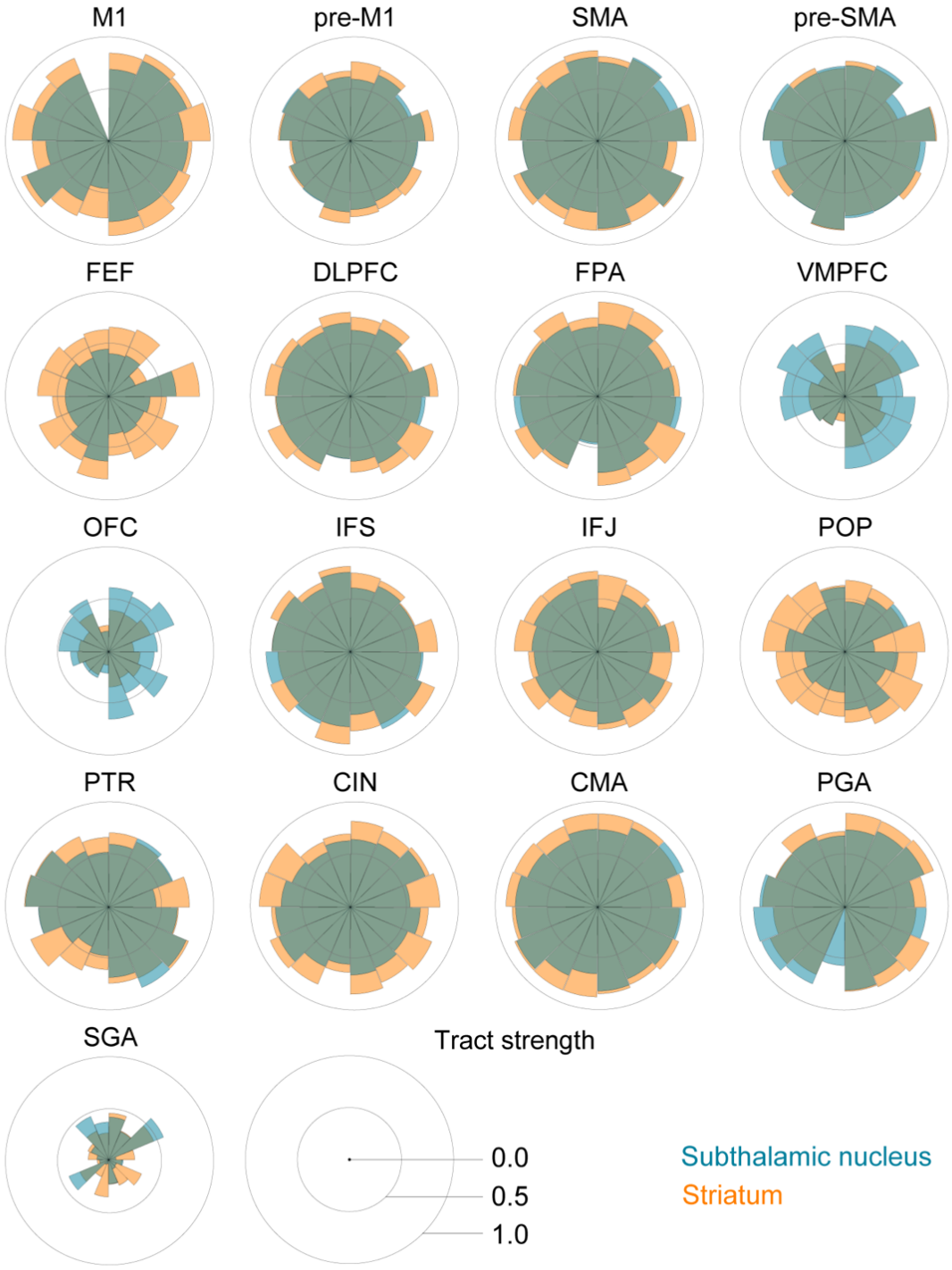

Figure 2: Star plots of the tract strengths between the STN, STR, and the different cortical regions per participant. The STN is color-coded using blue, the STR using orange, and both tracts are plotted with 50% opacity. Each segment corresponds to an individual participant.

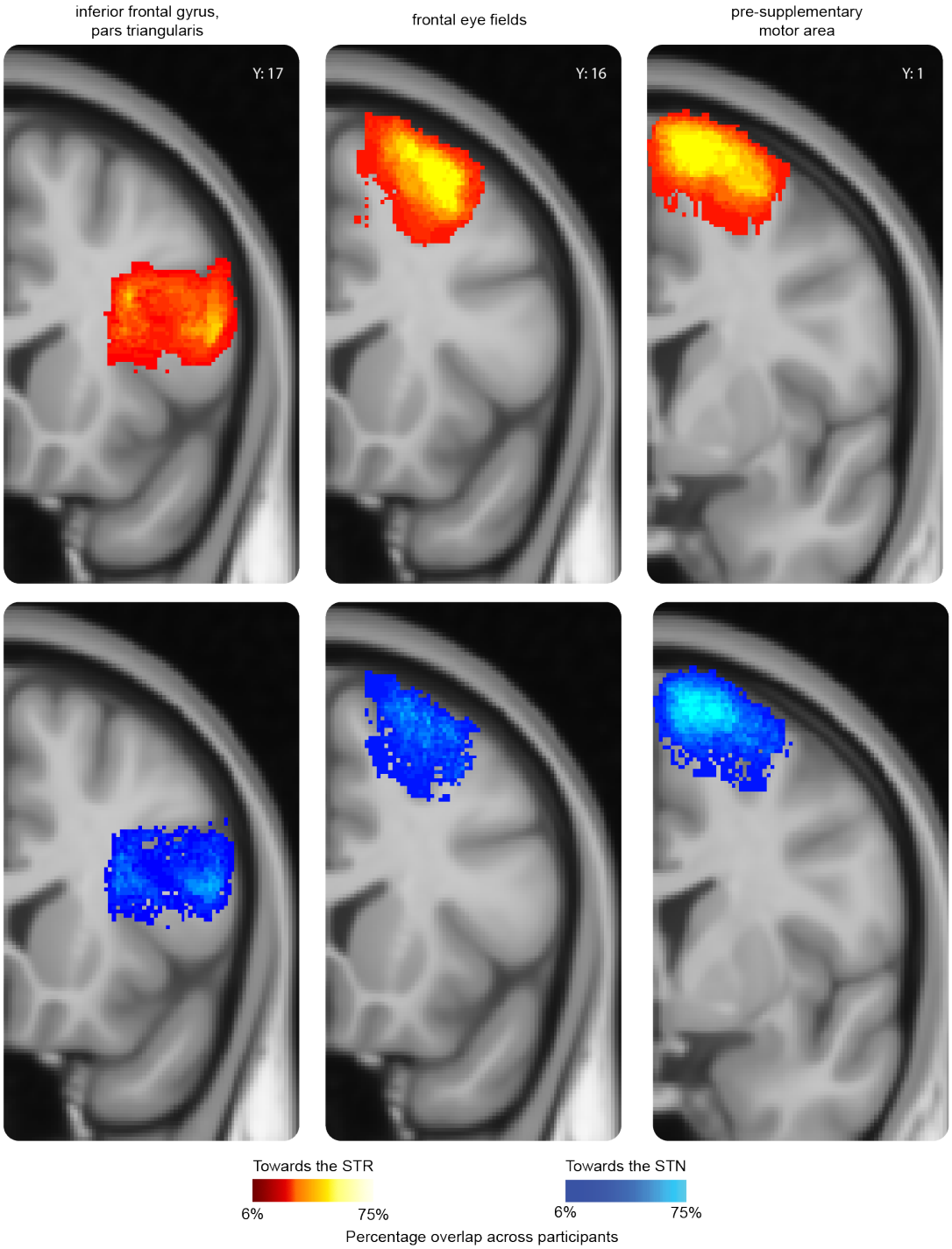

Figure 3: Probability map of 3 cortical regions projecting to the subcortex. For the pars triangularis (PTR), frontal eye fields (FEF), and pre-supplementary motor area (pre-SMA), a probability map was created using the individual thresholded seed masks. The thresholded seed masks only include those voxels which contained at least 50 samples in the tractography analysis. To be able to compare the results across participants, the thresholded seed masks were transformed back into MNI- space. Color intensity indicates the overlap across participants. In red-yellow the probability map of the thresholded seed masks towards the STR; in blue the probability map of the thresholded seed masks towards the STN. The Y value corresponds to the MNI coordinate system.

Tract strength differences for the STN & STR separately

To test for differences between tracts connecting subcortical areas, i.e., STN and STR, with the cortex, Bayesian paired t-tests were used (see table 5 for all the resulting Bayes factors). The paired t-tests indicated that the STN and the STR shared several similarities in their connectivity fingerprint to the cortex. Compared to other cortical areas, the SGA, frontal eye fields (FEF), orbitofrontal cortex (OFC), and the pars opercularis of the inferior frontal gyrus (POP) had lower tract strengths towards the STN (SGA: 16 out of 16 paired t-tests indicated substantial or more evidence in favor of lower tract strengths; FEF: 12 out of 16 paired t-tests indicated substantial or more evidence in favor of lower tract strengths; OFC: 13 out of 16 paired t-tests indicated substantial or more evidence in favor of lower tract strengths; and POP: 12 out of 16 paired t-tests indicated substantial or more evidence in favor of lower tract strengths). Similarly, compared to other cortical areas, the SGA, FEF, OFC, and POP had lower tract strengths towards the STR (SGA: 16 out of 16 paired t-tests indicated substantial or more evidence in favor of lower tract strengths; FEF: 12 out of 16 paired t-tests indicated substantial or more evidence in favor of lower tract strengths; OFC: 13 out of 16 paired t-tests indicated substantial or more evidence in favor of lower tract strengths; POP: 11 out of 16 paired t-tests indicated substantial or more evidence in favor of lower tract strengths). There were also a number of cortical areas that had relatively higher tract strengths towards both the STN and STR. Compared to the other cortical areas, the supplementary motor area (SMA), cingulate motor area (CMA), PGA, and pre-SMA had higher tract strengths towards the STN (SMA: 12 out of 16 paired t-tests indicated substantial or more evidence in favor of higher tract strengths; CMA: 12 out of 16 paired t-tests indicated substantial or more evidence in favor of higher tract strengths; PGA: 10 out of 16 paired t-tests indicated substantial or more evidence in favor of higher tract strengths; pre-SMA: 10 out of 16 paired t-tests indicated substantial or more evidence in favor of higher tract strengths). Similarly, compared to the other cortical areas, the CMA and SMA had higher tract strengths towards the STR (CMA: 12 out of 16 paired t-tests indicated substantial or more evidence in favor of higher tract strengths; SMA: 12 out of 16 paired t-tests indicated substantial or more evidence in

favor of higher tract strengths).

rs fMRI correlation differences between the STN & STR

There were no outliers for the rs-fMRI correlations. The JZS Bayesian mixed-effect model revealed that the model with main effects for subcortical structures and cortical structures, as well as an interaction between these two variables, is preferred to the model without the interaction with a Bayes factor of 130.74. The data, therefore, provide decisive evidence that the resting state BOLD correlation between the STN and cortex is generally lower than for the STR and cortex.

The post-hoc comparisons indicate that overall, the STR has a stronger rs-fMRI correlation to cortical areas compared to the STN (see table 6 for the paired t-tests between the STN and STR per tract, as well as figure 4). It is unlikely that this difference in rs-fMRI is due to the T_2* differences because the rs-fMRI sequence used short TE's optimized for the human subcortex at 7T (de Hollander et al., 2017; Keuken et al., 2015; 2017; Mestres-Missé et al., 2017). It might, however, be the case that there is more physiological noise in and around the STN, resulting in lower rs-fMRI correlations with the cortex (Altman and Krzywinski, 2015). Therefore, the direct comparison between the STN and STR as reported in table 3 and table 4 should be interpreted with caution.

Table 5. Paired t-tests within the STN and STR tracts. The right upper triangle displays the BF10 of the paired tests for the STR, while the lower-left triangle displays the BF10 for the STN pairs. To highlight the use of this table, in grey the BF10 for the IFJ indicated lower tract strengths compared to other cortical areas for both the STN (dark grey, lower triangle) and STR (light grey, upper triangle). For display purposes, all BF10 larger or equal to 1000 are noted as ≥1000.

	M1	Pre-M1	SMA	Pre-SMA	FEF	DLPFC	FPA	VMPFC	OFC	IFS	IFJ	POP	PTR	CIN	CMA	PGA	SGA
M1	-	15.17	18.65	0.46	≥1000	0.67	0.2	133.02	≥1000	0.2	67.37	≥1000	1.56	60	250.31	1.19	≥1000
Pre-M1	15.17	-	≥1000	≥1000	≥1000	2.15	9.66	1.05	≥1000	34.54	0.44	≥1000	0.2	0.19	≥1000	324.43	≥1000
SMA	18.65	≥1000	-	0.38	≥1000	457.49	5.39	≥1000	≥1000	2.93	≥1000	≥1000	97.17	≥1000	0.21	0.25	≥1000
Pre-SMA	0.46	≥1000	0.38	-	≥1000	≥1000	0.83	248.91	≥1000	1.96	≥1000	≥1000	10.66	359.66	0.26	0.19	≥1000
FEF	≥1000	≥1000	≥1000	≥1000	-	≥1000	≥1000	2.2	0.21	≥1000	32.15	0.34	133.78	≥1000	≥1000	≥1000	49.93
DLPFC	0.67	2.15	457.49	≥1000	≥1000	-	1.17	5.25	≥1000	1.62	4.59	≥1000	0.43	0.63	291.21	6.37	≥1000
FPA	0.2	9.66	5.39	0.83	≥1000	1.17	-	140.69	≥1000	0.19	10.67	≥1000	2.51	31.77	18.82	2.09	≥1000
VMPFC	133.02	1.05	≥1000	248.91	2.2	5.25	140.69	-	≥1000	18.65	0.34	1.28	0.9	1.21	≥1000	≥1000	≥1000
OFC	≥1000	≥1000	≥1000	≥1000	0.21	≥1000	≥1000	≥1000	-	≥1000	90.73	0.29	≥1000	≥1000	≥1000	≥1000	≥1000
IFS	0.2	34.54	2.93	1.96	≥1000	1.62	0.19	18.65	≥1000	-	227.44	≥1000	1.44	3.98	2.47	0.58	≥1000
IFJ	67.37	0.44	≥1000	≥1000	32.15	4.59	10.67	0.34	90.73	227.44	-	67.98	0.2	0.3	≥1000	243.21	≥1000
POP	≥1000	≥1000	≥1000	≥1000	0.34	≥1000	≥1000	1.28	0.29	≥1000	67.98	-	883.01	≥1000	≥1000	≥1000	≥1000
PTR	1.56	0.2	97.17	10.66	133.78	0.43	2.51	0.9	≥1000	1.44	0.2	883.01	-	0.2	215.06	13.3	≥1000
CIN	60	0.19	≥1000	359.66	≥1000	0.63	31.77	1.21	≥1000	3.98	0.3	≥1000	0.2	-	≥1000	≥1000	≥1000
CMA	250.31	≥1000	0.21	0.26	≥1000	291.21	18.82	≥1000	≥1000	2.47	≥1000	≥1000	215.06	≥1000	-	0.28	≥1000
PGA	1.19	324.43	0.25	0.19	≥1000	6.37	2.09	≥1000	≥1000	0.58	243.21	≥1000	13.3	≥1000	0.28	-	≥1000
SGA	≥1000	≥1000	≥1000	≥1000	49.93	≥1000	≥1000	≥1000	≥1000	≥1000	≥1000	≥1000	≥1000	≥1000	≥1000	≥1000	-

Table 6. Summary statistics of the rs-fMRI correlation coefficient for the STN and STR to cortex averaged over hemispheres. The BF_{10} are the resulting Bayes factors from the paired t-tests between the STN and STR to cortex pairs.

	STN		**STR**		***BF_{10}***
	Mean	***SD***	***Mean***	***SD***	
1) Primary motor cortex (M1)	0.12	0.19	0.41	0.43	743.67
2) Pre-motor cortex (pre-M1)	0.15	0.17	0.44	0.22	>1000
3) Supplementary motor area (SMA)	0.18	0.18	0.36	0.27	7.26
4) Pre-supplementary motor area (pre-SMA)	0.04	0.21	0.39	0.22	>1000
5) Frontal eye fields (FEF)	-0.02	0.23	0.38	0.21	>1000
6) Dorsolateral prefrontal cortex (DLPFC)	0.04	0.22	0.54	0.21	>1000
7) Frontopolar area (FPA)	0.08	0.21	0.54	0.21	>1000
8) Ventromedial and lateral prefrontal cortex (VMPFC)	0.16	0.23	0.63	0.21	>1000
9) Orbitofrontal cortex (OFC)	0.1	0.24	0.59	0.21	>1000
10) Inferior frontal sulcus (IFS)	0.07	0.23	0.45	0.23	>1000
11) Inferior frontal junction (IFJ)	0.07	0.19	0.43	0.16	>1000
12) Pars opercularis (POP)	0.13	0.18	0.46	0.21	>1000
13) Pars triangularis (PTR)	0.15	0.2	0.45	0.23	>1000
14) Cingulate cortex (CIN)	0.13	0.23	0.58	0.21	>1000
15) Cingulate motor area (CMA)	0.15	0.19	0.55	0.19	>1000
16) Perigenual area (PGA)	0.1	0.19	0.45	0.24	>1000
17) Subgenual area (SGA)	0.12	0.2	0.52	0.26	>1000

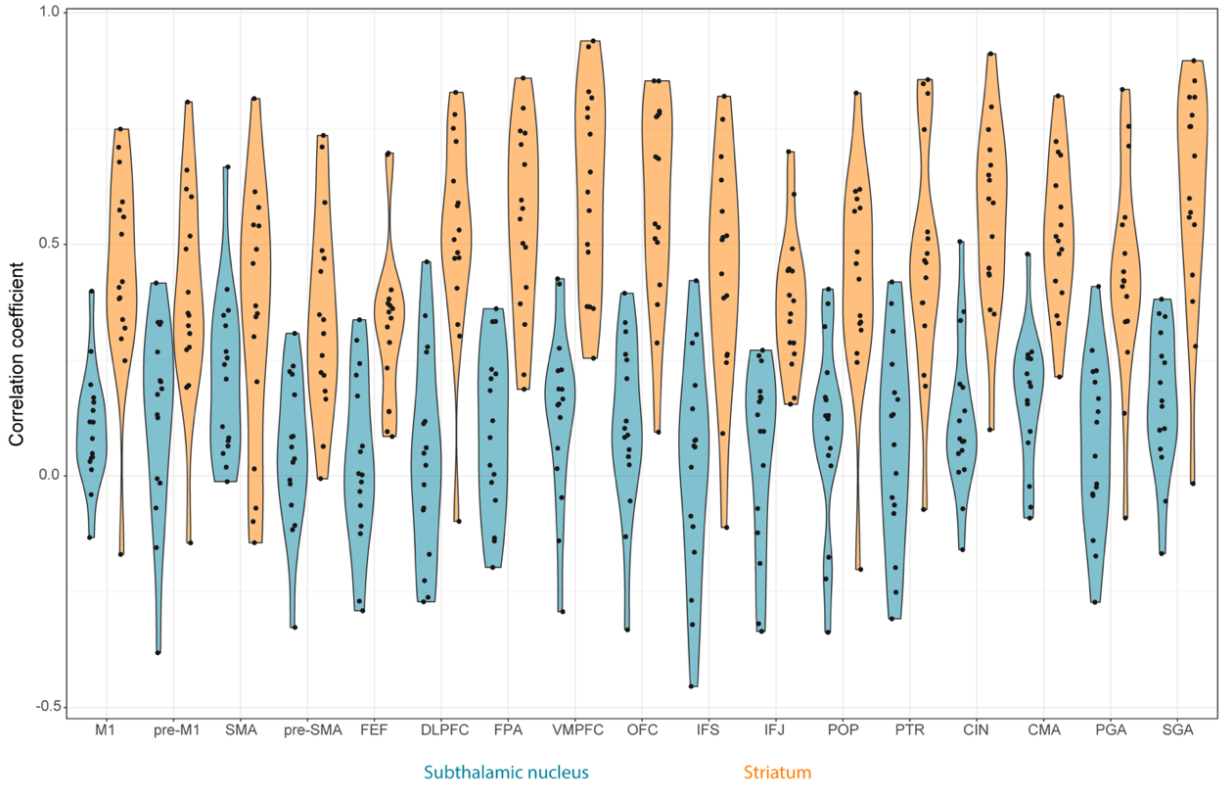

Figure 4: Violin plots of the rs-fMRI correlation between STN, STR, and the different cortical regions per participant. The STN is color-coded using blue, the STR using orange. The black circles correspond to the individual participants.

Correlation differences for the STN & STR separately

To test which of the resting-state correlations between the subcortical areas and cortex differed from each other, Bayesian paired t-tests for the STN and STR were run separately. The results indicated that the STN had a different resting-state fingerprint than the STR. Contrary to the tract strengths, most of the rs-fMRI correlations between the STN and cortical ROIs did not differ from each other (see table 7 for all the resulting Bayes factors). This was the case for the primary motor area (M1) (11 out of 16 paired t-tests indicated

substantial or more evidence in favor of no difference); SGA (10 out of 16 paired t-tests); pre-M1 (9 out of 16 paired t-tests); (POP; 9 out of 16 paired t-tests); the inferior frontal gyrus pars triangularis (PTR; 8 out of 16 paired t-tests); CMA (8 out of 16 paired t-tests); and OFC (8 out of 16 paired t-tests). There was a notable exception for the FEF were compared to the other cortical areas the resting state correlation with the STN was lower (13 out of 16 paired t-tests indicated substantial or more evidence in favor of a lower correlation). Contrary to the STN, the rs-fMRI correlations between the STR and the cortical ROIs seemed more heterogeneous. Several regions had a higher rs-fMRI correlation with the STR such as the ventral medial prefrontal cortex (VMPFC; 13 out of 16 paired t-tests indicated substantial or more evidence in favor of a higher correlation); OFC (10 out of 16 paired t-tests indicated substantial or more evidence in favor of a higher correlation); and the cingulate cortex (CIN; 10 out of 16 paired t-tests indicated substantial or more evidence in favor of a higher correlation).

Table 7. Paired t-tests for the resting state correlation between the STN, STR, and the cortical ROIs. The upper triangle displays the BF10 of the paired tests for the STR and cortical ROIs, while the lower triangle displays the BF10 for the STN pairs. As an example, to highlight the use of this table, in dark grey the BF10 for the FEF indicating lower correlations compared to other cortical areas for the STN (lower triangle), while in light grey the BF10 for the VMPFC indicating higher correlations for the STR (upper triangle). For display purposes, all BF10 larger than 1000 are noted as >1000.

	M1	Pre-M1	SMA	Pre-SMA	FEF	DLPFC	FPA	VMPFC	OFC	IFS	IFJ	POP	PTR	CIN	CMA	PGA	SGA
M1	-	0.30	0.43	0.22	0.24	14.0	9.74	579.85	107.47	0.26	0.20	0.41	0.29	436.16	78.01	0.27	0.65
Pre-M1	0.33	-	1.12	0.43	0.53	6.44	6.36	443.40	29.55	0.19	0.22	0.21	0.20	208.54	36.44	0.20	0.41
SMA	0.88	0.27	-	0.21	0.20	40.49	39.79	>1000	259.12	0.56	0.52	1.33	0.64	947.16	>1000	0.90	2.18
Pre-SMA	7.15	44.56	34.68	-	0.20	65.09	55.20	>1000	539.04	0.52	0.37	0.69	0.47	>1000	182.56	0.43	1.15
FEF	34.56	770.56	>1000	4.18	-	>1000	205.76	>1000	>1000	1.51	0.52	1.35	0.80	>1000	>1000	0.69	1.83
DLPFC	1.50	12.87	32	0.19	1.44	-	0.19	73.41	1.50	881.33	199.80	261.95	41.51	1.84	0.19	28.53	0.20
FPA	0.27	0.85	3.33	0.30	5.25	1.27	-	202.08	1.03	27.91	59.36	5.09	7.47	1.09	0.20	12.71	0.20
VMPFC	0.30	0.19	0.20	5.88	72.59	41.10	3.61	-	0.66	>1000	>1000	>1000	>1000	0.61	5.25	>1000	1.10
OFC	0.20	0.33	0.72	0.51	6.54	1.09	0.24	4.69	-	>1000	>1000	>1000	750.84	0.19	0.70	163.26	0.45
IFS	0.31	1.68	2.21	0.21	0.88	0.28	0.20	22.21	0.29	-	0.24	0.20	0.19	668.59	6.72	0.19	0.43
IFJ	0.46	9.82	2.73	0.26	1.90	0.27	0.20	3.65	0.26	0.19	-	0.39	0.25	>1000	870.92	0.25	0.78
POP	0.21	0.28	0.38	6.26	123.63	10.06	0.43	0.28	0.24	0.88	2.64	-	0.18	>1000	133.48	0.19	0.38
PTR	0.25	0.19	0.22	2.83	24.36	11.48	0.81	0.20	0.36	10.85	2.75	0.26	-	281.89	6.38	0.19	0.44
CIN	0.20	0.22	0.43	1.71	48.83	16.92	0.89	0.41	0.35	0.86	0.59	0.19	0.22	-	2.15	>1000	0.34
CMA	0.32	0.19	0.30	15.22	589.96	48.74	1.58	0.20	0.67	1.41	1.81	0.23	0.19	0.32	-	9.46	0.21
PGA	0.21	0.57	1.19	0.45	4.85	1.03	0.23	1.38	0.19	0.35	0.27	0.30	0.71	0.34	0.64	-	0.45
SGA	0.19	0.24	0.36	0.52	3.20	0.65	0.27	0.28	0.21	0.35	0.47	0.19	0.23	0.19	0.23	0.22	-

Discussion

This study set out to investigate the connectivity fingerprint of the STN and STR with the cortex using diffusion and rs-fMRI. The tract strengths indicate that for most cortical areas tested, the STR exhibits relatively higher tract strengths than the STN. It is unlikely that the lower tract strength for the STN was due to higher noise in the tractography as the absolute seed ratios were higher for the STN. For the rs-fMRI data, the correlations between the cortical ROI's and the STR were also consistently found to be higher than those for the STN. This finding is in line with the previous literature that notes that while the STN and STR are indeed directly connected to similar cortical areas, STN connections are more sparsely present (Albin et al., 1989; Alexander et al., 1986; Frankle et al., 2006).

There were, however, two notable exceptions for tract strengths. Namely for the OFC and VMPFC, where a higher tract strength was found for the STN relative to the STR. The OFC and VMPFC are two cortical regions thought to be essential for reward processing, choice bias, and mood (Haber and Knutson, 2009; Hollerman et al., 2000; Lim et al., 2015; Mulder et al., 2013). Reward-oriented behaviors require many mental processes, including motor, sensory, learning, memory, cognitive, executive, decision-making, motivational, and emotional functions (Crocker et al., 2013). Given the multifaceted and complex nature of limbic processes, having strong connections to the STN might be explained as a direct modulator of motor-related output for goal-directed behaviors (Espinosa-Parrilla et al., 2013; Mallet et al., 2008). Contrary to the structural connectivity, the rs-fMRI connectivity for the OFC and VMPFC was higher towards the STR than towards the STN. This is somewhat puzzling as previous comparisons between DTI and rs-fMRI indicate that increased structural connectivity would predict higher functional connectivity. Whether this finding indicates that the functional connectivity between the OFC, VMPFC, and STR is driven via a hidden third region remains unclear (Damoiseaux and Greicius, 2009).

Overall the relative structural connectivity fingerprint of the cortex towards the STN is very similar to the STR. Compared to the other tested cortical areas, both subcortical areas have relatively low tract strengths towards the SGA, FEF, OFC, and POP. Both the SGA and OFC are thought to be involved in limbic processing. The FEF is largely governed by attentional mechanisms (Schafer and Moore, 2007), and are essential for visuospatial

attention, visual awareness, and perceptual modulation such as the preparation and execution of eye movements (Bizzi, 1968) as well as smooth pursuit (MacAvoy et al., 1991) and fixation (Izawa et al., 2009). Eye movement in response to an external cue will often form the basis for action selection and appropriate motor response and are crucial to early inhibition processes (Jantz et al., 2017). In addition, it has been shown that high-frequency stimulation of the STN in Parkinson's disease patients is shown to modulate saccadic latencies (Temel et al., 2008). It was therefore surprising to also find low functional connectivity between the STN and the FEF.

Relatedly, we found a lack of white matter connectivity between the STN, STR, and the POP. This was somewhat surprising given the functional significance of the inferior frontal gyrus associated with response inhibition (Aron, 2007; Aron et al., 2014a; 2014b; Bari and Robbins, 2013; Swick et al., 2008). The low structural connectivity to the pars opercularis was complimented by relatively low functional connectivity (10 out of the 16 t-tests indicated substantial or more evidence in favor of lower functional connectivity for both the STN and STR).

There were also several cortical areas such as the CMA and SMA that compared to the other cortical areas had stronger structural connectivity towards the subcortex. Both the CMA and SMA are thought to be crucial in voluntary-based motor processes and highlight the role of the BG in action generation (Halsband et al., 1994; Shima and Tanji, 1998). The only functional connectivity that was inline with these structural connections was between the CMA and the STR.

The cortical regions were selected based on their connection with both the STN and STR as identified in non-human primate (NHP) tracer studies. Additionally, the cortical ROIs were created using atlases that parcellated the human cortex in terms of their structural and functional homolog with NHPs using DTI (Neubert et al., 2014; 2015; Sallet et al., 2013). While there is a general agreement that major fiber tracts in DTI in NHPs correspond to the known anatomy identified with neural tracers within species, it remains difficult to identify the anatomy at the very fine fiber level with tractography (Azadbakht et al., 2015; Dauguet et al., 2007; Donahue et al., 2016; Thomas et al., 2014). A direct comparison between the findings of an NHP tracer study and a human neuroimaging study is challenging, however

previous work using DWI has shown that NHP results can be compared to humans due to similar organizational principles (Jbabdi et al., 2013). Concerning the present study, our findings are in agreement with animal-based BG models, proposing that both the STN and STR function as BG input structures and both show connections with a-priori defined motor-related, cognitive, and limbic cortical areas known to be present in NHPs. Moreover, the STN shows higher structural connectivity with the SMA when compared with the primary motor area (M1), which is in accordance with models of action selection and inhibition within the hyperdirect pathway (Feingold et al., 2015; Haber et al., 1990; Haynes and Haber, 2013; Inase et al., 1999; Monakow et al., 1978; Nambu et al., 1996; 1997). Such a connectivity profile seems to be in line with previous work (Brunenberg et al., 2012; Lambert et al., 2012). Both the SMA and M1 connections to the STN seem to be clinically relevant as both cortico-subcortical connections are predictive for the DBS efficacy in Parkinson's disease patients (Horn et al., 2017).

Limitations

Several limitations need to be addressed. Even with a high spatial resolution of 1mm isotropic DWI data, it remains a challenge to precisely identify where the white matter tract exactly enters the cortex resulting in the so-called "gyral biases" (Jbabdi et al., 2015; Jones et al., 2013; Reveley et al., 2015; Schilling et al., 2017). While not feasible in this project, *postmortem* MRI and histological validation of these tracts could assist in validating the *in vivo* findings presented here (Forstmann et al., 2017; Mortazavi et al., 2017). Related is the tensor model used to fit the DWI data. Here we used a relatively simple ball-and-stick model (Behrens et al., 2007) as the acquisition parameters of the data did not lend themselves to more complex models such as spherical deconvolution (Dell'Acqua et al., 2012; Tournier et al., 2004; 2008).

Furthermore, the term "tract strength" should not be over-interpreted as it does not quantify the actual white matter fiber number. The term tract strength here is used to index a probability density function, quantifying the ratio of how many streamlines directly and continuously commence from a seed region and terminate at a target area. While this density function is a commonly used measure for inferring the strength of white matter tracts, it is

not without its limitations. A related limitation is the volumetric difference between the STN and STR. While the tract strength ratio was normalized for volume and a distance correction was applied, the volume difference might still influence the result that the STR has a higher tract strength than the STN. However, this would not explain the results in which the STN tract strengths to the OFC and VMPFC were found to be stronger compared to STR. Nonetheless, the direct statistical comparisons between the STN and STR should be interpreted with caution.

A final limitation is the anatomical specificity of the cortical ROIs used in this study and the relevance for computational models. Computational models have allowed us to generate quantifiable predictions about the role of the different structures in the cortico-BG-thalamic loops (Bogacz and Gurney, 2007; Brown et al., 2004; Forstmann et al., 2017; Forstmann and Wagenmakers, 2015; Frank, 2006; Rubchinsky et al., 2003). Within a number of these models, the cortex is ill-specified as a single node that can correspond to many distinct areas such as the lateral intraparietal area (LIP), the frontal eye field (FEF), pre-motor cortex, or simply "cortex". Based on the current results, these models can be further refined by incorporating more precise anatomical information regarding the cortical input. A straightforward way of improving the anatomical specificity is the use of DWI and rs-fMRI to identify per participant the voxels within these relatively large cortical areas connected to the BG. These individualized cortical ROIs can be used to test correlations during task-based fMRI (e.g., (Keuken et al., 2015; Marrelec and Fransson, 2011; Zhang et al., 2012)). For the STN and STR, we were able to manually parcellate the structure per individual using high resolution 7T MRI. Parcellating the entire cortex *in vivo* into the myelo- or cyto-architectonic areas per participant is, however, still very challenging (but see (De Martino et al., 2014; Dinse et al., 2015; Waehnert et al., 2015)). Recently there have been a number of cortical atlases that go well beyond the cortical parcellation scheme of Brodmann (Eickhoff et al., 2017; Glasser et al., 2016; Nieuwenhuys, 2012; Nieuwenhuys et al., 2014). Such atlases entail a fine-grained parcellation of the cortex, reducing the need to use non-specific terms such as the DLPFC, which reflects a functional rather than a single anatomical defined region (Petrides and Pandya, 1999). It is, however, unclear how these recent cortical parcellations translate to the anatomical nomenclature used in the animal tracer studies.

Conclusion

Using multimodal UHF-MRI we show that compared to other tested cortical areas, the STN and STR have relatively lower connectivity to areas thought to be involved in response inhibition and stronger connectivity to areas associated with voluntary based motor actions. Our results are consistent with previous literature in that the STN and STR are connected to similar cortical areas.

Acknowledgments
This work was supported by a Vidi grant from the Dutch Organization for Scientific Research (BUF), an ERC starter grant (BUF) and an ABC talent grant from the University of Amsterdam (MCK). We thank SURFsara (www.surfsara.nl) for the support in using the Lisa Computer Cluster and Domenica Wilfling and Gilles de Hollander for acquiring the resting-state fMRI data.

Six

Cortico-basal White Matter Alterations Occurring in Parkinson's Disease

Introduction

The subthalamic nucleus (STN) is a small region located in the basal ganglia (BG) that is integral to a range of motor behaviors and cognitive functions (Parent & Hazrati, 1995a; 1995b). Abnormal activity of the STN is implicated in several neurodegenerative and neurological disorders including Parkinson's disease (PD). Here, increased indirect pathway activity is thought to increase the inhibition of motor plans rather than reducing inhibitory control (Obeso et al., 2000). Accordingly, the STN is a common neurosurgical target for deep brain stimulation (DBS) for PD patients who no longer appropriately respond to pharmacological interventions, where standard targeting is facilitated by the use of MRI and stereotaxic atlases (Perlmutter & Mink, 2006).

However, these atlases are often based on a normal population and fail to account for neuroanatomical variability occurring for a variety of reasons, including age and disease (Dickie et al., 2017; Evans, 2012; Lucerna, Salpietro, Alafaci, & Tomasello, 2011; Nakano, Taneda, Watanabe, & Kato, 2012; Richter, Hoque, Halliday, Lozano, & Saint-Cyr, 2004; Xiao et al., 2014). It is widely acknowledged that the anatomy of the STN varies substantially across healthy individuals, with in-vivo size estimates ranging from 50mm3 to 270mm3 (see (Zwirner et al., 2017) and references therein). Additionally, the STN has been shown to move with age, shifting in the lateral direction in the elderly population (Alkemade et al., 2017; den Dunnen & Staal, 2005) with additional alterations of STN volume and location occurring in PD (Keuken et al., 2017; Kitajima et al., 2008; Pereira et al., 2016)

Moreover, the STN demonstrates a complex connectivity profile both within the BG and with the rest of the cortex (Baudrexel et al., 2011; Brunenberg et al., 2012; Dyrby et al., 2007; Jahanshahi, Obeso, Rothwell, & Obeso, 2015; Lambert et al., 2012; Lenglet et al., 2012; Nambu, 2008; Plantinga et al., 2018). With regards to PD, both the structural and functional connectivity of the STN has been shown to predict the future outcome and relative success of DBS treatment (Horn et al., 2017). This is supported by electrophysiological and functional (f)MRI results which show that specific cortico-basal connections are functionally altered in PD (Litvak et al., 2011; Rowe et al., 2002; Wu et al., 2009). Furthermore, the existing variability in the success of DBS suggests the presence of individual differences in the

integrity of specific connections between the STN and different cortical regions.

DBS of the STN is however associated with some psychiatric side-effects, cognitive, and emotional disturbances (Benabid et al., 2009; Wichmann & DeLong, 2006). One explanation for these side-effects relates to the somatotopic arrangement of functionally dissimilar cortical projections within the STN (Joel & Weiner, 1997; Miyachi et al., 2006; Nambu, Takada, Inase, & Tokuno, 2018; Romanelli, Esposito, Schaal, & Heit, 2005). In DBS, the implanted electrode may directly stimulate, due to suboptimal placement, or spread current to functionally disparate sub-regions of the nucleus which in-turn interfere with the typical connectivity between the STN and limbic or cognitive cortical areas (Saint-Cyr et al., 2002; Temel, Blokland, Steinbusch, & Visser-Vandewalle, 2005).

Given the neuroanatomical alterations that occur in the STN due to orthologic aging or PD, it is crucial to investigate whether group-specific changes extend to structural connectivity. The current paper first aims to investigate whether there are disease-specific alterations in the connectivity of cortical areas to the subthalamic nucleus in PD patients by using group-specific atlases of the STN, and second, to assess whether any connectivity measures may be correlated with disease progression. We chose six cortical areas based on their functional involvements in limbic, cognitive, and motor processes, known to be affected in PD (Hu & Dolcos, 2017; Kane & Engle, 2002; MacDonald, Cohen, Andrew Stenger, & Carter, 2000; Molnar-Szakacs, Iacoboni, Koski, & Mazziotta, 2005; Nambu, Tokuno, & Takada, 2002). Cortical areas consisted of the pars opercularis of the inferior frontal gyrus (POp), the anterior cingulate cortex (ACC), the dorsolateral prefrontal cortex (DLPFC), the primary motor cortex (M1), supplementary motor area (SMA), and pre-supplementary motor area (pre-SMA). Notably, we use these results to highlight the importance of using group-specific atlases for STN identification when ultra-high field (UHF) MRI is not available, given the scarcity of UHF-MRI sites relative to the number of DBS centers (Abosch, Yacoub, Ugurbil, & Harel, 2010; Beisteiner et al., 2011; Cho et al., 2008, 2011; Forstmann et al., 2012; Hoffmann et al., 2019).

Materials and methods

Subjects

Seventy PD patients and thirty-one age-matched healthy controls participated in the study (table 1) (see (Feis, Pelzer, Timmermann, & Tittgemeyer, 2015) for more details on the subject population). Patients were not required to discontinue their medication for this study. The gender imbalance in the PD group was since PD is 1.5 times more likely to occur in men than in women (Marceglia et al., 2006; Miller & Cronin-Golomb, 2010; Moisan et al., 2016). Disease related variables were obtained from PD patients, which include UPDRS III scores taken both on and off medication, duration of disease in years, and side of symptom onset (left or right), all obtained from an expert neurologist (Tomer, Levin, & Weiner, 1993). Disease progression, as a measure of severity, is calculated by dividing each patient's UPDRS off III scores by the duration of the disease in years (Baumann, Held, Valko, Wienecke, & Waldvogel, 2014). Medication response is calculated by dividing the UPDRS off III score by the respective UPDRS on (Bordelon et al., 2011). All healthy controls self-reported no history of psychiatric or neurological disease, and PD patients reported no other neurological complaints than PD. The study was approved by the ethical committee of the University Hospital of Cologne, Germany.

Table 1: Descriptive statistics. The means and standard deviations (S.D) demographic statistics for both the Parkinson's disease and healthy control group. UPDRS: Unified Parkinson's Disease Rating Scale.

Measure	Parkinson's Disease	Healthy Control
Age (years)	62.01(8.62)	61.94(10.21)
Gender	54m/16f	25m/6f
Disease Duration (years)	6.51(4.64)	-
UPDRS III on	14.46(7.03)	-
UPDRS III off	29.84(12.18)	-
Symptom onset (side)	33l/37r	-

MRI acquisition

Whole-brain anatomical T1-weighted and diffusion-weighted images were acquired for each subject with a Siemens 3T Trio scanner (Erlangen, Germany). T1-weighted images were obtained using a 12-channel array head coil with the following parameters: (MDEFT3D: repetition time (TR) = 1930 ms, inversion time (TI) = 650 ms, echo time (TE) = 5.8 ms, 128 sagittal slices, voxel size = 1 x 1 x 1.25 mm3, flip angle (FA) = 18°). dMRI images were obtained via a spin-echo echo planar imaging (EPI) sequence with a 32-channel array head coil (spin-echo EPI: TR = 11200 ms, TE = 87ms, 90 axial slices, voxel size = 1.7 mm isotropic, 60 directions isotropically distributed (b-value = 1000 s/mm2). Distortions due to eddy currents and head motion were corrected using FSL (Version 5.0; www.fmrib.ox.ac.uk/fsl) (Jenkinson, Beckmann, Behrens, Woolrich, & Smith, 2012). Additionally, to provide an anatomical reference for motion correction, seven images without diffusion weighting (b0 images) were acquired at the beginning and after each block per ten diffusion-weighted images. The diffusion-weighted images were then registered to these b0 images (see (Feis et al., 2015) for more details regarding the data acquisition).

Registration

MRI

All registration steps were conducted using both linear and nonlinear functions with FLIRT and FNIRT (as implemented in FSL version 5.0). All registrations were performed on skull stripped and brain extracted images. T1 weighted images were first linearly registered to the MNI152 T1 1mm brain template with a correlation ratio and 12 DOF and an additional nonlinear transform using the FNIRT function with standard settings. Individual T1-weighted scans in native space were registered to the respective no-diffusion (b0) images with a mutual information cost function and 6 DOF. A standardized midline exclusion mask in MNI152 space was registered to each subjects b0 images through multiple transforms, by combining the transformation matrices outputted via previous registrations. The midline exclusion mask was visually checked and realigned with an additional registration if necessary.

Each step during the registration process was visually assessed for misalignments by comparing several landmarks (ventricles, pons, corpus callosum, cortical surface).

Cortical Atlases

The six cortical areas were obtained from http://www.rbmars.dds.nl/CBPatlases.htm, created with tractography methods, based on both human and non-human primate neuroanatomy (Neubert, Mars, Sallet, & Rushworth, 2015; Neubert, Mars, Thomas, Sallet, & Rushworth, 2014; Sallet et al., 2013). The separate cortical masks were extracted from MNI152 1mm space. The cortical atlases were thresholded at 25% to minimize the occurrence of overestimating the region during registration procedures, which were achieved with a nonlinear transform from MNI152 1mm to individual b0 space using the previously generated transformation matrices from the anatomical registrations, with a nearest-neighbor interpolation and 12 DOF (see figure 1).

STN Atlases

Group specific PD and elderly probabilistic atlases of the STN were obtained for the respective groups from (Alkemade et al., 2017) (Figure 2) (see https://www.nitrc.org/projects/atag_pd/ for probabilistic atlases and ATAG data) and were transformed from MNI152 1mm space to individual b0 space using a nonlinear transform and thresholded by 25%. The non-zero voxel volume in mm3 for each atlas was as follows: PD left = 77; PD right = 70.13; HC left = 164.75; HC right = 138.38 and for the center of gravity (CoG) in MNI152 1mm space: PD left x = -10.44, y = -13.04, z = -8.16; PD right x = 11.84, y = -13.18, z = -8.9; HC left x = -10.56, y = -13.87, z = -7.10; HC right x = 12.10, y = -12.97, z = -6.20.

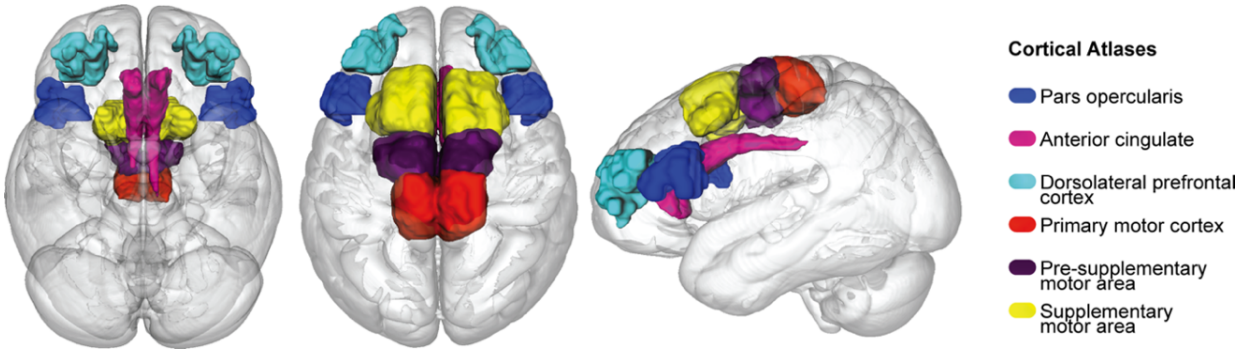

Figure 1: Cortical atlases used for probabilistic tractography and the diffusion tensor models in MNI152 1mm space, which consist of the pars opercularis (POp), anterior cingulate cortex (ACC), dorsolateral prefrontal cortex (DLPFC), the primary motor cortex (M1), pre-supplementary motor area (pre-SMA) and supplementary motor area (SMA).

Figure 2: STN atlases Representation of the group-specific (left and right) subthalamic nucleus (STN) atlas in MNI152 1mm space where the Parkinson's disease (PD) STN is in purple, and the healthy control (HC) is in orange.

Probabilistic Tractography

Probabilistic tractography was run between a priori defined cortical areas and group-specific STN's. Diffusion image preprocessing and analyses were achieved using FSL 5.0. The two most likely diffusion directions per voxel were estimated using the bedpostX function as implemented in the FDT toolbox with standard settings (Behrens, Berg, Jbabdi, Rushworth, & Woolrich, 2007). Subsequently, probabilistic tractography (probtrackX) was conducted to

calculate continuous structural connections between the respective seed and target region(s). ProbrackX was run with standard settings (curvature threshold 0.2, 5000 samples, 0.5mm step length, 2000 steps) in each subjects' native diffusion space, separately for left and right hemispheres and aided by the inclusion of a midline exclusion mask. The term tract strength is used here to index a probability density function, quantifying the ratio of how many streamlines directly and continuously commence from a seed region and terminate at a target area and vice versa (i.e., seed to target/target to seed). This density function is a commonly used measure for inferring the strength of structural white matter tracts (Behrens et al., 2007; Khalsa, Mayhew, Chechlacz, Bagary, & Bagshaw, 2014; van den Bos, Rodriguez, Schweitzer, & McClure, 2014). For more robust measurements, we created an average of each pair of seed-to-target and target-to-seed streamlines (Boekel, Forstmann, & Keuken, 2017; Forstmann et al., 2012). To control for spurious tracking, the tracts were thresholded by 10, whereby any voxel containing less than 10 direct samples were excluded from further analyses (Forstmann et al., 2012).

We calculated the axial diffusivity (AD), fractional anisotropy (FA), and mean diffusivity (MD) of the seed-to-target and target-to-seed paths derived from the tract strength probability density function approach mentioned in the above section. This was achieved by fitting a voxel-wise diffusion tensor model with a weighted least squares regression to each subjects' diffusion image using the DTIFIT function from FDT. Each FDT path was thresholded so that only paths with at least 75 samples were included for further analysis to yield a conservative anatomical representation. Then each pair of corresponding paths were combined (seed-to-target and target-to-seed), binarized, and averaged per hemisphere. From these normalized FDT paths, we extracted the AD, FA, and MD values per tract, per subject.

Statistical Methods

All statistical analyses were conducted within a Bayesian framework (see table i in the Introduction) using the BayesFactor toolbox (Morey & Wagenmakers, 2014) in R (R Development Core Team, 2011), interpreted in light of the assumptions proposed by (Jeffreys, 1961) and adapted by (Wetzels et al., 2011). To test whether there were any group

differences in either tract strength or DTI derived metrics (Woolrich et al., 2009), we used Bayesian ANOVAs. In this case, structure and tract strength or DTI metric are assessed for main effects and interactions, against the null. This results in four models, assessing for 1. Main effects of structure; 2. Main effects of group; 3. Main effects of both structure and group; and 4. An interaction between structure and group. Both subject and hemisphere were added as random factors, accounting for unequal sample sizes. BFs larger than 100, indexing decisive evidence for the alternative hypothesis, are noted as >100. All analyses included default prior scales (maximum likelihood) and r-scale prior probabilities.

To test whether disease progression correlated with either tract strength or the DTI derived metrics, we conducted Bayesian correlation analyses in JASP (JASP Team, 2019). Disease progression and medication response were used as separate indices of disease severity (Braak et al., 2006; Perlmutter, 2009). All Bayesian tests used a non-informative prior.

Open science

All scripts used to analyze the data can be found at https://osf.io/4uxxs/. There are ethical restrictions on sharing the de-identified dataset, as imposed by the ethical committee; Ethics Review Board of the University Clinics of Cologne (approval number 12-268). Moreover, multiple clinics were involved in the data acquisition, which at the time had different liability for the data protection. However, the data may be shared for purpose of reproducing the reported results if directly requested from the representative of the data protection officer of the Max Planck Society at the Max Planck Institute of Metabolism Research: Dr. Stefan Vollmar, vollmar@sf.mpg.de. However, to provide full disclosure, Dr. Vollmar will directly contact Marc Tittgemeyer as the project leader of the institute with regards to the informed consent of the participants.

Results

Group differences between HC and PD

Demographics

Two samples Bayesian t-tests were conducted to assess for differences in age and gender across groups. For age, the BF_{10} of 0.23 indicates moderate evidence in favor of the null hypothesis as does a BF_{10} of 0.24 for gender. Therefore, we can assume that there is no difference in gender or age between groups, and these variables are not included as covariates for further analyses.

Motion Parameters

Additional Bayesian t-tests were conducted to test for differences across groups in each of the directional (x, y, z) translation and rotation parameters, which index how much the subject moves during the MRI. All results were in favor of the null hypothesis (rotation x: $BF_{10} = 0.51$, rotation y: $BF_{10} = 0.33$, $BF_{10} = 0.25$, translation x: $BF_{10} = 0.40$, translation y: $BF_{10} = 0.34$, translation z: $BF_{10} = 0.49$). Accordingly, motion parameters are not included as a covariate in further analyses.

Tract Strengths

We first set out to test whether there were differences in tract strength between healthy control subjects and PD patients with an ANOVA, incorporating subject and hemisphere as random factors (see figure 3 and table 2) and run with 50,000 iterations. When using group-specific atlases of the STN, all models provide decisive evidence for the alternative, against the null (all $BF_{10} = > 100$, $\pm < 1.45\%$). The largest model included a main effect of group and structure, which is 197 times more likely than the model including an interaction. Therefore, we can assume that while tract strengths vary across structure and group, they do not vary within structure across PD and HC, therefore no within-group comparisons were conducted.

Table 2. Tract strength descriptive statistics per tract, per group.

Tract	HC	PD
ACC	0.28 (0.19)	0.21 (0.17)
DLPFC	0.25 (0.18)	0.20 (0.17)
M1	0.50 (0.14)	0.43 (0.16)
Pre-SMA	0.66 (0.08)	0.56 (0.16)
SMA	0.65 (0.09)	0.58 (0.15)
POp	0.44 (0.22)	0.34 (0.21)

The means and standard deviations (S.D) of tract strengths for tracts running between the subthalamic nucleus (STN) and the pars opercularis (POp), anterior cingulate cortex (ACC), dorsolateral prefrontal cortex (DLPFC), the primary motor cortex (M1), pre-supplementary motor area (pre-SMA) and supplementary motor area (SMA), for Parkinson's disease subjects (PD) and healthy controls (HC). (*Mean, (SD)*)

DTI metrics

To test whether there were group differences in the white matter composition, we extracted the AD, FA, and MD values of the six different tracts. Separate ANOVAs were run to assess AD, FA, and MD across groups (table 3), also with 50,000 iterations. For AD, the models including a main effect of structure, structure and group, as well as an interaction all provide decisive evidence for the alternative, against the null (all BF_{10} = > 100, ± < 1.4%). The winning model, including a main effect of only structure was twice as likely as the second winning model, which included main effects of both structure and group and decisively more likely by a BF_{10} of 283 than the model including an interaction. The model containing a main effect of only group provides anecdotal evidence for the null (BF_{10} = 0.36, ± 1.12%). Therefore, we can assume that while AD varies across structure and group, it does not vary within structure across PD and HC, therefore no within-group comparisons were conducted.

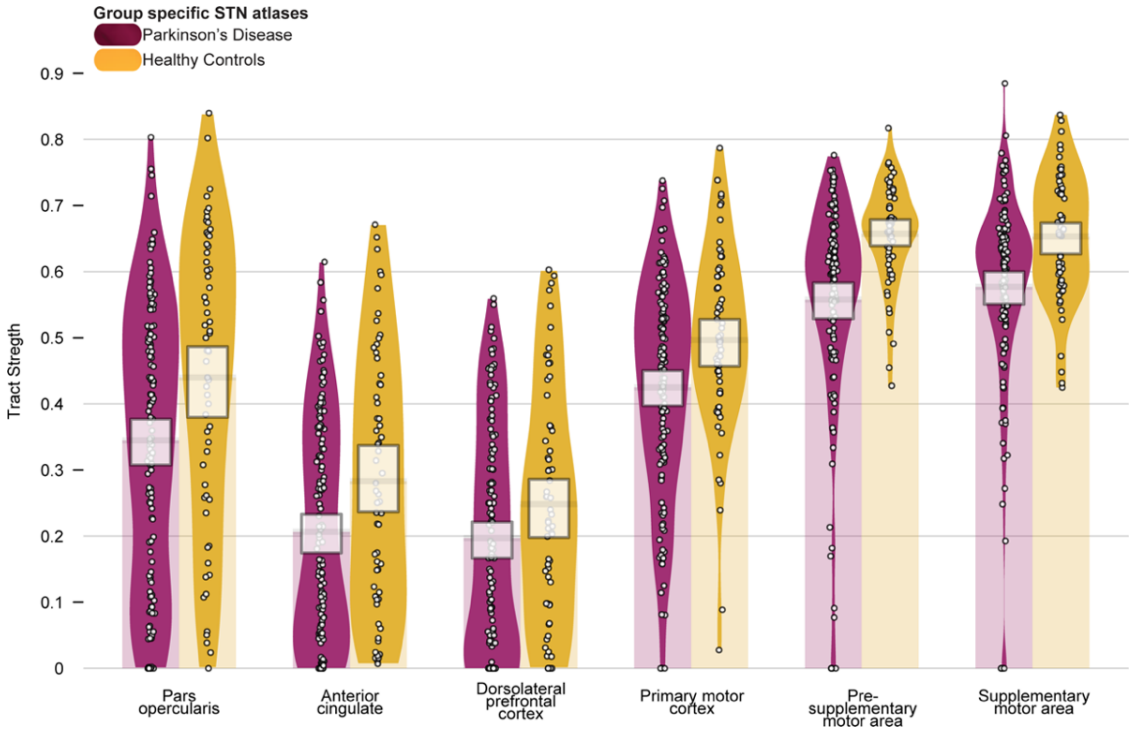

Figure 3: Tract strengths collapsed across hemisphere per structure (pars opercularis (POp), anterior cingulate cortex (ACC), dorsolateral prefrontal cortex (DLPFC), the primary motor cortex (M1), pre-supplementary motor area (pre-SMA), and supplementary motor area (SMA)), with healthy control (HC) subjects in orange and Parkinson's disease patients (PD) in purple. Tracts are measured from 0 to 1, which is representative of the ratio of the total number of tracts reported between the STN and the given cortical structure (and vice versa). Each point within each element represents a single subject. The width of each element represents the smoothed density. The columns overlapping each bar (each beginning at zero) represent the central tendency, and the bands overlapping each element reflect the 95% highest-density intervals and indicate that the tract strengths for PD are lower than healthy controls across all structures.

MD models showed the same trend as the AD, whereby a main effect of structure, structure and group, as well as an interaction all provide decisive evidence for the alternative, against the null (all BF_{10} = > 100, ± < 2%) and the model containing a main effect of only group provides moderate evidence for the null (BF_{10} = 0.14, ± 1.37%). The winning model, including a main effect of only structure is five times more likely (moderate evidence) than the second winning model, which included main effects of both structure and group. Moreover, the main effect of structure is decisively more likely than the interaction by a BF_{10} of 167.

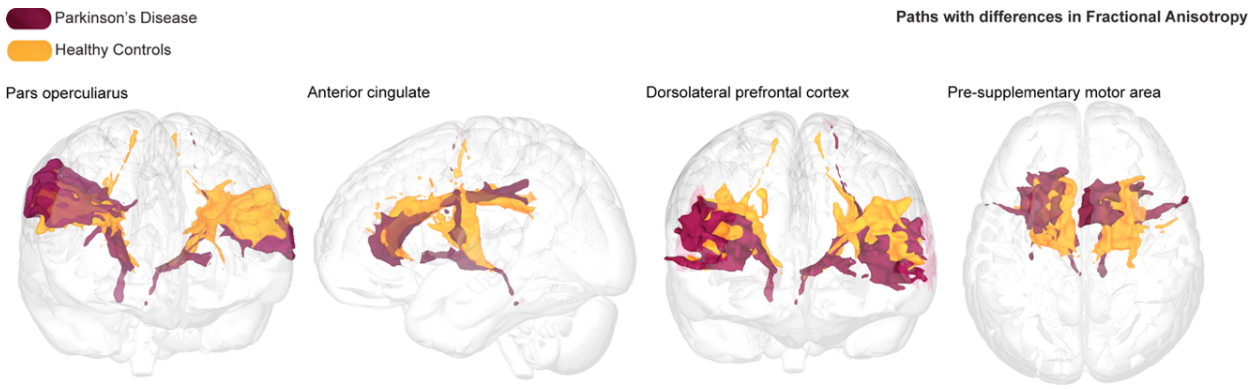

Figure 4: Averaged and thresholded fractional anisotropy (FA) tracts per group running between the subthalamic nucleus (STN) to the pars opercularis (POp), anterior cingulate cortex (ACC), dorsolateral prefrontal cortex (DLPFC), and pre-supplementary motor area (pre-SMA), with Parkinson's disease (PD) tracts in purple and healthy control (HC) tracts in orange. In all tracts, the FA was lower for PD compared to healthy controls.

When assessing FA, all models provide decisive evidence for the alternative, against the null (all BF_{10} = > 100, ± < 2.9%). The winning model includes the interaction term, and is four times more likely than the second winning model which includes a main effect of structure group, and is decisively more likely than the model including only a main effect of structure by a BF_{10} of 833. Post-hoc Bayesian t-tests were run to assess for differences between group per structure. Here we find strong evidence for differences between groups for FA values between STN and POp by a BF_{10} of 18.53, substantial evidence was found for FA values differing across groups between the STN and the ACC (BF_{10} = 3.05), and decisive evidence was found for the DLPFC (BF_{10} = 5.31e+10) and pre-SMA (BF_{10} = 68.31) connectivity profiles, all with higher FA values for HC than PD patients (Figure 4). Anecdotal evidence was found for higher FA for the SMA connectivity profiles in HC than PD (BF_{10} = 2.35).

Table 3: Mean and standard deviations (S.D) for DTI metrics

Tract	AD		FA		MD	
	HC	**PD**	**HC**	**PD**	**HC**	**PD**
ACC	1.1e-03 (5.1e-05)	1.2e-03 (4.5e-05)	**0.40 (0.02)**	**0.39 (0.03)**	8.2e-04 (5.0e-05)	8.1e-04 (5.0e-05)
DLPFC	1.2e-03 (4.7e-05)	1.2e-03 (5.5e-05)	**0.37 (0.02)**	**0.34 (0.02)**	8.6e-04 (4.5e-05)	8.6e-04 (5.6e-05)
M1	1.3e-03 (7.7e-05)	1.3e-03 (7.4e-05)	**0.42 (0.02)**	**0.41 (0.04)**	8.8e-04 (8.5e-05)	8.8e-04 (8.6e-05)
Pre-SMA	1.2e-0 (5.0e-05)	1.2e-0 (5.0e-05)	**0.40 (0.02)**	**0.39 (0.03)**	8.1e-04 (5.2e-05)	8.3e-04 (5.2e-05)
SMA	1.3e-03 (6.6e-05)	1.3e-03 (8.4e-05)	**0.39 (0.03)**	**0.38 (0.03)**	9.2e-04 (6.9e-05)	9.3e-04 (9.0e-05)
POp	1.3e-03 (6.6e-05)	1.2e-03 (6.1e-05)	**0.36 (0.02)**	**0.35 (0.02)**	9.3e-0 (6.3e-05)	9.4e-04 (5.6e-05)

Table 3. including axial diffusivity (AD), fractional anisotropy (FA) and mean diffusivity (MD) collapsed across hemisphere per structure (pars opercularis (POp), anterior cingulate cortex (ACC), dorsolateral prefrontal cortex (DLPFC), the primary motor cortex (M1), pre-supplementary motor area (pre-SMA) and supplementary motor area (SMA)) for healthy controls (HC) and Parkinson's disease patients (PD). FA values are marked in bold. There is evidence for group differences for the averaged FA values, which are lower in PD than HC. (*Mean, (SD)*)

Correlations

Bayesian paired correlations with a Pearson's Rho correlation coefficient was conducted to assess whether for each PD patient, disease progression or medication response correlated with either their tract strength or respective FA measures (Berry & Hochberg, 1999). Additionally, because the motor-related symptoms of PD often begin and continue to exhibit asymmetrically, the side in which symptom onset was first identified (i.e., left or right side of the body) was counterbalanced across hemisphere (Braak et al., 2006; Hilker et al., 2005; Sharott et al., 2014). Symptom onset initiating on the left side of the body was paired with

tract strength or FA values arising from the right hemisphere and vice versa for the left hemisphere (contralateral), and a separate correlation test was conducted for those tracts that occur in the hemisphere on the same side as symptom onset (ipsilateral). This was done to control for the lateralization effects of both symptom presentation and brain connectivity and to test whether tract strengths can act as an index of symptom severity.

For disease progression with tract strength, all results reported substantial evidence for no correlation between tract strengths and disease progression. For medication response with tract strength, all results reported anecdotal (ACC) or substantial (DLPFC, M1, pre-SMA, SMA, POp) evidence for no correlation between tract strengths and medication response. For disease progression with averaged FA, the only tract to show strong evidence of a correlation with disease progression was the DLPFC ipsilateral score ($r = 0.35$, $BF_{10} = 16.50$), where the side of symptom onset and hemisphere were the same. All other results reported either anecdotal or substantial evidence for no correlation between FA and disease progression. For medication response with averaged FA, all results reported substantial evidence for no correlation between FA and medication response. See the Supplementary Material below for the full results of the correlation analysis.

Discussion

The current study assessed the strength and microstructural changes occurring in predefined connectivity profiles between the STN and motor, limbic, and cognitive related cortical areas between PD patients and healthy elderly age-matched controls using group-specific atlases of the STN.

PD Disease-specific alterations

For all six cortical areas, the mean tract strengths were lower for the PD group, however, there was no statistical evidence to support substantial differences compared to healthy controls. Moreover, none of the tract strengths between the STN and the cortical areas correlated with measures of disease progression or medication response. It appears unlikely

that the strength of any of the measured tracts may be used as a biomarker for PD.

Diffusion tensor models were applied to draw quantitative measurements of each white matter tract. For the original analysis, we found evidence for a reduction in FA for the STN to POp, ACC, DLPFC, and pre-SMA tracts in PD patients compared to healthy controls. The POp is situated anterior to the premotor cortex and has been implicated in motor inhibition (Curley et al., 2018) which is referred to as the ability to suspend a premeditated motor response to a stimulus or an ongoing response (Aron, Robbins, & Poldrack, 2014). It has also been proposed that the POp is the origin of "stop signal" behaviors, whereby the inhibition of a motor response results from direct stimulation of the subthalamic nucleus (Chambers, Garavan, & Bellgrove, 2009). Moreover, the primary STN-ACC circuit functions to monitor behaviors that involve conflict and therefore task switching and changing decisions (Botvinik, 2007; Bryden et al., 2018; Schroeder, 2002). Structural and or functional alterations within the STN-POp and ACC connectivity profiles could reflect the symptomatic profile of PD (Kamagata et al., 2018; Theilmann et al., 2013).

Relatedly, associated functions of STN-pre-SMA circuit also include response inhibition (King et al., 2012), action choices (Boorman et al., 2007; Johansen-Berg, 2010; Neubert, Mars, Buch, Olivier, & Rushworth, 2010), task switching, and internally generated movements (Gowen & Miall, 2007; Nachev, Kennard, & Husain, 2008), which are shown to be disrupted in PD. Assuming structure both shapes and constrains function (Hagmann et al., 2010; Honey, Thivierge, & Sporns, 2010; Meuli et al., 2009), compromised white matter tracts indexed by increased diffusivity and reduced FA could result in abnormal functioning and lead to clinically overt behaviors (Tinaz, Lauro, Ghosh, Lungu, & Horovitz, 2017). Together, dysfunctional circuits between the POp, ACC and pre-SMA with the STN could result in parkinsonian symptoms including micrographia, dysarthria, bradykinesia, and hypokinesia, all of which involve a lack of appropriate action selection, timing, and irregular task switching (Artieda, Pastor, Lacruz, & Obeso, 1992; Frank, 2006; Wylie, Ridderinkhof, Bashore, & Van Den Wildenberg, 2010). A dysfunctional STN-DLPFC circuit could also reflect impaired motor control, PD-related cognitive decline, and affective complaints (Chaudhuri & Schapira, 2009; Forsaa et al., 2010; Santangelo et al., 2007). Furthermore, DLPFC dysfunction has been linked dopaminergic abnormalities that are also observed in

PD (Markett et al., 2017).

While reduced FA in specific STN-cortical circuits could be utilized as a biomarker for PD, it is difficult to infer the exact biological mechanisms underlying alterations in diffusion metrics relative to disease. FA has been considered as a summary measure of white matter integrity, that is highly sensitive to microstructural changes, but less sensitive to the type of change (Jones, Knösche, & Turner, 2013; Kim et al., 2013; Roberts, Anderson, & Husain, 2013; Ziegler et al., 2014), though theoretically, a reduction in FA could be driven by a singular or combination of altered AD, MD, or radial diffusivity.

Moreover, white matter consists not only of axons but oligodendrocytes, astrocytes, and microglia. Structural changes can affect any of these properties, each of which is associated with a different function (Rosenberg et al., 2011). Studies have shown that FA correlates with myelination which is associated with speed conduction, though this is dependent on the formation and remodeling of oligodendrocytes and differentiation of oligodendrocyte precursor cells (OCPs) whose function is to determine the production, length, and thickness of internodes and therefore also likely to contribute to the FA signal (Bechler, Swire, & ffrench-Constant, 2018; Johansen-Berg, Baptista, & Thomas, 2012; Sampaio-Baptista & Johansen-Berg, 2017; Swire & ffrench-Constant, 2018). Fewer studies have assessed diffusion parameters concerning astrocytes, though their contribution to FA signals is likely to be significant given their large occupying volume within both grey and white matter (Johansen-Berg et al., 2012; Walhovd, Johansen-Berg, & Káradóttir, 2014). Physiologically, a disruption or structural abnormality occurring anywhere along the axon, for example, due to changes in myelination, impaired astrocyte propagation, or suboptimal OCP proliferation and differentiation, would impede the rate of conduction and transmission between structures and consequently result in functional impairments (Fields, 2015).

Additionally, more widespread changes in myelin and internode plasticity can be driven by region-specific mechanisms (Auer, Vagionitis, & Czopka, 2018; Mitew et al., 2018). In the case of PD, local signals arising from dopaminergic cell loss with the substantia nigra, or the pathological hyperactivity of the STN could drive the observed structural changes in cortico-basal white matter connections. However, due to the complex timeline and microscopic spatial resolution of these neurochemical and anatomical changes, it is currently

not possible to identify which process corresponds with in-vivo human dMRI based FA measures.

Further, diffusivity has been correlated with partial voluming effects arising from free-water (Archer, Patten, & Coombes, 2017). Free-water reflects the presence of water molecules that are not restrained by cellular barriers and therefore do not show a preference for direction, which may be increased in the presence of cellular damage (Planetta et al., 2016). Thus, the presence of free-water may influence biases on diffusion metrics which can result in a changes in DTI metrics (Hoy, Koay, Kecskemeti, & Alexander, 2014; Metzler-Baddeley, O'Sullivan, Bells, Pasternak, & Jones, 2012). For instance, free-water present in diffusion has been shown to reflect FA changes occurring in other PD-affected areas such as the substantia nigra (Chung et al., 2017; Ofori et al., 2015).

Correlates of PD disease severity

Overall, we found no evidence for any correlation between either tract strengths or FA values with disease progression or medication response. With one exception, we found a positive correlation for FA values within the STN-DLPFC connectivity profile increasing with disease progression when the side of symptom onset was matched with hemisphere. An increased FA indicating restricted diffusion along a single direction is not necessarily compatible with explanations of neurodegenerative processes when assuming a higher FA implies increased myelination and axonal density which usually decreases with disease progression. It may be possible that the increased FA is explained by an attempted compensatory, neuroplasticity mechanism and or functional reorganization rather than a direct neurodegenerative process (Dayan & Browner, 2017; Mole et al., 2016), or a response to atypical dopaminergic modulation and levodopa intake (Akram et al., 2017; Herz et al., 2015; Ng et al., 2017). Such an adaptive reorganization of structural and functional pathways would, however, occur long before the onset of clinical symptoms, which is not in line with the rather progressed stage of the PD population within this study (Braak et al., 2006; Sharott et al., 2014). We, therefore, remain speculative as to the explanation of this result.

Considerations

The use of MRI poses several challenges when imaging small subcortical nuclei such as the STN (Forstmann, Isaacs, & Temel, 2017). In the current study, the resolution of the anatomical and diffusion sequences was rather large when considering the size of the STN (Isaacs, Forstmann, Temel, & Keuken, 2018). Imaging the STN is subject to partial voluming effects and blurring of the voxels near the borders of the nucleus, which may contain different tissue types and or fiber bundles of neighboring structures (Lorio et al., 2016; Plantinga et al., 2016). This is further complicated by probabilistic atlases being inherently larger than is often anatomically exact and require registration between a template and native space. Additionally, registration procedures that employ simple scaling factors that can fail to optimally incorporate morphometric and densitometric variability between individuals (Mazziotta, Toga, Evans, Fox, & Lancaster, 1995) which can, in turn, affect the accuracy of subsequent analysis. We account for this by using group-specific atlases, thresholding atlases, and incorporating both rigid and affine transformations during registration procedures**.** See the Supplementary Material below, which includes a number of additional analyses to investigate the effects of atlas accuracy. Manual segmentation of both the STN and cortical areas for all individuals would be the golden standard, however, the data in the current study did not allow for manual parcellation of the STN or structurally distinct cortical areas (de Hollander et al., 2014; Despotović, Goossens, & Philips, 2015). Relatedly, the visualization of the STN would benefit from the use of submillimeter resolution imaging with UHF-MRI and/or susceptibility-based contrasts (Keuken et al., 2017; Keuken, Isaacs, Trampel, van der Zwaag, & Forstmann, 2018).

We do not assess for gender differences. While sexual dimorphisms in PD have been reported (Farhadi et al., 2017; Miller & Cronin-Golomb, 2010; Smith & Dahodwala, 2014; Wylie et al., 2010), it remains controversial as to how sensitive standardized scores such as the UPDRS are at identifying gender differences (Augustine et al., 2015; Farhadi et al., 2017). In addition, we include a relatively small sample size with an unbalanced male to female ratio.

Finally, the measure of tract strength was taken via a probability density function (PDF), which despite being shown as a robust assessment, remains controversial.

Measurements indexing relative strength via dynamic causal models may offer additional information for instance by using previous tractography data to set priors for connection strengths between regions (Stephan, Tittgemeyer, Knösche, Moran, & Friston, 2009).

Conclusions and future directions

To conclude, the strength of white matter tracts within the hyperdirect pathway appears unaffected by the pathophysiology of PD. However, decreased FA values of the STN-POp, STN-ACC, STN-DLPFC, and STN-pre-SMA tracts may be used as a biomarker for disease, though the exact biological mechanisms driving these disease-specific alterations in FA remain elusive. The differences we find are in the connections to cortical areas involved in preparatory motor control, task monitoring, and decision making, rather than cortical areas governing direct motor output. Further, the results indicate that it is recommended to use an atlas that accounts for anatomical changes associated with PD rather than only age-matched controls. See the Supplementary Material for a control analysis to support the use of group-specific atlases. Future work should focus on the use of higher field strengths, alternative tractography methods, and harmonization of techniques used to investigate PD (Forstmann et al., 2017; Keuken et al., 2013). Until then, we show that using atlases that are specific to your population can aid analysis where UHF-MRI and or manual segmentations are not possible. Tractography methods hold great promise for their contribution to the identification of disease, differential diagnoses between subtypes of parkinsonian syndromes, and the application of DBS (Cochrane & Ebmeier, 2013; Seppi & Poewe, 2010). Such applications require the assessment of the biological foundations of diffusion metrics and neuroanatomical factors with specific subsets of disease scales used to evaluate presence and severity.

Supplementary Material 1: Control analysis

Rational and Method

Two additional sets of control analyses were conducted to assess whether any findings from the initial analyses were due to the use of age- and disease-specific atlases of the STN, which differ in both volume and location. For the first control analysis, the group-specific masks were interchanged, so that PD STN atlas was registered from standard MNI152 T1 1mm space to each healthy control subject, and the elderly subject STN atlas was registered from MNI to the individual space of each PD patient with a nonlinear transform. The first control analysis allows us to test whether the initial results are due to group differences in both volume and location of the probability atlas. For the second control analysis, a spherical region of interest was created in MNI space with a diameter of 9mm and resulted in a sphere volume of 383.88mm^3 (Figure A). The 9mm diameter corresponds to the average length of the healthy STN. The location of the sphere was based on the CoG of the group-specific probabilistic STN atlases. Subsequently, spheres were binarized and linearly registered to individual b0 space for each individual using the previously obtained transformation matrices.

Results

The statistical approach for the control analysis was conducted in the same manner as the initial analysis. For the first control analysis, the models including a main effect of structure, structure, and group, as well as an interaction all provide decisive evidence for the alternative, against the null (all $BF_{10} = > 100$, $\pm < 1.7\%$). Though the model containing a main effect of only group provides moderate evidence for the null ($BF_{10} = 0.13$, $\pm 1.12\%$). The winning model, including an interaction between group and structure, was 1325122 times more likely than the next largest model, with a main effect of structure, which according to the interpretation is decisive evidence for the superiority of the interaction over the main effect. See figure B and table A for descriptive statistics. Additional post-hoc Bayesian t-tests were conducted to assess which connectivity profiles were driving the structure by group interaction. Substantial evidence was found for increased tract strengths between the STN and the ACC for healthy control subjects with a BF_{10} of 3.76. Decisive evidence was found for increased tract strengths between the STN and M1 for PD patients with a BF_{10} of 253.67 and SMA with a BF_{10} of 18849.2. For the second control analysis, the results were in line with the initial analysis. The main effect of structure, main effects of structure and group, and the interaction all provide decisive evidence for the alternative, against the null (all $BF_{10} = > 100$, $\pm < 3\%$). The largest model included a main effect of both group and structure, which was 8 times more likely than the second-largest model that included a main effect of only structure, and 89 times more likely than the interaction. See figure C and table B for descriptive statistics.

Table A. Descriptive statistics per tract, per group, for the first control analysis which switches group-specific atlases (Mean, (SD)).

Tract	HC	PD
ACC	0.28 (0.18)	0.20 (0.17)
DLPFC	0.26 (0.17)	0.21 (0.16)
M1	0.38 (0.15)	0.48 (0.15)
Pre-SMA	0.59 (0.11)	0.60 (0.15)
SMA	0.54 (0.14)	0.67 (0.13)
POp	0.39 (0.18)	0.37 (0.22)

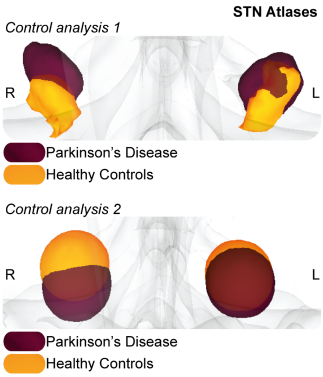

Figure A: Subthalamic nucleus (STN) atlas in MNI152 1mm space where the Parkinson's disease (PD) STN is in purple, and the healthy control (HC) in orange. The first control analysis is shown where the group-specific atlases were switched so that the PD STN was registered to each HC, and vice versa. The last image shows the second control analysis where spheres were derived from the group-specific center of gravity coordinates and expanded by 4.5mm.

Table B. Descriptive statistics per tract, per group, for the second control analysis which uses spherical ROIs as an atlas (Mean, (SD)).

Tract	HC	PD
ACC	0.26 (0.18)	0.19 (0.12)
DLPFC	0.23 (0.14)	0.18 (0.11)
M1	0.54 (0.14)	0.51 (0.15)
Pre-SMA	0.58 (0.11)	0.52 (0.16)
SMA	0.60 (0.11)	0.58 (0.15)
POp	0.41 (0.20)	0.36 (0.19)

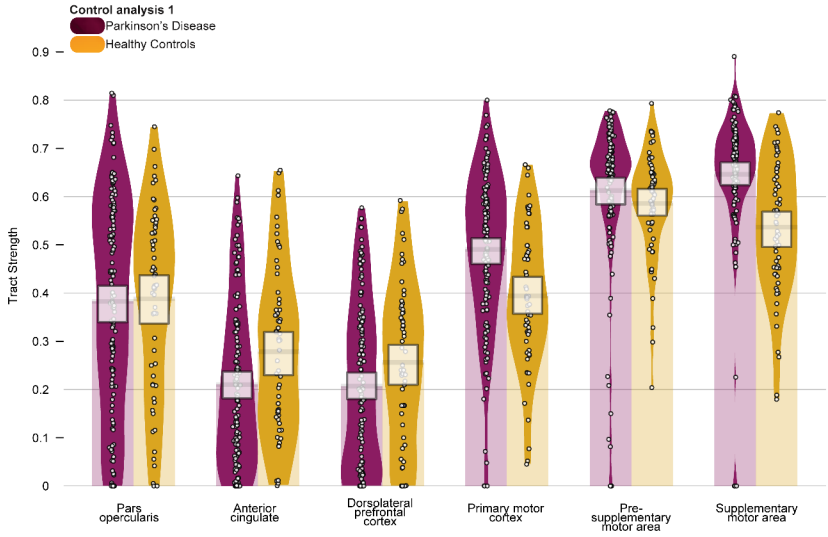

Figure B: Tract strengths for the first control analysis, collapsed across hemisphere per structure, with healthy control (HC) subjects in orange and Parkinson's disease (PD) patients in purple.

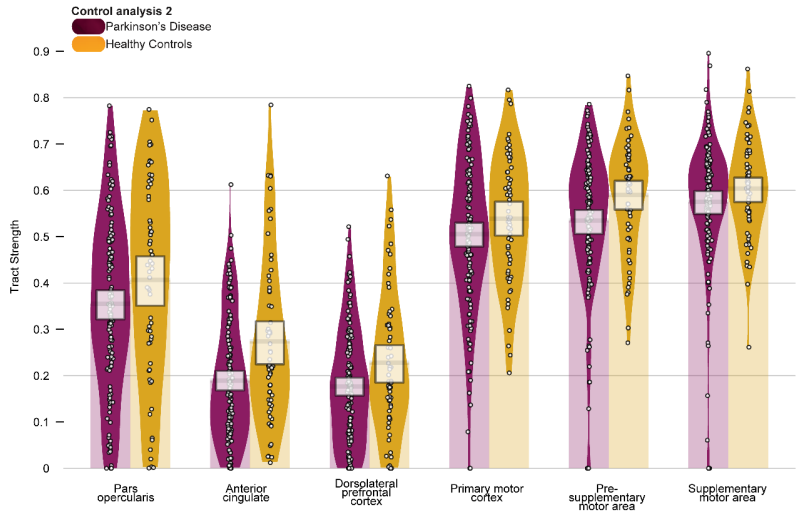

Figure C: Tract strengths for the second control analysis, collapsed across hemisphere per structure, with healthy control (HC) subjects in orange and Parkinson's disease (PD) patients in purple.

DTI Metrics

For the first control analysis for AD, the models including a main effect of structure, structure and group, as well as an interaction all provide decisive evidence for the alternative, against the null (all BF_{10} = > 100, ± < 2.5%). Though the model containing a main effect of only group provides anecdotal evidence for the alternative over the null (BF_{10} = 1.54, ± 2.6%). The winning model, including a main effect of both group and structure was 1.87 times more likely than the next largest model, with a main effect of structure, and 24.76 times more likely than the interaction, which provides anecdotal and strong evidence of the winning models' superiority respectively.

For the first control analysis for FA, the models including a main effect of structure, structure, and group, as well as an interaction all provide decisive evidence for the alternative, against the null (all BF_{10} = > 100, ± < 2.5%). Though the model containing a main effect of only group provides anecdotal evidence for the null (BF_{01} = 0.39, ± 3.3%). The winning model, including a main effect of structure was 1.71 times more likely than the next largest model, with a main effect of both group and structure, and 5.5 times more likely than the interaction, which provides anecdotal and moderate evidence of the winning models' superiority respectively.

For the first control analysis for MD, the models including a main effect of structure, structure, and group, as well as an interaction all provide decisive evidence for the alternative, against the null (all BF_{10} = > 100, ± < 3%). Though the model containing a main effect of only group provides anecdotal evidence for the alternative (BF_{10} = 1.58, ± 3%). The winning model, including a main effect of group and structure was twice as likely as the next largest model, with a main effect of only structure, and 18.13 times more likely than the interaction, which provides anecdotal and moderate evidence of the winning models' superiority respectively.

For the second control analysis for AD, the models including a main effect of structure, structure, and group, as well as an interaction all provide decisive evidence for the alternative, against the null (all BF_{10} = > 100, ± < 4.7%). Though the model containing a main effect of only group provides anecdotal evidence for the alternative over the null (BF_{10} = 1.47, ± 1.8%). The winning model, including a main effect of both group and structure was 1.79 times more likely than the next largest model, with a main effect of structure, and 23.12 times more likely than the interaction, which provides anecdotal and strong evidence of the winning models' superiority respectively.

For the second control analysis for FA, the models including a main effect of structure, structure, and group, as well as an interaction all provide decisive evidence for the alternative, against the null (all BF_{10} = > 100, ± < 2.5%). Though the model containing a main effect of only group provides anecdotal evidence for the null (BF_{01} = 0.44, ± 3.1%). The winning model, including a main effect of structure was 1.71 times more likely than the next largest model, with a main effect of both group and structure, and 5.6 times more likely than the interaction, which provides anecdotal and moderate evidence of the winning models' superiority respectively.

For the second control analysis for MD, the models including a main effect of structure, structure, and group, as well as an interaction all provide decisive evidence for the alternative, against the null (all BF_{10} = > 100, ± < 1.8%). Though the model containing a

main effect of only group provides moderate evidence for the null (BF_{01} = 0.25, ± 1.4%). The winning model, including a main effect of structure was three times as likely as the next largest model, with a main effect of both group and structure, and 327 times more likely than the interaction, which provides moderate and decisive evidence of the winning models' superiority respectively. See tables C and D.

Table C. Diffusion Tensor Imaging (DTI) descriptive statistics of axial diffusivity, fractional anisotropy and mean diffusivity per tract for the first control analysis (Mean, (SD)).

Tract	AD		FA		MD	
	HC	PD	HC	PD	HC	PD
ACC	1.2e-03 (5.3e-05)	1.2e-03 (4.4e-05)	0.38 (0.03)	0.40 (0.02)	8.43e-04 (5.46e-05)	8.2e-04 (5.2e-05)
DLPFC	1.2e-03 (5.0e-05)	1.2e-03 (5.3e-05)	0.33 (0.01)	0.35 (0.01)	8.73e-04 (4.97e-05)	8.5e-04 (5.4e-05)
M1	1.3e-03 (9.0e-05)	1.3e-03 (7.4e-05)	0.40 (0.04)	0.40 (0.04)	9.09e-04 (9.99e-05)	8.7e-04 (8.4e-05)
Pre-SMA	1.2e-03 (5.4e-05)	1.2e-03 (4.9e-05)	0.38 (0.01)	0.38 (0.03)	8.35e-04 (6.08e-05)	8.1e-04 (5.3e-05)
SMA	1.3e-03 (7.4e-05)	1.3e-03 (8.2e-05)	0.38 (0.03)	0.37 (0.02)	9.34e-04 (7.94e-05)	9.2e-04 (8.8e-05)
POp	1.3e-03 (7.4e-05)	1.1e-03 (5.8e-05)	0.33 (0.02)	0.36 (0.01)	9.64e-04 (7.08e-05)	9.3e-04 (5.5e-05)

Table D. Diffusion Tensor Imaging (DTI) descriptive statistics of axial diffusivity, fractional anisotropy, and mean diffusivity per tract, per group for the second control analysis (Mean, (SD)).

Tract	AD		FA		MD	
	HC	PD	HC	PD	HC	PD
ACC	1.1e-03 (4.4e-05)	1.2e-03 (4.0e-05)	0.43 (0.03)	0.42 (0.03)	8.2e-04 (5.0e-05)	8.1e-04 (4.6e-05)
DLPFC	1.1e-03 (4.2e-05)	1.2e-03 (4.9e-05)	0.39 (0.01)	0.38 (0.01)	8.4e-04 (4.0e-05)	8.4e-04 (4.7e-05)
M1	1.3e-03 (7.2e-05)	1.1e-03 (6.2e-05)	0.43 (0.00)	0.42 (0.02)	8.7e-04 (8.0e-05)	8.5e-04 (7.0e-05)
Pre-SMA	1.1e-03 (4.9e-05)	1.2e-03 (4.7e-05)	0.42 (0.23)	0.42 (0.01)	8.3e-04 (5.4e-05)	8.2e-04 (4.7e-05)
SMA	1.3e-03 (6.0e-05)	1.3e-03 (6.5e-05)	0.42 (0.03)	0.42 (0.03)	8.9e-04 (6.4e-05)	8.9e-04 (6.8e-05)
POp	1.3e-03 (5.8e-05)	1.1e-03 (5.1e-05)	0.39 (0.02)	0.39 (0.01)	9.0e-04 (5.6e-05)	9.0e-04 (4.6e-05)

Conclusions on the effect of STN atlas

To assess whether the use of separate probabilistic atlases for PD and HC produced more accurate results, we ran two sets of control analyses. For the first control analysis, interchanging the atlases across groups illustrated that failing to account for disease-specific changes influences the results. When using the HC probabilistic atlas in the PD group we find that the STN-M1 and SMA tract strengths increased for PD relative to controls. From a clinical perspective, the finding of increased connectivity in PD seems erroneous. While it is plausible that functional MRI (fMRI) studies may find increased connectivity between the STN and motor cortices in PD due to either pathological hyperactivity of the STN or some compensatory mechanism, previous DWI studies have reported a general decrease in cortico-basal connectivity for PD patients, though not specific to the STN.Therefore, our results are better explained by a false positive, whereby using a healthy STN atlas for probabilistic tractography in PD fails to account for the pathological shift of the STN and accordingly tracks from an incorrect location. Similarly, the second control analysis supports the use of group-specific atlases. Here, tracking from a sphere that accounts for location changes but not variations in shape and volume produces a similar trend as the original analyses though with less certainty, as indexed by the decrease in BF values. In sum, the results of both the first and second control analysis, show that the use of group-specific atlases is more accurate than using atlases that do not account for disease- and age-related structural alterations.

Supplementary Material 2: Correlation results

The second control analysis allows us to test whether the initial results are due to group differences in volume while taking the disease-specific changes in location into account. Bayesian paired correlations with a Pearson's Rho correlation coefficient (Table A) was conducted to assess whether for each PD patient, disease progression or medication response correlated with either their tract strength or respective FA measures. Below, contralateral is used to refer to the contralateral hemisphere to the side of symptom onset, and ipsilateral is used to refer to the ipsilateral hemisphere to the side of symptom onset.

Table A. Pearson's Rho Interpretation (Lambdin, 2012).

Coefficient, *r*		
Positive	**Negative**	**Size of correlation**
< 0	**< 0**	zero
0.1 to 0.3	**-0.1 to -0.3**	Small
0.3 to 0.5	**-0.3 to -0.5**	Medium
0.5 to 1.0	**-0.5 to 1.0**	Large

Disease progression with tract strength. All results reported substantial evidence for no correlation between tract strengths and disease progression (Table B)

Table B. Correlation between disease progression and tract strength.

Tract	**Contralateral**		**Ipsilateral**	
	Correlation	**BF_{10}**	**Correlation**	**BF_{10}**
ACC	- 0.06	0.18	- 0.03	0.16
DLPFC	- 0.21	0.15	- 0.04	0.17
M1	0.20	0.20	- 0.06	0.18
Pre-SMA	0.00	0.15	- 0.00	0.15
SMA	0.00	0.14	- 0.03	0.16
Pop	0.06	0.18	0.15	0.30

Medication response with tract strength All results reported anecdotal (ACC) or substantial (DLPFC, M1, pre-SMA, SMA, POp) evidence for no correlation between tract strengths and medication response (Table C).

Table C. Correlation between medication response and tract strength.

Tract	**Contralateral**		**Ipsilateral**	
	Correlation	**BF_{10}**	**Correlation**	**BF_{10}**
ACC	- 0.21	0.63	- 0.04	0.15
DLPFC	- 0.10	0.20	- 0.08	0.20
M1	- 0.13	0.30	0.11	0.22
Pre-SMA	0.11	0.21	0.14	0.31
SMA	0.04	0.16	0.05	0.17
POp	0.00	0.15	- 0.03	0.14

Disease progression with FA. The only averaged FA per tract to show strong evidence of a correlation with disease progression was the DLPFC ipsilateral score ($r = 0.35$, $BF_{10} = 16.50$). All other results reported either anecdotal or substantial evidence for no correlation between FA and disease progression (Table D).

Table D. Correlation between disease progression and fractional anisotropy.

Tract	Contralateral		Ipsilateral	
	Correlation	**BF**	**Correlation**	**BF**
ACC	0.13	0.28	0.20	0.71
DLPFC	0.20	0.61	0.35	16.50
M1	- 0.03	0.14	- 0.01	0.15
Pre-SMA	0.10	0.23	0.09	0.18
SMA	- 0.03	0.14	-0.00	0.15
POp	0.15	0.36	0.11	0.22

Medication response with FA. All results reported substantial evidence for no correlation between FA and medication response (Table E).

Table E. Correlation between medication response and fractional anisotropy.

Tract	Contralateral		Ipsilateral	
	Correlation	**BF**	**Correlation**	**BF**
ACC	0.13	0.25	0.02	0.14
DLPFC	0.10	0.21	0.02	0.14
M1	0.04	0.16	0.09	0.19
Pre-SMA	0.02	0.24	0.11	0.22
SMA	0.00	0.15	0.03	0.16
POp	0.06	0.17	- 0.03	0.16

Seven

3 versus 7 Tesla Magnetic Resonance Imaging for Parcellations of Subcortical Brain Structures in Clinical Settings

Introduction

The availability of 7 Tesla (T) Magnetic Resonance Imaging (MRI) scanners has rapidly increased in recent years (Forstmann, Isaacs, & Temel, 2017; Keuken, Isaacs, Trampel, van der Zwaag, & Forstmann, 2018; Ladd et al., 2018). The theoretical benefits of anatomical 7T MRI over lower field strengths can be attributed to the increased spatial resolution, contrast- and signal-to-noise ratios (CNR and SNR, respectively), which collectively result in higher quality imaging within feasible time frames (Kraff, Fischer, Nagel, Mönninghoff, & Ladd, 2014; Trattnig et al., 2018). Improved visibility of pathological alterations on 7T has been reported in the literature for brain tumors (Hoffmann et al., 2019), epilepsy (Bramerio et al., 2016), multiple sclerosis (Inglese, Fleysher, Oesingmann, & Petracca, 2018), stroke (Madai et al., 2012), and neurodegenerative diseases (McKiernan & O'Brien, 2017).

However, to what extent increased visibility afforded by 7T has the potential to improve clinical outcomes regarding invasive neuro interventions remains unknown. A promising clinical application of 7T MRI is the target visualization of structures for deep brain stimulation (DBS) surgery (Forstmann et al., 2017; Horn, 2019). DBS procedures target structures within the subcortex, which is comprised of a large number of small, iron, and calcium-rich nuclei that are located close to one another (Keuken et al., 2018). The main DBS targets for PD and dystonic disorders are the globus pallidus interna (GPi) and subthalamic nucleus (STN) (Kleiner-Fisman et al., 2006; Odekerken et al., 2016, 2013; Vidailhet et al., 2005). Identification of the STN benefits from the visualization of the substantia nigra (SN) border, which has also been targeted for epilepsy (Loddenkemper et al., 2008). Parcellation of the GPi benefits from visualizing the boundary with the external segment of the GP (GPe), and stimulation of the GPi has been shown to modulate functional connectivity in Huntington's disease patients (Ligot et al., 2011). Additionally, the red nucleus (RN) is often used as a landmark for the identification and orientation of the surrounding nuclei (Pollo et al., 2003).

Alterations in biometals such as iron in human tissue are commonly observed in pathological processes. The occurrence of dopaminergic neurodegeneration of the SN and iron accumulation in Parkinson's disease (PD) has been associated with disease-specific

structural alterations in shape, volume, and location (Aquino et al., 2009; Keuken et al., 2017; Zwirner et al., 2017). The neurophysical properties of both physiological and aberrant accumulation of biometals can be exploited to increase the visibility of structural boundaries with both ultra-high field (UHF) MRI and tailored post-processing techniques, such as quantitative susceptibility mapping (QSM) (Deistung et al., 2013; Schäfer et al., 2012; Schweser, Sommer, Deistung, & Reichenbach, 2012; Wang et al., 2017).

Conventional MRI can fail to capture the detailed local neuroanatomy due to weaker field strength, resulting in reduced spatial resolution, signal, and contrast. These limitations can be directly translated into a clinical setting with regards to the accuracy of MRI based targeting protocols for DBS implantations. DBS of the STN has been related to psychiatric, cognitive, and emotional disturbances (Temel, Blokland, Steinbusch, & Visser-Vandewalle, 2005). Moreover, a fraction of patients will fail to respond to stimulation and or maintain their parkinsonian symptoms and may require the removal or reimplantation of their DBS leads (Hariz et al., 2002; Temel et al., 2005). These failures to appropriately respond to neuro intervention can partially be attributed to the suboptimal placement of the DBS lead as a consequence of both inaccurate visualizations of the target and reliance on landmark identification (Low et al., 2019).

Additionally, DBS surgeries commonly incorporate intra-operative microelectrode recordings and behavioral testing in awake patients to confirm optimal lead placement (Hutchison et al., 1998; Limousin et al., 2002, 1995). This is a time-consuming procedure and distressing for the patient. The higher spatial accuracy than 7T MRI offers could contribute to more accurate surgical targeting and clinical efficacy. Higher precision planning could reduce the length of the surgery and the requirement for reimplantation and abolish the need for awake testing during surgery. Together, this would undoubtedly improve patient comfort (Forstmann et al., 2017; Lyons, Wilkinson, Overman, & Pahwa, 2004).

Clinical MRI often includes parallel imaging (PI) techniques to reduce acquisition time which is associated with an SNR penalty. This is warranted for both practical reasons, to improve image contrast, as well as clinical reasons, as patients with movement disorders cannot be scanned for extended periods. PI reconstructions result in spatially varying noise amplification and can result in both g-factor penalties or produce anatomically inaccurate and

distorted images (Keuken et al., 2018; Wiggins et al., 2009). Additionally, anisotropic voxel sizes are commonly employed to maintain a higher SNR in-plane and decrease acquisition time, but can result in partial voluming effects (PVE) which can also result in inaccurate imaging.

In our current study, we investigate the potential of 7T for improved targeting with a quantitative comparison of 3T with 7T MRI scans. We acquired two sets of 3T data; one representative of the resolution of clinical 3T (*c*3T) MRI typically used for DBS targeting, as well as an optimized set of 3T (*o*3T). Additionally, we obtained a set of 7T data from the same participants. We would like to clarify that we could not run the same optimized protocol at 3T and 7T. Running the 7T protocol at 3T would result in an unacceptably increased scan time at 3T which would preclude clinical implementation. Furthermore, the increase in specific-absorption-rates (SAR) escalating magnetization would result in local tissue heating, thereby posing a severe health risk to those scanned. Direct quantitative comparisons were drawn from both manual and semi-automated parcellations of the GPe, GPi, RN, SN, and STN. Given the iron-rich nature of these deep brain structures, we used QSM contrasts for parcellations (Alkemade et al., 2017). Additionally, a semi-automated parcellation approach was employed to parcellate the GP, RN, SN, and STN, to identify potential biases occurring with manual parcellations.

Methods

Participants

10 healthy participants (male = 2, female = 8, mean age = 25.9 y, S.D age = 5.8 y), healthy as assessed by self-report, were scanned at the Spinoza Centre for Neuroimaging in Amsterdam, The Netherlands, on a Philips 7T and 3T Achieva MRI system, with a 32-channel head array coil. The research was approved in writing by the LAB Ethics Review Board of the Faculty of Social and Behavioral Sciences, the local Ethical Committee of the Department of Psychology at the University of Amsterdam (ERB number 2016-DP-6897). All participants provided written informed consent before the scanning, and structural 7T

MRI data was included in the Amsterdam ultra-high field adult lifespan database (AHEAD) (Alkemade et al., 2020).

Data acquisition

c3 Tesla

Whole-brain T1-weighted images obtained with a 3D Turbo/Fast Field Echo (TFE) sequence with 1mm isotropic voxel sizes, field of view (FOV) = 240 x 188, 220 slices, echo time (TE) = 3.7 ms, repetition time (TR) = 8.2 ms, TFE factor = 142, TFE shots = 118, $SENSE_{PA}$ = 2.5, acquisition time (TA) = 04:42 min, obtained in the transverse plane. Whole-brain T2-weighted images obtained with a Turbo/Fast Spin Echo sequence (TSE) with 0.45 x 0.45 x 2mm voxel sizes, FOV = 230 x 182, 48 slices, TE = 80 ms. TR = 3000 ms, TSE factor = 15, TSE shots = 150, TA = 06:12 min, obtained in the transverse plane. Total acquisition time was 10:54 min.

o3 Tesla

Whole-brain T1-weighted images were obtained with a 3D Fast Field Echo (FFE) sequence with 1mm isotropic voxel sizes, FOV = 240 x 188, 220 slices, TE = 3.7 ms, TR = 8.2 ms, TFE factor = 142, TFE shots = 293, TA = 11:38 min in the transverse plane (no acceleration factor). Whole-brain T2-weighted images were acquired with 3D Fast Field Echo (FFE) sequence with voxel sizes 1mm isotropic, $TE_{1,-4}$ = 4.1 ms/ 9.8 ms / 13.85 ms / 19.55 ms / 23.60 ms, TR = 46 ms, echo spacing (ES) = 9.75 ms, FA = 20, FOV = 240 x 188, 140 slices, $SENSE_{PA}$ = 2, TA = 10:08 min. The main difference between the clinical and optimized 3T scans is the voxel size. Two separate scans were collected with *o*3T, with a total TA = 21:46 min. We would like to note that we were unable to match the *o*3T spatial resolution with that of the 7T due to specific absorption rate (SAR) limitations.

7 Tesla

For 7T, one scan incorporating both T1 and T2* contrasts was obtained using a MP2RAGEME (magnetization-prepared rapid gradient echo multi-echo) sequence (Caan et

al., 2018). The MP2RAGEME is an extension of the MP2RAGE sequence by (Marques et al., 2010) and consists of two rapid gradient echo ($GRE_{1,2}$) images that are acquired in sagittal plane after a 180° degrees inversion pulse and excitation pulses with inversion times $(TI)_{1,2}$ = 670 ms/ 3675.4 ms. A multi-echo readout was added to the second inversion at four TE_1 = 3ms, $TE_{2,1\text{-}4}$ = 3 ms / 11.5 ms / 19 ms / 28.5 ms. Other scan parameters include flip angles $FA_{1,2}$ = 4°/ 4°; $TR_{GRE1,2}$ = 6.2 ms / 31 ms; BW = 404.9 MHz; $TR_{MP2RAGE}$ = 6778 ms; $SENSE_{PA}$ = 2; FOV = 205 x 205 x 164 mm; acquired voxel size = 0.70 x 0.7 x 0.7 mm; acquisition matrix was 292 x 290; reconstructed voxel size = 0.64 x 0.64 x 0.7 mm; TFE = 150 resulting in 176 shots; TA = 19.53 min.

Image calculations

T2* maps for *o*3T and 7T MRI scans were created by least-squares fitting of the exponential signal decay over the multi-echo images of the second inversion. 7T T1-weighted images were generated by the complex ratio of the product of first and second inversion over the sum of their square (Marques et al., 2010).

A quantitative T1 map was also reconstructed from this T1-weighted image via a look-up table procedure (Marques et al., 2010). For QSM, the 3T data underwent more extensive clipping at the frontal and sinus regions as compared to the 7T MRI data. This was required since the algorithm is sensitive to non-local artifacts, which are more prominent in these regions on *o*3T MRI scans.

For QSM, phase maps were pre-processed using iHARPERELLA (integrated phase unwrapping and background phase removal using the Laplacian) of which the QSM images were computed using LSQR (Li, Avram, Wu, Xiao, & Liu, 2014; Li et al., 2015). Scans were reoriented and skull information was removed as described previously (Forstmann et al., 2014). The *c*3T MRI sequence did not allow the calculation of quantitative T2* maps or QSM images.

Parcellation methods

Manual parcellation

Inspection of the *c*3T scans revealed that despite the high in-plane resolution, which allowed the identification of the structures of interest in the axial plane, we were unable to create a biologically plausible 3-dimensional reconstruction of the structures of interest due to the anisotropic nature of the voxel sizes. We, therefore, decided not to pursue further analyses of the *c*3T MRI scans. Multi-echo data was not acquired, and therefore it was not possible to reconstruct QSM images for parcellations.

For *o*3T and 7T images, manual parcellations were performed in individual space using the QSM images for the GPe/i, RN, SN, and STN by two independent trained researchers. Given the level of familiarity of these raters with MRI data, we concluded that blinding for the scan sequence was impossible. T1-maps and/or T1-weighted images were used for additional anatomical orientation and identification of landmarks such as the ventricles, pons, and corpus callosum. T2*-maps were also used where appropriate. See Supplementary Information for the approach used for manual parcellations. Raters were blind to each other's parcellations, and inter-rater agreement was determined by the Dice correlation coefficient (see statistical methods).

Semi-automated parcellation: Multimodal Image Segmentation Tool (MIST)

Semi-automated parcellation was performed for the combined GPe/i, RN, SN, and STN with FSL's Multimodal Image Segmentation Tool (MIST) (Visser, Douaud, et al., 2016; Visser, Keuken, Forstmann, & Jenkinson, 2016). QSM-maps and T1-weighted images were used as input for MIST. MIST output parcellations were compared across field strength (*o*3T vs 7T), as well as across parcellation method (manual vs. semi-automated) to assess for potential biases in manual parcellations such as order or practice effects.

The *o*3T brain extracted T1-weighted and QSM maps were co-registered via a multi-step process, where first whole-brain T2*-maps were registered to the corresponding T1-weighted images using FLIRT (as implemented in FSL version 6.0.1) with 6 degrees of

freedom, nearest-neighbor interpolation, and mutual information cost function. This transformation was then applied to the QSM-maps, extrapolated from the fifth echo of the T2* sequence, also with 6 degrees of freedom, mutual information cost function, and instead a sinc interpolation. The same transforms were applied to the manual parcellations to allow for direct comparisons with MIST outputs. All registrations were visually inspected for misalignments by comparing the following landmarks: ventricles, pons, and corpus callosum. The 7T MP2RAGEME sequence allowed the calculation of all contrasts from a single sequence and thus in the same space, not requiring any registration steps. The MP2RAGE was used as the whole-brain anatomical reference image and the fourth echo of the second inversion was used for the T2* image. Resampling was achieved with Nibabel (version 2.3), with second-order spline interpolation, and constant mode parameter. Where appropriate, the header information was copied from the fourth echo of the second inversion to the MP2RAGE. Images were resampled as MIST only handles (near) isotropic voxel sizes. MIST was unable to perform parcellations in 0.7 mm isotropic voxels, which we attributed to the limited information provided by the prior derived from MNI-space for these small voxels. Images were therefore resampled to 0.8 mm which resolved the problem.

Dice coefficients

Dice coefficients were assessed to determine interrater reliability (Dice, 1945). Dice scores were compared between *o*3T and 7T images to test the directed hypothesis that 7T images result in a higher inter-rater agreement as compared to *o*3T images. The Dice coefficient was calculated as follows

$$Dice\ coefficient\ = \frac{2 * |m_1 \cap m_2|}{|m_1| + |m_2|}$$

Where $|m_i|$ is the size of mask *i* and $|m_1 \cap m_2|$ is the size of the conjunct mask of mask 1 and 2. A conjunct mask of a set of masks M only includes voxels included by both raters (Dice, 1945).

Volume calculations

For manual parcellations, all volume calculations were performed using the conjunct volume of the individual raters, as described previously. For manual parcellations, Dice coefficients were calculated in the space in which the parcellations were performed (Alkemade et al., 2017; Keuken et al., 2013). Masks from the MIST output were compared with manually parcellated conjunction masks resampled to 0.8mm for the 7T data and the masks that were registered from T2* to T1 for the *o*3T MRI data.

Anatomical distance

The anatomical distance between the centers of gravity of the individual structures in the left and right hemisphere was assessed using the Euclidean Distance. This provided a measure for changes in the perceived location of the individual structures across field strengths. We expected that altered visibility of specific anatomical borders would be reflected in a bilateral shift in the center of gravity and as a result an altered anatomical distance. Distances were calculated as follows:

$$Euclidean\ Distance(l,r) = \sqrt{\sum_{i=1}^{n}(l_i - r_i)^2}$$

l and r correspond to the left and right hemispheres. The square root of the sum is obtained by adding the power of the left *x*, *y*, and *z* coordinates of the center of gravity of the individual structures l and r (Ledez, 2002).

Contrast to noise ratios

Contrast-to-noise ratios (CNRs) of the QSM images were calculated to assess differences in visibility of the anatomical structure under investigation. Intensities of non-zero voxels were

extracted using the *segmentation_statistics* implemented in Nighres (Huntenburg, Steele, & Bazin, 2018). The CNR was calculated as follows:

$$CNR = \frac{S_{I-}s_O}{\sigma_O}$$

S_I is the signal inside the mask, represented by the mean value of all the voxels in the conjunct mask. S_O is the signal outside the mask, calculated as the mean value of all voxels that directly border the outside of the disjunct mask (all voxels scored inside the mask of a single rater). σ_0 is the standard deviation of the set of QSM intensities in these voxels. This approach was adopted to ensure that voxels outside the mask were not part of the separate individual masks.

Statistical Methods

All statistical analyses were conducted within a Bayesian framework using the BayesFactor toolbox (Morey & Wagenmakers, 2014) in R (Team, 2015), interpreted in light of the assumptions proposed by (Jeffreys, 1961) and adapted by (Wetzels et al., 2011) (table i in the Introduction). We incorporated a within-subjects' approach, and for all analyses data was collapsed across hemisphere. Each test is performed independently of the others so we assume multiple comparisons are not a confounder in the present study (Berry & Hochberg, 1999; Evans & Wagenmakers, 2019).

Manual o3T v 7T

For manual parcellations, we hypothesized that Dice scores and CNRs are higher for 7T compared to *o*3T MRI scans, as assessed with one-tailed paired samples t-tests per structure. For each one-tailed test, two models were obtained. The first model (M_1) tested for a positive effect in support of our hypotheses, and a second model (M_2), tested for a negative effect in which 7T is either no different or is outperformed by the *o*3T MRI data. The preferred model, which was the model for which the strongest evidence was present, was then reported along

with the model comparisons. We had no hypotheses on the direction of potential changes in volumes or anatomical distances across field strengths and therefore conducted two-tailed paired samples t-tests. These analyses provided a single model testing for a difference either way, compared to the null hypothesis. Where appropriate, we calculated the reciprocal to determine the evidence supporting the null-hypothesis.

Manual v semi-automated

Similarly, when assessing manual and semi-automated parcellations within field strength (manual *o*3T v MIST 3T and manual 7T v MIST 7T), two-tailed paired samples t-tests were conducted for CNRs, volumes, and anatomical distances, which we did not expect to differ. The Dice score for the MIST output parcellations is comprised of a conjunction mask including only the voxels selected by both the MIST parcellation and the resampled manual conjunction mask. Therefore, Dice scores were not directly tested across parcellation methods.

Semi-automated o3T v 7T

*o*3T and 7T MIST parcellation Dice scores and CNRs were compared with a one-tailed paired samples t-test, under the assumption that both Dice scores and CNRs would be higher for 7T than for *o*3T, indicating that 7T is subject to fewer biases than *o*3T. Volumes and anatomical distances were again assessed with two-tailed paired samples t-tests.

Data sharing and accessibility statement

All anonymized data and analysis scripts are available from https://osf.io/4nrku/ under the terms of the Creative Commons Attribution License and comply with the rules of the General Data Protection Regulation (EU) 2016/679.

Results

The MR contrasts are illustrated in figure 1. QSM contrasts obtained from *o*3T and 7T sequences allowed for manual parcellation of the brain structures under investigation, resulting in biologically plausible 3D reconstructions (see figure 2 and 3). As previously mentioned, the *c*3T images provided excellent in-plane resolution, though did not reasonably allow for anatomically accurate reconstructions due to the anisotropic voxel sizes. Therefore, no formal analyses were pursued for the clinical scans. All results have been averaged across hemisphere, and presented with a margin of error of <0.1%. See table 1 for the results of the manual parcellations, and table 2(a,b) and figure 4 for MIST parcellations.

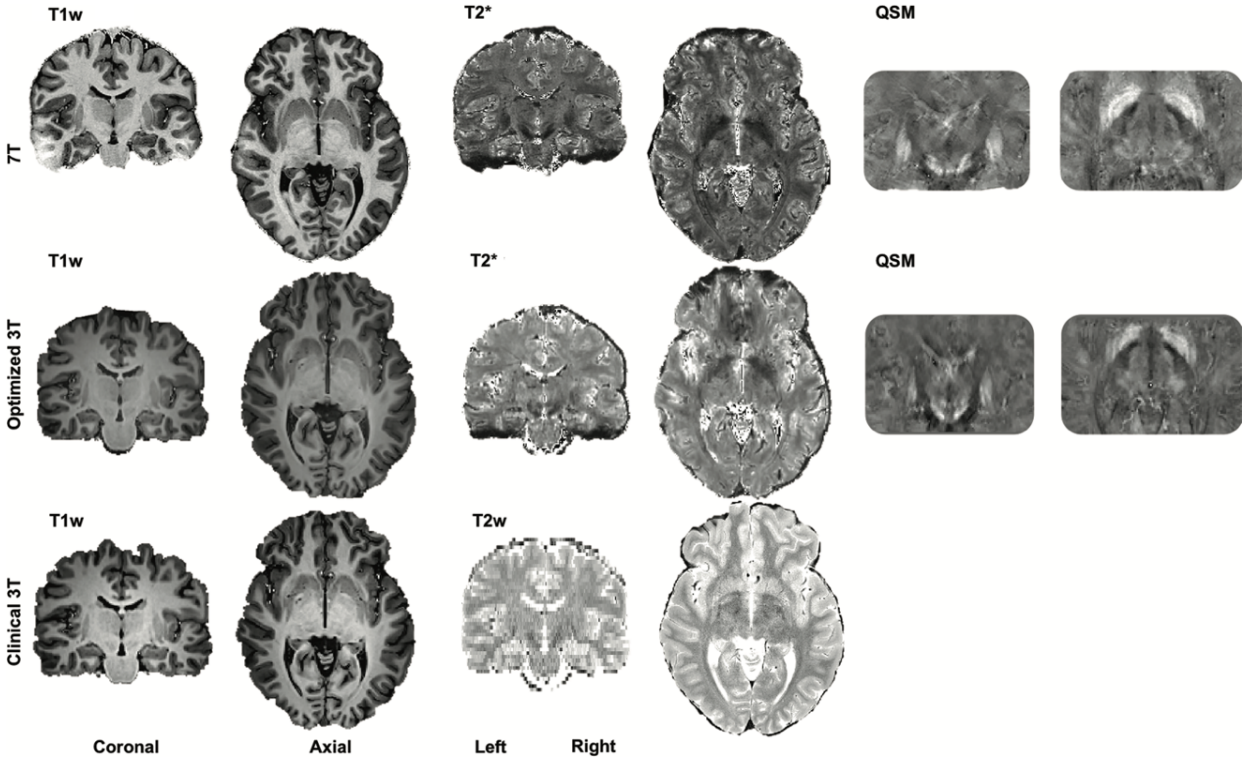

Figure 1: Contrasts. A single subject's 7T (T1-weighted, T2* map, and QSM images), optimized 3T (*o*3T) (T1-weighted, T2* map and QSM images) and clinical 3T (*c*3T) (T1- and T2*-weighted) in the coronal and axial planes. Brightness and contrast levels were chosen to best visualize the basal ganglia.

Manual parcellations: *o*3T v 7T

Dice Scores

Dice scores for the GPe (BF_{10} = 4.11), GPi (BF_{10} = 4.22) and RN (BF_{10} = 7.20) all reported substantial evidence in favor of 7T parcellations having a higher Dice than *o*3T. Additionally, these models were 33, 54, and 64 times (respectively) more likely than either no difference or *o*3T having a higher Dice than 7T (referred to in the following sections as the alternative). For the SN (BF_{10} = 1.06) and STN (BF_{01} = 1.85), only anecdotal evidence was found in favor of 7T over *o*3T, which were 7 and 13 times more likely than the alternative, respectively. All winning models noted here were at least moderately more likely than the second model.

Volumes

When assessing for differences in volumes across field strength per structure, we found consistent anecdotal evidence for no difference for the GPe (BF_{01} = 0.58), GPi (BF_{01} = 0.31), RN (BF_{01} = 0.47), SN (BF_{01} = 0.35) and STN (BF_{01} = 0.51). Substantial evidence was found for differences in volumes per rater for *o*3T parcellations for the RN (BF_{10} = 3.89), and SN (BF_{10} = 6.72), and at 7T, strong evidence was found for the SN (BF_{10} = 29.87). All other structures showed either anecdotal or no evidence for differences across raters. Surprisingly, the GPe, GPi, SN, and STN showed higher standard deviations at 7T than *o*3T. Additionally, Pearson's Rho correlation indicated that for *o*3T, Dice scores correlated with volumes for tor the GPe (*r* = 0.49), GPi (*r* = 0.76), RN (*r* = 0.45), SN (*r* = 0.14) and STN (*r* = 0.61), and at 7T for the GPe (*r* = 0.61), GPi (*r* = 0.86), RN (r = 0.41), SN (*r* = 0.80) and STN (*r* = 0.42). This is indicative of a bias where larger structures have a higher Dice score.

Anatomical Distance

When assessing for differences in distances across field strengths per structure, we found consistent evidence for no differences for the GPe (BF_{01} = 0.86, *anecdotal*), GPi (BF_{01} = 0.89, *anecdotal*), RN (BF_{01} = 0.32, *substantial*), SN (BF_{01} = 0.31, *substantial*), and STN (BF_{01} = 0.34, *anecdotal*).

QSM CNRs

When assessing for differences in QSM CNRs for manual parcellations across field strength per structure, we found very strong evidence for higher CNRs for the STN for 7T than *o*3T (BF_{10} = 61.75), which was 630 times, and decisively more likely than no difference, or higher CNRs at *o*3T. However, the RN (BF_{10} = 1.64) and SN (BF_{10} = 1.20) showed only anecdotal evidence for increased CNRs at 7T than 3T, which are 12 and 8 times more likely than no differences or higher CNRs at *o*3T, respectively. For the GPi (BF_{01} = 0.66) anecdotal and for the GPe (BF_{10} = 5.43), substantial evidence was found for increased CNR at *o*3T than 7T, which was 47 times more likely than higher CNRs at 7T.

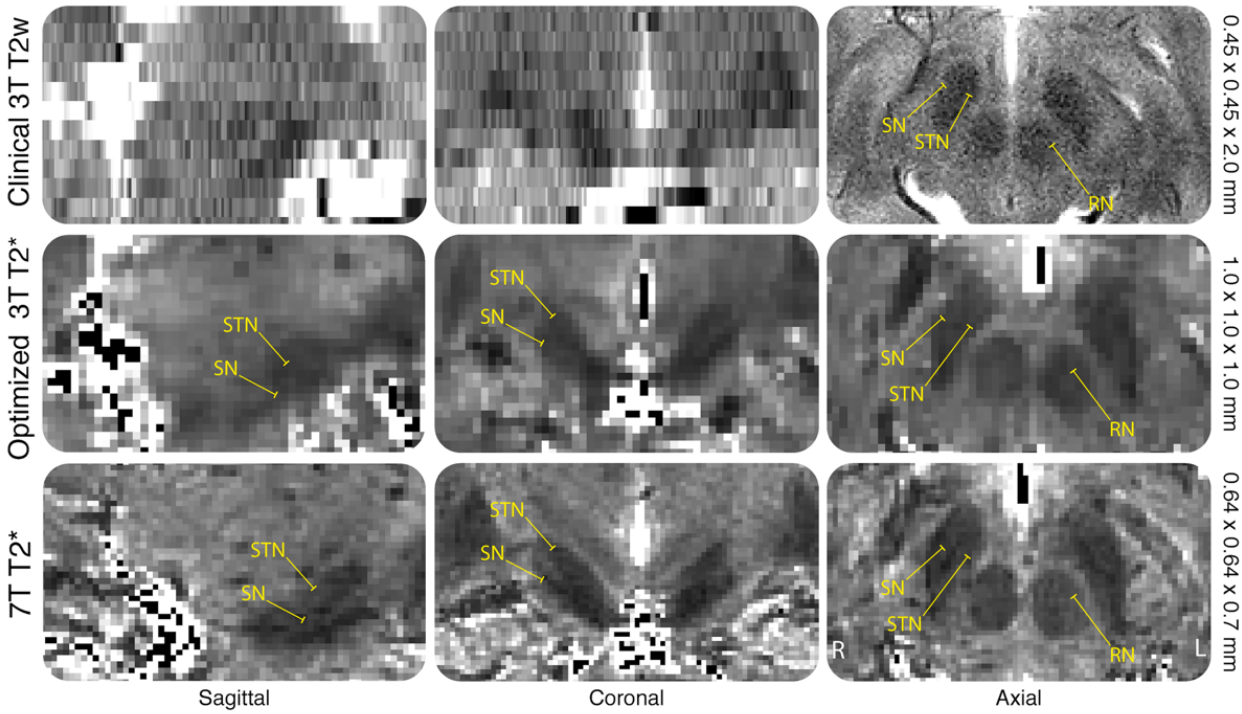

Figure 2: Voxel sizes. Example of a single subjects clinical 3T (*c*3T) T2 weighted, optimized 3T (*o*3T) and 7T T2* maps in the coronal, sagittal, and axial planes. Voxel sizes are indicated on the right side of the figure. The RN, SN, and STN are highlighted to exemplify the difficulty in identification of the nuclei in the coronal and sagittal planes for the *c*3T compared to the *o*3T and 7T due to the anisotropic voxel sizes, making 3D parcellations impossible. T2 weighted images and T2* maps are presented as they show the iron-rich RN, SN, and STN as hypointense structures. This was done since the *c*3T scan did not allow for QSM calculations, which would result in a hyperintense contrast of these brain nuclei.

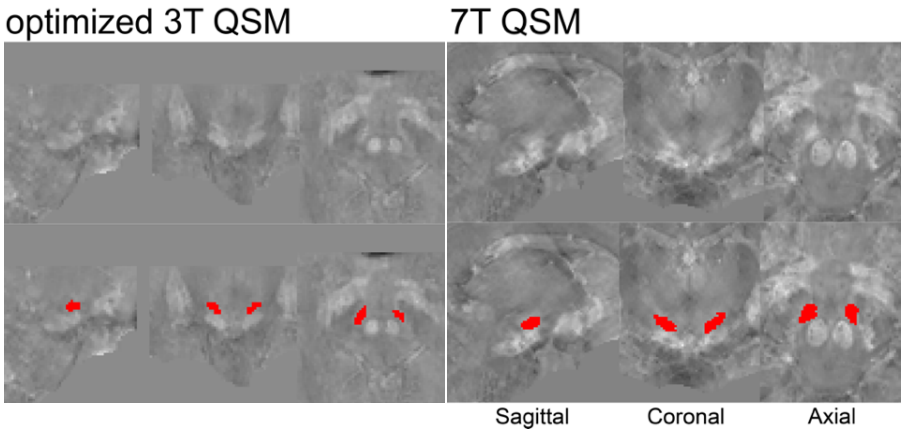

Figure 3: QSM of manual STN parcellations. Example of a single subject parcellation of the STN on QSM images. Unlabelled and parcellated images reflect the same anatomical level in native space.

Table 1: Comparison of manual parcellations across optimized 3T and 7T MRI

Structure	Dice scores One-tailed			Conjunct Volumes Two-tailed			Anatomical Distance Two-tailed			QSM CNRs One-tailed		
	o3T	***7T***	***BF***	***o3T***	***7T***	***BF***	***o3T***	***7T***	***BF***	***o3T***	***7T***	***BF***
GPe	0.77 (0.04)	0.81 (0.05)	M_1 **BF_{10}=4.11** (*Mc* **BF_{10}=34.26)**	1047 (127.46)	999.52 (136.57)	**BF_{01}=0.58**	37.35 (1.67)	36.72 (1.22)	**BF_{01}=0.86**	1.22 (0.16)	1.09 (0.14)	M_2 **BF_{10}=5.43** (*Mc* **BF_{10}=46.65)**
GPi	0.71 (0.06)	0.76 (0.05)	M_1 **BF_{10}=4.22** (*Mc* **BF_{10}=35.13)**	420.25 (85.71)	415.09 (95.59)	**BF_{01}=0.31**	31.35 (2.00)	31.95 (1.40)	**BF_{01}=0.89**	0.81 (0.16)	0.75 (0.15)	M_2 **BF_{01}=0.66** (*Mc* **BF_{10}=3.62)**
RN	0.80 (0.06)	0.85 (0.03)	M_1 **BF_{10}=7.20** (*Mc* **BF_{10}=63.73)**	233.40 (45.44)	227.44 (32.59)	**BF_{01}=0.47**	8.73 (0.41)	8.71 (0.43)	**BF_{01}=0.32**	1.92 (0.51)	2.05 (0.42)	M_1 **BF_{10}=1.64** (*Mc* **BF_{10}=11.76)**
SN	0.78 (0.07)	0.81 (0.03)	M_1 **BF_{10}=1.06** (*Mc* **BF_{10}=6.89**	434.45 (75.49)	401.39 (91.94)	**BF_{01}=0.35**	16.49 (0.83)	16.45 (0.48)	**BF_{01}=0.31**	1.62 (0.17)	1.78 (0.32)	M_1 **BF_{10}=1.20** (*Mc* **BF_{10}=7.87)**
STN	0.69 (0.06)	0.74 (0.06)	M_1 **BF_{10}= 1.85** (*Mc* **BF_{10}=13.59)**	88.90 (15.12)	87.35 (23.20)	**BF_{01}=0.51**	17.93 (1.34)	17.71 (1.47)	**BF_{01}=0.34**	1.04 (0.26)	1.33 (0.32)	M_1 **BF_{10}=61.75** (*Mc* **BF_{10}=629.61)**

Table 1: Dice scores, conjunct volumes, Anatomical distances, and QSM CNRs are averaged across hemisphere and presented as mean values and standard deviations for *o*3T and 7T MRI contrasts. BF_{10} indicates evidence for the alternative, and BF_{01} refers to evidence for the null hypothesis. Dice scores and QSM CNRs were compared using a Bayesian one-tailed paired samples t-test, where BF_{10} assumes that in both cases 7T is higher than *o*3T (model 1 (M_1)), and BF_{01} assumes either no difference or a decrease in 7T compared to *o*3T (model 2 (M_2)). For one-tailed paired samples t-tests, only the BF for the winning model is noted, and the likelihood ratio is calculated between the winning and losing models and is noted by 'Mc' (standing for model comparisons). Conjunct volumes and Anatomical distances were compared between 3T and 7T with two-tailed paired-samples t-tests. *o*3T = optimized 3T, QSM = quantitative susceptibility mapping, CNR = contrast to noise ratio, GPe = globus pallidus externa, GPi = globus pallidus interna, RN = red nucleus, SN = substantia nigra, STN = subthalamic nucleus.

MIST parcellations

Dice Scores

Dice scores were calculated per field strength, per structure with a one-tailed paired samples t-test for manual and semi-automated parcellations. For the GPe/i (BF_{10} = 631.44), we found decisive evidence that 7T Dice scores were higher than *o*3T, which was 22501 times more likely than no difference, or higher Dice scores at *o*3T (referred to as the alternative). For the RN (BF_{10} = 9.15), we found substantial evidence that 7T Dice scores were higher than *o*3T, which is 83 times more likely than the alternative. For the SN (BF_{01} = 0.61), we found anecdotal evidence for the alternative, with increased Dice scores at *o*3T than 7T which is 3 times more likely than the initial hypothesis that 7T Dice scores are higher than *o*3T. For the STN (BF_{10} = 1.04), only anecdotal evidence was found for higher Dice scores at 7T than *o*3T which was 7 times more likely than the alternative (see figure 4).

Volumes

Two-tailed paired samples t-tests were conducted to assess differences in the volume of manual parcellations compared to the MIST output parcellations per field strength. For *o*3T, resulting MIST parcellation volumes were smaller than those resulting from manual parcellations for GPe/i (BF_{10} = 456.18, *decisive*) and STN (BF_{10} = 11.96, *strong*). For *o*3T SN volumes larger for MIST than for manual parcellations (BF_{10} = 4.10, *substantial*). For the *o*3T RN (BF_{01}=0.14, *substantial*) we have evidence for no difference. For 7T, we found evidence for no difference between manual and MIST parcellations for the RN (BF_{01} = 0.33, *substantial*), SN (BF_{01} = 0.74, *anecdotal*), and STN (BF_{01} = 0.31, *substantial*). However, the GPe/i showed very strong evidence for increased volumes for manual parcellations than MIST (BF_{10} = 36.11). Next, the volumes of MIST parcellations were compared across *o*3T and 7T. Again, for the RN (BF_{01} = 0.33, *substantial*), SN (BF_{01} = 0.31, *substantial*), and STN (BF_{01} = 0.88, *anecdotal*), no differences in volumes were found. Finally, for the GPe/i, we found very strong evidence for increased volumes at 7T than *o*3T for MIST parcellations (BF_{10} = 69.08).

Anatomical Distances

Two-tailed paired samples t-tests were conducted to assess for differences in the anatomical distance of manual parcellations with the MIST output parcellations per field strength. For *o*3T, the GPe/i (BF_{01} = 0.43), RN (BF_{01} = 0.34), SN (BF_{01} = 0.40), and STN (BF_{01} = 0.51) all showed anecdotal evidence for no difference. For 7T, anecdotal evidence for no difference was found for the GPe/i (BF_{01} = 0.37), RN (0.37) and STN (0.60), and for the SN we found anecdotal evidence for an increase in distance for MIST parcellations compared to manual (BF_{10} = 1.33).

QSM CNRs

Two-tailed paired samples t-tests were conducted to assess differences in the CNR of manual parcellations with the MIST output parcellations per field strength. For *o*3T, the GPe/i (BF_{10} = 138.13, *decisive*) and the SN (BF_{10} = 3.58, *substantial*) showed evidence for increased CNRs with manual over MIST parcellations. The *o*3T RN (BF_{01} = 0.32, *substantial*) and STN (BF_{01} = 0.66, *anecdotal*) showed evidence for no difference in CNRs. For 7T, the GPe/i (BF_{10} = 1.42) showed anecdotal evidence for higher CNRs for manual parcellations than MIST, the RN (BF_{01} = 0.30) showed substantial evidence for no difference, and the SN (BF_{10} = 3.54, *substantial*) and STN (BF_{10} = 29.89, *strong*) evidence for increased CNRs for manual parcellations than MIST. Next, CNRs of MIST parcellations were compared across *o*3T and 7T. The GPe/i (BF_{01} = 0.70), RN (BF_{01} = 0.38) and STN (BF_{01} = 0.61) all showed anecdotal evidence for no difference in CNR across field strength. The SN (BF_{10} = 6.02) showed substantial evidence for increased CNR at *o*3T than 7T and was 51 times more likely than 7T CNRs being higher than *o*3T. Each winning model showed substantial evidence that it was more likely than the alternative.

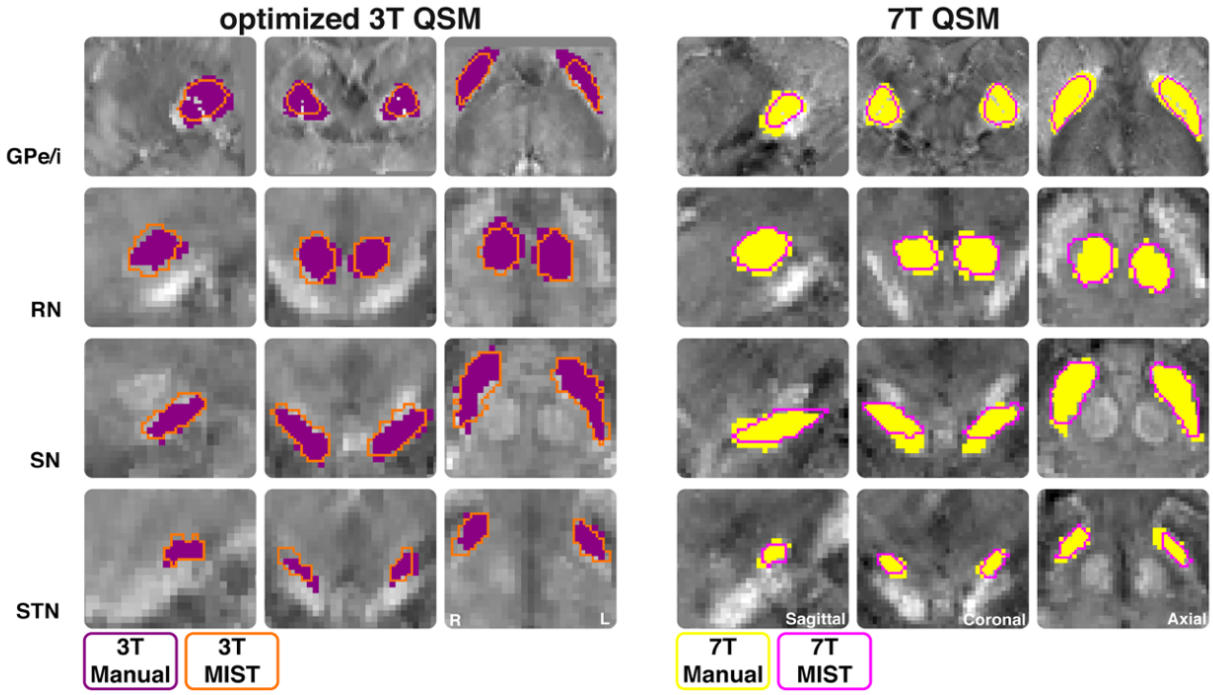

Figure 4: MIST Outline of masks for each structure manually parcellated on optimized 3T (*o*3T) (left) and 7T (right) from a single subject. Manual masks are shown in purple for *o*3T and yellow for 7T. MIST masks are shown as an orange outline for *o*3T and a pink outline for 7T; in the coronal, sagittal, and axial planes. QSM contrasts were used for parcellations. QSM=quantitative susceptibility mapping, GPe/i = combined globus pallidus externa and interna, RN = red nucleus, SN = substantia nigra, STN = subthalamic nucleus.

Table 2a: Comparison of manual and semi-automated within and across field strength (Dice scores and volumes)

	Dice Scores			Volumes						
	o3T*	***7T****	***3T v 7T MIST ** BF***	***o3T Manual***	***o3T MIST***	***o3T MIST v Manual BF***	***7T Manual***	***7T MIST***	***7T MIST v 7T Manual BF***	***o3T v 7T MIST BF***
GPe/i	0.74 (0.02)	0.82 (0.03)	***M*$_1$ BF$_{10}$=631.44 (*Mc* BF$_{10}$=22501**	1466.20 (161.59)	1171.91 (72.41)	**BF$_{10}$=456.18**	1467.49 (193.23)	1258.50 (80.45)	**BF$_{10}$=36.11**	**BF$_{10}$=69.08**
RN	0.81 (0.06)	0.85 (0.04)	***M*$_1$ BF$_{10}$=9.15 (*Mc* BF$_{10}$=82.93**	233.40 (45.45)	236.55 (54.65)	**BF$_{01}$=0.14**	236.26 (31.16)	239.77 (39.16)	**BF$_{01}$=0.33**	**BF$_{01}$=0.33**
SN	0.78 (0.02)	0.75 (0.12)	***M*$_2$ BF$_{01}$=0.61 (*Mc* BF$_{10}$=3.17)**	434.55 (475.36)	503.60 (101.65)	**BF$_{10}$=4.10**	445.47 (58.41)	497.64 (127.78)	**BF$_{01}$=0.74**	**BF$_{01}$=0.31**
STN	0.67 (0.08)	0.70 (0.07)	***M*$_1$ BF$_{10}$=1.04 (*Mc* BF$_{10}$=6.61**	88.95 (15.15)	75.25 (16.49)	**BF$_{10}$=11.96**	90.01 (15.69)	91.06 (24.15)	**BF$_{01}$=0.31**	**BF$_{01}$=0.88**

* overlap between manual and semi-automated parcellations, ** preferred model

Table 2b: Comparison of manual and semi-automated within and across field strength (Anatomical distance and QSM CNRs)

	Anatomical Distance Two-tailed							**QSM CNRs One-tailed**						
	o3T Manual	***o3T MIST***	***o3T MIST v Manual BF***	***7T Manual***	***7T MIST***	***7T MIST v Manual BF***	***o3T v 7T MIST BF***	***o3T Manual***	***o3T MIST***	***o3T MIST v Manual BF***	***7T Manual***	***7T MIST***	***7T MIST v Manual BF***	***o3T v 7T MIST*** [1] ***BF***
GPe/i	35.61 (1.70)	35.32 (1.38)	**BF_{01} = 0.43**	35.32 (1.16)	35.45 (1.32)	**BF_{01} = 0.37**	**BF_{01} = 0.42**	1.39 (0.17)	1.21 (0.13)	**BF_{10} = 138.13**	1.36 (0.17)	1.25 (0.20)	**BF_{10} = 1.42**	***M_1*** **BF_{01}= 0.70 (*Mc* BF_{10}=3.88)**
RN	8.73 (0.40)	8.67 (0.51)	**BF_{01} = 0.34**	8.77 (0.44)	8.91 (0.69)	**BF_{01} = 0.37**	**BF_{10} = 1.22**	1.89 (0.50)	1.86 (0.47)	**BF_{01} = 0.32**	1.89 (0.34)	1.89 (0.36)	**BF_{01} = 0.30**	***M_1*** **BF_{01}= 0.38 (*Mc* BF_{10}=1.48)**
SN	16.48 (0.82)	16.34 (0.74)	**BF_{01} = 0.40**	16.44 (0.45)	17.10 (1.27)	**BF_{10} = 1.33**	**BF_{10} = 2.03**	1.91 (0.18)	1.80 (0.15)	**BF_{10} = 3.58**	1.94 (0.26)	1.50 (0.35)	**BF_{10} = 3.54**	***M_1*** **BF_{10}= 6.02 (*Mc* BF_{10}=52.39)**
STN	17.93 (1.33)	17.55 (0.83)	**BF_{01} = 0.51**	17.72 (1.44)	17.98 (1.31)	**BF_{01} = 0.60**	**BF_{01} = 0.60**	1.05 (0.15)	1.11 (0.27)	**BF_{01} = 0.66**	1.36 (0.19)	1.19 (0.20)	**BF_{10} = 29.89**	***M_1*** **BF_{01}= 0.61 (*Mc* BF_{10}=3.17)**

[1] 7T MIST is the preferred model, Two-tailed paired samples t-tests were used for these comparisons

Table 2a and 2b: Dice scores, conjunct volumes, Anatomical distances, and QSM CNRs are averaged across hemispheres and presented as mean values and standard deviations for *o*3T and 7T MRI contrasts. BF10 indicates evidence for the alternative, and BF01 refers to evidence for the null hypothesis. Dice scores of the agreement between manual and MIST parcellations are compared across o3T and 7T with a one-tailed paired samples t-tests where BF10 assumes that 7T is higher than *o*3T (model 1 (M1)), and BF01 assumes no difference or a decrease in 7T compared to *o*3T (model 2 (M2)). The volume, Anatomical distance, and QSM CNRs are calculated for manual and MIST parcellations and are compared both within *o*3T and 7T, as well as across field strength for MIST parcellations only. Volumes and Anatomical distances are compared with a two-tailed paired samples t-test. CNRs are additionally compared with a one-tailed paired samples t-tests wherein each case the BF10 assumes that 7T CNRs are higher than *o*3T (model 1 (M1)), and BF01 assumes no difference or a decrease in 7T compared to *o*3T (model 2 (M2)). For one-tailed paired samples t-tests, only the BF for the winning model is noted, and the likelihood ratio is calculated between the winning and losing models and is noted by Mc = model comparisons). QSM = quantitative susceptibility mapping, CNR = contrast to noise ratio, GPe/i = combined globus pallid us externa and interna, RN = red nucleus, SN = substantia nigra, STN = subthalamic nucleus.

Discussion

We set out to investigate whether a clinically feasible 7T sequence can outperform optimized and clinically feasible 3T MRI protocols for the visualization of a selection of subcortical DBS and landmarks including the GPe, GPi, RN, SN, and STN. Our main findings can be summarized as follows: 1) clinical 3T MRI did not allow for accurate manual 3D parcellation of subcortical nuclei primarily due to anisotropic voxel sizes. 2) 7T outperformed the optimized 3T MRI protocol for manual parcellations for larger structures (GPe, GPi, and RN); 3) We found increased QSM CNR at 7T for the STN when manually parcellated; 4) When using MIST for semi-automatic parcellations, Dice scores did not indicate that 7T outperformed optimized 3T.

A stated, clinical MRI commonly employs anisotropic voxels to increase SNR along a single direction within a shorter timeframe (of around 4 minutes) (Knowles, Friedrich, Fischer, Paech, & Ladd, 2019; Polders, Leemans, Luijten, & Hoogduin, 2012; Springer et al., 2016). Voxels in other dimensions are elongated and inherently suffer from PVE (Mulder, Keuken, Bazin, Alkemade, & Forstmann, 2019; Ranjan et al., 2018). As a result, biologically plausible 3D renderings of small subcortical structures could not be obtained. Therefore, we did not attempt to parcellate or calculate Dice coefficients using the *c*3T protocol. We have included the scan parameters and qualitative target identifications to illustrate the variation in target visibility (Figure 2). It is conceivable that the resultant Dice coefficients would have revealed a high level of interrater agreement, as well as statistically significant differences. However, given the lack of anatomical relevance of these parcellations, we deemed such analyses erroneous.

For manual parcellations, we found varying evidence in support of higher inter-rater agreement at 7T compared to the *o*3T MRI, suggesting that larger nuclei, and to a lesser extent, smaller nuclei have higher visibility at increased field strengths. Additionally, the volumes were smaller for all structures at 7T, which could be explained by smaller voxels and increased SNR that collectively counter the effects of PVE observed with lower field strengths and larger voxel sizes (Mulder et al., 2019). If the changes in volume were the result of altered visibility of a specific anatomical border, this would likely result in a position shift

of the center of gravity. Since such a shift may be present in both hemispheres, we expected it to be reflected in a change in anatomical distance. However, it is possible that an equal but opposite effect in the other hemisphere could obscure shifts in the center of gravity.

CNR values were lower for 7T than *o*3T for the GPe/i. CNRs for the RN, SN, and STN were slightly higher at 7T than *o*3T, though did not result in a higher agreement between raters. This discrepancy may be explained by a raters bias with regards to prior information about size, shape, and surrounding anatomy (Despotović, Goossens, & Philips, 2015). Moreover, while QSM is a quantitative measure, a strict consensus on the susceptibility values of specific structures is still lacking (Fang, Bao, Li, van Zijl, & Chen, 2019). Additionally, smaller voxel sizes provide more precise information regarding the size and shape. However, in high resolution imaging, as the number of voxels required to define a structure increases, choice and uncertainty margins get larger, which may not actually improve the accuracy of manual parcellations. For example, the STN Dice scores showed only a minor increase at 7T compared to *o*3T, despite there being evidence for increased CNR at 7T. Notably, larger voxels tend to make labelling more reproducible, they are not necessarily more anatomically accurate.

For semi-automated parcellations, two sets of comparisons were computed. First, we set out to compare within field strength the differences between manual and MIST parcellations to assess for biases that may occur with manual parcellations. Second, we compared MIST parcellations across field strength, as we initially did for the manual parcellations, to determine whether semi-automated protocols benefit from 7T MRI. Of note, the *o*3T MRI data was pre-registered to a common 1mm isotropic space to allow for computations using MIST. Similarly, to maintain the high spatial resolution but ensure compatibility, the 7T images were downsampled to 0.8 mm isotropic. It is therefore possible that our results using MIST may have underestimated the effects resulting from the higher spatial resolution that can be achieved using 7T, though we are of course limited by available models. The largely absent CNR differences indicate that differences in spatial resolution can, at least in part, explain the differences observed using MIST. Downsampling of the 7T data may have led to an underestimation of the effect of the higher spatial resolution that was obtained from 7T scanning.

Volumes for the GPe/i were very different across the segmentation method. This inconsistency could be explained by the fact that manual raters parcellated the GPe and GPi separately, but were combined in MIST as a single structure. Moreover, the MIST prior for the GP includes the medial medullary lamina which we did not include in our manual parcellations. Dice scores were calculated for the manual and MIST parcellations per field strength and then compared across *o*3T and 7T. The RN and STN Dice scores were higher for 7T than *o*3T across the parcellation method. Interestingly the SN Dice scores were higher for *o*3T than 7T. *o*3T MIST parcellations had smaller volumes for the GPe/i, RN, and STN, and larger for the SN compared to manual parcellations. For 7T, MIST volumes were more consistent with manual parcellations. MIST parcellated volumes did not differ across field strength for the RN, SN, and STN, however, the GPe/i did, which suggests larger structures may be more accurately parcellated with 7T than *o*3T. Generally, CNRs were higher for manual than for MIST parcellations at *o*3T, apart from the STN which had a higher CNR for MIST. Similarly, for 7T all CNRs were higher or equal for manual parcellations than for MIST. We found no difference in CNRs across field strength for the MIST parcellations of the palladium, RN, and STN. Additionally, the MIST SN had higher a CNR for *o*3T than 7T. These findings suggest that overall, the semi-automated parcellation procedures that were applied do not appear to rely as heavily on CNR as manual parcellations and are therefore not subject to the same biases as manual parcellation. However, the SN and STN at *o*3T may be an exception. It may be that for smaller nuclei, semi-automated methods using lower field strengths or images with larger voxel sizes rely more on CNR for identification of structural boundaries, whereas higher field strengths or images with a submillimeter resolution instead rely on the spatial information.

Applications

It is important to consider the relevance of these findings in light of neurosurgical applications. Previous work has shown that while the visualization of the STN at 7T shows increased SNR, target localization is not necessarily improved (Bot et al., 2019; Hamel et al., 2017; van Laar et al., 2016). We cannot conclude whether this lack of improvement can be

attributed to the MRI imaging or is the result of other factors, including the variation between surgeons (Hamel et al., 2017). Our findings indicate that optimization of 3T MRI scans through the use of isotropic voxels and QSM do indeed allow for accurate visualization of the surgical target. We have provided an optimized 3T protocol including calculation of QSM maps that is within reach for clinical application without the need for the investment in new hardware (Milchenko et al., 2018; Wu et al., 2010).

Quantitative maps have a higher sensitivity to subtle global brain changes. We did not compare quantitative MRI to conventional weighted MRI images, and we, therefore, cannot conclude that quantitative MRI positively influences parcellation results. However, the theoretical benefits of removing bias, and the potential application of quantitative MRI as a biomarker argues for the calculation of quantitative MRI contrasts.

We have shown that an *o*3T scan can be obtained in a timeframe that is sensible within clinical practice and can account for age-related increases in the pathological iron deposition by using multiple and increasing echo times without superseding SAR limitations. This is a particularly important finding given the limitations of both *c*3T and 7T imaging, which include proneness to increased geometric distortions which reduce spatial accuracy and increase artifacts, B1 field inhomogeneity, power deposition, and altered specific absorption rates (Keuken et al., 2018; van Osch & Webb, 2014). In the MP2RAGEME, B0 inhomogeneities are automatically canceled through the use of a ratio image (Marques et al., 2010). Additionally, the subcortical parcellations presented in the current studies are largely dependent on grey matter contrasts, and we optimized contrast using flip angles of 4/4 instead of 7/6 degrees.

Considerations

The cohort tested in this study consists of young healthy participants, and it is well known that older participants and PD patients have increased iron content in basal structures (Wang et al., 2016). Since the effects on QSM increase with age and disease, we may underestimate the clinical relevance of these findings (Alkemade et al., 2017). Moreover, the *o*3T consists of two separate scans that would require registration in a clinical setting, whereas the 7T

acquisition includes a multi-contrast scan obtained within a single session. A multi-contrast scan at lower fields would have resulted in an increased scanning time, and therefore be arguably more difficult for scanning with patient populations, especially those with movement disorders. A direct comparison between the 3T and 7T data would require co-registration to the same space involving resampling of the data. We decided not to perform this analysis since the outcomes of such a comparison could differ substantially depending on the registration approach chosen.

Further, while 3T image quality could be more closely matched with 7T MRI, the resulting protocol would have limited use for clinical application. Specifically, increasing the signal and contrast would require more repetitions, resulting in longer acquisition times. This will increase SAR and the impact of motion artifacts, making the potential gains in SNR and CNR arbitrary, as the scan protocol cannot be deployed clinically. Contrarily, patient-related contraindications such as metal and or electronic implants, prostheses and foreign bodies, vascular or renal disorders, weight, and claustrophobia can limit the potential patient population able to undergo a 7T MRI (Ladd et al., 2018; Moser, Stahlberg, Ladd, & Trattnig, 2012; Van Der Kolk, Hendrikse, Zwanenburg, Visser, & Luijten, 2013). Thus, while our results indicate that 7T is to an extent superior to 3T, *o*3T could provide a more clinically viable option.

We would like to note that despite improved anatomical orientation, individual variation in the internal structure of the STN may continue to require awake testing of patients during surgery to obtain the desired clinical effect.

Conclusions

We set out to test whether 7T outperformed 3T MRI in the context of target visualization for DBS surgery. We conclude that in some instances, 7T outperforms 3T protocols. *c*3T protocols do not allow the rendering of biologically plausible 3D representations of small deep brain structures. *o*3T protocols using isotropic voxels strongly improved the imaging of the surgical area and we call for caution in the application of anisotropic voxels. The constraints posed by the clinical applicability of the imaging protocol contributed to

limitations including differences in voxel sizes, scan sequences, field homogeneity. The results presented should therefore be interpreted within the clinical framework, as they are not an account of the limits of 3T and 7T imaging within a research setting. Given the limited availability and compatibility restrictions in the patient population of 7T MRI systems for clinical application, our results have merit for more short-term improvement of clinical neuroimaging procedures for surgical purposes.

Acknowledgments
This research was supported by a Vidi and Vici grant from the Dutch Organization for Scientific Research (BUF), and an NWO-STW grant from the Dutch Organization for Scientific Research (BUF, MJM, AA)

Eight

Methodological Considerations for Neuroimaging in Deep Brain Stimulation of the Subthalamic Nucleus

Introduction

Longevity is increasing and consequently triggering a surge in age-related, multimorbid neurodegenerative diseases (Rossi et al., 2018; Van Oostrom et al., 2016). One of these diseases is Parkinson's disease (PD). PD is the second most common neurodegenerative disorder worldwide and typically occurs after 50 years of age (Sveinbjornsdottir, 2016). This is a multi-systems disease primarily characterized by symptoms that affect movement control, such as bradykinesia, tremor, rigidity, postural instability, and gait difficulties (Sveinbjornsdottir, 2016).

Drug treatments for PD are symptomatic in nature and function to replace the dopamine deficiency within the brain that occurs due to loss of nigrostriatal dopamine neurons (Evans & Lees, 2004; Lang & Obeso, 2004; Olanow, Obeso, & Stocchi, 2006). While dopaminergic medications relieve the motor-related symptoms of PD, they do not address non-motor symptoms, further complications, or disease progression (Lang & Obeso, 2004). Moreover, drug therapy in PD is associated with side effects that include but are not limited to nausea and vomiting, sleep disorders, hallucinations, and delusions. Furthermore, as the disease progresses, initially beneficial drug treatments become less effective in about 40% of patients. At this stage, the therapeutic window begins to narrow and the medication may wear off faster, resulting in the re-emergence or worsening of motor fluctuations (Ahlskog, 1999; Holloway et al., 2000). Chronic drug treatment and disease progression are also associated with levodopa-induced dyskinesias, which refer to involuntary, uncontrolled movements that occur when medications are most effective (Ahlskog, 1999; Ahlskog & Muenter, 2001; Holloway et al., 2000). Increasing the dosages in response to reduced durability of levodopa or dopamine agonists is not always feasible. Alternative treatments such as device-aided therapies may then be considered.

The next step for a subset of patients is neurosurgery intervention through deep brain stimulation (DBS) of the subthalamic nucleus (STN) (Benabid et al., 2009; Limousin et al., 2002, 1995; Odekerken et al., 2016). The STN is a small, glutamatergic, biconvex structure with a high iron content that is located within the subcortex (Alkemade et al., 2019; de Hollander et al., 2014). DBS involves the implantation of electrodes that emit persistent high-

frequency stimulation in this nucleus (Benabid et al., 2009; Limousin et al., 2002, 1995). The STN is a viable target for DBS as it modulates the output of both the indirect and hyper-direct cortico-basal pathways, whose functions are assumed to suppress undesirable motor behavior and inappropriate movements, respectively (Chiken & Nambu, 2016; Stefani et al., 2019). However, the exact mechanisms underlying DBS are still poorly understood, although the consensus is that DBS results in a functional normalization of pathologically overactive circuits (Bosco, LaVoie, Petsko, & Ringe, 2011; Petsko, 2012; Stefani et al., 2019).

While DBS may ameliorate between 60 to 90% of the motor-related symptoms of PD, it can produce neuropsychiatric side effects and emotional or associative disturbances, with side effects ranging from hypomania; apathy; hallucinations; and, as well as general changes in moral competency, personality and reckless behavior (Cyron, 2016; Deuschl et al., 2006; Obeso et al., 2001; Weaver et al., 2009). A fraction of patients will fail to exhibit a long-term clinical benefit in the reduction of parkinsonian symptoms (Forstmann, Isaacs, & Temel, 2017; Temel, Blokland, Steinbusch, & Visser-Vandewalle, 2005). Revisions or removals of the DBS system occur in between 15 and 34% of operated patients, 17% of which are attributed solely to electrode misplacement (Hartmann, Fliegen, Groiss, Wojtecki, & Schnitzler, 2019; Rolston, Englot, Starr, & Larson, 2016). Additional risks can arise from the surgery itself, with implantation posing a 15% risk of "minor and reversible problems", and a 2–3% risk of fatal or hemorrhagic events, infection, lead fracture, and dislocation (Fenoy & Simpson, 2014). Between 2013 and 2017, there were 711 bilateral DBS placement surgeries in The Netherlands, a subset of which were suffering from PD. Of those 711 surgeries, 169 patients required the DBS system to be either replaced or removed entirely ("DIS open data", 2019). These side effects and adverse outcomes can partially be attributed to the suboptimal placement of the DBS lead, which is dependent on the accuracy of the pre-operative planning procedures (Kloc, Kosutzka, Steno, & Valkovic, 2017; Nagy & Tolleson, 2016).

Using MRI to Target the STN in PD for DBS

As noted, the success of DBS treatment is partly determined by the accuracy of targeting the

STN. Further, targeting is dependent on stereotaxic precision, neuroimaging methods, and electrophysiological mappings (Tonge, Kocabicak, Ackermans, Kuijf, & Temel, 2016). Identification of the STN can be achieved in two ways: indirectly or directly. Indirect targeting refers to the identification of the DBS target via the application of reformatted anatomical atlases, formulae coordinates, and distances from anatomical landmarks. These standard targets can be applied to a patient's magnetic resonance imaging (MRI) or can be used as a coordinate for navigation with a stereotaxic reference system (see next paragraph). Additionally, intra-operative microelectrode recordings, macrostimulation, and intra-operative behavioral feedback are commonly used for verification with indirect targeting (Tonge et al., 2016; Tu et al., 2018). Direct targeting refers to visualization of the STN on patient-specific MRI images (Cho et al., 2010; Machado et al., 2006).

For indirect targeting, the most common landmarks are the mid-way point between the anterior and posterior commissure (AC and PC, respectively), which are visualized and marked on a T1-weighted (T1w) MRI, computer tomography (CT), or ventriculography (Landi, Grimaldi, Antonini, Parolin, & Zincone, 2003; Tu et al., 2018). The native brain is commonly realigned to the AC-PC with a Euclidean transform (Duchin et al., 2018; Rabie, Metman, & Slavin, 2016). This transform provides an augmented matrix with a 3D homogenous coordinate system, allowing for the application of formulae coordinates and distances. The standardized STN coordinates are defined as 12 mm lateral, 4 mm posterior, and 5 mm inferior to the mid commissural point (Starr, 2002). Some centers may utilize their own reference points, such as the top of the red nucleus (Andrade-Souza et al., 2005; Bejjani et al., 2000; Pallavaram et al., 2015).

Direct targeting with patient-specific MRI is generally preferred as the STN is known to shift with both age and disease, as well as vary in size, shape, and location across individuals (Ashkan et al., 2007; Isaacs et al., 2019; Kaya et al., 2019; Keuken et al., 2014; Xiao et al., 2014). Clinical MRI typically visualizes the STN using T2-weighted (T2w) images, which present the nucleus as a hypointense region relative to surrounding tissue. The optimal part of the STN is considered to be the ventral dorsolateral portion, also termed the somatosensory region, and is assumed to have direct connections with pre-motor cortical areas (Welter et al., 2014). As with indirect targeting, direct targeting also incorporates AC-

PC alignment, which provides the common reference system required for frame-based stereotaxic surgeries. Additionally, AC-PC alignment allows for comparisons between planned target location, actual target location, and post-operative verification. Therefore, clinical identification of the STN is usually achieved with a combination of both direct and indirect targeting methods.

The presence of extreme side effects and lack of clinical effect that can occur with DBS may arise from either direct or indirect targeting. One method for increasing the success and efficacy of DBS is to optimize pre-operative planning procedures via neuroimaging techniques. For instance, advanced MRI can be used to increase visualization and understanding of anatomy, connectivity, and functioning of the STN. This information can then be used to inform on optimal electrode placement on a patient-specific basis.

The goal of this paper is to explain the current procedures for structural target identification of the STN for DBS in PD using MRI. We identify limitations that may contribute to suboptimal identification of the STN and provide alternatives for optimizing MRI to visualize the STN. The organization of topics is as follows: field strength; current procedures for intra- and post-operative verification with microelectrode recordings; SAR limitations; shimming and magnetic field corrections; sequence types and contrasts; voxel sizes; motion correction; registration and image fusion; quantitative maps; complications unrelated to pre-operative planning; and conclusions. The suggestions are presented with the underlying expectation that more accurate visualization can translate into targeting and implantation with increased precision.

Field Strength

Pre-operative MRIs are obtained to both visualize the DBS target and to assess for potential comorbidity and identify venous architecture to ensure a safe entry route for surgery. The quality of MRI is dependent on a large number of factors. One of these factors is the signal-to-noise ratio (SNR), which is strongly influenced by field strength (Tesla or T for short) (see figure 2 in chapter 2 for an example) (Forstmann et al., 2017; McRobbie, Moore, Graves, & Prince, 2006; Rutt & Lee, 1996). SNR can be defined as the difference in signal intensity

arising from true anatomy compared to noise and random variation (Edelstein, Glover, Hardy, & Redington, 1986; Springer et al., 2016). Low-field MRIs such as 1.5 or 3T are routinely used for DBS targeting. Additionally, an ultra-high field (UHF) 7T MRI system has been approved for medical neuroimaging however at present these UHF systems are less available than lower field MRI (U.S. Food and Drug Administration, 2017). Compared to 7T, 1.5 and 3T MRI tend to suffer from both inherently lower SNR. Additionally, low field MRI suffers from comparatively low contrast-to-noise (CNR). CNR reflects the difference in SNR between different tissue types which is essential for specificity (de Zwart, Ledden, Kellman, van Gelderen, & Duyn, 2002; Pohmann, Speck, & Scheffler, 2015). High SNR and CNR are essential for imaging the STN as it is a very small structure located within a deep and dense portion of the basal ganglia, surrounded by structures containing similar chemical compositions. The difficulty of accurate STN identification is exemplified by inconsistencies in observed volumetric measures, size, and location estimates reported at low field strengths (Isaacs et al., 2019; Kaya et al., 2019; Keuken et al., 2014).

The quality of the magnetic field is also determined by magnetic field gradients. MRI gradients are characterized by the change in the magnetic field as a function of distance. The MRI gradient arises from gradient coils, which are a set of electromagnetic components within the scanner that are used to control the magnetic field (Turner, 1993; Winkler et al., 2018). Weaker gradients arising from lower magnetic fields cause g-factor penalties, whereby an inhomogeneous B1 field causes artificial signal differences and noise amplification in tissues further from the coil in the subcortex at 3T compared with 7T MRI (Hendriks, Luijten, Klomp, & Petridou, 2019; Setsompop et al., 2012). Relatedly, SNR is lower in subcortical structures relative to the cortex due to the larger distance between the center of the brain and receiver coil elements, and these differences are amplified at low field compared to UHF (de Hollander, Keuken, van der Zwaag, Forstmann, & Trampel, 2017; Forstmann, de Hollander, Van Maanen, Alkemade, & Keuken, 2016; Wiggins et al., 2009).

SNR scales supra-linearly with the static magnetic field, with up to a sixfold increase at 7T compared to 3T MRI (de Zwart et al., 2002; Pohmann et al., 2015). This means that UHF-MRI can provide better quality images at a higher spatial resolution, increased contrast, and shorter acquisition times (Duyn, 2012; Edelstein et al., 1986; van der Zwaag, Schäfer,

Marques, Turner, & Trampel, 2015). The reduced acquisition time is essential, as clinical radiologists are often under strict time pressures that are intrinsically linked to value-based healthcare systems and cost-effectiveness rather than scientific value (van Beek et al., 2019). Numerous empirical studies and reviews have noted the advantages of utilizing UHF-MRI in clinical settings, performing direct comparisons between low- and high-field strengths for visualizing finer details of smaller nuclei, which are common targets for DBS (Beisteiner et al., 2011; Cho et al., 2008, 2010; Duchin, Abosch, Yacoub, Sapiro, & Harel, 2012; Kraff, Fischer, Nagel, Mönninghoff, & Ladd, 2014; Plantinga et al., 2018; Springer et al., 2016).

Developments in array coil designs and parallel imaging techniques have resulted in the possibility to measure specific portions of tissue simultaneously. The simultaneous measurement increases SNR by a factor of 3 to 10 when compared to standard volume coils used at clinical field strengths, which are unable to selectively excite separate portions of tissue (Duyn, 2012; Wiggins et al., 2009). This is discussed in more detail later in the paper.

Importantly, there are caveats with regards to the implementation of UHF-MRI. The Siemens 7T MAGNETOM Terra is the only UHF-MR system to have obtained Food and Drug Administration (FDA) 510(k) clearance for clinical neuroradiology. Other applications of 7T MRI are therefore considered experimental. Expense and accessibility are among the most important and most time-limiting factors in implementing UHF-MRI into clinical settings; less than one hundred 7T systems exist worldwide, making up about 0.2% of all MRI systems (Forstmann et al., 2017; Ladd et al., 2018). Moreover, increased specific absorption rates (SAR), field inhomogeneities, local signal intensity variations, and signal dropout are factors that can reduce the benefits of 7T MRI when not properly accounted for (Truong, Chakeres, Beversdorf, Scharre, & Schmalbrock, 2006). These can be countered with optimized shimming and pre-processing techniques such as bias field correction. However, these techniques require expertise that is not typically available within clinical settings (Juchem, 2013; Mao, Smith, & Collins, 2006; Stockmann et al., 2016).

Current Procedures for Intra- and Post-Operative Verification with Microelectrode Recordings

Current standard practices within The Netherlands includes both pre-operative planning with neuroimaging methods and intra-operative verification with microelectrode recordings (MER). In this case, once the target has been decided, the DBS system will be implanted in two steps. First, the surgeon will create a burr hole in the skull on both hemispheres. If MER are used, the MER leads will be inserted into predefined coordinates. In 0.5 to 2 mm intervals from around 10 mm above the target coordinate, MER will start recording activity through macrostimulation. Multiple MERs may be placed into the STN at around 2 mm apart within the anterior, posterior, central, medial, and lateral portions. The MER lead that outputs consistent oscillations of beta bursts that are indicative of STN activity will be selected for test stimulation and subsequent implantation. If the patient is awake, additional intra-operative behavioral testing may be performed to assess the therapeutic effect of specific stimulation programs. Once the target has been verified via intra-operative neuroimaging (CT or ultra-low field MRI), the leads will be permanently implanted and then connected to a cortical grid and a stimulator will be inserted under the chest (Anderson & Lenz, 2006; Ashkan, Wallace, Bell, & Benabid, 2004; Aviles-Olmos et al., 2014; Gielen, 2003).

Not all centers use pre-operative CT or MRI and instead rely on standard coordinates with MER verification (and vice versa). Some reports suggest MER significantly improves DBS outcomes (Chen et al., 2006), and that MER fails to show any significant benefit compared to direct targeting (Patel, Heywood, O'Sullivan, Love, & Gill, 2002). Moreover, there remains a mismatch of around 20% in the planned target coordinate based on MRI, compared to the actual optimal location identified with MER when using 1.5 and 3T (Frequin et al., 2020; Lozano et al., 2019). Further, the use of intra-operative ultra-low field MRI for identification of the test leads during surgery has shown to be as effective as MER in improving post-operative motor symptoms (Ostrem et al., 2013). While not a strictly scientific issue, the application of MER more than doubles the cost of a bilateral STN surgery (McClelland, 2011). See (Habets, Isaacs, Vinke, & Kubben, 2019) for an extensive overview on comparisons between MER and MRI for STN identification in PD.

Lastly, post-operative management requires the identification of optimal stimulation parameters. These parameters can vary per patient, and some patients may require DBS in combination with medication. Microlesioning effects and acute foreign body reactions can impact the homeostasis of STN function and lead to a misinterpretation of DBS efficacy. Therefore the patient should ideally be assessed several times at different stages after the surgery (Tykocki, Nauman, Koziara, & Mandat, 2013). Baseline motor function is initially obtained after the total withdrawal of dopaminergic medication (Slotty, Wille, Kinfe, & Vesper, 2014). Axial motor symptoms such as bradykinesia, rigidity, stability, gait, posture, and dysarthria are assessed with rating scales such as the Unified Parkinson's Disease Rating Scale Part 3 (UPDRS, III) or the Movement Disorders Society (MDS)-UPDRS (Aviles-Olmos et al., 2014; Kleiner-Fisman et al., 2006). As the DBS lead consists of multiple contact points, each point is tested separately through monopolar stimulation, beginning with a standard frequency of 130 Hz and pulse width of 60 μs (Moro et al., 2002). Amplitudes are varied in a step-wise manner and the lowest amplitude that results in the highest suppression of clinical symptoms with the absence of sustained adverse effects will be chosen as the optimal stimulation parameters (Hartmann et al., 2019). More in-depth literature on practices for post-operative verification, stimulation programming, and care can be found in (Aubignat, Lefranc, Tir, & Krystkowiak, 2020; de Oliveira Godeiro, Moro, & Montgomery, 2020; Esselink & Kuijf, 2020) and the references therein.

SAR Limitations

SAR refers to the amount of energy deposited into the body due to the radio frequency (RF) pulses applied with MRI sequences. RF pulses are emitted via electrical currents through coils, being used to generate the B1 field (Mao et al., 2006). RF deposition can result in tissue heating, and to ensure that the absorbed energy does not induce local thermal damage, there are SAR limitations based on the region of interest, where the amount of SAR depending on tissue type (Food and Drug Administration, 1998; International Standard, 2002). Field inhomogeneities increase with field strength, as the RF wavelength scales according to the size of the object being imaged, which then reduces its ability to penetrate the brain with a

uniform power (Balchandani & Naidich, 2015; Vaughan et al., 2001). In the case of UHF-MRI, stronger gradients are required to magnetize tissues in the middle of the brain and to create a homogenous field, which results in higher SAR. Therefore, the safety limits are reached sooner at UHF than with a lower field. Moreover, SAR can vary from person to person due to individual differences in anatomy. This means that scan acquisition can require real-time parameter adaptation. Maintaining a low SAR can be achieved by increasing the repetition time (TR), reducing the flip angle (FA), or by reducing the number of acquired slices. Unfortunately, introducing these parameter changes to MR sequences can negatively affect the quality of the scan (Allison & Yanasak, 2015; Van Den Bergen, Van Den Berg, Bartels, & Lagendijk, 2007). This invites an ethical debate as to whether future FDA-approved sequences and image pre-processing methods at UHF would allow for such real-time deviations in a clinical protocol where SAR limitations are reached.

Further, there are more absolute and relative contraindications at UHF including pacemakers, surgical implants and prosthesis, and foreign bodies, even if they are not metallic or comprised of diamagnetic materials due to potential local heating and subsequent torque and increased SAR. Moreover, in our experience, many DBS candidates may not be scanned due to site-specific criteria. For instance, while a non-metallic or non-paramagnetic dental bridge is not listed as a contraindication, the guidelines for the 7T site at some locations required such patients to be excluded. Even more contraindications exist at 7T, including circulatory and clotting disorders, which makes UHF-MRI less compatible with a larger portion of the elderly population, including the majority of PD DBS patients (Ghadimi & Sapra, 2020). Therefore, optimizing 3T remains a viable option where UHF-MRI cannot be applied. However, while 3T may theoretically be optimized to allow for increased visualization of subcortical nuclei, it is essential to remember that acquisition times will be much longer than that of an analogous 7T sequence (Forstmann et al., 2017; Horn et al., 2017; Marques, Simonis, & Webb, 2019; Schmitz, Aschoff, Hoffmann, & Grön, 2006); this concept will be discussed throughout the paper.

Shimming and Magnetic Field Corrections

Shimming refers to the process of homogenizing either the main magnetic field (B0) or the radiofrequency field (B1). Inhomogeneity of the B0 field occurs when materials with different magnetic properties and susceptibility enter the bore, resulting in image distortion and signal loss. For example, the interface between brain tissue and air arising from the sinuses can cause artifacts within the frontal and temporal areas. These brain–air interface-induced artifacts can result in large shifts in the observed anatomical locations of nearby brain structures and cortical surfaces (Krupa & Bekiesińska-Figatowska, 2015). While post-processing techniques exist to correct some of these erroneous signals, they cannot control for complete signal loss and dropout. Therefore, the field needs to be shimmed before the acquisition of the main MRI scan.

Shimming the B0 field can occur passively by strategically placing ferromagnetic sheets within the bore itself to form the distribution of the magnetic field toward a more uniform state (Wachowicz, 2014) or by using patient-related inserts such as an intra-oral pyrolytic carbon plate (Wilson, Jenkinson, & Jezzard, 2002). This process is useful for removing field imperfections related to hardware, although is not generally utilized in clinical practice as it is laborious, inflexible, and temperature-dependent. More commonly, the field can be actively shimmed, which uses currents within the MRI system to generate corrective magnetic fields in areas showing inhomogeneous signals (Wachowicz, 2014).

Active shimming is limited by the ability to model and reproduce the distortions that occur within the field. Shimming is generally based on the principles of spherical harmonics (SH), which use orthonormal equations to index changes in signal waveforms representative of field inhomogeneity. The mapping and the correction for inhomogeneities are achieved by superimposing the magnetic field with an opposing corrective field equal to and a reversal of the polarity within a spatial distribution deemed erroneous by the SH coefficients (Golay, 1958; Roméo & Hoult, 1984).

The order of SH is dependent on the number of dedicated current-driven coils. Traditional clinical and low-field MR systems will employ lower-order shimming methods mainly due to cost and space restraints (Winkler et al., 2018). Low-order shims primarily

utilize linear terms including addition, scaling, and rotation of the SH coefficients to model the magnetic field. Linear SH coefficients function to resemble and compensate large-scale, shallow magnetic field components that can be corrected with a current offset applied with a standard gradient coil. This is typically achieved automatically with the use of a pre-scan B0 map. More local changes can be compensated for with dynamic shimming. However, this is most commonly used for multi-slice MR, which is prone to additional eddy current distortions and requires dedicated amplifier hardware. The optimal shim method will depend on the desired contrast and each sequence should require an additional shim (Bitar et al., 2006).

As field inhomogeneities increase with field strength, higher-order harmonics are therefore required for UHF. Higher-order SH allows for correcting more complex-shaped inhomogeneities by incorporating an additional non-linear quadratic field variation that allows for modeling the bending of curves in space. This requires supplementary dedicated shim coils, which can counter-intuitively induce additional distortions in the middle of the brain. Despite efforts to harmonize parameters, shimming is often site- and field-dependent, and manual iterative shimming is not always possible due to time constraints and/or limited expertise.

Additional B1 mapping is essential for accurate quantitative measures of signal intensities within the correct geometric space. Inhomogeneous B1 fields can result in distorted flip angles (FAs). FAs index the amount of net magnetization rotation experienced during the application of an RF pulse. If FAs are incorrectly calculated, geometric distortions occur, which reduces the accuracy in T1 and T2 values. B1 mapping allows for the correction of FA values before acquiring a structural scan. Primary B1+ mapping methods can be incorporated into sequence acquisition. This is most commonly achieved with the double angle method (DAM), which estimates local FAs from the ratio of two images obtained with different FA values. An additional 3D multi-shot method can be incorporated, which uses non-selective excitation to minimize inhomogeneous spin excitation across slices. Alternatively, spoiled gradient echo (GRE) sequences with variable FAs (VFA) and actual FA imaging (AFI) are commonly employed, which sample multiple T1 values to simulate signal differences across tissues (Cheng & Wright, 2006; Eggenschwiler, Kober, Magill,

Gruetter, & Marques, 2012; Hurley et al., 2012; Yarnykh, 2010).

Pre-processing of gradient non-linearities (GNL) and intensity non-uniformity with retrospective image-based interpolation is also possible. Corrections for GNL are rarely accomplished in clinical settings but are commonplace for research-based applications. The magnitude of GNL increases with distance from the isocenter and can cause the visualization of structures to shift by up to 5 mm, which is detrimental for pre-operative planning (Karger, Höss, Bendl, Canda, & Schad, 2006). Correcting for GNL can be achieved by incorporating a low-pass filter to remove smooth spatially varying functions. Other GNL correction schemes include surface fitting and feature matching that rely on intensity-based methods. Intensity-based methods assume that different tissue intensities do not vary significantly unless they are subject to an erroneous bias field, where variations within one area can be corrected from the field of another spatial location within the image. Alternatively, histogram-based methods use a priori knowledge and manual input of known intensity and gradient probability distributions to correct images. B1 corrections can be achieved offline via image pre-processing steps with the FMRIB Software Library(FSL), Statistical Parametric Mapping (SPM), or Advanced Normalization Tools (ANTs) (Ganzetti, Wenderoth, & Mantini, 2016; Sled, Zijdenbos, & Evans, 1998; Tustison et al., 2010; Zhang, Brady, & Smith, 2001). However, these methods must be considered experimental and their use in image correction for MRI in pre-operative planning is not currently FDA-approved.

Sequence Types and Contrasts

T1

As discussed, accurate DBS implantation requires careful trajectory planning and identification of vasculature to limit the risk of hemorrhagic complications. Visualization of larger venous architecture is most commonly achieved with an anatomical T1w scan with added gadolinium (Falk Delgado et al., 2019; Oliveira, Hedgire, Li, Ganguli, & Prabhakar, 2016). In its most basic form, T1w can be viewed as an anatomical scan that approximates the appearance of macroscopic tissues. T1w will visualize white matter as hyperintense; fluid,

e.g., cerebral spinal fluid (CSF) as hypointense; and grey matter at intermediate intensity. A T1w contrast is achieved with a short echo time (TE) and repetition time (TR) and is a function of the longitudinal relaxation time, referring to the time it takes excited protons to return to their equilibrium after the application of an RF pulse. T1 is more sensitive to fat and fluid and therefore provides excellent differentiation between grey and white matter. Additional intravenous contrast agents will cause the recovery of the longitudinal magnetization of blood to quicken and therefore increase further contrast between veins and white matter (Barral et al., 2010; Bloem, Reijnierse, Huizinga, & Van Der Helm-Van Mil, 2018; Vymazal et al., 1995). For visualization of venous architecture, some centers may use any or a combination of T1w structural imaging, or they may use post-processing techniques such as susceptibility-weighted imaging (SWI) and venography, which can be created from GRE-based sequences with flow compensation, or time-of-flight angiography. These types of sequences apply multiple RF pulses with short TRs to over-saturate static tissues and therefore suppress their signal, causing moving components such as blood to appear more hyperintense (Barnes & Haacke, 2009; Bériault et al., 2014; Ko, Kim, Kim, & Roh, 2006). T1w MRI can also be used to rule out co-morbidities such as edema, tumors, or other brain pathologies. See figure 1 for an example of different contrasts.

T2

T2w images visualize grey matter as intermediate intensity and white matter as hypointense, although deep grey matter structures can appear even darker depending on the ferromagnetism of their tissue composition. As mentioned, visualization of STN is traditionally achieved with T2w sequences (Aquino et al., 2009; Dormont et al., 2004; Drayer, 1989). T2w MRI represents transverse relaxation, referring to the amount of time it takes excited protons to lose phase coherence. This dephasing is a tissue-specific process and takes longer for areas with high paramagnetic metal deposition such as iron. As the STN is iron-rich, the contrast is increased, and the nucleus appears hypointense compared to white matter tracts and surrounding grey matter structures. Typically, T2w contrasts within the clinic will come from fast-spin echo sequences that have both a long TE and TR, which are relatively

immune to magnetic susceptibility artifacts. However, there is no consensus as to the optimal sequence required for prime STN imaging. Theoretically, various sequences can achieve the same weighting but vary significantly in terms of their ability to accurately visualize the STN (Keuken, Isaacs, Trampel, van der Zwaag, & Forstmann, 2018). Moreover, the type of sequence will depend on the field strength, and contrasts are not always analogous across, for instance, 3 and 7T (Marques & Norris, 2017). Similarly, different MRI vendors will supply similar contrasts via sequences and sequence parameters with different names, making it difficult to draw comparisons between them (Chavhan, Babyn, Jankharia, Cheng, & Shroff, 2008; Hargreaves, 2012; McRobbie et al., 2006).

T2* and Susceptibility-Based Contrasts

Traditional clinical T2w sequences suffer from low signal and contrast. An alternative contrast that can be used to image the STN directly comes from 3D gradient echo (GRE) sequences, which can be used to create T2* images. Typically, GRE sequences will include a low FA, long TEs, and long TRs. Moreover, gradients are applied to initiate dephasing, as opposed to an RF pulse in traditional spin-echo sequences (Bitar et al., 2006; Tang, Chen, Zhang, & Huang, 2014). These gradients do not refocus field inhomogeneities such as RF pulses do. Therefore the T2* contrast arising from GRE reflects magnetic field inhomogeneities caused by the dephasing of neighboring areas that occurs at different rates, and further interact with the signal of adjacent voxels (Chavhan et al., 2009). As GRE sequences assess macroscopic intervoxel and microscopic intravoxel magnetic susceptibilities, it is important to adapt sequence parameters according to the tissue of interest (Haacke, Tkach, & Parrish, 1989). The tissue characteristics of the STN undergo PD-specific changes, such as dopaminergic denervation and excessive iron deposit, which require adjusted parameters such as TE for optimal contrast (Kosta, Argyropoulou, Markoula, & Konitsiotis, 2006; Pyatigorskaya, Gallea, Garcia-Lorenzo, Vidailhet, & Lehericy, 2014). Similarly, iron increases with normal aging require different adaptations to TEs (Keuken et al., 2013). GRE sequences also incorporate multiple echoes to account for differences in magnetic susceptibility across tissues. Further, susceptibility effects are stronger for smaller

voxel sizes as the dephasing is reduced (Chavhan et al., 2009). This makes T2* imaging more appropriate for higher field strength MR, as smaller voxel sizes can be achieved with faster acquisition times (Abosch, Yacoub, Ugurbil, & Harel, 2010; Keuken et al., 2018). These T2* images can be further processed to create quantitative maps that will be discussed in later sections.

Alternatively, susceptibility-weighted images (SWI) can be created from T2*-based sequences by independently processing magnitude and phase images. Magnitude images reflect the overall MR signal, and their corresponding phase image contains information about field inhomogeneity, differences in local precession frequencies, and motion (Haacke, Mittal, Wu, Neelavalli, & Cheng, 2008). Phase images were largely discarded before the implementation of SWI as they require complex unwrapping, referring to the extraction of their original numerical range, which is constrained in the outputted image to $[-\pi, +\pi]$ (Ishimori, Monma, Kohno, & Kohno, 2009). However, phase can be used to visualize information that would otherwise be barely visible in magnitude images. Small structures result in field variations with high spatial frequencies, which can be used to enhance contrast by applying a high pass filter. The resulting SWI image is the product of multiplying the phase mask with the magnitude image (Elolf et al., 2007; Ishimori et al., 2009; Rauscher, Sedlacik, Barth, Mentzel, & Reichenbach, 2005). It remains somewhat controversial to what extent SWI signal increases from 1.5 T to 3T MRI. Moreover, there is little evidence for increased accuracy for SWI at 3T compared to classic T2 imaging (Bot et al., 2019; Bus et al., 2018).

However, SWI is significantly more accurate compared to traditional contrasts at higher field strengths (Keuken et al., 2017). GRE-based sequences and T2* contrasts can provide more detail regarding the shape, surface, and location of the STN compared to standard T2w spin echo-based sequences. This could translate to more accurate DBS targeting if it were used for pre-operative planning. Improvements can refer to a smaller deviation between planned and actual lead location, a reduction in reimplantation or removal requirements, increased clinical efficacy, or a decrease in associated side effects. However, the use of T2* contrasts and UHF-MRI remains widely debated and requires further validation (Bot et al., 2016; Bus et al., 2018; Duchin et al., 2018; Elolf et al., 2007; Plantinga et al., 2018; Vertinsky et al., 2009).

We attempted to use a T2*-based UHF-MRI with a GRE-ASPIRE sequence (Eckstein et al., 2018) on a 7T Siemens MAGNETOM system (Siemens Healthcare, Erlangen, Germany) for STN DBS planning in PD patients. The 7T T2* scan consisted of a partial volume covering the subcortex, obtained with multiple echoes (TE1–4 = 2.47, 6.75, 13.50, 20.75) and 0.5 mm isotropic voxel sizes in just under 8 min. This was overlaid with a 3T T2w turbo field echo sequence obtained on a 3Tesla Phillips Ingenia system, with a single TE of 80 ms and voxel sizes of 0.45 × 0.45 × 2 mm, and an acquisition time of around 6 min. When merging the 3T and 7T data, the STN appeared elongated along the posterior direction on 7T. The optimal target coordinate appeared more superior, posterior, and lateral on the 7T image than the optimal coordinate on 3T. Here, the 7T coordinate was used as the posterior test site sampled with MER during DBS surgery. Typical STN activity was not observed, although intra-operative behavioral testing revealed that patients would exhibit a beneficial clinical effect. Such a finding may be explained by the fact that the test electrode was instead stimulating white matter fibers exciting the STN, such as the fasciculus lenticularis or medial fiber bundles. It is, however, unclear as to whether this discrepancy in optimal STN coordinate is due to errors in registration across field strength, smoothing factors, and interpolation automatically applied by the pre-operative planning system that reduced the resolution of the 7T data, magnetic field inhomogeneity, or geometric distortions of the T2* image. The issues regarding image correction and manipulation are discussed in later sections. It is entirely plausible that the discrepancy in optimal target location across field strength was due to human error, and the operating surgeons perhaps were not used to interpreting the high-resolution susceptibility-based images. Therefore, factors other than contrast and sequence type can influence the usability and accuracy of susceptibility-based imaging for neurosurgical applications.

It is important to note that the sequences described in this specific instance are not standardized across centers, and scanner vendors, field strengths, contrasts, and sequence parameters, even within the same sequence type, will differ across DBS centers and research institutes. This makes direct comparison across the quality and replicability of MRI scans very difficult, and unless systems are harmonized, interpretations should be site-specific. See (Habets et al., 2019; Keuken et al., 2018) for a comprehensive review on sequences used for

imaging the STN.

Multi-Contrast MRI

Multi-contrast sequences may offer a novel alternative for eliminating the requirement of registration and resampling of separate scans while simultaneously reducing scan acquisition time (figure 1) (Weiskopf, Mohammadi, Lutti, & Callaghan, 2015). A recently developed multiparametric imaging sequence is the Multi Echo (ME) MP2RAGE, which is largely unaffected by B1 inhomogeneities (Caan et al., 2019; Choi, Kawaguchi, Matsuoka, Kober, & Kida, 2018; Kerl et al., 2012; Marques et al., 2010; Metere, Kober, Möller, & Schäfer, 2017; Shin, Shin, Oh, & Lowe, 2016; Sun et al., 2020; Tsialios, Thrippleton, & Pernet, 2017). This allows for the acquisition of T2*-based contrasts from which subsequent SWI and quantitative susceptibility maps (QSM) can be created in the same space as the T1 images (Caan et al., 2019; Metere et al., 2017). Other benefits of multiple contrasts are that they contain complementary information that can be used to jointly denoise and improve the SNR of the acquired images (Bazin et al., 2019; Visser, Douaud, et al., 2016; Visser, Keuken, Forstmann, & Jenkinson, 2016).

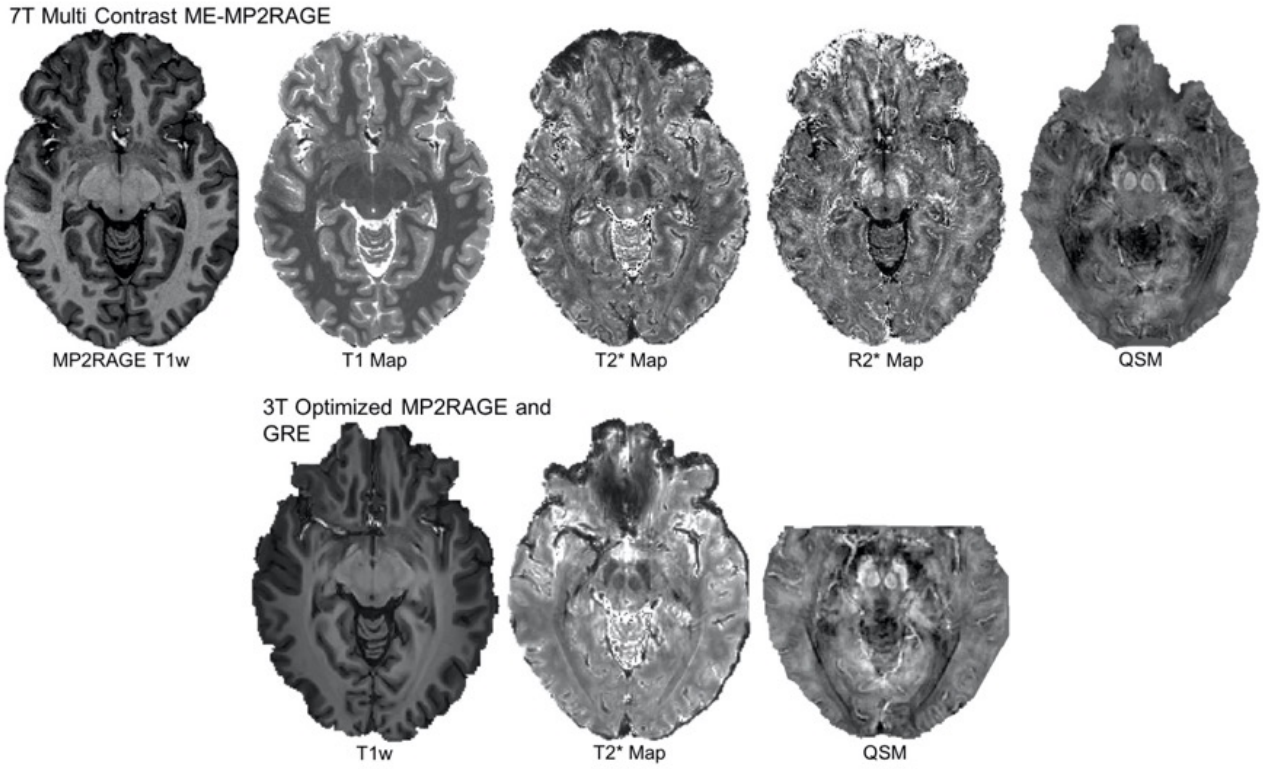

Figure 1. Multi-contrast imaging. The top row shows MP2RAGE T1-weighted, T1, T2*, and R2* maps and a quantitative susceptibility map (QSM) image obtained at 7T within a single multi-echo (ME) MP2RAGE sequence. Below are a 3T T1-weighted map, a T2* map, and a QSM image, where each T1 and T2* were obtained with different sequences but were optimized to provide a contrast comparable to those obtainable at 7T but without the inversions required for creating T1 maps. Both the 3 and 7T images came from the same subject and are shown in the axial plane. The contrast and visibility of subcortical structures are indeed comparable across field strengths (Isaacs et al., 2020).

Voxel Sizes

Clinical T2w images often incorporate anisotropic voxel sizes with large slice thickness in the z-direction. This allows for higher in-plane resolution along the axial plane, which is primarily used for targeting (see figure 2 in chapter 7 for an example) (Bot et al., 2019; Bus et al., 2018). Voxel sizes will typically range between 0.45 × 0.45 × 2 mm and 1 × 1 × 3 mm. The lower resolution allows for shorter acquisition times of around 5 min, simultaneously limiting the

effect of artifacts due to subject movement. However, anisotropic voxels suffer from partial voluming effects (PVE), which refer to the blurring of signals across voxels, resulting in averaging different tissue types and reducing specificity (Somasundaram & Kalavathi, 2012). PVE are especially problematic for small structures such as the STN. Volume estimates are commonly used as an index of scan quality and have shown consistent deviations of more than 50% from ground truths when slice thicknesses were three times the size of the alternate planes (Mulder, Keuken, Bazin, Alkemade, & Forstmann, 2019). Moreover, anisotropic voxels will decrease the accuracy of resampling to super resolutions, which is an automatically incorporated step of pre-operative planning systems (Van Reeth, Tham, Tan, & Poh, 2012). As the spatial resolution is dependent on voxel size; smaller voxels should allow for more detailed and finer-grained visualization of smaller structures. Voxel sizes can be reduced by increasing the acquisition matrix, reducing slice thickness, or decreasing the field of view. However, these factors can each negatively affect the SNR. The loss of SNR can be compensated by simply including more repetitions per sequence, which is an issue for PD populations as it necessitates an increase in acquisition time and requires the patient to be still. However, this is often not possible for patients with movement disorders (Mulder et al., 2019). The loss of SNR caused by decreasing voxel sizes at lower fields can be counteracted through the use of UHF-MRI (Keuken et al., 2018).

When targets in clinical MRI are verified with MER, the large slice thickness means that the spatial resolution is penalized along the z-axis. Therefore the depth of the electrode cannot be optimally planned and electrophysiological samplings are conducted to identify the ideal electrode placement (Andrade-Souza et al., 2005; Rabie et al., 2016; Tonge et al., 2016). This testing often requires that the patient is awake and endures behavioral assessments, which are stressful and physically demanding, prolong the time of the surgery, and can increase the risk of infection or hemorrhaging (Chen, Tsai, & Li, 2011; Chen et al., 2018; Hardaway, Raslan, & Burchiel, 2017). If smaller voxels can increase the spatial resolution, three-dimensional anatomical accuracy, and tissue specificity, the requirement for intra-operative microelectrode recordings, multiple test electrode implantations, and awake behavioral testing could be eliminated, ultimately increasing patient comfort and reducing operation time.

However, voxels with a sub-millimeter isotropic resolution used purely for identification of DBS targets, rather than for instance venous architecture, may not directly improve targeting accuracy. This is because the spatial resolution of stereotaxic coordinate systems is around 1.2 mm and chronically implanted conventional DBS electrodes are larger than 1 mm (Pouratian, 2020). In addition, segmented DBS leads with directional steering may offer increased spatial resolution when recording local field potentials compared to traditional omnidirectional contacts (Aman et al., 2020; Tinkhauser et al., 2018). Further, the development of microscale DBS contacts via multiresolution electrodes would allow for finer control of the stimulation volume and more precise targeting of smaller regions, matching the order and spatial resolution of submillimeter resolution MRI (Anderson et al., 2019).

Motion Correction

Generally, clinical MRI for pre-operative planning for DBS does not correct for motion and accurate imaging requires the subject to remain still. If a patient scan exhibits severe motion artifacts, the scan is simply run again. MR images can be distorted by multiple sources of motion arising from breathing, cardiac movement, blood flow, pulsation of cerebrospinal fluid, and patient movement (Krupa & Bekiesińska-Figatowska, 2015). This can cause distortions in the image such as ghosting, signal loss, and blurring, as well as Gibb's and chemical shift artifacts (Budrys et al., 2018). Such artifacts can mask or simulate pathological effects (Krupa & Bekiesińska-Figatowska, 2015). Motion artifacts are particularly prevalent when imaging patients with movement disorders but can be controlled for in several ways such as timing medication to be most optimal during the time of scanning or administering additional sedatives during the scan. Moreover, the head and neck should be supported with pads to improve patient comfort, which will also limit movement.

The most logical method of limiting motion artifacts is to decrease the acquisition time. Sequence paraments can be manipulated to shorten the acquisition time by obtaining larger voxel sizes, a partial field of view (FOV), incorporating simultaneous multi-slice 3D imaging and parallel imaging techniques, signal averaging, or obtaining multi-contrast images. To correctly utilize these potential solutions, each factor should be considered relative to one

another. For instance, partial FOVs can induce aliasing, fold over artifacts, and reduce the SNR, which can, to a certain extent, be countered by isolating the excitation to a localized region by using either multiple pulses, signal averaging, or fat suppression methods. Contrary to this, it may increase the effects of field inhomogeneity but be combated with factors such as spatial pre-saturation. Such issues highlight the dynamic nature and interplay of sequence parameters and hardware, which can be largely overcome through the use of stronger field strengths such as 7T.

Parallel imaging (PI) is a reconstruction technique commonly employed to accelerate acquisition time (Brau, 2007). MRI are not directly collected but instead stored in a Cartesian grid, representing a spatial frequency domain known as k-space, collected via superimposing spatially varying magnetic field gradients onto the main magnetic field (de Zwart et al., 2002; Deshmane, Gulani, Griswold, & Seiberlich, 2012). Generalized auto-calibrating partial parallel acquisition (GRAPPA) methods speed up acquisition time by under-sampling each line of k-space in the phase-encoding direction. Alternatively, acquisition can be sped up by obtaining partial FOVs collected independently, corrected, and then reconstructed within the frequency domain (Blaimer et al., 2004; Brau, Beatty, Skare, & Bammer, 2008; Griswold et al., 2002). Sensitive encoding methods (SENSE or ASSET) shorten scan times using multiple independent receiver channels where each coil is sensitive to a specific volume of tissue, which is then unfolded and recombined to form the image (Deshmane et al., 2012). However, PI methods are associated with several artifacts including ghosting, speckling, wrap-around, and g factor penalties and ought to be used with caution (Havsteen et al., 2017; Noël, Bammer, Reinhold, & Haider, 2009; Zaitsev, Maclaren, & Herbst, 2015).

Motion correction can be conducted prospectively in real-time by updating the image geometry during the scan, or retrospectively by post-acquisition registration techniques and manipulations during image reconstructions (Godenschweger et al., 2016). Additional hardware is required for prospective methods that are implemented within the scanner itself. In this case, fiducials can be attached to the patient's head, which assesses the extent of movement and adjusts the gradients accordingly. Alternatively, you can employ optical tracking or reflective markers, which are linked to a camera inside the bore. Motion correction is then achieved by either re-registration slice-by-slice during the scan, adjusting first order

shims, and/or varying the gradient system online (Callaghan et al., 2015; Maclaren, Herbst, Speck, & Zaitsev, 2012). As discussed, motion artifacts do not have to come from patient movement but can arise on a much smaller scale at the proton level. Protons in blood, for example, exhibit a non-static magnetic field due to the variation of gradients in space. That is, they can miss rephasing pulses and therefore decay in the signal before it can be read out by the scanner, especially for spin-echo sequences that are used for obtaining T2w images (Wadghiri, Johnson, & Turnbull, 2001). This phenomenon is known as flow-related dephasing and results in artifactual phase shifts and signal distortion. In some instances, this can be useful, for example in angiography sequences, the negative effect is larger in sequences with longer TEs, such as those required for accurately imaging the STN. Adding in flow compensation or gradient moment nulling, which applies additional gradient pulses before the signal readout to compensate for signal decay, can compensate for this dephasing (Duerk & Simonetti, 1991; Felmlee, Ehman, Riederer, & Korin, 1991). However, this is a computationally heavy process and is largely only suitable for partial FOVs. Alternatively, the sequence may be synchronized so that the acquisition occurs in time with the cardiac or respiratory cycle, which is known as cardiac gating and can utilize pulse recordings and electrocardiograms (Krupa & Bekiesińska-Figatowska, 2015).

Registration and Image Fusion

Using MRI to visualize targets for DBS is a multi-stage process that involves the acquisition of multiple separate contrasts which require registration to a common, patient-specific native space. For pre-operative planning, at least two sets of image registrations are required: (i) anatomical T2 to T1 and (ii) pre-registered anatomical T1 and T2 to stereotaxic space defined by the CT or MRI including the coordinate frame. In this section, we focus on the registration and fusion of MRI. For literature including alternative imaging modalities such as CT and ventriculography, see (Geevarghese, Ogorman Tuura, Lumsden, Samuel, & Ashkan, 2016; Mirzadeh, Chapple, Lambert, Dhall, & Ponce, 2014).

Image registration refers to the process of aligning a moving source image onto a fixed target through an estimated mapping between the pair of images. While the exact

parameters incorporated within pre-operative planning systems are mostly proprietary, the general process will require a linear/rigid registration, defined by six parameters: translation and rotations along the *x*-, *y*-, and *z*-axes. This refers to the spatial transformation of how a voxel can move from one space to another (Nandish, Prabhu, & Rajagopal, 2017). Transformations require additional parameters such as interpolation and cost function. Interpolation refers to the process of re-gridding voxels from the source image to the target, an essential procedure as each voxel within the transformed image may not represent a whole integer within the target image. This is especially true when T2w images consist of anisotropic voxel sizes and the T1 images are isotropic. Clinical neuroimaging traditionally employs the simplest intensity-based methods such as nearest-neighbor interpolation, also known as point sampling, which assumes that similar values in different images are closer together and therefore constitute the same location (Charles Stud & Ramamurthy, 2019; Doltra et al., 2013). Cost functions are used to assess the suitability of a given transform. This can be achieved with either similarity metrics such as mutual information, which compares, based on pixel intensities, the differences between the transformed source and target image (Woods, Grafton, Holmes, Cherry, & Mazziotta, 1998). These registration steps are conducted automatically within pre-operative planning systems, with the only manual alterations relating to viewing criteria such as brightness and intensity. As registrations often need tweaking and the exact parameters used in clinical imaging remain unknown, it becomes challenging to suggest exact methods for optimizing registrations in a preoperative setting.

However, intensity methods can be optimized to incorporate local patches that account for textures and geometric information that are missed when assessing for global identical intensities. An example is boundary-based registration, which forms the basis of intra-subject registration of T2 to T1 images within the Human Connectome Project minimal processing pipeline (Glasser et al., 2013; Greve & Fischl, 2009). Registrations could be optimized to include an additional affine transform that incorporates scaling or sheering (Iglesias & Sabuncu, 2015). Alternatively, deformable registrations via attribute matching and mutual saliency (DRAMMS) can be achieved. DRAMMS applies confidence weightings for matching voxels across contrast and will relax deformation in local regions where contrast-specific tissues are mutually exclusive to image type. DRAMMS has proven useful in

accounting for pathology, subcortical structures, and cortical thinning, which are all factors to consider when imaging PD patients (Ou, Sotiras, Paragios, & Davatzikos, 2011). Further, no quality or standardized evaluation for registration accuracy currently exists in clinical neuroimaging beyond subjective visual assessment. This is problematic as it becomes unclear as to whether the initial rigid body transforms are an accurate spatial representation of individual anatomy, which, if erroneous, could result in targeting errors and DBS lead placement. The gold standard of accuracy is instead dependent on the stereotaxic frame, which is an extrinsic marker and does not include information directly related to the MR image.

Medical imaging often incorporates automated image fusion, which refers to the process of aligning, resampling, smoothing, and combining the information of multiple images into a more informative and descriptive output; for instance, by combining T1 and T2 into a single image. Fusion occurs after registration to interpolate and smooth MRI images to make them more visually appealing, which can theoretically recover a signal within the data despite the noise (El-Gamal, Elmogy, & Atwan, 2016). However, smoothing and resampling voxel sizes will reduce anatomical variability and location accuracy as they can include a signal from neighboring structures, leading to an erroneous increase in the size of the nucleus and PVEs (de Hollander, Keuken, & Forstmann, 2015; Mulder et al., 2019). Such smoothing methods may not be compatible with quantitative images such as T2* maps and QSM, as these images represent distinct signal intensities of specific voxels that are outside the predefined values of the planning system. In effect, this could be a simple viewing error, rather than a total incompatibility.

Quantitative Maps

Broadly speaking, MR contrasts are driven by how much T1 or T2 signal contributes to the image. These T1w or T2w images are qualitative and fail to accurately assess tissue parameters such as recovery or relaxation time. Certain sequences allow for parametric mapping (quantitative MRI or qMRI), where the intensities within each pixel are proportional to the T1 or T2. These values can be used to quantify intrinsic, biologically meaningful tissue

information (Caan et al., 2018). Additionally, qMRI allows for direct comparison across time, across subjects, and across scanners or sites, which is essential for the development of neuroscientific research and its application to the clinical situation (Lambert, Lutti, Helms, Frackowiak, & Ashburner, 2013). Moreover, quantitative measures can aid the identification and visualization of target structures with an objective approach and can minimize human error resulting from subjective interpretation. qMRI can only be made from specific sequences that comply with the principles of differential weightings, which incorporate an inversion or saturation recovery parameter with multiple inversion times or spoiled gradient echo sequences with variable flip angles (Jara, 2013). Further, post-processing is often required and relies on the expertise that is again typically not available within a standard clinical setting (Dekkers et al., 2020; Metere et al., 2017). Additionally, in our experience, quantitative sequences at 3T take at least twice as long as weighted MRI sequences used in clinical settings.

As mentioned, quantitative maps are used to index anatomical composition. For instance, the observed relaxation of T1 is extremely fast in myelinated white matter. The inverse of longitudinal relaxation rates, known as R1 (Stüber et al., 2014), is thought to be linearly related to myelin concentrations (Harkins et al., 2016; Polders, 2012). T1 maps have been utilized clinically, for example, with quantifying perfusion; imaging hemorrhages and infarctions; evaluating contrast uptake; monitoring of tumors, gliosis, and multiple sclerosis lesions (Deoni, 2007; Deoni, Peters, & Rutt, 2005; Stüber et al., 2014). Quantitative T1 maps usually post-processing, most commonly achieved with the look-up table method, which functions to relate pixel-wise T1 values within the native map with predefined and validated intensity values (Marques et al., 2010). The automated creation of these T1 parametric maps can be built into the sequence at a cost of both time and capacity.

For DBS of the STN, T2* maps can be used to improve visualization of the STN because iron content causes the T2* relaxation time to shorten, which for the STN at 7T is around 15 ms (de Hollander et al., 2017; Keuken et al., 2017). A frequently used method to create T2* maps is done by fitting an exponential decay curve to the signal intensities per pixel from each of the multiple echoes obtained from a GRE sequence (Milford, Rosbach, Bendszus, & Heiland, 2015). Moreover, the pixel intensities of reciprocal T2* maps (R2*) are

proportional to iron load, with STN R2* values hovering around 67 s^{-1} (1/15 ms) at 7T (Acosta-Cabronero et al., 2018; Cronin et al., 2016; Liu, Li, Tong, Yeom, & Kuzminski, 2014; Schweser, Sommer, Deistung, & Reichenbach, 2012; Sun et al., 2020).

Alternatively, T2* images can be post-processed to create quantitative susceptibility maps (QSM), which quantify a tissue's magnetic susceptibility distribution based on its perturbation of the magnetic field (Schweser, Sommer, Deistung, & Reichenbach, 2012). They are similar to SWI in that they are made from the separate magnitude and phase images of a GRE sequence, but they comprise multiple echoes and allow for quantitative measures rather than weightings. QSM requires initial phase unwrapping, background field extraction, and calculation of locally generated phase offsets, which refer to the fact that the phase of a single voxel can be expressed as either positive or negative, depending on its orientation relative to the magnetic field (Cronin et al., 2016). These phase-offsets are then deconvolved, typically with a dipole kernel, from which the underlying tissue susceptibility can be extracted per voxel, independently of surrounding voxels (Acosta-Cabronero et al., 2018). Moreover, QSMs are preferred over SWI, as SWI is limited by the non-local orientation-dependent effects of phase, which means that the same tissues can appear with different intensities based on their location, whereas QSM solves this problem by convolving dipole fields (Langkammer et al., 2012; Liu et al., 2014). Background removal methods based on principles of sophisticated harmonic artifact reduction for phase data (SHARP, also known as spherical mean value (SMV) filtering) and projection onto dipole fields (PDF) are commonly employed. SHARP is based on a theory similar to shimming, in that static magnetic fields and the corresponding phase maps are represented by harmonic functions. In regions of inhomogeneous susceptibility, the field will be non-harmonic, and harmonic background fields are eliminated from the phase data by subtraction (Fang, Bao, Li, van Zijl, & Chen, 2019; Schweser, Sommer, Deistung, & Reichenbach, 2012). The PDF method removes background fields by comparing the magnetic fields of dipoles inside a region of interest with those directly outside (Fortier & Levesque, 2018; Wang & Liu, 2015). Alternatively, Laplacian boundary values can be used, which are based on a finite difference scheme (Zhou, Liu, Spincemaille, & Wang, 2014). However, quantifying an arbitrary distribution of susceptibility from the phase signal is challenging and poses an inverse problem whereby effects are first

calculated from which parameters or causes are then determined, resulting in a noise amplification of the ensuing signal. The inversion problem can be solved with a calculation of susceptibility through multiple orientation sampling (COSMOS). However, this method requires the acquisition of multiple head orientations, which is time-consuming and impractical for clinical use (Liu, Spincemaille, De Rochefort, Kressler, & Wang, 2009; Schweser, Sommer, Deistung, Reichenbach, et al., 2012). Morphology-enabled dipole inversion, or MEDI, will match the boundaries of each dipole with those observed in the T2*-weighted magnitude images (Liu et al., 2009). Quantitative susceptibility and residual mapping (QUASAR) accounts for biophysical frequency contributions, which acknowledges that the notion that the local Larmor frequency is affected by the static field perturbations related to tissue susceptibility, as well as the magnetic field, chemical shifts, directional alignment of axons, and energy exchange between water and macromolecules (Schweser & Zivadinov, 2018). Alternatively, some algorithms solve the entire equation within a single step by incorporating SHARP principles with simultaneous total generalized variation (TGV)-regularized dipole inversion (Chatnuntawech et al., 2017; Langkammer et al., 2018). Similarly, phase removal using the Laplacian operator (HARPERELLA) simultaneously combines phase unwrapping and background removal (Li, Avram, Wu, Xiao, & Liu, 2014). These methods comprise toolboxes that are largely available in Matlab or Python (see (Alkemade et al., 2017) and the references therein).

The clinical potential of QSM lies in its sensitivity to variations in iron stored in ferritin and hemosiderin, lipids and calcium, levels of differential oxygenation-saturation present in venous blood, and identification of sub-millimeter white matter microstructure (Fan et al., 2014; Wang et al., 2017; Wharton & Bowtell, 2015). Further, QSM has been shown as superior to T2* in parcellations of the STN, which could translate into better visualization and targeting for DBS (Alkemade et al., 2017; Schweser, Deistung, Lehr, & Reichenbach, 2010; Schweser, Sommer, Deistung, Reichenbach, et al., 2012). T2 relaxometry has been shown to predict motor outcome in some PD patients with STN DBS, where patients who have low T2 values may fail to show a clinical benefit (Lönnfors-Weitzel et al., 2016). It is possible that this can be explained by the fact that patients with low T2 relaxometry will have less contrast between the STN and the surrounding tissue, hindering the accurate

visualization and targeting of the structure, which could be solved by employing QSM. However, QSM obtained during a scanning session is still experimental and under development. Further, there are many competing post-processing methods for creating QSM images, which makes translation challenging.

Complications Unrelated to Pre-Operative Planning

Lastly, while this paper specifically refers to the suboptimal placement of DBS leads due to the limitations of neuroimaging, negative outcomes of DBS application can arise independently of planning procedures and surgical expertise. For example, neurosurgery has been linked to brain deformation and shift, changes in cerebral spinal fluid volume, and intracranial pressure, which may induce spatial variability both during the surgery and cause a shift in the implanted lead location during recovery (Hartmann et al., 2019; Xiao et al., 2020). Similarly, DBS surgeries are associated with infection (mostly found in the chest and connector) (Bernstein, Kashyap, Ray, & Ananda, 2019); reactive gliosis and gliotic scarring (Vedam-Mai et al., 2018); hemorrhage either during the surgery or delayed (in less than 5%) (Park, Jung, Kim, & Chang, 2017); and, although rare, cerebral pneumocephalus (Albano, Rohatgi, Kashanian, Bari, & Pouratian, 2020). In all these cases, the DBS system may require reimplantation, replacement, or removal.

Conclusions

In this paper, we have discussed some of the differences in current clinical MRI practices with optimized and UHF-MRI methods employed in research environments. Clinical MRI hinges on weighted imaging with anisotropic voxel sizes and maintaining short acquisition, therefore being limited in signal and resolution. These current clinical practices are FDA-approved and are therefore deemed acceptable for neurosurgical purposes. However, side effects and non-responding patients exists nonetheless. Optimized 3T and UHF-MRI tend to incorporate isotropic high-resolution imaging with quantitative and susceptibility-based contrasts for better visualization of deep brain structures, which, require more complex pre-

processing and longer scan durations. The limitations incurred regarding reduced signal in clinical MRI and increased acquisition time with optimized 3T can be largely overcome with the use of UHF-MRI. However, many of the image registration, correction, and post-processing techniques may require expertise that is outside of clinical settings. Importantly, UHF-MRI and alternative contrasts such as QSM can only be implemented once planning systems and software allow for their compatibility, which may require further FDA approval not only for the MRI system but also for specific sequences. Approval for clinical use may be required for processing, such as the algorithms used for registration or calculation of quantitative maps.

We propose where UHF-MRI is not accessible, higher quality imaging can be obtained with optimized 3T, although this will take longer than is perhaps clinically feasible for patients with severe movement disorders. Direct collaboration between fundamental neuroscience researchers and clinicians will be essential for the development of optimized 3T and UHF-MRI in the pre-operative planning for DBS. Multi-site clinical trials can facilitate optimization and validation of certain sequences. Sequences with identical parameters should be compared on identical MRI systems and at different sites to ensure harmonization and reliability. Deviations between planned and actual target locations should be compared across vendors and systems as well as across sequences. Similarly, access agreements to work-in-progress protocols from MR vendors would facilitate the development and optimization of sequences, and would open access to underlying algorithms and adjustable parameters within software vendors (e.g., Medtronic, St. Judes, Brainlab, Abott, Nextim, and Boston Scientific). This paper focused specifically on the STN as the most popular target for DBS in PD. However alternative targets also exist (for example, see figure 2 in chapter 2). Some centers have long preferred the internal segment of the globus pallidus, and more recent research is being conducted on the suitability of alternate areas such as the ventral intermediate nucleus or the pedunculopontine nucleus for DBS targets. For a more in-depth review, please see (Anderson, Beecher, & Ba, 2017; Mao et al., 2019; Odekerken et al., 2016) and references therein.

References

Abduljalil, A. M., Schmalbrock, P., Novak, V., & Chakeres, D. W. (2003). Enhanced gray and white matter contrast of phase susceptibility-weighted images in ultra-high-field magnetic resonance imaging. *Journal of Magnetic Resonance Imaging*, *18*(3), 284–290. https://doi.org/10.1002/jmri.10362

Abosch, A., Yacoub, E., Ugurbil, K., & Harel, N. (2010). An assessment of current brain targets for deep brain stimulation surgery with susceptibility-weighted imaging at 7 tesla. *Neurosurgery*, *67*(6), 1745–1756. https://doi.org/10.1227/NEU.0b013e3181f74105

Acosta-Cabronero, J., Milovic, C., Mattern, H., Tejos, C., Speck, O., & Callaghan, M. F. (2018). A robust multi-scale approach to quantitative susceptibility mapping. *NeuroImage*, *183*, 7–24. https://doi.org/10.1016/j.neuroimage.2018.07.065

Aggarwal, M., Zhang, J., Pletnikova, O., Crain, B., Troncoso, J., & Mori, S. (2013). Feasibility of creating a high-resolution 3D diffusion tensor imaging based atlas of the human brainstem: A case study at 11.7T. *NeuroImage*, *74*, 117–127. https://doi.org/10.1016/j.neuroimage.2013.01.061

Ahlskog, J. E. (1999). Medical Treatment of Later-Stage Motor Problems of Parkinson Disease. *Mayo Clinic Proceedings*, *74*(12), 1239–1254. https://doi.org/10.4065/74.12.1239

Ahlskog, J. E., & Muenter, M. D. (2001). Frequency of levodopa-related dyskinesias and motor fluctuations as estimated from the cumulative literature. *Movement Disorders*, *16*(3), 448–458. https://doi.org/10.1002/mds.1090

Akaike, H. (1998). Likelihood and the Bayes procedure. In *Selected Papers of Hirotugu Akaike* (pp. 309-332). Springer, New York, NY. https://doi.org/10.1007/978-1-4612-1694-0_24

Akkal, D., Dum, R. P., & Strick, P. L. (2007). Supplementary motor area and presupplementary motor area: Targets of basal ganglia and cerebellar output. *Journal of Neuroscience*, *27*(40), 10659–10673. https://doi.org/10.1523/JNEUROSCI.3134-07.2007

Akram, H., Wu, C., Hyam, J., Foltynie, T., Limousin, P., De Vita, E., … Zrinzo, L. (2017). l-Dopa responsiveness is associated with distinctive connectivity patterns in advanced Parkinson's disease. *Movement Disorders*. https://doi.org/10.1002/mds.27017

Al-Helli, O., Thomas, D. L., Massey, L., Foltynie, T., Limousin, P., Holton, J. L., … Zrinzo, L. (2015). Deep brain stimulation of the subthalamic nucleus: histological verification and 9.4-T MRI correlation. *Acta Neurochirurgica*, *157*(12), 2143–2147. https://doi.org/10.1007/s00701-015-2599-x

Al-Radaideh, A. M., Wharton, S. J., Lim, S.-Y., Tench, C. R., Morgan, P. S., Bowtell, R. W., … Gowland, P. A. (2013). Increased iron accumulation occurs in the earliest stages of demyelinating disease: an ultra-high field susceptibility mapping study in Clinically Isolated Syndrome. *Multiple Sclerosis Journal*, *19*(7), 896–903. https://doi.org/10.1177/1352458512465135

Alarcon, C., de Notaris, M., Palma, K., Soria, G., Weiss, A., Kassam, A., & Prats-Galino, A. (2014). Anatomic Study of the Central Core of the Cerebrum Correlating 7-T Magnetic Resonance Imaging and Fiber Dissection With the Aid of a Neuronavigation System. *Operative Neurosurgery*, *10*(2), 294–304. https://doi.org/10.1227/neu.0000000000000271

Albano, L., Rohatgi, P., Kashanian, A., Bari, A., & Pouratian, N. (2020). Symptomatic Pneumocephalus after Deep Brain Stimulation Surgery: Report of 2 Cases. *Stereotactic and Functional Neurosurgery*, *98*(1), 30–36. https://doi.org/10.1159/000505078

Albin, R. L., Young, A. B., & Penney, J. B. (1989). The functional anatomy of basal ganglia disorders. *Trends in Neurosciences*, *12*(10), 366–375. https://doi.org/10.1016/0166-2236(89)90074-X

Alexander, G. E., & Crutcher, M. D. (1990). Functional architecture of basal ganglia circuits: neural substrates of parallel processing. *Trends in Neurosciences*, *13*(7), 266–271. https://doi.org/10.1016/0166-2236(90)90107-L

Alexander, G. E., Crutcher, M. D., & DeLong, M. R. (1991). Basal ganglia-thalamocortical circuits: Parallel substrates for motor, oculomotor, prefrontal and limbic functions. *Progress in Brain Research*, 119–146.

Alexander, G. E., DeLong, M. R., & Strick, P. L. (1986). Parallel Organization of Functionally Segregated Circuits Linking Basal Ganglia and Cortex. *Annual Review of Neuroscience*, *9*(1), 357–381. https://doi.org/10.1146/annurev.ne.09.030186.002041

Alho, E. J. L., Grinberg, L., Heinsen, H., & Talamoni, E. (2011). Review of Printed and Electronic Stereotactic Atlases of the Human Brain. In *Neuroimaging for Clinicians - Combining Research and Practice*. https://doi.org/10.5772/24897

Alkemade, A., de Hollander, G., Keuken, M. C., Schäfer, A., Ott, D. V. M. M., Schwarz, J., … Forstmann, B. U. (2017). Comparison of T2*-weighted and QSM contrasts in Parkinsons disease to visualize the STN with MRI. *PLoS ONE*, *12*(4), e0176130. https://doi.org/10.1371/journal.pone.0176130

Alkemade, A., de Hollander, G., Miletic, S., Keuken, M. C., Balesar, R., de Boer, O., … Forstmann, B. U. (2019). The functional microscopic neuroanatomy of the human subthalamic nucleus. *Brain Structure and Function*, *224*(9), 3213–3227. https://doi.org/10.1007/s00429-019-01960-3

Alkemade, A., de Hollander, G., Miletic, S., Keuken, M. C., Balesar, R., de Boer, O., … Forstmann, B. U. (2019). The functional microscopic neuroanatomy of the human subthalamic nucleus. *Brain Structure and Function*, *224*(9), 3213–3227. https://doi.org/10.1007/s00429-019-01960-3

Alkemade, A., Keuken, M. C., & Forstmann, B. U. (2013). A perspective on terra incognita: uncovering the neuroanatomy of the human subcortex. *Frontiers in Neuroanatomy*, *7*. https://doi.org/10.3389/fnana.2013.00040

Alkemade, A., Mulder, M. J., Groot, J. M., Isaacs, B. R., van Berendonk, N., Lute, N., … Forstmann, B. U. (2020). The Amsterdam Ultra-high field adult lifespan database (AHEAD): A freely available multimodal 7 Tesla submillimeter magnetic resonance imaging database. *NeuroImage*, *221*, 117200. https://doi.org/10.1016/j.neuroimage.2020.117200

Alkemade, A., Schnitzler, A., & Forstmann, B. U. (2015). Topographic organization of the human and non-human primate subthalamic nucleus. *Brain Structure and Function*, *220*(6), 3075–3086. https://doi.org/10.1007/s00429-015-1047-2

Allison, J., & Yanasak, N. (2015). What MRI sequences produce the highest specific absorption rate (SAR), and is there something we should be doing to reduce the SAR during standard examinations? *American Journal of Roentgenology*, *205*(2). https://doi.org/10.2214/AJR.14.14173

Alterman, R. L., & Weisz, D. (2012). Microelectrode recording during deep brain stimulation and ablative procedures. *Movement Disorders*, *27*(11), 1347–1349. https://doi.org/10.1002/mds.25068

Altman, N., & Krzywinski, M. (2015). Points of Significance: Association, correlation and causation. *Nature Methods*, *12*(10), 899–900. https://doi.org/10.1038/nmeth.3587

Aman, J. E., Johnson, L. A., Sanabria, D. E., Wang, J., Patriat, R., Hill, M., … Vitek, J. L. (2020). Directional deep brain stimulation leads reveal spatially distinct oscillatory activity in the globus pallidus internus of Parkinson's disease patients. *Neurobiology of Disease*, *139*, 104819. https://doi.org/10.1016/j.nbd.2020.104819

Amirnovin, R., Williams, Z. M., Cosgrove, G. R., & Eskandar, E. N. (2006). Experience with microelectrode guided subthalamic nucleus deep brain stimulation. *Neurosurgery*, *58*. https://doi.org/10.1227/01.NEU.0000192690.45680.C2

Amunts, K., Lepage, C., Borgeat, L., Mohlberg, H., Dickscheid, T., Rousseau, M.-E., … Evans, A. C. (2013). BigBrain: An Ultrahigh-Resolution 3D Human Brain Model. *Science*, *340*(6139), 1472–1475. https://doi.org/10.1126/science.1235381

Amunts, K., Schleicher, A., Burgel, U., Mohlberg, H., Uylings, H. B. M., & Zilles, K. (1999). Broca's region revisited: Cytoarchitecture and intersubject variability. *The Journal of Comparative Neurology*, *412*(2), 319–341. https://doi.org/10.1002/(sici)1096-9861(19990920)412:2<319::aid-cne10>3.0.co;2-7

Anderson, D. N., Anderson, C., Lanka, N., Sharma, R., Butson, C. R., Baker, B. W., & Dorval, A. D. (2019). The µDBS: Multiresolution, Directional Deep Brain Stimulation for Improved Targeting of Small Diameter Fibers. *Frontiers in Neuroscience*, *13*. https://doi.org/10.3389/fnins.2019.01152

Anderson, D., Beecher, G., & Ba, F. (2017). Deep Brain Stimulation in Parkinson's Disease: New and Emerging Targets for Refractory Motor and Nonmotor Symptoms. *Parkinson's Disease*, Vol. 2017. https://doi.org/10.1155/2017/5124328

Anderson, W. S., & Lenz, F. (2006). Surgery insight: Deep brain stimulation for movement disorders. *Nature Clinical Practice Neurology*, *2*(6), 310–320. https://doi.org/10.1038/ncpneuro0193

Andrade-Souza, Y. M., Schwalb, J. M., Hamani, C., Eltahawy, H., Hoque, T., Saint-Cyr, J., & Lozano, A. M. (2005). Comparison of three methods of targeting the subthalamic nucleus for chronic stimulation in Parkinson's disease. *Neurosurgery*, *56*, 360–368; discussion 360-8. https://doi.org/10.1227/01.NEU.0000156547.24603.EE

Anteraper, S. A., Guell, X., Whitfield-Gabrieli, S., Triantafyllou, C., Mattfeld, A. T., Gabrieli, J. D., … Geddes, M. R. (2018). Resting-State Functional Connectivity of the Subthalamic Nucleus to Limbic, Associative, and Motor Networks. *Brain Connectivity*, *8*(1), 22–32. https://doi.org/10.1089/brain.2017.0535

Aquino, D., Bizzi, A., Grisoli, M., Garavaglia, B., Bruzzone, M. G., Nardocci, N., … Chiapparini, L. (2009). Age-related Iron Deposition in the Basal Ganglia: Quantitative Analysis in Healthy Subjects. *Radiology*, *252*(1), 165–172. https://doi.org/10.1148/radiol.2522081399

Archer, D. B., Patten, C., & Coombes, S. A. (2017). Free-water and free-water corrected fractional anisotropy in primary and premotor corticospinal tracts in chronic stroke. *Human Brain Mapping*. https://doi.org/10.1002/hbm.23681

Aron, A. R. (2007). The neural basis of inhibition in cognitive control. *Neuroscientist*, *13*(3), 214–228. https://doi.org/10.1177/1073858407299288

Aron, A. R., & Poldrack, R. A. (2006). Cortical and subcortical contributions to stop signal response inhibition: Role of the subthalamic nucleus. *Journal of Neuroscience*, *26*(9), 2424–2433. https://doi.org/10.1523/JNEUROSCI.4682-05.2006

Aron, A. R., Robbins, T. W., & Poldrack, R. A. (2014a). Inhibition and the right inferior frontal cortex: One decade on. *Trends in Cognitive Sciences*, *18*(4), 177–185. https://doi.org/10.1016/j.tics.2013.12.003

Aron, A. R., Robbins, T. W., & Poldrack, R. A. (2014b). Right inferior frontal cortex: Addressing the rebuttals. *Frontiers in Human Neuroscience*, *8*, https://doi.org/10.3389/fnhum.2014.00905

Artieda, J., Pastor, M. A., Lacruz, F., & Obeso, J. A. (1992). Temporal discrimination is abnormal in parkinson's disease. *Brain*. https://doi.org/10.1093/brain/115.1.199

Ashkan, K., Blomstedt, P., Zrinzo, L., Tisch, S., Yousry, T., Limousin-Dowsey, P., & Hariz, M. I. Variability of the subthalamic nucleus: The case for direct MRI guided targeting. , 21 British Journal of Neurosurgery § (2007).

Ashkan, K., Wallace, B., Bell, B. A., & Benabid, A. L. (2004). Deep brain stimulation of the subthalamic nucleus in Parkinson's Disease 1993-2003: Where are we 10 years on? *British Journal of Neurosurgery*, *18*(1), 19–34. https://doi.org/10.1080/02688690410001660427

Aubignat, M., Lefranc, M., Tir, M., & Krystkowiak, P. (2020). Deep brain stimulation programming in Parkinson's disease: Introduction of current issues and perspectives. *Revue Neurologique*. https://doi.org/10.1016/j.neurol.2020.02.009

Auer, F., Vagionitis, S., & Czopka, T. (2018). Evidence for Myelin Sheath Remodeling in the CNS Revealed by In Vivo Imaging. *Current Biology*. https://doi.org/10.1016/j.cub.2018.01.017

Augustinack, J. C., van der Kouwe, A. J. W., Salat, D. H., Benner, T., Stevens, A. A., Annese, J., … Corkin, S. (2014). H.M.'s contributions to neuroscience: A review and autopsy studies. *Hippocampus*, *24*(11), 1267–1286. https://doi.org/10.1002/hipo.22354

Augustine, E. F., Pérez, A., Dhall, R., Umeh, C. C., Videnovic, A., Cambi, F., … Suchowersky, O. (2015). Sex differences in clinical features of early, treated Parkinson's disease. *PLoS ONE*. https://doi.org/10.1371/journal.pone.0133002

Aviles-Olmos, I., Kefalopoulou, Z., Tripoliti, E., Candelario, J., Akram, H., Martinez-Torres, I., … Limousin, P. (2014). Long-term outcome of subthalamic nucleus deep brain stimulation for Parkinson's disease using an MRI-guided and MRI-verified approach. *Journal of Neurology, Neurosurgery & Psychiatry*, *85*(12), 1419–1425. https://doi.org/10.1136/jnnp-2013-306907

Azadbakht, H., Parkes, L., & Parker, G. (2015). Validation of High-Resolution Tractography Against In Vivo Tracing in the Macaque Visual Cortex. *Cerebral Cortex*, *25*(11), 4299–4309. htttps://doi.org/10.1093/cercor/bhu326

Balchandani, P., & Naidich, T. P. (2015). Ultra-high-field MR neuroimaging. *American Journal of Neuroradiology*, *36*(7), 1204–1215. https://doi.org/10.3174/ajnr.A4180

Bammer, R. (2003). Basic principles of diffusion-weighted imaging. *European Journal of Radiology*, *45*(3), 169–184. https://doi.org/10.1016/S0720-048X(02)00303-0

Bao, L., Li, X., Cai, C., Chen, Z., & van Zijl, P. C. M. (2017). Quantitative Susceptibility Mapping Using Structural Feature Based Collaborative Reconstruction (SFCR) in the Human Brain. *IEEE Transactions on Medical Imaging*, *35*(9), 2040–2050. https://doi.org/10.1109/tmi.2016.2544958

Bari, A., & Robbins, T. W. (2013). Inhibition and impulsivity: Behavioral and neural basis of response control. *Progress in Neurobiology*, *108*, 44–79. https://doi.org/10.1016/j.pneurobio.2013.06.005

Barnes, S. R. S., & Haacke, E. M. (2009). Susceptibility-Weighted Imaging: Clinical Angiographic Applications. *Magnetic Resonance Imaging Clinics of North America*, *17*(1), 47–61. https://doi.org/10.1016/j.mric.2008.12.002

Barral, J. K., Gudmundson, E., Stikov, N., Etezadi-Amoli, M., Stoica, P., & Nishimura, D. G. (2010). A robust methodology for in vivo T1 mapping. *Magnetic Resonance in Medicine*, *64*(4), 1057–1067. https://doi.org/10.1002/mrm.22497

Barry, R. L., Coaster, M., Rogers, B. P., Newton, A. T., Moore, J., Anderson, A. ., … Gore, J. C. (2013). On the Origins of Signal Variance in FMRI of the Human Midbrain at High Field. *PLoS ONE*, *8*(4), e62708. https://doi.org/10.1371/journal.pone.0062708

Bartels, A. L., & Leenders, K. L. (2009). Parkinson's disease: The syndrome, the pathogenesis and pathophysiology. *Cortex*, *45*(8), 915–921. https://doi.org/10.1016/j.cortex.2008.11.010

Barth, M., & Poser, B. A. (2011). Advances in High-Field BOLD fMRI. *Materials*, *4*(11), 1941–1955. https://doi.org/10.3390/ma4111941

Basser, P. J., Mattiello, J., & LeBihan, D. (1994). MR diffusion tensor spectroscopy and imaging. *Biophysical Journal*, *66*(1), 259–267. https://doi.org/10.1016/S0006-3495(94)80775-1

Bastide, M., Meissner, W., & Picconi, B. (2015). Pathophysiology of L-dopa-induced motor and non-motor complications in Parkinson's disease. *Progress in Neurobiology*, *132*, 96–168.

Batson, M. A., Petridou, N., Klomp, D. W. J., Frens, M. A., & Neggers, S. F. W. (2015). Single Session Imaging of Cerebellum at 7 Tesla: Obtaining Structure and Function of Multiple Motor Subsystems in Individual Subjects. *PLoS ONE*, *10*(8), e0134933. https://doi.org/10.1371/journal.pone.0134933

Baudrexel, S., Witte, T., Seifried, C., von Wegner, F., Beissner, F., Klein, J. C., … Hilker, R. (2011). Resting state fMRI reveals increased subthalamic nucleus-motor cortex connectivity in Parkinson's disease. *NeuroImage*, *55*(4), 1728–1738. https://doi.org/10.1016/j.neuroimage.2011.01.017

Baumann, C. R., Held, U., Valko, P. O., Wienecke, M., & Waldvogel, D. (2014). Body side and predominant motor features at the onset of Parkinson's disease are linked to motor and nonmotor progression. *Movement Disorders*. https://doi.org/10.1002/mds.25650

Bazin, P.-L., Alkemade, A., van der Zwaag, W., Caan, M., Mulder, M. J., & Forstmann, B. U. (2019). Denoising High-Field Multi-Dimensional MRI With Local Complex PCA. *Frontiers in Neuroscience*, *13*. https://doi.org/10.3389/fnins.2019.01066

Bazin, P.-L., Alkemade, A., Mulder, M. J., Henry, A. G., & Forstmann, B. U. (2020). Multi-contrast anatomical subcortical structures parcellation. *eLife, 9,* e59430. https://doi.org/10.7554/eLife.59430

Bechler, M. E., Swire, M., & ffrench-Constant, C. (2018). Intrinsic and adaptive myelination—A sequential mechanism for smart wiring in the brain. *Developmental Neurobiology*. https://doi.org/10.1002/dneu.22518

Behrens, T. E. J., Berg, H. J., Jbabdi, S., Rushworth, M. F. S. F. S., & Woolrich, M. W. W. (2007). Probabilistic diffusion tractography with multiple fibre orientations: What can we gain? *NeuroImage*, *34*(1), 144–155. https://doi.org/10.1016/j.neuroimage.2006.09.018

Behrens, T. E. J., Johansen-Berg, H., Woolrich, M. W., Smith, S. M., Wheeler-Kingshott, C. A. M., Boulby, P. A., … Matthews, P. M. (2003). Non-invasive mapping of connections between human thalamus and cortex using diffusion imaging. *Nature Neuroscience*, *6*(7), 750–757. https://doi.org/10.1038/nn1075

Beisteiner, R., Robinson, S., Wurnig, M., Hilbert, M., Merksa, K., Rath, J., … Geissler, A. (2011). Clinical fMRI: Evidence for a 7T benefit over 3T. *NeuroImage*, *57*(3), 1015–1021. https://doi.org/10.1016/j.neuroimage.2011.05.010

Bejjani, B. P., Dormont, D., Pidoux, B., Yelnik, J., Damier, P., Arnulf, I., … Cornu, P. (2000). Bilateral subthalamic stimulation for Parkinson's disease by using three-dimensional stereotactic magnetic resonance imaging and electrophysiological guidance. *Journal of Neurosurgery*, *92*(4), 615–625. https://doi.org/10.3171/jns.2000.92.4.0615

Ben-Haim, S., Asaad, W. F., Gale, J. T., & Eskandar, E. N. (2009). Risk factors for hemorrhage during microelectrode-guided deep brain stimulation and the introduction of an improved microelectrode design. *Neurosurgery*, *64*(4), 754–762. https://doi.org/10.1227/01.NEU.0000339173.77240.34

Benabid, A. L., Chabardes, S., Mitrofanis, J., Pollak, P., Tanei, T., Kajita, Y., … Wakabayashi, T. (2009). Deep brain stimulation of the subthalamic nucleus for the treatment of Parkinson's disease. *The Lancet Neurology*, *8*(1), 67–81. https://doi.org/10.1016/S1474-4422(08)70291-6

Benjamin, P., Viessmann, O., MacKinnon, A. D., Jezzard, P., & Markus, H. S. (2015). 7 Tesla MRI in Cerebral Small Vessel Disease. *International Journal of Stroke*, *10*(5), 659–664. https://doi.org/10.1111/ijs.12490

Bergh, D. van den, Doorn, J. van, Marsman, M., Draws, T., Kesteren, E.-J. van, Derks, K., Dablander, F., Gronau, Q. F., Kucharský, Š., Gupta, A. R. K. N., Sarafoglou, A., Voelkel, J. G., Stefan, A., Ly, A., Hinne, M., Matzke, D., & Wagenmakers, E.-J. (2020). A Tutorial on Conducting and Interpreting a Bayesian ANOVA in JASP. *LAnnee psychologique*, *Vol. 120*(1), 73–96.

Bériault, S., Sadikot, A. F., Alsubaie, F., Drouin, S., Collins, D. L., & Pike, G. B. (2014). Neuronavigation using susceptibility-weighted venography: Application to deep brain stimulation and comparison with gadolinium contrast: Technical note. *Journal of Neurosurgery*, *121*(1), 131–141. https://doi.org/10.3171/2014.3.JNS131860

Bernstein, J. E., Kashyap, S., Ray, K., & Ananda, A. (2019). Infections in Deep Brain Stimulator Surgery. *Cureus*, *11*(8). https://doi.org/10.7759/cureus.5440

Berry, D. A., & Hochberg, Y. (1999). Bayesian perspectives on multiple comparisons. *Journal of Statistical Planning and Inference*, *82*(1–2), 215–227. https://doi.org/10.1016/S0378-3758(99)00044-0

Betts, M. J., Acosta-Cabronero, J., Cardenas-Blanco, A., Nestor, P. J., & Düzel, E. (2016). High-resolution characterisation of the aging brain using simultaneous quantitative susceptibility mapping (QSM) and R2* measurements at 7 T. *NeuroImage*, *138*, 43–63. https://doi.org/10.1016/j.neuroimage.2016.05.024

Beuls, E., Gelan, J., & Vandersteen, M. (1993). Microanatomy of the excised human spinal cord and the cervicomedullary junction examined with high-resolution MR imaging at 9.4 Tesla. *AJNR Am J Neuroradiol*, *14*, 699–707.

Beuls, E., Vanormelingen, L., van Aalst, J., Vandersteen, M., Adriaensen, P., Cornips, E., … Gelan, J. (2003). The Arnold-Chiari Type II Malformation at Midgestation. *Pediatric Neurosurgery*, *39*(3), 149–158. https://doi.org/10.1159/000071653

Bianciardi, M., Strong, C., Toschi, N., Edlow, B. L., Fischl, B., Brown, E. N., … Wald, L. L. (2017). A probabilistic template of human mesopontine tegmental nuclei from in vivo 7 T MRI. *NeuroImage*, *170*, 222–230. https://doi.org/10.1016/j.neuroimage.2017.04.070

Bianciardi, M., Toschi, N., Edlow, B. L., Eichner, C., Setsompop, K., Polimeni, J. R., … Wald, L. L. (2015). Toward an In Vivo Neuroimaging Template of Human Brainstem Nuclei of the Ascending Arousal, Autonomic, and Motor Systems. *Brain Connectivity*, *5*(10), 597–607. https://doi.org/10.1089/brain.2015.0347

Bitar, R., Leung, G., Perng, R., Tadros, S., Moody, A. R., Sarrazin, J., … Roberts, T. P. (2006). MR pulse sequences: What every radiologist wants to know but is afraid to ask. *Radiographics*, *26*(2), 513–537. https://doi.org/10.1148/rg.262055063

Bizzi, E. (1968). Discharge of frontal eye field neurons during saccadic and following eye movements in unanesthetized monkeys. *Experimental Brain Research*, *6*(1), 69–80. https://doi.org/10.1007/BF00235447

Blaimer, M., Breuer, F., Mueller, M., Heidemann, R. M., Griswold, M. A., & Jakob, P. M. (2004). SMASH, SENSE, PILS, GRAPPA. How to Choose the Optimal Method. *Topics in Magnetic Resonance Imaging*, *15*(4), 223–236. https://doi.org/10.1097/01.rmr.0000136558.09801.dd

Blazejewska, A., Al-Radaideh, A. M., Wharton, S., Lim, S. Y., Bowtell, R. W., Constantinescu, C. S., & Gowland, P. A. (2014). Increase in the iron content of the substantia nigra and red nucleus in multiple sclerosis and clinically isolated syndrome: A 7 Tesla MRI study. *Journal of Magnetic Resonance Imaging*, *41*(4), 1065–1070. https://doi.org/10.1002/jmri.24644

Blazejewska, A., Schwarz, S. T., Pitiot, A., Stephenson, M. C., Lowe, J., Bajaj, N., … Gowland, P. A. (2013). Visualization of nigrosome 1 and its loss in PD: Pathoanatomical correlation and in vivo 7 T MRI. *Neurology*, *81*(6), 534–540. https://doi.org/10.1212/wnl.0b013e31829e6fd2

Bloem, J. L., Reijnierse, M., Huizinga, T. W. J., & Van Der Helm-Van Mil, A. H. M. (2018). MR signal intensity: Staying on the bright side in MR image interpretation. *RMD Open*, *4*(1), e000728. https://doi.org/10.1136/rmdopen-2018-000728

Boekel, W., Forstmann, B. U., & Keuken, M. C. (2017). A test-retest reliability analysis of diffusion measures of white matter tracts relevant for cognitive control. *Psychophysiology*, *54*(1), 24–33. https://doi.org/10.1111/psyp.12769

Bogacz, R., & Gurney, K. (2007). The basal ganglia and cortex implement optimal decision making between alternative actions. *Neural Computation*, *19*(2), 442–477. https://doi.org/10.1162/neco.2007.19.2.442

Bogovic, J. A., Prince, J. L., & Bazin, P.-L. (2013). A multiple object geometric deformable model for image segmentation. *Computer Vision and Image Understanding*, *117*(2), 145–157. https://doi.org/10.1016/j.cviu.2012.10.006

Boorman, E. D. D., O'Shea, J., Sebastian, C., Rushworth, M. F. S. F. S. S., Johansen-Berg, H., O'Shea, J., … Johansen-Berg, H. (2007).

Individual Differences in White-Matter Microstructure Reflect Variation in Functional Connectivity during Choice. *Current Biology*, *17*(16), 1426–1431. https://doi.org/10.1016/j.cub.2007.07.040

Bordelon, Y. M., Hays, R. D., Vassar, S. D., Diaz, N., Bronstein, J., & Vickrey, B. G. (2011). Medication responsiveness of motor symptoms in a population-based study of parkinson disease. *Parkinson's Disease*. https://doi.org/10.4061/2011/967839

Borra, E., Gerbella, M., Rozzi, S., & Luppino, G. (2015). Projections from caudal ventrolateral prefrontal areas to brainstem preoculomotor structures and to Basal Ganglia and cerebellar oculomotor loops in the macaque. *Cerebral Cortex*, *25*(3), 748–764. https://doi.org/10.1093/cercor/bht265

Bosco, D. A., LaVoie, M. J., Petsko, G. A., & Ringe, D. (2011). Proteostasis and movement disorders: Parkinson's disease and amyotrophic lateral sclerosis. *Cold Spring Harbor Perspectives in Biology*, *3*(10), 1–24. https://doi.org/10.1101/cshperspect.a007500

Bot, M., Bour, L., De Bie, R. M., Contarino, M. F., Schuurman, P. R., & Van Den Munckhof, P. (2016). Can We Rely on Susceptibility-Weighted Imaging for Subthalamic Nucleus Identification in Deep Brain Stimulation Surgery? *Neurosurgery*, *78*(3), 353–359. https://doi.org/10.1227/NEU.0000000000001130

Bot, M., Schuurman, P. R., Odekerken, V. J. J., Verhagen, R., Contarino, F. M., De Bie, R. M. A., & van den Munckhof, P. (2018). Deep brain stimulation for Parkinson's disease: defining the optimal location within the subthalamic nucleus. *Journal of Neurology, Neurosurgery, and Psychiatry*, *89*(5), 493–498. https://doi.org/10.1136/jnnp-2017-316907

Bot, M., Verhagen, O., Caan, M., Potters, W. V., Dilai, Y., Odekerken, V. J. J., … van den Munckhof, P. (2019). Defining the dorsal STN border using 7.0-Tesla MRI: a comparison to microelectrode recordings and lower field strength MRI. *Brain Stimulation*, *97*(2), 587. https://doi.org/10.1016/j.brs.2018.12.952

Botvinik, M. M. (2007). Conflict monitoring and decision making: Reconciling two perspectives on anterior cingulate function. *Cognitive, Affective and Behavioral Neuroscience*, *7*(4), 356–366. https://doi.org/10.3758/CABN.7.4.356

Bour, L. J., Contarino, M. F., Foncke, E. M. J., De Bie, R. M. A., Van Den Munckhof, P., Speelman, J. D., & Schuurman, P. R. (2010). Long-term experience with intraoperative microrecording during DBS neurosurgery in STN and GPi. *Acta Neurochirurgica*, *152*(12), 2069–2077. https://doi.org/10.1007/s00701-010-0835-y

Bourekas, E. C., Christoforidis, G. A., Abduljalil, A. M., Kangarlu, A., Chakeres, D. W., Spigos, D. G., & Robitaille, P.-M. L. (1999). High Resolution MRI of the Deep Gray Nuclei at 8 Tesla. *Journal of Computer Assisted Tomography*, *23*(6), 867–874. https://doi.org/10.1097/00004728-199911000-00009

Bouvy, W. H., Biessels, G. J., Kuijf, H. J., Kappelle, L. J., Luijten, P. R., & Zwanenburg, J. J. M. (2014). Visualization of Perivascular Spaces and Perforating Arteries With 7 T Magnetic Resonance Imaging. *Investigative Radiology*, *49*(5), 307–313. https://doi.org/10.1097/rli.0000000000000027

Bouvy, W. H., Zwanenburg, J. J. M., Reinink, R., Wisse, L. E. M., Luijten, P. R., Kappelle, L. J., … Biessels, G. J. (2016). Perivascular spaces on 7 Tesla brain MRI are related to markers of small vessel disease but not to age or cardiovascular risk factors. *Journal of Cerebral Blood Flow & Metabolism*, *36*(10), 1708–1717. https://doi.org/10.1177/0271678x16648970

Braak, H., & Del Tredici, K. (2008). Cortico-basal ganglia-cortical circuitry in Parkinson's disease reconsidered. *Experimental Neurology*, *212*(1), 226–229. https://doi.org/10.1016/j.expneurol.2008.04.001

Braak, H., Bohl, J. R., Müller, C. M., Rüb, U., de Vos, R. A. I., & Del Tredici, K. (2006). Stanley Fahn lecture 2005: The staging procedure for the inclusion body pathology associated with sporadic Parkinson's disease reconsidered. *Movement Disorders*. https://doi.org/10.1002/mds.21065

Bramerio, M., Guerrini, R., Biagi, L., De Ciantis, A., Pelliccia, V., Costagli, M., … Guerrini, R. (2016). 7T MRI in focal epilepsy with unrevealing conventional field strength imaging. *Epilepsia*, *57*(3), 445–454. https://doi.org/10.1111/epi.13313

Brau, A. (2007). New Parallel Imaging Method Enhances Imaging Speed and Accuracy. *A GE Healthcare MR Publication*, 36–38.

Brau, A., Beatty, P. J., Skare, S., & Bammer, R. (2008). Comparison of reconstruction accuracy and efficiency among autocalibrating data-driven parallel imaging methods. *Magnetic Resonance in Medicine*, *59*(2), 382–395. https://doi.org/10.1002/mrm.21481

Brodsky, M. A., Anderson, S., Murchison, C., Seier, M., Wilhelm, J., Vederman, A., & Burchiel, K. J. (2017). Clinical outcomes of asleep vs awake deep brain stimulation for Parkinson disease. *Neurology*, *89*(19), 1944–1950. https://doi.org/10.1212/wnl.0000000000004630

Bronfeld, M., & Bar-Gad, I. (2011). Loss of specificity in basal ganglia related movement disorders. *Frontiers in Systems Neuroscience*, *5*, 38. https://doi.org/10.3389/fnsys.2011.00038

Bronstein, J. M., Tagliati, M., Alterman, R. L., Lozano, A. M., Volkmann, J., Stefani, A., … DeLong, M. R. (2011). Deep brain stimulation for Parkinson disease an expert consensus and review of key issues. *Archives of Neurology*, *68*(1), 165–171. https://doi.org/10.1001/archneurol.2010.260

Brown, J. W., Bullock, D., & Grossberg, S. (2004). How laminar frontal cortex and basal ganglia circuits interact to control planned and reactive saccades. *Neural Networks*, *17*(4), 471–510. https://doi.org/10.1016/j.neunet.2003.08.006

Brown, R. (1828). A brief account of microscopical observations on the particles contained in the pollen of plants. *Philosoph Mag Ann Philosophy* , *4*(21), 1–16.

Brunenberg, E. J. L. L., Moeskops, P., Backes, W. H., Pollo, C., Cammoun, L., Vilanova, A., … Platel, B. (2012). Structural and Resting State Functional Connectivity of the Subthalamic Nucleus: Identification of Motor {STN} Parts and the Hyperdirect Pathway. *PLoS ONE*, *7*(6), e39061. https://doi.org/10.1371/journal.pone.0039061

Bryden, D. W., Brockett, A. T., Blume, E., Heatley, K., Zhao, A., & Roesch, M. R. (2018). Single Neurons in Anterior Cingulate Cortex Signal the Need to Change Action During Performance of a Stop-change Task that Induces Response Competition. *Cerebral Cortex*. https://doi.org/10.1093/cercor/bhy008

Budde, J., Shajan, G., Hoffmann, J., Ugurbil, K., & Pohmann, R. (2010). Human imaging at 9.4 T using T2*-, phase-, and susceptibility-weighted contrast. *Magnetic Resonance in Medicine*, *65*(2), 544–550. https://doi.org/10.1002/mrm.22632

Budde, J., Shajan, G., Scheffler, K., & Pohmann, R. (2014). Ultra-high resolution imaging of the human brain using acquisition-weighted imaging at 9.4T. *NeuroImage*, *86*, 592–598. https://doi.org/10.1016/j.neuroimage.2013.08.013

Budinger, T. F., Bird, M. D., Frydman, L., Long, J. R., Mareci, T. H., Rooney, W. D., … Wald, L. L. (2016). Toward 20~T magnetic resonance for human brain studies: opportunities for discovery and neuroscience rationale. *Magnetic Resonance Materials in Physics, Biology and Medicine*, *29*(3), 617–639. https://doi.org/10.1007/s10334-016-0561-4

Budrys, T., Veikutis, V., Lukosevicius, S., Gleizniene, R., Monastyreckiene, E., & Kulakiene, I. (2018). Artifacts in magnetic resonance imaging: How it can really affect diagnostic image quality and confuse clinical diagnosis? *Journal of Vibroengineering*, *20*(2), 1202–1213. https://doi.org/10.21595/jve.2018.19756

Burchiel, K. J., McCartney, S., Lee, A., & Raslan, A. M. (2013). Accuracy of deep brain stimulation electrode placement using intraoperative computed tomography without microelectrode recording. *Journal of Neurosurgery*, *119*(2), 301–306. https://doi.org/10.3171/2013.4.JNS122324

Bus, S., van den Munckhof, P., Bot, M., Pal, G., Ouyang, B., Sani, S., … Verhagen Metman, L. (2018). Borders of STN determined by MRI versus the electrophysiological STN. A comparison using intraoperative CT. *Acta Neurochirurgica*, *160*(2), 373–383. https://doi.org/10.1007/s00701-017-3432-5

Caan, M. W. A., Bazin, P. L., Marques, J. P., de Hollander, G., Dumoulin, S. O., & van der Zwaag, W. (2019). MP2RAGEME: T 1 , T 2* , and QSM mapping in one sequence at 7Tesla. *Human Brain Mapping*, *40*(6), 1786–1798. https://doi.org/10.1002/hbm.24490

Cabezas, M., Oliver, A., Lladó, X., Freixenet, J., & Cuadra, M. B. (2011). A review of atlas-based segmentation for magnetic resonance brain images. *Computer Methods and Programs in Biomedicine*, *104*(3), e158--e177. https://doi.org/10.1016/j.cmpb.2011.07.015

Cacciola, A., Calamuneri, A., Milardi, D., Mormina, E., Chillemi, G., Marino, S., … Quartarone, A. (2017). A connectomic analysis of the human basal ganglia network. *Frontiers in Neuroanatomy*, *11*. https://doi.org/10.3389/fnana.2017.00085

Cakmakli, G. Y., Oruckaptan, H., Saka, E., & Elibol, B. (2009). Reversible acute cognitive dysfunction induced by bilateral STN stimulation. *Journal of Neurology*, *256*(8), 1360–1362. https://doi.org/10.1007/s00415-009-5103-9

Calabresi, P., Centonze, D., & Bernardi, G. (2000). Electrophysiology of dopamine in normal and denervated striatal neurons. *Trends in Neurosciences*, *23*(10), S57–S63. https://doi.org/10.1016/S1471-1931(00)00017-3

Calamante, F., Oh, S.-H., Tournier, J.-D., Park, S.-Y., Son, Y.-D., Chung, J.-Y., … Cho, Z.-H. (2013). Super-resolution track-density imaging of thalamic substructures: Comparison with high-resolution anatomical magnetic resonance imaging at 7.0T. *Human Brain Mapping*, *34*(10), 2538–2548. https://doi.org/10.1002/hbm.22083

Callaghan, M. F., Josephs, O., Herbst, M., Zaitsev, M., Todd, N., & Weiskopf, N. (2015). An evaluation of prospective motion correction (PMC) for high resolution quantitative MRI. *Frontiers in Neuroscience*, *9*(MAR), 97. https://doi.org/10.3389/fnins.2015.00097

Calzavara, R., Mailly, P., & Haber, S. N. (2007). Relationship between the corticostriatal terminals from areas 9 and 46, and those from area 8A, dorsal and rostral premotor cortex and area 24c: An anatomical substrate for cognition to action. *European Journal of Neuroscience*, *26*(7), 2005–2024. https://doi.org/10.1111/j.1460-9568.2007.05825.x

Chalifoux, J. R., Perry, N., Katz, J. S., Wiggins, G. C., Roth, J., Miles, D., … Milla, S. S. (2013). The ability of high field strength 7-T magnetic resonance imaging to reveal previously uncharacterized brain lesions in patients with tuberous sclerosis complex. *Journal of Neurosurgery: Pediatrics*, *11*(3), 268–273. https://doi.org/10.3171/2012.12.peds12338

Chambers, C. D., Garavan, H., & Bellgrove, M. A. (2009). Insights into the neural basis of response inhibition from cognitive and clinical neuroscience. *Neuroscience and Biobehavioral Reviews*. https://doi.org/10.1016/j.neubiorev.2008.08.016

Chandran, A. S., Bynevelt, M., & Lind, C. R. P. P. (2015). Magnetic resonance imaging of the subthalamic nucleus for deep brain stimulation. *Journal of Neurosurgery*, *124*(1), 96–105. https://doi.org/10.3171/2015.1.jns142066

Charles Stud, A., & Ramamurthy, N. (2019). Interpolation of the histogramed MR brain images for resolution enhancement. *International Journal of Innovative Technology and Exploring Engineering*, *8*(11), 1253–1256. https://doi.org/10.35940/ijitee.J9425.0981119

Chatnuntawech, I., McDaniel, P., Cauley, S. F., Gagoski, B. A., Langkammer, C., Martin, A., … Bilgic, B. (2017). Single-step quantitative susceptibility mapping with variational penalties. *NMR in Biomedicine*, *30*(4). https://doi.org/10.1002/nbm.3570

Chaudhuri, K. R., & Schapira, A. H. (2009). Non-motor symptoms of Parkinson's disease: dopaminergic pathophysiology and treatment. *The Lancet Neurology*, *8*(5), 464–474. https://doi.org/10.1016/S1474-4422(09)70068-7

Chavhan, G. B., Babyn, P. S., Jankharia, B. G., Cheng, H. L. M., & Shroff, M. M. (2008). Steady-state MR imaging sequences: Physics, classification, and clinical applications. *Radiographics*, *28*(4), 1147–1160. https://doi.org/10.1148/rg.284075031

Chavhan, G. B., Babyn, P. S., Thomas, B., Shroff, M. M., Mark Haacke, E., & Haacke, E. M. (2009). Principles, Techniques, and Applications of T2*-based MR Imaging and Its Special Applications. *RadioGraphics*, *29*(5), 1433–1449. https://doi.org/10.1148/rg.295095034

Chen, S. Y., Lee, C. C., Lin, S. H., Hsin, Y. L., Lee, T. W., Yen, P. S., … Lin, S. Z. (2006). Microelectrode recording can be a good adjunct in magnetic resonance image-directed subthalamic nucleus deep brain stimulation for parkinsonism. *Surgical Neurology*, *65*(3), 253–260.

https://doi.org/10.1016/j.surneu.2005.06.029

Chen, S. Y., Tsai, S., & Li, S. H. (2011). Controversial Issues in Deep Brain Stimulation in Parkinson's Disease. *Towards New Therapies for Parkinson's Disease*. https://doi.org/10.5772/16705

Chen, T., Mirzadeh, Z., & Ponce, F. A. (2017). "Asleep" Deep Brain Stimulation Surgery: A Critical Review of the Literature. *World Neurosurgery*, *105*, 191–198. https://doi.org/10.1016/j.wneu.2017.05.042

Chen, T., Mirzadeh, Z., Chapple, K. M., Lambert, M., Shill, H. A., Moguel-Cobos, G., … Ponce, F. A. (2018). Clinical outcomes following awake and asleep deep brain stimulation for Parkinson disease. *Journal of Neurosurgery*, *130*(1), 109–120. https://doi.org/10.3171/2017.8.jns17883

Chen, T., Mirzadeh, Z., Chapple, K., Lambert, M., Dhall, R., & Ponce, F. A. (2016). Asleep deep brain stimulation for essential tremor. *Journal of Neurosurgery*, *124*(6), 1842–1849. https://doi.org/10.3171/2015.6.JNS15526

Chen, Z., Johnston, L. A., Kwon, D.-H., Oh, S. H., Cho, Z. H. E., & Gary, F. (2010). An optimised framework for reconstructing and processing MR phase images. *NeuroImage*, *49*(2), 1289–1300. https://doi.org/10.1016/j.neuroimage.2009.09.071

Cheng, H. L. M., & Wright, G. A. (2006). Rapid high-rsolution T1 mapping by variable flip angles: Accurate and precise measurements in the presence of radiofrequency field inhomogeneity. *Magnetic Resonance in Medicine*, *55*(3), 566–574. https://doi.org/10.1002/mrm.20791

Chiken, S., & Nambu, A. (2016). Mechanism of Deep Brain Stimulation: Inhibition, Excitation, or Disruption? *The Neuroscientist : A Review Journal Bringing Neurobiology, Neurology and Psychiatry*, *22*(3), 313–322. https://doi.org/10.1177/1073858415581986

Chilla, G. S., Tan, C. H., Xu, C., & Poh, C. L. (2015). Diffusion weighted magnetic resonance imaging and its recent trend-a survey. *Quantitative Imaging in Medicine and Surgery*, *5*(3), 407–422. https://doi.org/10.3978/j.issn.2223-4292.2015.03.01

Cho, Z.-H. (2016). Review of Recent Advancement of Ultra High Field Magnetic Resonance Imaging: from Anatomy to Tractography. *Investigative Magnetic Resonance Imaging*, *20*(3), 141. https://doi.org/10.13104/imri.2016.20.3.141

Cho, Z.-H., Choi, S. H., Chi, J.-G., & Kim, Y.-B. B. (2011). Classification of the venous architecture of the pineal gland by 7T MRI. *Journal of Neuroradiology*, *38*(4), 238–241. https://doi.org/10.1016/j.neurad.2011.02.010

Cho, Z.-H., Han, J.-Y., Hwang, S., Kim, D.-S., Kim, K.-N., Kim, N.-B., … Kim, Y. B. B. (2010). Quantitative analysis of the hippocampus using images obtained from 7.0~T MRI. *NeuroImage*, *49*(3), 2134–2140. https://doi.org/10.1016/j.neuroimage.2009.11.002

Cho, Z.-H., Kim, Y.-B. B., Han, J.-Y. Y., Min, H.-K. K., Kim, K.-N. N., Choi, S.-H. H., … Shepp, L. A. (2008). New brain atlas-mapping the human brain in vivo with 7.0 T MRI and comparison with postmortem histology: Will these images change modern medicine? *International Journal of Imaging Systems and Technology*, *18*(1), 2–8. https://doi.org/10.1002/ima.20143

Cho, Z.-H., Oh, S.-H., Kim, J.-M., Park, S.-Y., Kwon, D.-H., Jeong, H.-J., … Jeon, B. S. (2011). Direct visualization of Parkinsons disease by in vivo human brain imaging using 7.0T magnetic resonance imaging. *Movement Disorders*, *26*(4), 713–718. https://doi.org/10.1002/mds.23465

Cho, Z.-H., Son, Y.-D., Kim, H.-K., Kim, N.-B., Choi, E.-J., Lee, S.-Y., … Ogawa, S. (2011). Observation of Glucose Metabolism in the Thalamic Nuclei by Fusion PET/MRI. *Journal of Nuclear Medicine*, *52*(3), 401–404. https://doi.org/10.2967/jnumed.110.081281

Choi, U.-S., Kawaguchi, H., Matsuoka, Y., Kober, T., & Kida, I. (2018). Brain tissue segmentation based on MP2RAGE multi-contrast images in 7T MRI. *BioRxiv*, 455576. https://doi.org/10.1101/455576

Christoforidis, G. A., Bourekas, E. C., Baujan, M., Abduljalil, A. M., Kangarlu, A., Spigos, D. G., … Robitaille, P.-M. L. (1999). High Resolution MRI of the Deep Brain Vascular Anatomy at 8 Tesla: Susceptibility-Based Enhancement of the Venous Structures. *Journal of Computer Assisted Tomography*, *23*(6), 857–866. https://doi.org/10.1097/00004728-199911000-00008

Chung, J. W., Burciu, R. G., Ofori, E., Shukla, P., Okun, M. S., Hess, C. W., & Vaillancourt, D. E. (2017). Parkinson's disease diffusion MRI is not affected by acute antiparkinsonian medication. *NeuroImage: Clinical*. https://doi.org/10.1016/j.nicl.2017.02.012

Cochrane, C. J., & Ebmeier, K. P. (2013). Diffusion tensor imaging in parkinsonian syndromes: A systematic review and meta-analysis. *Neurology*. https://doi.org/10.1212/WNL.0b013e318284070c

Cock, P. J. A., Antao, T., Chang, J. T., Chapman, B. A., Cox, C. J., Dalke, A., … de Hoon, M. J. L. (2009). Biopython: freely available Python tools for computational molecular biology and bioinformatics. *Bioinformatics*, *25*(11), 1422–1423. https://doi.org/10.1093/bioinformatics/btp163

Cohen-Adad, J., Polimeni, J. R., Helmer, K. G., Benner, T., McNab, J. A., Wald, L. L., … Mainero, C. (2012). T2 mapping and B0 orientation-dependence at 7T reveal cyto- and myeloarchitecture organization of the human cortex. *NeuroImage*, *60*(2), 1006–1014. https://doi.org/10.1016/j.neuroimage.2012.01.053

Contarino, M. F., Bour, L. J., Verhagen, R., Lourens, M. A. J., De Bie, R. M. A., Van Den Munckhof, P., & Schuurman, P. R. (2014). Directional steering: A novel approach to deep brain stimulation. *Neurology*, *83*(13), 1163–1169. https://doi.org/10.1212/WNL.0000000000000823

Cosottini, M., Frosini, D., Pesaresi, I., Costagli, M., Biagi, L., Ceravolo, R., … Tosetti, M. (2014). MR Imaging of the Substantia Nigra at 7 T Enables Diagnosis of Parkinson Disease. *Radiology*, *271*(3), 831–838. https://doi.org/10.1148/radiol.14131448

Cosottini, M., Frosini, D., Pesaresi, I., Donatelli, G., Cecchi, P., Costagli, M., … Tosetti, M. (2015). Comparison of 3T and 7T Susceptibility-Weighted Angiography of the Substantia Nigra in Diagnosing Parkinson Disease. *American Journal of Neuroradiology*, *36*(3), 461–466. https://doi.org/10.3174/ajnr.a4158

Costagli, M., Symms, M. R., Angeli, L., Kelley, D. A. C., Biagi, L., Farnetani, A., … Cosottini, M. (2015). Assessment of Silent T1-weighted head imaging at 7~T. *European Radiology*, *26*(6), 1879–1888. https://doi.org/10.1007/s00330-015-3954-2

Crocker, L. D., Heller, W., Warren, S. L., O'Hare, A. J., Infantolino, Z. P., & Miller, G. A. (2013). Relationships among cognition, emotion, and motivation: Implications for intervention and neuroplasticity in psychopathology. *Frontiers in Human Neuroscience*, *7*, 261. https://doi.org/10.3389/fnhum.2013.00261

Cronin, M. J., Wharton, S., Al-Radaideh, A., Constantinescu, C., Evangelou, N., Bowtell, R., & Gowland, P. A. (2016). A comparison of phase imaging and quantitative susceptibility mapping in the imaging of multiple sclerosis lesions at ultrahigh field. *Magnetic Resonance Materials in Physics, Biology and Medicine*, *29*(3), 543–557. https://doi.org/10.1007/s10334-016-0560-5

Curley, L. B., Newman, E., Thompson, W. K., Brown, T. T., Hagler, D. J., Akshoomoff, N., … Jernigan, T. L. (2018). Cortical morphology of the pars opercularis and its relationship to motor-inhibitory performance in a longitudinal, developing cohort. *Brain Structure and Function*. https://doi.org/10.1007/s00429-017-1480-5

Cyron, D. (2016). Mental side effects of deep brain stimulation (DBS) for movement disorders: The futility of denial. *Frontiers in Integrative Neuroscience*, *10*(4). https://doi.org/10.3389/fnint.2016.00017

Dammann, P., Kraff, O., Wrede, K. H., Özkan, N., Orzada, S., Mueller, O. M., … Gasser, T. (2011). Evaluation of Hardware-related Geometrical Distortion in Structural MRI at 7 Tesla for Image-guided Applications in Neurosurgery. *Academic Radiology*, *18*(7), 910–916. https://doi.org/10.1016/j.acra.2011.02.011

Damoiseaux, J. S., & Greicius, M. D. (2009). Greater than the sum of its parts: a review of studies combining structural connectivity and resting-state functional connectivity. *Brain Structure and Function*, *213*(6), 525–533. https://doi.org/10.1007/s00429-009-0208-6

Daniluk, S., Davies, K. G., Ellias, S. A., Novak, P., & Nazzaro, J. M. (2009). Assessment of the variability in the anatomical position and size of the subthalamic nucleus among patients with advanced Parkinson's disease using magnetic resonance imaging. *Acta Neurochirurgica*, *152*(2), 201–210. https://doi.org/10.1007/s00701-009-0514-z

Dauguet, J., Delzescaux, T., Condé, F., Mangin, J. F., Ayache, N., Hantraye, P., & Frouin, V. (2007). Three-dimensional reconstruction of stained histological slices and 3D non-linear registration with in-vivo MRI for whole baboon brain. *Journal of Neuroscience Methods*, *164*(1), 191–204. https://doi.org/10.1016/j.jneumeth.2007.04.017

Dayan, E., & Browner, N. (2017). Alterations in striato-thalamo-pallidal intrinsic functional connectivity as a prodrome of Parkinson's disease. *NeuroImage: Clinical*. https://doi.org/10.1016/j.nicl.2017.08.003

de Hollander, G., Keuken, M. C., & Forstmann, B. U. (2015). The Subcortical Cocktail Problem; Mixed Signals from the Subthalamic Nucleus and Substantia Nigra. *PLoS ONE*, *10*(3), e0120572. https://doi.org/10.1371/journal.pone.0120572

de Hollander, G., Keuken, M. C., Bazin, P.-L., Weiss, M., Neumann, J., Reimann, K., … Schäfer, A. (2014). A gradual increase of iron toward the medial-inferior tip of the subthalamic nucleus. *Human Brain Mapping, 35*(9), 4440–4449. https://doi.org/10.1002/hbm.22485

de Hollander, G., Keuken, M. C., van der Zwaag, W., Forstmann, B. U., & Trampel, R. (2017). Comparing functional MRI protocols for small, iron-rich basal ganglia nuclei such as the subthalamic nucleus at 7 T and 3 T. *Human Brain Mapping*, *38*(6), 3226–3248. https://doi.org/10.1002/hbm.23586

de Martino, F., Moerel, M., van de Moortele, P. F., Ugurbil, K., Goebel, R., Yacoub, E., & Formisano, E. (2013). Spatial organization of frequency preference and selectivity in the human inferior colliculus. *Nature Communications*, *4*(1). https://doi.org/10.1038/ncomms2379

de Martino, F., Moerel, M., Xu, J., van de Moortele, P. F., Ugurbil, K., Goebel, R., … Formisano, E. (2014). High-Resolution Mapping of Myeloarchitecture In Vivo: Localization of Auditory Areas in the Human Brain. *Cerebral Cortex (New York, N.Y. : 1991)*, *25*(10), 3394–3405. https://doi.org/10.1093/cercor/bhu150

de Oliveira Godeiro, C., Moro, E., & Montgomery, E. B. (2020). Programming: General Aspects. In *Fundamentals and Clinics of Deep Brain Stimulation* (pp. 93–125). https://doi.org/10.1007/978-3-030-36346-8_8

De Reuck, J. L., Auger, F., Durieux, N., Deramecourt, V., Maurage, C.-A., Cordonnier, C., … Bordet, R. (2017). Frequency and topography of small cerebrovascular lesions in vascular and in mixed dementia: a post-mortem 7-tesla magnetic resonance imaging study with neuropathological correlates. *Folia Neuropathologica*, *1*, 31–37. https://doi.org/10.5114/fn.2017.66711

De Reuck, J. L., Caparros-Lefebvre, D., Deramecourt, V., Defebvre, L., Auger, F., Durieux, N., … Maurage, C.-A. (2014). Original article Prevalence of small cerebral bleeds in patients with progressive supranuclear palsy: a~neuropathological study with 7.0-Tesla magnetic resonance imaging correlates. *Folia Neuropathologica*, *4*, 421–427. https://doi.org/10.5114/fn.2014.47843

De Reuck, J. L., Deramecourt, V., Auger, F., Durieux, N., Cordonnier, C., Devos, D., … Bordet, R. (2014). Iron deposits in post-mortem brains of patients with neurodegenerative and cerebrovascular diseases: a semi-quantitative 7.0~T magnetic resonance imaging study. *European Journal of Neurology*, *21*(7), 1026–1031. https://doi.org/10.1111/ene.12432

De Reuck, J. L., Deramecourt, V., Auger, F., Durieux, N., Cordonnier, C., Devos, D., … Bordet, R. (2015). The Significance of Cortical Cerebellar Microbleeds and Microinfarcts in Neurodegenerative and Cerebrovascular Diseases. *Cerebrovascular Diseases*, *39*(2), 138–143. https://doi.org/10.1159/000371488

de Rotte, A. A. J., Groenewegen, A., Rutgers, D. R., Witkamp, T., Zelissen, P. M. J., Meijer, F. J. A., … Hendrikse, J. (2015). High resolution pituitary gland MRI at 7.0 tesla: a clinical evaluation in Cushing's disease. *European Radiology*, *26*(1), 271–277. https://doi.org/10.1007/s00330-015-3809-x

de Zwart, J. A., Ledden, P. J., Kellman, P., van Gelderen, P., & Duyn, J. H. (2002). Design of a SENSE-optimized high-sensitivity MRI

receive coil for brain imaging. *Magnetic Resonance in Medicine*, *47*(6), 1218–1227. https://doi.org/10.1002/mrm.10169

Deistung, A., Schäfer, A., Schweser, F., Biedermann, U., Güllmar, D., Trampel, R., … Reichenbach, J. R. (2013). High-Resolution MR Imaging of the Human Brainstem In vivo at 7 Tesla. *Frontiers in Human Neuroscience*, *7*. https://doi.org/10.3389/fnhum.2013.00710

Deistung, A., Schäfer, A., Schweser, F., Biedermann, U., Turner, R., & Reichenbach, J. R. (2013). Toward in vivo histology: A comparison of quantitative susceptibility mapping (QSM) with magnitude-, phase-, and R 2* -imaging at ultra-high magnetic field strength. *NeuroImage*, *65*, 299–314. https://doi.org/10.1016/j.neuroimage.2012.09.055

Dekkers, I. A., de Boer, A., Sharma, K., Cox, E. F., Lamb, H. J., Buckley, D. L., … Francis, S. (2020). Consensus-based technical recommendations for clinical translation of renal T1 and T2 mapping MRI. *Magnetic Resonance Materials in Physics, Biology and Medicine*, *33*(1), 163–176. https://doi.org/10.1007/s10334-019-00797-5

Dell'Acqua, F., Simmons, A., Williams, S. C. R., & Catani, M. (2013). Can spherical deconvolution provide more information than fiber orientations? Hindrance modulated orientational anisotropy, a true-tract specific index to characterize white matter diffusion. *Human Brain Mapping*, *34*(10), 2464–2483. https://doi.org/10.1002/hbm.22080

den Dunnen, W. F. A. A., & Staal, M. J. (2005). Anatomical alterations of the subthalamic nucleus in relation to age: A postmortem study. *Movement Disorders*, *20*(7), 893–898. https://doi.org/10.1002/mds.20417

Denison, R. N., Vu, A. T., Yacoub, E., Feinberg, D. A., & Silver, M. A. (2014). Functional mapping of the magnocellular and parvocellular subdivisions of human LGN. *NeuroImage*, *102*, 358–369. https://doi.org/10.1016/j.neuroimage.2014.07.019

Deoni, S. C. L. (2007). High-resolution T1 mapping of the brain at 3T with driven equilibrium single pulse observation of T1 with high-speed incorporation of RF field inhomogeneities (DESPOT1-HIFI). *Journal of Magnetic Resonance Imaging*, *26*(4), 1106–1111. https://doi.org/10.1002/jmri.21130

Deoni, S. C. L., Peters, T. M., & Rutt, B. K. (2005). High-resolution T1 and T2 mapping of the brain in a clinically acceptable time with DESPOT1 and DESPOT2. *Magnetic Resonance in Medicine*, *53*(1), 237–241. https://doi.org/10.1002/mrm.20314

Derix, J., Yang, S., Lüsebrink, F., Fiederer, L. D. J., Schulze-Bonhage, A., Aertsen, A., … Ball, T. (2014). Visualization of the amygdalo-hippocampal border and its structural variability by 7T and 3T magnetic resonance imaging. *Human Brain Mapping*, *35*(9), 4316–4329. https://doi.org/10.1002/hbm.22477

Deshmane, A., Gulani, V., Griswold, M. A., & Seiberlich, N. (2012). Parallel MR imaging. *Journal of Magnetic Resonance Imaging*, *36*(1), 55–72. https://doi.org/10.1002/jmri.23639

Despotović, I., Goossens, B., & Philips, W. (2015). MRI Segmentation of the Human Brain: Challenges, Methods, and Applications. *Computational and Mathematical Methods in Medicine*. https://doi.org/10.1155/2015/450341

Deuschl, G., Schade-Brittinger, C., Krack, P., Volkmann, J., Schäfer, H., Bötzel, K., … Voges, J. (2006). A randomized trial of deep-brain stimulation for Parkinson's disease. *New England Journal of Medicine*, *355*(9), 896–908. https://doi.org/10.1056/NEJMoa060281

Devlin, J. T., & Poldrack, R. A. (2007). In praise of tedious anatomy. *NeuroImage*, *37*(4), 1033–1041. https://doi.org/10.1016/j.neuroimage.2006.09.055

Dezortova, M., Herynek, V., Krssak, M., Kronerwetter, C., Trattnig, S., & Hajek, M. (2012). Two forms of iron as an intrinsic contrast agent in the basal ganglia of PKAN patients. *Contrast Media & Molecular Imaging*, *7*(6), 509–515. https://doi.org/10.1002/cmmi.1482

Di Ieva, A., Tschabitscher, M., Galzio, R. J., Grabner, G., Kronnerwetter, C., Widhalm, G., … Trattnig, S. (2011). The veins of the nucleus dentatus: Anatomical and radiological findings. *NeuroImage*, *54*(1), 74–79. https://doi.org/10.1016/j.neuroimage.2010.07.045

Di Martino, A., Scheres, A., Margulies, D. S., Kelly, A. M. C., Uddin, L. Q., Shehzad, Z., … Milham, M. P. (2008). Functional connectivity of human striatum: A resting state fMRI study. *Cerebral Cortex*, *18*(12), 2735–2747. https://doi.org/10.1093/cercor/bhn041

Dice, L. R. (1945). Measures of the Amount of Ecologic Association Between Species. *Ecology*, *26*(3), 297–302. https://doi.org/10.2307/1932409

Dickie, D. ., Shenkin, S. D., Anblagan, D., Lee, J., Blesa Cabez, M., Rodriguez, D., … Wardlaw, J. M. (2017). Whole Brain Magnetic Resonance Image Atlases: A Systematic Review of Existing Atlases and Caveats for Use in Population Imaging. *Frontiers in Neuroinformatics*. https://doi.org/10.3389/fninf.2017.00001

Diedrichsen, J., Maderwald, S., Küper, M., Thürling, M., Rabe, K., Gizewski, E. R., … Timmann, D. (2011). Imaging the deep cerebellar nuclei: A probabilistic atlas and normalization procedure. *NeuroImage*, *54*(3), 1786–1794. https://doi.org/10.1016/j.neuroimage.2010.10.035

Ding, L., & Gold, J. L. L. (2013). The Basal Ganglia's Contributions to Perceptual Decision Making. *Neuron*, *79*(4), 640–649. https://doi.org/10.1016/j.neuron.2013.07.042

Ding, S. L., Royall, J. J., Sunkin, S. M., Ng, L., Facer, B. A. C., Lesnar, P., … Lein, E. S. (2016). Comprehensive cellular-resolution atlas of the adult human brain. *Journal of Comparative Neurology*, *524*(16), Spc1--Spc1. https://doi.org/10.1002/cne.24097

Dinse, J., Härtwich, N., Waehnert, M. D., Tardif, C. L., Schäfer, A., Geyer, S., … Bazin, P.-L. L. (2015). A cytoarchitecture-driven myelin model reveals area-specific signatures in human primary and secondary areas using ultra-high resolution in-vivo brain MRI. *NeuroImage*, *114*, 71–87. https://doi.org/10.1016/j.neuroimage.2015.04.023

Dirckx, J. H. (1998). Federative Committee on Anatomical Terminology FCAT. Terminologia Anatomica. International Anatomical Terminology. In *Federative Committee on Anatomical Terminology FCAT. Terminologia Anatomica. International Anatomical Terminology* (Vol. 5). https://doi.org/10.1075/term.5.2.14dir

DIS open data. (2019). Retrieved February 24, 2020, from https://www.opendisdata.nl/

Doan, N. T., de Xivry, J. O., & Macq, B. (2010, March). Effect of inter-subject variation on the accuracy of atlas-based segmentation applied to human brain structures. *Medical Imaging 2010: Image Processing*. https://doi.org/10.1117/12.845586

Doltra, A., Dietrich, T., Schneeweis, C., Kelle, S., Doltra, A., Stawowy, P., & Fleck, E. (2013). Magnetic Resonance Imaging of Cardiovascular Fibrosis and Inflammation: From Clinical Practice to Animal Studies and Back Cardiovascular MRI View project Magnetic Resonance Imaging of Cardiovascular Fibrosis and Inflammation: From Clinical Practice to Ani. *BioMed Research International*, *676489*(10), 1–2. https://doi.org/10.1155/2013

Donahue, C. J., Sotiropoulos, S. N., Jbabdi, S., Hernandez-Fernandez, M., Behrens, T. E., Dyrby, T. B., … Glasser, M. F. (2016). Using diffusion tractography to predict cortical connection strength and distance: A quantitative comparison with tracers in the monkey. *Journal of Neuroscience*, *36*(25), 6758–6770. https://doi.org/10.1523/JNEUROSCI.0493-16.2016

Dormont, D., Ricciardi, K. G., Tandé, D., Parain, K., Menuel, C., Galanaud, D., … Yelnik, J. (2004). Is the subthalamic nucleus hypointense on T2-weighted images? A correlation study using MR imaging and stereotactic atlas data. *American Journal of Neuroradiology*, *25*(9), 1516–1523.

Dortch, R. D., Moore, J., Li, K., Jankiewicz, M., Gochberg, D. F., Hirtle, J. A., … Smith, S. A. (2013). Quantitative magnetization transfer imaging of human brain at 7T. *NeuroImage*, *64*, 640–649. https://doi.org/10.1016/j.neuroimage.2012.08.047

Draganski, B., Kherif, F., Klöppel, S., Cook, P. A., Alexander, D. C., Parker, G. J. M., … Frackowiak, R. S. J. (2008). Evidence for segregated and integrative connectivity patterns in the human basal ganglia. *Journal of Neuroscience*, *28*(28), 7143–7152. https://doi.org/10.1523/JNEUROSCI.1486-08.2008

Drayer, B. P. (1989). Basal ganglia: significance of signal hypointensity on T2-weighted MR images. *Radiology*, *173*(2), 311–312. https://doi.org/10.1148/radiology.173.2.2798863

Duchin, Y., Abosch, A., Yacoub, E., Sapiro, G., & Harel, N. (2012). Feasibility of Using Ultra-High Field (7T) MRI for Clinical Surgical Targeting. *PLoS ONE*, *7*(5), e37328. https://doi.org/10.1371/journal.pone.0037328

Duchin, Y., Shamir, R. R., Patriat, R., Kim, J., Vitek, J. L., Sapiro, G., & Harel, N. (2018). Patient-specific anatomical model for deep brain stimulation based on 7 Tesla MRI. *PLoS ONE*, *13*(8), e0201469. https://doi.org/10.1371/journal.pone.0201469

Duerk, J. L., & Simonetti, O. P. (1991). Theoretical aspects of motion sensitivity and compensation in echo-planar imaging. *Journal of Magnetic Resonance Imaging*, *1*(6), 643–650. https://doi.org/10.1002/jmri.1880010605

Dula, A. N., Welch, E. B., Creasy, J. L., Gatenby, J. C., Stringer, E. A., Chen, L. M., … Gore, J. C. (2010). Challenges and Opportunities of Ultra-High Field MRI. In *FMBE Proceedings* (pp. 1–5). https://doi.org/10.1007/978-3-642-12020-6_1

Dumoulin, S. O., Fracasso, A., van der Zwaag, W., Siero, J. C. W., & Petridou, N. (2018). Ultra-high field MRI: Advancing systems neuroscience towards mesoscopic human brain function. *NeuroImage*, *168*, 345–357. https://doi.org/10.1016/j.neuroimage.2017.01.028

Dunbar, R. I. M. (1992). Neocortex size as a constraint on group size in primates. *Journal of Human Evolution*, *22*(6), 469–493. https://doi.org/10.1016/0047-2484(92)90081-j

Duyn, J. (2010). Study of brain anatomy with high-field MRI: recent progress. *Magnetic Resonance Imaging*, *28*(8), 1210–1215. https://doi.org/10.1016/j.mri.2010.02.007

Duyn, J. H. (2012). The future of ultra-high field MRI and fMRI for study of the human brain. *NeuroImage*, *62*(2), 1241–1248. https://doi.org/10.1016/j.neuroimage.2011.10.065

Dyrby, T. B., Søgaard, L. V., Parker, G. J., Alexander, D. C., Lind, N. M., Baaré, W. F. C. ., … Jelsing, J. (2007). Validation of in vitro probabilistic tractography. *NeuroImage*, *37*(4), 1267–1277. https://doi.org/10.1016/j.neuroimage.2007.06.022

Eapen, M., Zald, D. H., Gatenby, J. C., Ding, Z., & Gore, J. C. (2011). Using High-Resolution MR Imaging at 7T to Evaluate the Anatomy of the Midbrain Dopaminergic System. *American Journal of Neuroradiology*, *32*(4), 688–694. https://doi.org/10.3174/ajnr.a2355

Eckstein, K., Dymerska, B., Bachrata, B., Bogner, W., Poljanc, K., Trattnig, S., & Robinson, S. D. (2018). Computationally Efficient Combination of Multi-channel Phase Data From Multi-echo Acquisitions (ASPIRE). *Magnetic Resonance in Medicine*, *79*(6), 2996–3006. https://doi.org/10.1002/mrm.26963

Edelstein, W. A., Glover, G. H., Hardy, C. J., & Redington, R. W. (1986). The intrinsic signal-to-noise ratio in NMR imaging. *Magnetic Resonance in Medicine*, *3*(4), 604–618. https://doi.org/10.1002/mrm.1910030413

Eggenschwiler, F., Kober, T., Magill, A. W., Gruetter, R., & Marques, J. P. (2012). SA2RAGE: A new sequence for fast B1+-mapping. *Magnetic Resonance in Medicine*, *67*(6), 1609–1619. https://doi.org/10.1002/mrm.23145

Eickhoff, S. B., Constable, R. T., & Yeo, B. T. T. (2018). Topographic organization of the cerebral cortex and brain cartography. *NeuroImage*, *170*, 332–347. https://doi.org/10.1016/j.neuroimage.2017.02.018

El-Gamal, F. E. Z. A., Elmogy, M., & Atwan, A. (2016). Current trends in medical image registration and fusion. *Egyptian Informatics Journal*, *17*(1), 99–124. https://doi.org/10.1016/j.eij.2015.09.002

Elolf, E., Bockermann, V., Gringel, T., Knauth, M., Dechent, P., & Helms, G. (2007). Improved visibility of the subthalamic nucleus on high-resolution stereotactic MR imaging by added susceptibility (T2*) contrast using multiple gradient echoes. *American Journal of Neuroradiology*, *28*(6), 1093–1094. https://doi.org/10.3174/ajnr.A0527

Elster, A. D. (1988). An index system for comparative parameter weighting in MR imaging. *Journal of Computer Assisted Tomography*, *12*, 130–134.

Espinosa-Parrilla, J. F., Baunez, C., & Apicella, P. (2013). Linking reward processing to behavioral output: Motor and motivational integration in the primate subthalamic nucleus. *Frontiers in Computational Neuroscience*, *7,* 175. https://doi.org/10.3389/fncom.2013.00175

Esselink, R. A. J., & Kuijf, M. L. (2020). Organization of Care for Patients Treated by Deep Brain Stimulation. In *Fundamentals and Clinics of Deep Brain Stimulation* (pp. 161–168). https://doi.org/10.1007/978-3-030-36346-8_11

Evans, A. C. (2012). Brain templates and atlases. *NeuroImage*, *62*(2), 911–922. https://doi.org/10.1016/J.NEUROIMAGE.2012.01.024

Evans, A. H., & Lees, A. J. (2004). Dopamine dysregulation syndrome in Parkinson's disease. *Current Opinion in Neurology*, *17*(4), 393–398. https://doi.org/10.1097/01.wco.0000137528.23126.41

Evans, N. J., & Wagenmakers, E.-J. (2019). Theoretically meaningful models can answer clinically relevant questions. *Brain*, *142*(5), 1170–1172. https://doi.org/10.1093/brain/awz096

Falk Delgado, A., Van Westen, D., Nilsson, M., Knutsson, L., Sundgren, P. C., Larsson, E. M., & Falk Delgado, A. (2019). Diagnostic value of alternative techniques to gadolinium-based contrast agents in MR neuroimaging—a comprehensive overview. *Insights into Imaging*, *10*(1), 1–15. https://doi.org/10.1186/s13244-019-0771-1

Fan, A. P., Bilgic, B., Gagnon, L., Witzel, T., Bhat, H., Rosen, B. R., & Adalsteinsson, E. (2014). Quantitative oxygenation venography from MRI phase. *Magnetic Resonance in Medicine*, *72*(1), 149–159. https://doi.org/10.1002/mrm.24918

Fang, J., Bao, L., Li, X., van Zijl, P. C. M., & Chen, Z. (2019). Background field removal for susceptibility mapping of human brain with large susceptibility variations. *Magnetic Resonance in Medicine*, *81*(3), 2025–2037. https://doi.org/10.1002/mrm.27492

Farhadi, F., Vosoughi, K., Shahidi, G. A., Delbari, A., Lökk, J., & Fereshtehnejad, S. M. (2017). Sexual dimorphism in Parkinson's disease: Differences in clinical manifestations, quality of life and psychosocial functioning between males and females. *Neuropsychiatric Disease and Treatment*. https://doi.org/10.2147/NDT.S124984

Faull, O. K., Jenkinson, M., Clare, S., & Pattinson, K. T. S. (2015). Functional subdivision of the human periaqueductal grey in respiratory control using 7tesla fMRI. *NeuroImage*, *113*, 356–364. https://doi.org/10.1016/j.neuroimage.2015.02.026

FDA. (2003). Criteria for Significant Risk Investigations of Magnetic Resonance Diagnostic Devices - Guidance for Industry and Food and Drug Administration Staff | FDA. Retrieved from https://www.fda.gov/regulatory-information/search-fda-guidance-documents/criteria-significant-risk-investigations-magnetic-resonance-diagnostic-devices-guidance-industry-and

Federau, C., & Gallichan, D. (2016). Motion-Correction Enabled Ultra-High Resolution In-Vivo 7T-MRI of the Brain. *PLoS ONE*, *11*(5), e0154974. https://doi.org/10.1371/journal.pone.0154974

Feingold, J., Gibson, D. J., Depasquale, B., & Graybiel, A. M. (2015). Bursts of beta oscillation differentiate postperformance activity in the striatum and motor cortex of monkeys performing movement tasks. *Proceedings of the National Academy of Sciences of the United States of America*, *112*(44), 13687–13692. https://doi.org/10.1073/pnas.1517629112

Feis, D.-L., Pelzer, E. A., Timmermann, L., & Tittgemeyer, M. (2015). Classification of symptom-side predominance in idiopathic Parkinson's disease. *Npj Parkinson's Disease*, *1*(1), 15018. https://doi.org/10.1038/npjparkd.2015.18

Felmlee, J. P., Ehman, R. L., Riederer, S. J., & Korin, H. W. (1991). Adaptive motion compensation in MRI: Accuracy of motion measurement. *Magnetic Resonance in Medicine*, *18*(1), 207–213. https://doi.org/10.1002/mrm.1910180121

Fenoy, A. J., & Simpson, R. K. (2014). Risks of common complications in deep brain stimulation surgery: Management and avoidance - Clinical article. *Journal of Neurosurgery*, *120*(1), 132–139. https://doi.org/10.3171/2013.10.JNS131225

Ferry, A., An, X., & Price, J. (2000). Prefrontal cortical projections to the striatum in macaque monkeys: evidence for an organization related to prefrontal networks. *The Journal of Comparative Neurology*, *425*(3), 447. https://doi.org/10.1002/1096-9861(20000925)425:3<447::AID-CNE9>3.0.CO;2-V

Fields, R. D. (2015). A new mechanism of nervous system plasticity: Activity-dependent myelination. *Nature Reviews Neuroscience*. https://doi.org/10.1038/nrn4023

Follett, K. A., Weaver, F. M., Stern, M., Hur, K., Harris, C. L., Luo, P., … Reda, D. J. (2010). Pallidal versus subthalamic deep-brain stimulation for Parkinson's disease. *New England Journal of Medicine*, *362*(22), 2077–2091. https://doi.org/10.1056/NEJMoa0907083

Foltynie, T., Zrinzo, L., Martinez-Torres, I., Tripoliti, E., Petersen, E., Holl, E., … Limousin, P. (2010). MRI-guided STN DBS in Parkinson's disease without microelectrode recording: efficacy and safety. *Journal of Neurology, Neurosurgery & Psychiatry*, *82*(4), 358–363. https://doi.org/10.1136/jnnp.2010.205542

Food and Drug Administration. (1998). Guidance for the Submission of Premarket Notifications for Magnetic Resonance Diagnostic Devices.

Foroutan, P., Murray, M. E., Fujioka, S., Schweitzer, K. J., Dickson, D. W., Wszolek, Z. K., & Grant, S. C. (2013). Progressive Supranuclear Palsy: High-Field-Strength MR Microscopy in the Human Substantia Nigra and Globus Pallidus. *Radiology*, *266*(1), 280–288. https://doi.org/10.1148/radiol.12102273

Forsaa, E. B., Larsen, J. P., Wentzel-Larsen, T., Goetz, C. G., Stebbins, G. T., Aarsland, D., & Alves, G. (2010). A 12-Year Population-Based Study of Psychosis in Parkinson Disease. *Archives of Neurology*, *67*(8), 996–1001. https://doi.org/10.1001/archneurol.2010.166

Forstmann, B. U., & Wagenmakers, E. J. (2015). An introduction to model-based cognitive neuroscience. In *An Introduction to Model-Based Cognitive Neuroscience*. https://doi.org/10.1007/978-1-4939-2236-9

Forstmann, B. U., Anwander, A., Schäfer, A., Neumann, J., Brown, S., Wagenmakers, E. J., … Turner, R. (2010). Cortico-striatal connections predict control over speed and accuracy in perceptual decision making. *Proceedings of the National Academy of Sciences*, *107*(36), 15916–

15920. https://doi.org/10.1073/pnas.1004932107

Forstmann, B. U., de Hollander, G., Van Maanen, L., Alkemade, A., & Keuken, M. C. (2016, January 15). Towards a mechanistic understanding of the human subcortex. *Nature Reviews Neuroscience*, Vol. 18, pp. 57–65. https://doi.org/10.1038/nrn.2016.163

Forstmann, B. U., Isaacs, B. R., & Temel, Y. (2017). Ultra High Field MRI-Guided Deep Brain Stimulation. *Trends in Biotechnology*, *35*(10), 904–907. https://doi.org/10.1016/j.tibtech.2017.06.010

Forstmann, B. U., Isaacs, B. R., & Temel, Y. (2017). Ultra-High Field MRI Guided Deep Brain Stimulation. *Trends in Biotechnology*.

Forstmann, B. U., Keuken, M. C., Jahfari, S., Bazin, P.-L., Neumann, J., Schäfer, A., … Turner, R. (2012). Cortico-subthalamic white matter tract strength predicts interindividual efficacy in stopping a motor response. *NeuroImage*, *60*(1), 370–375. https://doi.org/10.1016/j.neuroimage.2011.12.044

Forstmann, B. U., Keuken, M. C., Jahfari, S., Bazin, P.-L., Neumann, J., Schäfer, A., … Turner, R. (2012). Cortico-subthalamic white matter tract strength predicts interindividual efficacy in stopping a motor response. *NeuroImage*, *60*(1), 370–375. https://doi.org/10.1016/j.neuroimage.2011.12.044

Forstmann, B. U., Keuken, M. C., Schafer, A., Bazin, P. L., Alkemade, A., & Turner, R. (2014). Multi-modal ultra-highresolution structural 7-Tesla MRI data repository. *Scientific Data*.

Fortier, V., & Levesque, I. R. (2018). Phase processing for quantitative susceptibility mapping of regions with large susceptibility and lack of signal. *Magnetic Resonance in Medicine*, *79*(6), 3103–3113. https://doi.org/10.1002/mrm.26989

Fracasso, A., van Veluw, S. J., Visser, F., Luijten, P. R., Spliet, W., Zwanenburg, J. J. M., … Petridou, N. (2016). Lines of Baillarger in vivo and ex vivo: Myelin contrast across lamina at 7 T MRI and histology. *NeuroImage*, *133*, 163–175. https://doi.org/10.1016/j.neuroimage.2016.02.072

Francis, S., & Panchuelo, R. S. (2014). Physiological measurements using ultra-high field fMRI: a review. *Physiological Measurement*, *35*(9), R167--R185. https://doi.org/10.1088/0967-3334/35/9/r167

Frank, M. J. (2006). Hold your horses: A dynamic computational role for the subthalamic nucleus in decision making. *Neural Networks*, *19*(8), 1120–1136. https://doi.org/10.1016/j.neunet.2006.03.006

Frank, M. J., Samanta, J., Moustafa, A. A., & Sherman, S. J. (2007). Hold your horses: Impulsivity, deep brain stimulation, and medication in Parkinsonism. *Science*. https://doi.org/10.1126/science.1146157

Frankle, W. G., Laruelle, M., & Haber, S. N. (2006). Prefrontal cortical projections to the midbrain in primates: Evidence for a sparse connection. *Neuropsychopharmacology*, *31*(8), 1627–1636. https://doi.org/10.1038/sj.npp.1300990

Freedman, L., Insel, T., & Smith, Y. (2000). Subcortical projections of area 25 (subgenual cortex) of the macaque monkey. *The Journal of Comparative Neurology*, *421*(2), 172–188. https://doi.org/10.1002/(SICI)1096-9861(20000529)421:2<172::AID-CNE4>3.0.CO;2-8

Frequin, H., Bot, M., Dilai, J., Scholten, M. N., Postma, M., Bour, L. J., … Van Den Munckhof, P. (2020). Relative Contribution of Magnetic Resonance Imaging, Microelectrode Recordings, and Awake Test Stimulation in Final Lead Placement during Deep Brain Stimulation Surgery of the Subthalamic Nucleus in Parkinson's Disease. *Stereotactic and Functional Neurosurgery*, *98*, 118–128. https://doi.org/10.1159/000505710

Fritzsch, D., Reiss-Zimmermann, M., Trampel, R., Turner, R., Hoffmann, K. T., & Schäfer, A. (2014). Seven-Tesla Magnetic Resonance Imaging in Wilson Disease Using Quantitative Susceptibility Mapping for Measurement of Copper Accumulation. *Investigative Radiology*, *49*(5), 299–306. https://doi.org/10.1097/rli.0000000000000010

Frosini, D., Ceravolo, R., Tosetti, M., Bonuccelli, U., & Cosottini, M. (2017). Nigral involvement in atypical parkinsonisms: evidence from a pilot study with ultra-high field MRI. *Journal of Neural Transmission*, *123*(5), 509–513. https://doi.org/10.1007/s00702-016-1529-2

Fujioka, S., Murray, M. E., Foroutan, P., Schweitzer, K. J., Dickson, D. W., Grant, S. C., & Wszolek, Z. K. (2011). Magnetic resonance imaging with 21.1 T and pathological correlations -diffuse Lewy body disease. *Rinsho Shinkeigaku*, *51*(8), 603–607. https://doi.org/10.5692/clinicalneurol.51.603

Fukunaga, M., Li, T.-Q., van Gelderen, P., de Zwart, J. A., Shmueli, K., Yao, B., … Duyn, J. H. (2010). Layer-specific variation of iron content in cerebral cortex as a source of MRI contrast. *Proceedings of the National Academy of Sciences*, *107*(8), 3834–3839. https://doi.org/10.1073/pnas.0911177107

Gallichan, D. (2018). Diffusion MRI of the human brain at ultra-high field (UHF): A review. *NeuroImage*, *168*, 172–180. https://doi.org/10.1016/j.neuroimage.2017.04.037

Gallichan, D., Marques, J. P., & Gruetter, R. (2016). Retrospective correction of involuntary microscopic head movement using highly accelerated fat image navigators (3D FatNavs) at 7T. *Magnetic Resonance in Medicine*, *75*(3). https://doi.org/10.1002/mrm.26157

Ganzetti, M., Wenderoth, N., & Mantini, D. (2016). Quantitative Evaluation of Intensity Inhomogeneity Correction Methods for Structural MR Brain Images. *Neuroinformatics*, *14*(1), 5–21. https://doi.org/10.1007/s12021-015-9277-2

Geevarghese, R., Ogorman Tuura, R., Lumsden, D. E., Samuel, M., & Ashkan, K. (2016). Registration Accuracy of CT/MRI Fusion for Localisation of Deep Brain Stimulation Electrode Position: An Imaging Study and Systematic Review. *Stereotactic and Functional Neurosurgery*, *94*(3), 159–163. https://doi.org/10.1159/000446609

Ghadimi, M., & Sapra, A. (2020). Magnetic Resonance Imaging (MRI), Contraindications. In *StatPearls*. [Internet: Retrieved from http://www.ncbi.nlm.nih.gov/pubmed/31869133]. StatPearls Publishing.

Ghaznawi, R., de Bresser, J., van der Graaf, Y., Zwartbol, M. H. T., Witkamp, T. D., Geerlings, M. I., & Hendrikse, J. (2017). Detection and characterization of small infarcts in the caudate nucleus on 7 Tesla MRI: The SMART-MR study. *Journal of Cerebral Blood Flow & Metabolism*, *38*(9), 1609–1617. https://doi.org/10.1177/0271678x17705974

Gielen, F. L. H. (2003). Deep brain stimulation: Current practice and challenges for the future. *International IEEE/EMBS Conference on Neural Engineering, NER*, *2003-January*, 489–491. https://doi.org/10.1109/CNE.2003.1196869

Giguère, N., Nanni, S. B., & Trudeau, L. E. (2018). On cell loss and selective vulnerability of neuronal populations in Parkinson's disease. *Frontiers in Neurology*, *9*, 455. https://doi.org/10.3389/fneur.2018.00455

Giller, C. A., & Jenkins, P. (2015). Some technical nuances for deep brain stimulator implantation. *Interdisciplinary Neurosurgery*, *2*(1), 29–39. https://doi.org/10.1016/j.inat.2014.11.001

Gilmore, G., Lee, D. H., Parrent, A., & Jog, M. (2017). The current state of postoperative imaging in the presence of deep brain stimulation electrodes: Imaging in the Presence of DBS Electrodes. *Movement Disorders*, *32*(6), 833–838. https://doi.org/10.1002/mds.27028

Giuliano, A., Donatelli, G., Cosottini, M., Tosetti, M., Retico, A., & Fantacci, M. E. (2017). Hippocampal subfields at ultra high field MRI: An overview of segmentation and measurement methods. *Hippocampus*, *27*(5), 481–494. https://doi.org/10.1002/hipo.22717

Gizewski, E. R., de Greiff, A., Maderwald, S., Timmann, D., Forsting, M., & Ladd, M. E. (2007). fMRI at 7~T: Whole-brain coverage and signal advantages even infratentorially? *NeuroImage*, *37*(3), 761–768. https://doi.org/10.1016/j.neuroimage.2007.06.005

Gizewski, E. R., Maderwald, S., Linn, J., Dassinger, B., Bochmann, K., Forsting, M., & Ladd, M. E. (2013). High-resolution anatomy of the human brain stem using 7-T MRI: improved detection of inner structures and nerves? *Neuroradiology*, *56*(3), 177–186. https://doi.org/10.1007/s00234-013-1312-0

Gizewski, E. R., Mönninghoff, C., & Forsting, M. (2015). Perspectives of Ultra-High-Field MRI in Neuroradiology. *Clinical Neuroradiology*, *25*(S2), 267–273. https://doi.org/10.1007/s00062-015-0437-4

Glasser, M. F., Coalson, T. S., Robinson, E. C., Hacker, C. D., Harwell, J., Yacoub, E., … Van Essen, D. C. (2016). A multi-modal parcellation of human cerebral cortex. *Nature*, *536*(7615), 171–178. https://doi.org/10.1038/nature18933

Glasser, M. F., Sotiropoulos, S. N., Wilson, J. A., Coalson, T. S., Fischl, B., Andersson, J. L., … Jenkinson, M. (2013). The minimal preprocessing pipelines for the Human Connectome Project. *NeuroImage*, *80*, 105–124. https://doi.org/10.1016/j.neuroimage.2013.04.127

Glover, G. H. (2011). Overview of functional magnetic resonance imaging. *Neurosurgery Clinics of North America*, *22*(4), 133–139. https://doi.org/10.1016/j.nec.2010.11.001

Godenschweger, F., Kägebein, U., Stucht, D., Yarach, U., Sciarra, A., Yakupov, R., … Speck, O. (2016). Motion correction in MRI of the brain. *Physics in Medicine and Biology*, *61*(5), R32–R56. https://doi.org/10.1088/0031-9155/61/5/R32

Golay, M. J. E. (1958). Field homogenizing coils for nuclear spin resonance instrumentation. *Review of Scientific Instruments*, *29*(4), 313–315. https://doi.org/10.1063/1.1716184

Goldman, P. S., & Nauta, W. J. H. (1977). An intricately patterned prefronto-caudate projection in the rhesus monkey. *Journal of Comparative Neurology*, *171*(3), 369–385. https://doi.org/10.1002/cne.901710305

Gorka, A. X., Torrisi, S., Shackman, A. J., Grillon, C., & Ernst, M. (2018). Intrinsic functional connectivity of the central nucleus of the amygdala and bed nucleus of the stria terminalis. *NeuroImage*, *168*, 392–402. https://doi.org/10.1016/j.neuroimage.2017.03.007

Gowen, E., & Miall, R. C. (2007). Differentiation between external and internal cuing: An fMRI study comparing tracing with drawing. *NeuroImage*, *36*(2), 396–410. https://doi.org/10.1016/j.neuroimage.2007.03.005

Grabner, G., Poser, B. A., Fujimoto, K., Polimeni, J. R., Wald, L. L., Trattnig, S., … Barth, M. (2014). A study-specific fMRI normalization approach that operates directly on high resolution functional EPI data at 7Tesla. *NeuroImage*, *100*, 710–714. https://doi.org/10.1016/j.neuroimage.2014.06.045

Greve, D. N., & Fischl, B. (2009). Accurate and robust brain image alignment using boundary-based registration. *NeuroImage*, *48*(1), 63–72. https://doi.org/10.1016/j.neuroimage.2009.06.060

Griswold, M. A., Jakob, P. M., Heidemann, R. M., Nittka, M., Jellus, V., Wang, J., … Haase, A. (2002). Generalized Autocalibrating Partially Parallel Acquisitions (GRAPPA). *Magn Reson Med*, *47*, 1202–1210. https://doi.org/10.1002/mrm.10171

Grossman, R. I., Gomori, J. M., Ramer, K. N., Lexa, F. J., & Schnall, M. D. (1994). Magnetization transfer: theory and clinical applications in neuroradiology. *RadioGraphics*, *14*(2), 279–290. https://doi.org/10.1148/radiographics.14.2.8190954

Haacke, E. M., Mittal, S., Wu, Z., Neelavalli, J., & Cheng, Y.-C. N. (2008). Susceptibility-Weighted Imaging: Technical Aspects and Clinical Applications, Part 1. *American Journal of Neuroradiology*, *30*(1), 19–30. https://doi.org/10.3174/ajnr.a1400

Haacke, E. M., Tkach, J. A., & Parrish, T. B. (1989). Reduction of T2* dephasing in gradient field-echo imaging. *Radiology*, *170*(2), 457–462. https://doi.org/10.1148/radiology.170.2.2911669

Haase, A., Frahm, J., Matthaei, D., Hanicke, W., & Merboldt, K. D. (1986). FLASH imaging. Rapid NMR imaging using low flip-angle pulses. *Journal of Magnetic Resonance (1969)*, *67*(2), 258–266. https://doi.org/10.1016/0022-2364(86)90433-6

Haber, S. N., & Calzavara, R. (2009). The cortico-basal ganglia integrative network: The role of the thalamus. *Brain Research Bulletin*, *78*(2–3), 69–74. https://doi.org/10.1016/j.brainresbull.2008.09.013

Haber, S. N., & Knutson, B. (2010). The reward circuit: Linking primate anatomy and human imaging. *Neuropsychopharmacology*, *35*(1), 4–26. https://doi.org/10.1038/npp.2009.129

Haber, S. N., Kunishio, K., Mizobuchi, M., & Lynd-Balta, E. (1995). The orbital and medial prefrontal circuit through the primate basal ganglia. *Journal of Neuroscience*, *15*(7 I), 4851–4867. https://doi.org/10.1523/jneurosci.15-07-04851.1995

Haber, S. N., Lynd, E., Klein, C., & Groenewegen, H. J. (1990). Topographic organization of the ventral striatal efferent projections in the rhesus monkey: An anterograde tracing study. *Journal of Comparative Neurology*, *293*(2), 282–298. https://doi.org/10.1002/cne.902930210

Habets, J., Isaacs, B., Vinke, S., & Kubben, P. (2019). Controversies in Deep Brain Stimulation Surgery: Micro-Electrode Recordings. In *Evidence for Neurosurgery* (pp. 97–109). https://doi.org/10.1007/978-3-030-16323-5_8

Hagmann, P., Sporns, O., Madan, N., Cammoun, L., Pienaar, R., Wedeen, V. J., … Grant, P. E. (2010). White matter maturation reshapes structural connectivity in the late developing human brain. *Proceedings of the National Academy of Sciences*. https://doi.org/10.1073/pnas.1009073107

Hallgren, B., & Sourander, P. (1958). The Effect Of Age On The Non-Haemin Iron In The Human Brain. *Journal of Neurochemistry*, *3*(1), 41–51. https://doi.org/10.1111/j.1471-4159.1958.tb12607.x

Halsband, U., Matsuzaka, Y., & Tanji, J. (1994). Neuronal activity in the primate supplementary, pre-supplementary and premotor cortex during externally and internally instructed sequential movements. *Neuroscience Research*, *20*(2), 149–155. https://doi.org/10.1016/0168-0102(94)90032-9

Hamani, C., Saint-Cyr, J. A., Fraser, J., Kaplitt, M., & Lozano, A. M. (2004). The subthalamic nucleus in the context of movement disorders. *Brain*, Vol. 127, pp. 4–20. https://doi.org/10.1093/brain/awh029

Hamel, W., Köppen, J. A., Alesch, F., Antonini, A., Barcia, J. A., Bergman, H., … Lozano, A. M. (2017). Targeting of the Subthalamic Nucleus for Deep Brain Stimulation: A Survey Among Parkinson Disease Specialists. *World Neurosurgery*, *99*, 41–46. https://doi.org/10.1016/j.wneu.2016.11.012

Hammond, K. E., Lupo, J. M., Xu, D., Metcalf, M., Kelley, D. A. C., Pelletier, D., … Nelson, S. J. (2008). Development of a robust method for generating 7.0~T multichannel phase images of the brain with application to normal volunteers and patients with neurological diseases. *NeuroImage*, *39*(4), 1682–1692. https://doi.org/10.1016/j.neuroimage.2007.10.037

Hammond, K. E., Metcalf, M., Carvajal, L., Okuda, D. T., Srinivasan, R., Vigneron, D., … Pelletier, D. (2008). Quantitative in vivo magnetic resonance imaging of multiple sclerosis at 7 Tesla with sensitivity to iron. *Annals of Neurology*, *64*(6), 707–713. https://doi.org/10.1002/ana.21582

Hardaway, F. A., Raslan, A. M., & Burchiel, K. J. (2017). Deep Brain Stimulation-Related Infections: Analysis of Rates, Timing, and Seasonality. *Neurosurgery*, *83*(3), 540–547. https://doi.org/10.1093/neuros/nyx505

Hargreaves, B. (2012). Rapid gradient-echo imaging. *Journal of Magnetic Resonance Imaging*, *36*(6), 1300–1313. https://doi.org/10.1002/jmri.23742

Hariz, M. I., Beric, A., Kelly, P. J., Rezai, A., Sterio, D., Mogilner, A., … Kopell, B. (2002). Complications of deep brain stimulation surgery. *Stereotactic and Functional Neurosurgery*, *77*(1–4), 73–78. https://doi.org/10.1159/000064600

Harkins, K. D., Xu, J., Dula, A. N., Li, K., Valentine, W. M., Gochberg, D. F., … Does, M. D. (2016). The microstructural correlates of T1 in white matter. *Magnetic Resonance in Medicine*, *75*(3), 1341–1345. https://doi.org/10.1002/mrm.25709

Hartmann, C. J., Fliegen, S., Groiss, S. J., Wojtecki, L., & Schnitzler, A. (2019). An update on best practice of deep brain stimulation in Parkinson's disease. *Therapeutic Advances in Neurological Disorders*, *12*, 175628641983809. https://doi.org/10.1177/1756286419838096

Hashemi, R., Bradley, W., & Lisanti, C. (2010). *MRI: The Basics: The Basics* (3rd ed.). Philidelphia: Lippincott Williams and Wilkins.

Havsteen, I., Ohlhues, A., Madsen, K. H., Nybing, J. D., Christensen, H., & Christensen, A. (2017). Are movement artifacts in magnetic resonance imaging a real problem?-a narrative review. *Frontiers in Neurology*, *8*, 232. https://doi.org/10.3389/fneur.2017.00232

Haynes, W. I. A., & Haber, S. N. (2013). The organization of prefrontal-subthalamic inputs in primates provides an anatomical substrate for both functional specificity and integration: Implications for basal ganglia models and deep brain stimulation. *Journal of Neuroscience*, *33*(11), 4804–4814. https://doi.org/10.1523/JNEUROSCI.4674-12.2013

Heidemann, R. M., Porter, D. A., Anwander, A., Feiweier, T., Heberlein, K., Knösche, T. R., & Turner, R. (2010). Diffusion imaging in humans at 7T using readout-segmented EPI and GRAPPA. *Magnetic Resonance in Medicine*, *64*(1), 9–14. https://doi.org/10.1002/mrm.22480

Hendriks, A. D., Luijten, P. R., Klomp, D. W. J., & Petridou, N. (2019). Potential acceleration performance of a 256-channel whole-brain receive array at 7T. *Magnetic Resonance in Medicine*, *81*(3), 1659–1670. https://doi.org/10.1002/mrm.27519

Herbst, M., Maclaren, J., Lovell-Smith, C., Sostheim, R., Egger, K., Harloff, A., … Zaitsev, M. (2013). Reproduction of motion artifacts for performance analysis of prospective motion correction in MRI. *Magnetic Resonance in Medicine*, *71*(1), 182–190. https://doi.org/10.1002/mrm.24645

Hershey, T., Campbell, M. C., Videen, T. O., Lugar, H. M., Weaver, P. M., Hartlein, J., Karimi, M., Tabbal, S. D., & Perlmutter, J. S. (2010). Mapping Go–No-Go performance within the subthalamic nucleus region. *Brain*, *133*(12), 3625–3634. https://doi.org/10.1093/brain/awq256

Herz, D. M., Haagensen, B. N., Christensen, M. S., Madsen, K. H., Rowe, J. B., Løkkegaard, A., & Siebner, H. R. (2015). Abnormal dopaminergic modulation of striato-cortical networks underlies levodopa-induced dyskinesias in humans. *Brain*.

https://doi.org/10.1093/brain/awv096

Hilker, R., Schweitzer, K., Coburger, S., Ghaemi, M., Weisenbach, S., Jacobs, A. H., … Heiss, W.-D. D. (2005). Nonlinear progression of Parkinson disease as determined by serial positron emission tomographic imaging of striatal fluorodopa F 18 activity. *Archives of Neurology*, *62*(3), 378. https://doi.org/10.1001/archneur.62.3.378

Ho, A. L., Ali, R., Connolly, I. D., Henderson, J. M., Dhall, R., Stein, S. C., & Halpern, C. H. (2018). Awake versus asleep deep brain stimulation for Parkinson's disease: a critical comparison and meta-analysis. *Journal of Neurology, Neurosurgery, and Psychiatry*, *89*(7), 687–691. https://doi.org/10.1136/jnnp-2016-314500

Hoffmann, A. L. L., Mottaghy, F. M. M., Janssen, F., Peerlings, J., Compter, I., Wiggins, C. J. J., … Hoffmann, A. L. L. (2019). Characterizing geometrical accuracy in clinically optimised 7T and 3T magnetic resonance images for high-precision radiation treatment of brain tumours. *Physics and Imaging in Radiation Oncology*, *9*, 35–42. https://doi.org/10.1016/j.phro.2018.12.001

Hollerman, J. R., Tremblay, L., & Schultz, W. (2000). Involvement of basal ganglia and orbitofrontal cortex in goal-directed behavior. *Progress in Brain Research*, *126*, 193–215. https://doi.org/10.1016/S0079-6123(00)26015-9

Holloway, R., Shoulson, I., Kieburtz, K., McDermott, M., Tariot, P., Kamp, C., … Welsh, M. (2000). Pramipexole vs Levodopa as initial treatment for Parkinson disease: A randomized controlled trial. *Journal of the American Medical Association*, *284*(15), 1931–1938. https://doi.org/10.1001/jama.284.15.1931

Honey, C. J., Thivierge, J. P., & Sporns, O. (2010). Can structure predict function in the human brain? *NeuroImage*. https://doi.org/10.1016/j.neuroimage.2010.01.071

Horn, A. (2019). The impact of modern-day neuroimaging on the field of deep brain stimulation. *Current Opinion in Neurology*, *32*(4), 1. https://doi.org/10.1097/wco.0000000000000679

Horn, A., Li, N., Dembek, T. A., Kappel, A., Boulay, C., Ewert, S., Tietze, A., Husch, A., Perera, T., Neumann, W.-J., Reisert, M., Si, H., Oostenveld, R., Rorden, C., Yeh, F.-C., Fang, Q., Herrington, T. M., Vorwerk, J., & Kühn, A. A. (2019). Lead-DBS v2: Towards a comprehensive pipeline for deep brain stimulation imaging. *NeuroImage*, *184*, 293–316. https://doi.org/10.1016/j.neuroimage.2018.08.068

Horn, A., Reich, M., Vorwerk, J., Li, N., Wenzel, G., Fang, Q., … Fox, M. D. (2017). Connectivity Predicts deep brain stimulation outcome in Parkinson disease. *Annals of Neurology*, *82*(1), 67–78. https://doi.org/10.1002/ana.24974

Houser, M. C., & Tansey, M. G. (2017). The gut-brain axis: is intestinal inflammation a silent driver of Parkinson's disease pathogenesis? *Npj Parkinson's Disease*, *3*(1). https://doi.org/10.1038/s41531-016-0002-0

Hoy, A. R., Koay, C. G., Kecskemeti, S. R., & Alexander, A. L. (2014). Optimization of a free water elimination two-compartment model for diffusion tensor imaging. *NeuroImage*. https://doi.org/10.1016/j.neuroimage.2014.09.053

Hu, Y., & Dolcos, S. (2017). Trait anxiety mediates the link between inferior frontal cortex volume and negative affective bias in healthy adults. *Social Cognitive and Affective Neuroscience*. https://doi.org/10.1093/scan/nsx008

Huntenburg, J. M., Steele, C. J., & Bazin, P. L. (2018). Nighres: processing tools for high-resolution neuroimaging. *GigaScience*, *7*(7). https://doi.org/10.1093/gigascience/giy082

Hurley, S. A., Yarnykh, V. L., Johnson, K. M., Field, A. S., Alexander, A. L., & Samsonov, A. A. (2012). Simultaneous variable flip angle - Actual flip angle imaging method for improved accuracy and precision of three-dimensional T 1 and B 1 measurements. *Magnetic Resonance in Medicine*, *68*(1), 54–64. https://doi.org/10.1002/mrm.23199

Hutchison, W. D., Allan, R. J., Opitz, H., Levy, R., Dostrovsky, J. O., Lang, A. E., & Lozano, A. M. (1998). Neurophysiological identification of the subthalamic nucleus in surgery for Parkinson's disease. *Annals of Neurology*, *44*(4), 622–628. https://doi.org/10.1002/ana.410440407

Iglesias, J. E., & Sabuncu, M. R. (2015). Multi-atlas segmentation of biomedical images: A survey. *Medical Image Analysis*, *24*(1), 205–219. https://doi.org/10.1016/j.media.2015.06.012

Inase, M., Tokuno, H., Nambu, A., Akazawa, T., & Takada, M. (1999). Corticostriatal and corticosubthalamic input zones from the presupplementary motor area in the macaque monkey: comparison with the input zones from the supplementary motor area. *Brain Research*, *833*(2), 191–201. https://doi.org/10.1016/S0006-8993(99)01531-0

Inglese, M., Fleysher, L., Oesingmann, N., & Petracca, M. (2018). Clinical applications of ultra-high field magnetic resonance imaging in multiple sclerosis. *Expert Review of Neurotherapeutics*, *18*(3), 221–230. https://doi.org/10.1080/14737175.2018.1433033

International Standard. (2002). Particular requirements for the safety of the magnetic resonance equipment for medical diagnosis. In *International Electrotechnical Commission 60601-2-33*.

Isaacs, B. R., Forstmann, B. U., Temel, Y., & Keuken, M. C. (2018). The Connectivity Fingerprint of the Human Frontal Cortex, Subthalamic Nucleus, and Striatum. *Frontiers in Neuroanatomy*, *12*. https://doi.org/10.3389/fnana.2018.00060

Isaacs, B. R., Keuken, M. C., Alkemade, A., Temel, Y., Bazin, P.-L., & Forstmann, B. U. (2020). Methodological Considerations for Neuroimaging in Deep Brain Stimulation of the Subthalamic Nucleus in Parkinson's Disease Patients. *Journal of Clinical Medicine*, *9*(10), 3124. https://doi.org/10.3390/jcm9103124

Isaacs, B. R., Mulder, M. J., Groot, J., van Beendonk, N., Lute, N., Bazin, P.-L., … Alkemade, A. (2020). 3 versus 7Tesla MRI for parcellations of subcortical brain structures. *PLoS ONE*, *15*(11), e0236208.

Isaacs, B. R., Trutti, A. C., Pelzer, E., Tittgemeyer, M., Temel, Y., Forstmann, B. U., & Keuken, M. C. (2019). Cortico-basal white matter

alterations occurring in Parkinson's disease. *PLoS ONE*, *14*(8). https://doi.org/10.1371/journal.pone.0214343

Ishimori, Y., Monma, M., Kohno, Y., & Kohno, & Y. (2009). Artifact Reduction of Susceptibility-Weighted Imaging Using a Short-Echo Phase Mask. *Acta Radiologica*, *50*(9), 1027–1034. https://doi.org/10.3109/02841850903147061

Izawa, Y., Suzuki, H., & Shinoda, Y. (2009). Response Properties of Fixation Neurons and Their Location in the Frontal Eye Field in the Monkey. *Journal of Neurophysiology*, *102*(4), 2410–2422. https://doi.org/10.1152/jn.00234.2009

Jahanshahi, M., Obeso, I., Baunez, C., Alegre, M., & Krack, P. (2015). Parkinson's disease, the subthalamic nucleus, inhibition, and impulsivity. *Movement Disorders*, *30*(2), 128–140. https://doi.org/10.1002/mds.26049

Jahanshahi, M., Obeso, I., Rothwell, J. C., & Obeso, J. A. (2015). A fronto-striato-subthalamic-pallidal network for goal-directed and habitual inhibition. *Nature Reviews Neuroscience*, *16*(1), 719–732. https://doi.org/10.1038/nrn4038

Jantz, J. J., Watanabe, M., Levy, R., & Munoz, D. P. (2017). Evidence for a task-dependent switch in subthalamo-nigral basal ganglia signaling. *Nature Communications*, *8*(1), 1039. https://doi.org/10.1038/s41467-017-01023-3

Jara, H. (2013). Theory of quantitative magnetic resonance imaging. In *Theory of Quantitative Magnetic Resonance Imaging*. https://doi.org/10.1142/7625

JASP Team. (2019). JASP. *[Computer Software]*. (Love, J., Selker, R., Marsman, M., Jamil, T., Dropmann, D., Verhagen, J., ... & Wagenmakers, E. J. (2019). JASP: Graphical statistical software for common statistical designs. *Journal of Statistical Software*, *88*(2), 1-17.)

Jbabdi, S., & Johansen-Berg, H. (2011). Tractography: Where Do We Go from Here? *Brain Connectivity*, *1*(3), 169–183. https://doi.org/10.1089/brain.2011.0033

Jbabdi, S., Lehman, J. F., Haber, S. N., & Behrens, T. E. (2013). Human and monkey ventral prefrontal fibers use the same organizational principles to reach their targets: Tracing versus tractography. *Journal of Neuroscience*, *33*(7), 3190–3201. https://doi.org/10.1523/JNEUROSCI.2457-12.2013

Jbabdi, S., Sotiropoulos, S. N., Haber, S. N., Van Essen, D. C., & Behrens, T. E. (2015). Measuring macroscopic brain connections in vivo. *Nature Neuroscience*, Vol. 18, pp. 1546–1555. https://doi.org/10.1038/nn.4134

Jeffreys, H. (1961). *The Theory of Probability* (3rd ed). OUP, Oxford.

Jenkinson, M., Beckmann, C. F., Behrens, T. E. J., Woolrich, M. W., & Smith, S. M. (2012). FSL. *NeuroImage*, *62*(2), 782–790. https://doi.org/10.1016/j.neuroimage.2011.09.015

Joel, D., & Weiner, I. (1997). The connections of the primate subthalamic nucleus: Indirect pathways and the open-interconnected scheme of basal ganglia-thalamocortical circuitry. *Brain Research. Brain Research Reviews*, *23*(1–2), 62–78. https://doi.org/10.1016/S0165-0173(96)00018-5

Johansen-Berg, H. (2010). Behavioural relevance of variation in white matter microstructure. *Current Opinion in Neurology*, 1. https://doi.org/10.1097/WCO.0b013e32833b7631

Johansen-Berg, H. (2013). Human connectomics - What will the future demand? *NeuroImage*, *80*, 541–544. https://doi.org/10.1016/j.neuroimage.2013.05.082

Johansen-Berg, H., Baptista, C. S., & Thomas, A. G. (2012). Human Structural Plasticity at Record Speed. *Neuron*. https://doi.org/10.1016/j.neuron.2012.03.001

Jones, D. K., Knösche, T. R., & Turner, R. (2013). White matter integrity, fiber count, and other fallacies: The do's and don'ts of diffusion MRI. *NeuroImage*, *73*, 239–254. https://doi.org/10.1016/j.neuroimage.2012.06.081

Juchem, C. (2013). Shimming: Fields, Coils & Control. Proceedings of the International Society for Magnetic Resonance in Medicine, 21.

Kamagata, K., Zalesky, A., Hatano, T., Di Biase, M. A., El Samad, O., Saiki, S., … Pantelis, C. (2018). Connectome analysis with diffusion MRI in idiopathic Parkinson's disease: Evaluation using multi-shell, multi-tissue, constrained spherical deconvolution. *NeuroImage: Clinical*. https://doi.org/10.1016/j.nicl.2017.11.007

Kane, M. J., & Engle, R. W. (2002). The role of prefrontal cortex in working-memory capacity, executive attention, and general fluid intelligence: An individual-differences perspective. *Psychonomic Bulletin and Review*. https://doi.org/10.3758/BF03196323

Kanowski, M., Voges, J., Buentjen, L., Stadler, J., Heinze, H.-J., & Tempelmann, C. (2014). Direct Visualization of Anatomic Subfields within the Superior Aspect of the Human Lateral Thalamus by MRI at 7T. *American Journal of Neuroradiology*, *35*(9), 1721–1727. https://doi.org/10.3174/ajnr.a3951

Karger, C. P., Höss, A., Bendl, R., Canda, V., & Schad, L. (2006). Accuracy of device-specific 2D and 3D image distortion correction algorithms for magnetic resonance imaging of the head provided by a manufacturer. *Physics in Medicine and Biology*, *51*(12), N253-61. https://doi.org/10.1088/0031-9155/51/12/N04

Kaya, M. O., Ozturk, S., Ercan, I., Gonen, M., Serhat Erol, F., & Kocabicak, E. (2019). Statistical Shape Analysis of Subthalamic Nucleus in Patients with Parkinson Disease. *World Neurosurgery*, *126*, e835–e841. https://doi.org/10.1016/j.wneu.2019.02.180

Kemp, J., & Powell T. (1970). The cortico-striate projection in the monkey. *Brain*, *93*(6), 525–546. https://doi.org/10.1093/brain/93.3.525

Kemper, V., de Martino, F., Emmerling, T., Yacoub, E., & Goebel, R. (2018). High resolution data analysis strategies for mesoscale human functional MRI at 7 and 9.4 T. *NeuroImage*, *164*, 48–58. https://doi.org/10.1016/j.neuroimage.2017.03.058

Keren, N. I., Taheri, S., Vazey, E. M., Morgan, P. S., Granholm, A.-C. E., Aston-Jones, G. S., & Eckert, M. A. (2015). Histologic validation of

locus coeruleus MRI contrast in post-mortem tissue. *NeuroImage*, *113*, 235–245. https://doi.org/10.1016/j.neuroimage.2015.03.020

Kerl, H. U. (2013). Imaging for deep brain stimulation: The zona incerta at 7 Tesla. *World Journal of Radiology*, *5*(1), 5. https://doi.org/10.4329/wjr.v5.i1.5

Kerl, H. U., Gerigk, L., Pechlivanis, I., Al-Zghloul, M., Groden, C., & Nölte, I. (2012). The subthalamic nucleus at 3.0 Tesla: Choice of optimal sequence and orientation for deep brain stimulation using a standard installation protocol: Clinical article. *Journal of Neurosurgery*, *117*(6), 1155–1165. https://doi.org/10.3171/2012.8.JNS111930

Kerl, H. U., Gerigk, L., Pechlivanis, I., Al-Zghloul, M., Groden, C., & Nölte, I. S. (2012). The subthalamic nucleus at 7.0 Tesla: evaluation of sequence and orientation for deep-brain stimulation. *Acta Neurochirurgica*, *154*(11), 2051–2062. https://doi.org/10.1007/s00701-012-1476-0

Keuken, M. C., & Forstmann, B. U. (2015). A probabilistic atlas of the basal ganglia using 7 T MRI. *Data in Brief*, *4*, 577–582. https://doi.org/10.1016/j.dib.2015.07.028

Keuken, M. C., Bazin, P. L., Backhouse, K., Beekhuizen, S., Himmer, L., Kandola, A., … Forstmann, B. U. (2017). Effects of aging on T1 , T2∗ , and QSM MRI values in the subcortex. *Brain Structure and Function*, *222*(6), 2487–2505. https://doi.org/10.1007/s00429-016-1352-4

Keuken, M. C., Bazin, P.-L., Crown, L., Hootsmans, J., Laufer, A., Müller-Axt, C., … Forstmann, B. U. (2014). Quantifying inter-individual anatomical variability in the subcortex using 7T structural MRI. *NeuroImage*, *94*, 40–46. https://doi.org/10.1016/j.neuroimage.2014.03.032

Keuken, M. C., Bazin, P.-L., Schafer, A., Neumann, J., Turner, R., & Forstmann, B. U. (2013). Ultra-High 7T MRI of Structural Age-Related Changes of the Subthalamic Nucleus. *Journal of Neuroscience*, *33*(11), 4896–4900. https://doi.org/10.1523/jneurosci.3241-12.2013

Keuken, M. C., Isaacs, B. R., Trampel, R., van der Zwaag, W., & Forstmann, B. U. (2018). Visualizing the Human Subcortex Using Ultra-high Field Magnetic Resonance Imaging. *Brain Topography*, *31*(4), 513–545. https://doi.org/10.1007/s10548-018-0638-7

Keuken, M. C., Schäfer, A., & Forstmann, B. U. (2016). Can We Rely on Susceptibility-Weighted Imaging (SWI) for Subthalamic Nucleus Identification in Deep Brain Stimulation Surgery? *Neurosurgery*, *79*(6), E945–E946. https://doi.org/10.1227/NEU.0000000000001395

Keuken, M. C., Uylings, H. B. M., Geyer, S., Schäfer, A., Turner, R., & Forstmann, B. U. (2012). Are there three subdivisions in the primate subthalamic nucleus? *Frontiers in Neuroanatomy*, Vol. 6, p. 14. https://doi.org/10.3389/fnana.2012.00014

Keuken, M. C., Van Maanen, L., Bogacz, R., Schäfer, A., Neumann, J., Turner, R., & Forstmann, B. U. (2015). The subthalamic nucleus during decision-making with multiple alternatives. *Human Brain Mapping*, *36*(10), 4041–4052. https://doi.org/10.1002/hbm.22896

Khabipova, D., Wiaux, Y., Gruetter, R., & Marques, J. P. (2015). A modulated closed form solution for quantitative susceptibility mapping - A thorough evaluation and comparison to iterative methods based on edge prior knowledge. *NeuroImage*, *107*, 163–174. https://doi.org/10.1016/j.neuroimage.2014.11.038

Khalsa, S., Mayhew, S. D., Chechlacz, M., Bagary, M., & Bagshaw, A. P. (2014). The structural and functional connectivity of the posterior cingulate cortex: Comparison between deterministic and probabilistic tractography for the investigation of structure-function relationships. *NeuroImage*, *102*(P1), 118–127. https://doi.org/10.1016/j.neuroimage.2013.12.022

Khanna, N., Altmeyer, W., Zhuo, J., & Steven, A. (2015). Functional neuroimaging: fundamental principles and clinical applications. *Neuroradiology Journal*, 28(2), 87–96. https://doi.org/10.1177/1971400915576311

Kim, H. S., Kim, S. J., Choi, C. G., Kim, N., Han, S., Jang, E. H., … Lee, C. S. (2013). Alterations of mean diffusivity in brain white matter and deep gray matter in Parkinson's disease. *Neuroscience Letters*, *550*, 64–68. https://doi.org/10.1016/j.neulet.2013.06.050

Kim, J. H., Son, Y. D., Kim, J. M., Kim, H. K., Kim, Y. B., Lee, C., & Oh, C. H. (2018). Interregional correlations of glucose metabolism between the basal ganglia and different cortical areas: an ultra-high resolution PET/MRI fusion study using 18F FDG. *Brazilian Journal of Medical and Biological Research*, *51*(1). https://doi.org/10.1590/1414-431x20176724

Kim, J. H., Son, Y.-D., Joo, Y.-H., Lee, S.-Y., Kim, H.-K., & Woo, M.-K. (2017). Altered interregional correlations between serotonin transporter availability and cerebral glucose metabolism in schizophrenia: A high-resolution PET study using 11 C DASB and 18 F FDG. *Schizophrenia Research*, *182*, 55–65. https://doi.org/10.1016/j.schres.2016.10.020

Kim, J. H., Son, Y.-D., Kim, J. H., Choi, E.-J., Lee, S.-L., Lee, J. L., … Kim, Y. B. B. (2015). Serotonin transporter availability in thalamic subregions in schizophrenia: A study using 7.0-T MRI with 11C DASB high-resolution PET. *Psychiatry Research: Neuroimaging*, *231*(1), 50–57. https://doi.org/10.1016/j.pscychresns.2014.10.022

Kim, J. H., Son, Y.-D., Kim, J., Choi, E.-J., Lee, S.-L., Joo, Y.-H., … Cho, Z.-H. (2015). Self-transcendence trait and its relationship with in vivo serotonin transporter availability in brainstem raphe nuclei: An ultra-high resolution PET-MRI study. *Brain Research*, *1629*, 63–71. https://doi.org/10.1016/j.brainres.2015.10.006

Kim, J. M., Jeong, H.-J., Bae, Y. J., Park, S.-Y., Kim, E., Kang, S. Y., … Cho, Z. H. K. (2016). Loss of substantia nigra hyperintensity on 7 Tesla MRI of Parkinson's disease, multiple system atrophy, and progressive supranuclear palsy. *Parkinsonism & Related Disorders*, *26*, 47–54. https://doi.org/10.1016/j.parkreldis.2016.01.023

Kim, J., Lenglet, C., Duchin, Y., Sapiro, G., & Harel, N. (2014). Semiautomatic Segmentation of Brain Subcortical Structures From High-Field MRI. {*IEEE*} *Journal of Biomedical and Health Informatics*, *18*(5), 1678–1695. https://doi.org/10.1109/jbhi.2013.2292858

Kim, N. R., Chi, J. G., Choi, S. H., Kim, Y. B., Hwang, H.-Y., & Cho, Z.-H. (2011). Identification and Morphologic Assessment of Mesocoelic Recess by In Vivo Human Brain Imaging With 7.0-T Magnetic Resonance Imaging. *Journal of Computer Assisted Tomography*,

35(4), 486–491. https://doi.org/10.1097/rct.0b013e31821de1cc

King, A. V., Linke, J., Gass, A., Hennerici, M. G., Tost, H., Poupon, C., & Wessa, M. (2012). Microstructure of a three-way anatomical network predicts individual differences in response inhibition: a tractography study. *NeuroImage*, *59*(2), 1949–1959. https://doi.org/10.1016/j.neuroimage.2011.09.008

Kirov, I. I., Hardy, C. J., Matsuda, K., Messinger, J., Cankurtaran, C. Z., Warren, M., … Gonen, O. (2013). In vivo 7Tesla imaging of the dentate granule cell layer in schizophrenia. *Schizophrenia Research*, *147*(2–3), 362–367. https://doi.org/10.1016/j.schres.2013.04.020

Kitajima, M., Korogi, Y., Kakeda, S., Moriya, J., Ohnari, N., Sato, T., … Yamashita, Y. (2008). Human subthalamic nucleus: evaluation with high-resolution MR imaging at 3.0 T. *Neuroradiology*, *50*(8), 675–681. https://doi.org/10.1007/s00234-008-0388-4

Kleiner-Fisman, G., Herzog, J., Fisman, D. N., Tamma, F., Lyons, K. E., Pahwa, R., … Deuschl, G. (2006). Subthalamic nucleus deep brain stimulation: Summary and meta-analysis of outcomes. *Movement Disorders*, *21*(S14), S290--S304. https://doi.org/10.1002/mds.20962

Klingelhoefer, L., & Reichmann, H. (2017). Parkinson's disease as a multisystem disorder. *Journal of Neural Transmission*, *124*(6), 709–713. https://doi.org/10.1007/s00702-017-1692-0

Kloc, M., Kosutzka, Z., Steno, J., & Valkovic, P. (2017). Prevalent placement error of deep brain stimulation electrode in movement disorders (technical considerations). *Bratislava Medical Journal*, *118*(11), 647–653. https://doi.org/10.4149/BLL_2017_123

Knowles, B. R., Friedrich, F., Fischer, C., Paech, D., & Ladd, M. E. (2019). Beyond T2 and 3T: New MRI techniques for clinicians. *Clinical and Translational Radiation Oncology*. https://doi.org/10.1016/j.ctro.2019.04.009

Ko, S. B., Kim, D. E., Kim, S. H., & Roh, J. K. (2006). Visualization of venous systems by time-of-flight magnetic resonance angiography. *Journal of Neuroimaging*, *16*(4), 353–356. https://doi.org/10.1111/j.1552-6569.2006.00057.x

Kochanski, R. B., & Sani, S. (2018, January 19). Awake versus asleep deep brain stimulation surgery: Technical considerations and critical review of the literature. *Brain Sciences*, Vol. 8. https://doi.org/10.3390/brainsci8010017

Koenig, S. H. (1991). Cholesterol of myelin is the determinant of gray-white contrast in MRI of brain. *Magnetic Resonance in Medicine*, *20*(2), 285–291. https://doi.org/10.1002/mrm.1910200210

Kollia, K., Maderwald, S., Putzki, N., Schlamann, M., Theysohn, J. M., Kraff, O., … Wanke, I. (2009). First Clinical Study on Ultra-High-Field MR Imaging in Patients with Multiple Sclerosis: Comparison of 1.5T and 7T. *American Journal of Neuroradiology*, *30*(4), 699–702. https://doi.org/10.3174/ajnr.a1434

Kosta, P., Argyropoulou, M. I., Markoula, S., & Konitsiotis, S. (2006). MRI evaluation of the basal ganglia size and iron content in patients with Parkinson's disease. *Journal of Neurology*, *253*(1), 26–32. https://doi.org/10.1007/s00415-005-0914-9

Kraff, O., Fischer, A., Nagel, A. M., Mönninghoff, C., & Ladd, M. E. (2014). MRI at 7 tesla and above: Demonstrated and potential capabilities. *Journal of Magnetic Resonance Imaging*, *41*(1), 13–33. https://doi.org/10.1002/jmri.24573

Krupa, K., & Bekiesińska-Figatowska, M. (2015). Artifacts in magnetic resonance imaging. *Polish Journal of Radiology*, *80*(1), 93–106. https://doi.org/10.12659/PJR.892628

Künzle, H., & Akert, K. (1977). Efferent connections of cortical, area 8 (frontal eye field) in Macaca fascicularis. A reinvestigation using the autoradiographic technique. *Journal of Comparative Neurology*, *173*(1), 147–163. https://doi.org/10.1002/cne.901730108

Künzle, Heinz. (1975). Bilateral projections from precentral motor cortex to the putamen and other parts of the basal ganglia. An autoradiographic study in Macaca fascicularis. *Brain Research*, *88*(2), 195–209. https://doi.org/10.1016/0006-8993(75)90384-4

Küper, M., Dimitrova, A., Thürling, M., Maderwald, S., Roths, J., Elles, H. G., … Timmann, D. (2011). Evidence for a motor and a non-motor domain in the human dentate nucleus - An fMRI study. *NeuroImage*, *54*(4), 2612–2622. https://doi.org/10.1016/j.neuroimage.2010.11.028

Küper, M., Wünnemann, M. J. S., Thürling, M., Stefanescu, R. M., Maderwald, S., Elles, H. G., … Timmann, D. (2013). Activation of the cerebellar cortex and the dentate nucleus in a prism adaptation fMRI study. *Human Brain Mapping*, *35*(4), 1574–1586. https://doi.org/10.1002/hbm.22274

Kwak, S., & Jung, M. W. (2019). Distinct roles of striatal direct and indirect pathways in value-based decision making. *ELife*, *8*. https://doi.org/10.7554/eLife.46050

Kwon, D.-H., Kim, J., Oh, S.-H., Jeong, H.-J., Park, S.-Y., Oh, E.-S., … Cho, Z.-H. (2012). Seven-tesla magnetic resonance images of the substantia nigra in Parkinson disease. *Annals of Neurology*, *71*(2), 267–277. https://doi.org/10.1002/ana.22592

Ladd, M. E., Bachert, P., Meyerspeer, M., Moser, E., Nagel, A. M., Norris, D. G., … Zaiss, M. (2018). Pros and cons of ultra-high-field MRI/MRS for human application. *Progress in Nuclear Magnetic Resonance Spectroscopy*, *109*, 1–50. https://doi.org/10.1016/j.pnmrs.2018.06.001

Lahtinen, M. J., Haapaniemi, T. H., Kauppinen, M. T., Salokorpi, N., Heikkinen, E. R., & Katisko, J. P. (2020). A comparison of indirect and direct targeted STN DBS in the treatment of Parkinson's disease—surgical method and clinical outcome over 15-year timespan. *Acta Neurochirurgica*, *162*(5), 1067–1076. https://doi.org/10.1007/s00701-020-04269-x

Lambdin, C. (2012). Significance tests as sorcery: Science is empirical—significance tests are not. *Theory & Psychology*, *22*(1), 67–90. https://doi.org/10.1177/0959354311429854

Lambert, C., Lutti, A., Helms, G., Frackowiak, R., & Ashburner, J. (2013). Multiparametric brainstem segmentation using a modified multivariate mixture of Gaussians. *NeuroImage: Clinical*, *2*(1), 684–694. https://doi.org/10.1016/j.nicl.2013.04.017

Lambert, C., Zrinzo, L., Nagy, Z., Lutti, A., Hariz, M., Foltynie, T., … Frackowiak, R. (2012). Confirmation of functional zones within the human subthalamic nucleus: Patterns of connectivity and sub-parcellation using diffusion weighted imaging. *NeuroImage*, *60*(1), 83–94. https://doi.org/10.1016/j.neuroimage.2011.11.082

Landi, A., Grimaldi, M., Antonini, A., Parolin, M., & Zincone, A. (2003). MRI indirect stereotactic targeting for deep brain stimulation in Parkinson's disease. *Journal of Neurosurgical Sciences*, *47*(1), 26–32.

Landis, J. R., & Koch, G. G. (1977). The Measurement of Observer Agreement for Categorical Data. *Biometrics*, *33*(1), 159. https://doi.org/10.2307/2529310

Lang, A. E., & Obeso, J. A. (2004). Challenges in Parkinson's disease: Restoration of the nigrostriatal dopamine system is not enough. *Lancet Neurology*, *3*(5), 309–316. https://doi.org/10.1016/S1474-4422(04)00740-9

Langkammer, C., Schweser, F., Krebs, N., Deistung, A., Goessler, W., Scheurer, E., … Reichenbach, J. R. (2012). Quantitative susceptibility mapping (QSM) as a means to measure brain iron? A post mortem validation study. *NeuroImage*, *62*(3), 1593–1599. https://doi.org/10.1016/j.neuroimage.2012.05.049

Langkammer, C., Schweser, F., Shmueli, K., Kames, C., Li, X., Guo, L., … Bilgic, B. (2018). Quantitative susceptibility mapping: Report from the 2016 reconstruction challenge. *Magnetic Resonance in Medicine*, *79*(3), 1661–1673. https://doi.org/10.1002/mrm.26830

Larkman, D. J. (2007). The g-Factor and Coil Design. In *Parallel Imaging in Clinical {MR} Applications* (pp. 37–48). https://doi.org/10.1007/978-3-540-68879-2_3

Larkman, D. J., & Nunes, R. G. (2007). Parallel magnetic resonance imaging. *Physics in Medicine and Biology*, *52*(7). https://doi.org/10.1088/0031-9155/52/7/R01

Lau, J. C., Khan, A. R., Zeng, T. Y., MacDougall, K. W., Parrent, A. G., & Peters, T. M. (2018). Quantification of local geometric distortion in structural magnetic resonance images: Application to ultra-high fields. *NeuroImage*, *168*, 141–151. https://doi.org/10.1016/j.neuroimage.2016.12.066

Ledez, D. (2002). Euclidean distance mapping: geological applications. *Terra Nostra (Proc. IAMG)*, *4*, 25–30.

Lee, J., Jeong, H. J., Lee, H., Kim, Y. J., Kim, E. Y., Kim, Y. Y., … Kim, Y.-B. B. (2014). An Investigation of Lateral Geniculate Nucleus Volume in Patients With Primary Open-Angle Glaucoma Using 7 Tesla Magnetic Resonance Imaging. *Investigative Opthalmology & Visual Science*, *55*(6), 3468. https://doi.org/10.1167/iovs.14-13902

Lee, J., Shmueli, K., Fukunaga, M., van Gelderen, P., Merkle, H., Silva, A. C., & Duyn, J. H. (2010). Sensitivity of MRI resonance frequency to the orientation of brain tissue microstructure. *Proceedings of the National Academy of Sciences*, *107*(11), 5130–5135. https://doi.org/10.1073/pnas.0910222107

Lee, Weiner, G. M., Corson, D., Kappel, J., Chang, Y.-F., Suski, V. R., … Richardson, R. M. (2018). Outcomes of Interventional-MRI Versus Microelectrode Recording-Guided Subthalamic Deep Brain Stimulation. *Frontiers in Neurology*, *9*. https://doi.org/10.3389/fneur.2018.00241

Lehericy, S., Vaillancourt, D. E., Seppi, K., Monchi, O., Rektorova, I., Antonini, A., … Siebner, H. R. (2017). The role of high-field magnetic resonance imaging in parkinsonian disorders: Pushing the boundaries forward. *Movement Disorders*, Vol. 32, pp. 510–525. https://doi.org/10.1002/mds.26968

Lenglet, C., Abosch, A., Yacoub, E., de Martino, F., Sapiro, G., & Harel, N. (2012). Comprehensive in vivo Mapping of the Human Basal Ganglia and Thalamic Connectome in Individuals Using 7T MRI. *PLoS ONE*, *7*(1), e29153. https://doi.org/10.1371/journal.pone.0029153

Lenroot, R. K., & Giedd, J. N. (2008). The changing impact of genes and environment on brain development during childhood and adolescence: Initial findings from a neuroimaging study of pediatric twins. *Development and Psychopathology*, *20*(4), 1161–1175. https://doi.org/10.1017/s0954579408000552

Li, W., Avram, A. V., Wu, B., Xiao, X., & Liu, C. (2014). Integrated Laplacian-based phase unwrapping and background phase removal for quantitative susceptibility mapping. *NMR in Biomedicine*, *27*(2), 219–227. https://doi.org/10.1002/nbm.3056

Li, W., Wang, N., Yu, F., Han, H., Cao, W., Romero, R., … Liu, C. (2015). A method for estimating and removing streaking artifacts in quantitative susceptibility mapping. *NeuroImage*, *108*, 111–122. https://doi.org/10.1016/j.neuroimage.2014.12.043

Liberti, L., Lavor, C., Maculan, N., & Mucherino, A. (2014). Euclidean Distance Geometry and Applications. *SIAM Review*, *56*(1), 3–69. https://doi.org/10.1137/120875909

Liem, M. K., Oberstein, S. A. J. L., Versluis, M. J., Maat-Schieman, M. L. C., Haan, J., Webb, A. G., … van der Grond, J. (2012). phantom 7T MRI reveals diffuse iron deposition in putamen and caudate nucleus in CADASIL. *Journal of Neurology, Neurosurgery & Psychiatry*, *83*(12), 1180–1185. https://doi.org/10.1136/jnnp-2012-302545

Ligot, N., Krystkowiak, P., Simonin, C., Goldman, S., Peigneux, P., Van Naemen, J., … De Tiège, X. (2011). External globus pallidus stimulation modulates brain connectivity in Huntington's disease. *Journal of Cerebral Blood Flow and Metabolism*, *31*(1), 41–46. https://doi.org/10.1038/jcbfm.2010.186

Liles, S. L., & Updyke, B. V. (1985). Projection of the digit and wrist area of precentral gyrus to the putamen: Relation between topography and physiological properties of neurons in the putamen. *Brain Research*, *339*(2), 245–255. https://doi.org/10.1016/0006-8993(85)90089-7

Lim, L. W., Janssen, M. L. F., Kocabicak, E., & Temel, Y. (2015). The antidepressant effects of ventromedial prefrontal cortex stimulation is

associated with neural activation in the medial part of the subthalamic nucleus. *Behavioural Brain Research*, *279*, 17–21. https://doi.org/10.1016/j.bbr.2014.11.008

Limousin, P., & Foltynie, T. (2019). Long-term outcomes of deep brain stimulation in Parkinson disease. *Nature Reviews Neurology*, *15*(4), 234–242. https://doi.org/10.1038/s41582-019-0145-9

Limousin, P., Krack, P., Pollak, P., Benazzouz, A., Ardouin, C., Hoffmann, D., & Benabid, A.-L. (2002). Electrical Stimulation of the Subthalamic Nucleus in Advanced Parkinson's Disease. *New England Journal of Medicine*, *339*(16), 1105–1111. https://doi.org/10.1056/nejm199810153391603

Limousin, P., Pollak, P., Benazzouz, A., Hoffmann, D., Le Bas, J. F., Perret, J. E., … Broussolle, E. (1995). Effect on parkinsonian signs and symptoms of bilateral subthalamic nucleus stimulation. *The Lancet*, *345*(8942), 91–95. https://doi.org/10.1016/S0140-6736(95)90062-4

Litvak, V., Jha, A., Eusebio, A., Oostenveld, R., Foltynie, T., Limousin, P., … Brown, P. (2011). Resting oscillatory cortico-subthalamic connectivity in patients with Parkinson's disease. *Brain*, *134*(2), 359–374. https://doi.org/10.1093/brain/awq332

Liu, C., Li, W., Tong, K. A., Yeom, K. W., & Kuzminski, S. (2014). Susceptibility-weighted imaging and quantitative susceptibility mapping in the brain. *Journal of Magnetic Resonance Imaging*, *42*(1), 23–41. https://doi.org/10.1002/jmri.24768

Liu, F., Zhang, Z., Lin, X., Teng, G., Meng, H., Yu, T., … Liu, S. (2011). Development of the human fetal cerebellum in the second trimester: a post mortem magnetic resonance imaging evaluation. *Journal of Anatomy*, *219*(5), 582–588. https://doi.org/10.1111/j.1469-7580.2011.01418.x

Liu, T., Eskreis-Winkler, S., Schweitzer, A. D., Chen, W., Kaplitt, M. G., Tsiouris, A. J., & Wang, Y. (2013). Improved Subthalamic Nucleus Depiction with Quantitative Susceptibility Mapping. *Radiology*, *269*(1), 216–223. https://doi.org/10.1148/radiol.13121991

Liu, T., Spincemaille, P., De Rochefort, L., Kressler, B., & Wang, Y. (2009). Calculation of susceptibility through multiple orientation sampling (COSMOS): A method for conditioning the inverse problem from measured magnetic field map to susceptibility source image in MRI. *Magnetic Resonance in Medicine*, *61*(1), 196–204. https://doi.org/10.1002/mrm.21828

Liu, X., Zhang, J., Fu, K., Gong, R., Chen, J., & Zhang, J. (2017). Microelectrode Recording Guided Versus Intraoperative Magnetic Resonance Imaging Guided Subthalamic Nucleus Deep Brain Stimulation Surgery for Parkinson Disease: A 1-Year Follow-Up Study. *World Neurosurgery*, *107*, 900–905. https://doi.org/10.1016/j.wneu.2017.08.077

Loddenkemper, T., Pan, A., Neme, S., Baker, K. B., Rezai, A. R., Dinner, D. S., ... & Lüders, H, O., & Marks, W. J. (2008). Deep Brain Stimulation in Epilepsy. In *Deep Brain Stimulation in Neurological and Psychiatric Disorders* (pp. 561–569). https://doi.org/10.1007/978-1-59745-360-8_28

Longhi, M., Ricciardi, G., Tommasi, G., Nicolato, A., Foroni, R., Bertolasi, L., … Gerosa, M. (2015). The role of 3T magnetic resonance imaging for targeting the human subthalamic nucleus in deep brain stimulation for Parkinson disease. *Journal of Neurological Surgery, Part A: Central European Neurosurgery*, *76*(3), 181–189. https://doi.org/10.1055/s-0033-1354749

Lönnfors-Weitzel, T., Weitzel, T., Slotboom, J., Kiefer, C., Pollo, C., Schüpbach, M., … Wiest, R. (2016). T2-relaxometry predicts outcome of DBS in idiopathic Parkinson's disease. *NeuroImage: Clinical*, *12*, 832–837. https://doi.org/10.1016/j.nicl.2016.09.019

Lönnfors-Weitzel, T., Weitzel, T., Slotboom, J., Kiefer, C., Pollo, C., Schüpbach, M., … Wiest, R. (2016). T2-relaxometry predicts outcome of DBS in idiopathic Parkinson's disease. *NeuroImage: Clinical*, *12*, 832–837. https://doi.org/10.1016/j.nicl.2016.09.019

Lorio, S., Fresard, S., Adaszewski, S., Kherif, F., Chowdhury, R., Frackowiak, R. S., … Draganski, B. (2016). New tissue priors for improved automated classification of subcortical brain structures on MRI. *NeuroImage*, *130*, 157–166. https://doi.org/10.1016/j.neuroimage.2016.01.062

Lorio, S., Lutti, A., Kherif, F., Ruef, A., Dukart, J., Chowdhury, R., … Draganski, B. (2014). Disentangling in vivo the effects of iron content and atrophy on the ageing human brain. *NeuroImage*, *103*, 280–289. https://doi.org/10.1016/j.neuroimage.2014.09.044

Lotfipour, A. K., Wharton, S., Schwarz, S. T., Gontu, V., Schäfer, A., Peters, A. M., … Bajaj, N. P. S. (2011). High resolution magnetic susceptibility mapping of the substantia nigra in Parkinson's disease. *Journal of Magnetic Resonance Imaging*, *35*(1), 48–55. https://doi.org/10.1002/jmri.22752

Low, H. L., Ismail, M. N. bin M., Taqvi, A., Deeb, J., Fuller, C., & Misbahuddin, A. (2019). Comparison of posterior subthalamic area deep brain stimulation for tremor using conventional landmarks versus directly targeting the dentatorubrothalamic tract with tractography. *Clinical Neurology and Neurosurgery*, *185*, 105466. https://doi.org/10.1016/j.clineuro.2019.105466

Lozano, C. S., Ranjan, M., Boutet, A., Xu, D. S., Kucharczyk, W., Fasano, A., & Lozano, A. M. (2019). Imaging alone versus microelectrode recording guided targeting of the STN in patients with Parkinson's disease. *Journal of Neurosurgery*, *130*(6), 1847–1852. https://doi.org/10.3171/2018.2.jns172186

Lucerna, S., Salpietro, F. M., Alafaci, C., & Tomasello, F. (2011). The Reference System: The ca-cp Plane. In *In Vivo Atlas of Deep Brain Structures* (pp. 1–1). https://doi.org/10.1007/978-3-642-56381-2_1

Lüsebrink, F., Wollrab, A., & Speck, O. (2013). Cortical thickness determination of the human brain using high resolution 3T and 7T MRI data. *NeuroImage*, *70*, 122–131. https://doi.org/10.1016/j.neuroimage.2012.12.016

Lutti, A., Dick, F., Sereno, M. I., & Weiskopf, N. (2014). Using high-resolution quantitative mapping of R1 as an index of cortical myelination. *NeuroImage*, *93*, 176–188. https://doi.org/10.1016/j.neuroimage.2013.06.005

Lyons, K. E., Wilkinson, S. B., Overman, J., & Pahwa, R. (2004). Surgical and hardware complications of subthalamic stimulation: A series of 160 procedures. *Neurology*, Vol. 63, pp. 612–616. https://doi.org/10.1212/01.WNL.0000134650.91974.1A

Macavoy, M. G., Gottlieb, J. P., & Bruce, C. J. (1991). Smooth-pursuit eye movement representation in the primate frontal eye field. *Cerebral Cortex*, *1*(1), 95–102. https://doi.org/10.1093/cercor/1.1.95

MacDonald, A. W., Cohen, J. D., Andrew Stenger, V., & Carter, C. S. (2000). Dissociating the role of the dorsolateral prefrontal and anterior cingulate cortex in cognitive control. *Science*. https://doi.org/10.1126/science.288.5472.1835

Machado, A., Rezai, A. R., Kopell, B. H., Gross, R. E., Sharan, A. D., & Benabid, A.-L. (2006). Deep brain stimulation for Parkinson's disease: Surgical technique and perioperative management. *Movement Disorders*, *21*(S14), S247–S258. https://doi.org/10.1002/mds.20959

Maclaren, J., Armstrong, B. S. R., Barrows, R. T., Danishad, K. A., Ernst, T., Foster, C. L., … Zaitsev, M. (2012). Measurement and Correction of Microscopic Head Motion during Magnetic Resonance Imaging of the Brain. *PLoS ONE*, *7*(11). https://doi.org/10.1371/journal.pone.0048088

Maclaren, J., Herbst, M., Speck, O., & Zaitsev, M. (2012). Prospective motion correction in brain imaging: A review. *Magnetic Resonance in Medicine*, *69*(3), 621–636. https://doi.org/10.1002/mrm.24314

Madai, V. I., von Samson-Himmelstjerna, F. C., Bauer, M., Stengl, K. L., Mutke, M. A., Tovar-Martinez, E., … Sobesky, J. (2012). Ultrahigh-field mri in human ischemic stroke - a 7 Tesla study. *PLoS ONE*, *7*(5). https://doi.org/10.1371/journal.pone.0037631

Makris, N., Swaab, D. F., van der Kouwe, A., Abbs, B., Boriel, D., Handa, R. J., … Goldstein, J. M. (2013). Volumetric parcellation methodology of the human hypothalamus in neuroimaging: Normative data and sex differences. *NeuroImage*, *69*, 1–10. https://doi.org/10.1016/j.neuroimage.2012.12.008

Mallet, L., Polosan, M., Jaafari, N., Baup, N., Welter, M. L., Fontaine, D., … Pelissolo, A. (2008). Subthalamic nucleus stimulation in severe obsessive-compulsive disorder. *New England Journal of Medicine*, *359*(20), 2121–2134. https://doi.org/10.1056/NEJMoa0708514

Mao, W., Smith, M. B., & Collins, C. M. (2006). Exploring the limits of RF shimming for high-field MRI of the human head. *Magnetic Resonance in Medicine*, *56*(4), 918–922. https://doi.org/10.1002/mrm.21013

Mao, Z., Ling, Z., Pan, L., Xu, X., Cui, Z., Liang, S., & Yu, X. (2019). Comparison of efficacy of deep brain stimulation of different targets in Parkinson's disease: A network meta-analysis. *Frontiers in Aging Neuroscience*, Vol. 10, p. 23. https://doi.org/10.3389/fnagi.2019.00023

Marceglia, S., Mrakic-Sposta, S., Foffani, G., Cogiamanian, F., Caputo, E., Egidi, M., … Priori, A. (2006). Gender-related differences in the human subthalamic area: A local field potential study. *European Journal of Neuroscience*. https://doi.org/10.1111/j.1460-9568.2006.05208.x

Markett, S., de Reus, M. A., Reuter, M., Montag, C., Weber, B., Schoene-Bake, J. C., & van den Heuvel, M. P. (2017). Variation on the dopamine D2 receptor gene (DRD2) is associated with basal ganglia-to-frontal structural connectivity. *NeuroImage*. https://doi.org/10.1016/j.neuroimage.2017.04.005

Marques, J. P., & Gruetter, R. (2013). New Developments and Applications of the MP2RAGE Sequence - Focusing the Contrast and High Spatial Resolution R1 Mapping. *PLoS ONE*, *8*(7), e69294. https://doi.org/10.1371/journal.pone.0069294

Marques, J. P., & Norris, D. G. (2017). How to choose the right MR sequence for your research question at 7T and above? *NeuroImage*, *168*, 119–140. https://doi.org/10.1016/j.neuroimage.2017.04.044

Marques, J. P., Khabipova, D., & Gruetter, R. (2017). Studying cyto and myeloarchitecture of the human cortex at ultra-high field with quantitative imaging: R1, R2 and magnetic susceptibility. *NeuroImage*, *147*, 152–163. https://doi.org/10.1016/j.neuroimage.2016.12.009

Marques, J. P., Kober, T., Krueger, G., Van Der Zwaag, W., Van De Moortele, P.-F., & Gruetter, R. (2010). MP2RAGE, a self bias-field corrected sequence for improved segmentation and T 1-mapping at high field. *NeuroImage*, *49*, 1271–1281. https://doi.org/10.1016/j.neuroimage.2009.10.002

Marques, J. P., Kober, T., Krueger, G., Van Der Zwaag, W., Van De Moortele, P.-F., & Gruetter, R. (2010). MP2RAGE, a self bias-field corrected sequence for improved segmentation and T 1-mapping at high field. *NeuroImage*, *49*, 1271–1281. https://doi.org/10.1016/j.neuroimage.2009.10.002

Marques, J. P., Simonis, F. F. J., & Webb, A. G. (2019). Low-field MRI: An MR physics perspective. *Journal of Magnetic Resonance Imaging*, *49*(6), 1528–1542. https://doi.org/10.1002/jmri.26637

Marques, J. P., van der Zwaag, W., Granziera, C., Krueger, G., & Gruetter, R. (2010). Cerebellar Cortical Layers: In Vivo Visualization with Structural High-Field-Strength MR Imaging. *Radiology*, *254*(3), 942–948. https://doi.org/10.1148/radiol.09091136

Marrakchi-Kacem, L., Vignaud, A., Sein, J., Germain, J., Henry, T. R., Poupon, C., … Chupin, M. (2016). Robust imaging of hippocampal inner structure at 7T: in vivo acquisition protocol and methodological choices. *Magnetic Resonance Materials in Physics, Biology and Medicine*, *29*(3), 475–489. https://doi.org/10.1007/s10334-016-0552-5

Marrelec, G., & Fransson, P. (2011). Assessing the influence of different ROI Selection Strategies on functional connectivity analyses of fMRI Data acquired during steady-state conditions. *PLoS ONE*, *6*(4), e14788. https://doi.org/10.1371/journal.pone.0014788

Martin, A. J., Starr, P. A., Ostrem, J. L., & Larson, P. S. (2017). Hemorrhage detection and incidence during magnetic resonance-guided deep brain stimulator implantations. *Stereotactic and Functional Neurosurgery*, *95*(5), 307–314. https://doi.org/10.1159/000479287

Massey, L. A., Miranda, M. A., Zrinzo, L., Al-Helli, O., Parkes, H. G., Thornton, J. S., … Yousry, T. A. (2012). High resolution MR anatomy of the subthalamic nucleus: Imaging at 9.4T with histological validation. *NeuroImage*, *59*(3), 2035–2044. https://doi.org/10.1016/j.neuroimage.2011.10.016

Mathai, A., & Smith, Y. (2011). The Corticostriatal and Corticosubthalamic Pathways: Two Entries, One Target. So What? *Frontiers in Systems Neuroscience*. https://doi.org/10.3389/fnsys.2011.00064

Mavridis, I., Boviatsis, E., & Anagnostopoulou, S. (2013). Anatomy of the Human Subthalamic Nucleus: A Combined Morphometric Study. *Anatomy Research International*, *2013*, 319710. https://doi.org/10.1155/2013/319710

Mayeux, R., Denaro, J., Hemenegildo, N., Marder, K., Tang, M. X., Cote, L. J., & Stern, Y. (1992). A Population-Based Investigation of Parkinson's Disease With and Without Dementia: Relationship to Age and Gender. *Archives of Neurology*, *49*(5), 492–497. https://doi.org/10.1001/archneur.1992.00530290076015

Mazziotta, J. C., Toga, A. W., Evans, A. C., Fox, P., & Lancaster, J. (1995). A Probabilistic Atlas of the Human Brain: Theory and Rationale for Its Development. *NeuroImage*, *2*(2), 89–101. https://doi.org/10.1006/nimg.1995.1012

McClelland, S. (2011). A cost analysis of intraoperative microelectrode recording during subthalamic stimulation for Parkinson's disease. *Movement Disorders*, *26*(8), 1422–1427. https://doi.org/10.1002/mds.23787

McClelland, S. (2011). A cost analysis of intraoperative microelectrode recording during subthalamic stimulation for Parkinson's disease. *Movement Disorders*, *26*(8), 1422–1427. https://doi.org/10.1002/mds.23787

McEvoy, J., Ughratdar, I., Schwarz, S., & Basu, S. (2015). Electrophysiological validation of STN-SNr boundary depicted by susceptibility-weighted MRI. *Acta Neurochirurgica*, *157*(12), 2129–2134. https://doi.org/10.1007/s00701-015-2615-1

McFarland, N. R., & Haber, S. N. (2000). Convergent inputs from thalamic motor nuclei and frontal cortical areas to the dorsal striatum in the primate. *Journal of Neuroscience*, *20*(10), 3798–3813. https://doi.org/10.1523/jneurosci.20-10-03798.2000

McKiernan, E. F., & O'Brien, J. T. (2017). 7T MRI for neurodegenerative dementias in vivo: A systematic review of the literature. *Journal of Neurology, Neurosurgery and Psychiatry*, *88*(7), 564–574. https://doi.org/10.1136/jnnp-2016-315022

McNeely, M., Hershey, T., Campbell, M., Tabbal, S., Karimi, M., Hartlein, J., Lugar, H., Revilla, F., Perlmutter, J., & Earhart, G. (2011). Effects of deep brain stimulation of dorsal versus ventral subthalamic nucleus regions on gait and balance in Parkinson disease. *Journal of neurology, neurosurgery, and psychiatry*, *82*(11), 1250–1255. https://doi.org/10.1136/jnnp.2010.232900

McRobbie, D. W., Moore, E. A., Graves, M. J., & Prince, M. R. (2006). MRI From Picture to Proton. In *MRI from Picture to Proton*. https://doi.org/10.1017/cbo9780511545405

Meijer, F. J. A., Steens, S. C., van Rumund, A., van Cappellen van Walsum, A.-M., Küsters, B., Esselink, R. A. J., … Goraj, B. (2016). Nigrosome-1 on Susceptibility Weighted Imaging to Differentiate Parkinson's Disease From Atypical Parkinsonism: An In Vivo and Ex Vivo Pilot Study. *Polish Journal of Radiology*, *81*, 363–369. https://doi.org/10.12659/pjr.897090

Meng, H., Zhang, Z., Geng, H., Lin, X., Feng, L., Teng, G., … Liu, S. (2012). Development of the subcortical brain structures in the second trimester: assessment with 7.0-T MRI. *Neuroradiology*, *54*(10), 1153–1159. https://doi.org/10.1007/s00234-012-1069-x

Mestres-Missé, A., Bazin, P.-L., Trampel, R., Turner, R., & Kotz, S. A. (2014). Dorsomedial striatum involvement in regulating conflict between current and presumed outcomes. *NeuroImage*, *98*, 159–167. https://doi.org/10.1016/j.neuroimage.2014.05.002

Metere, R., Kober, T., Möller, H. E., & Schäfer, A. (2017). Simultaneous quantitative MRI mapping of T1, T2∗ and magnetic susceptibility with Multi-Echo MP2RAGE. *PLoS ONE*, *12*(1). https://doi.org/10.1371/journal.pone.0169265

Metzler-Baddeley, C., O'Sullivan, M. J., Bells, S., Pasternak, O., & Jones, D. K. (2012). How and how not to correct for CSF-contamination in diffusion MRI. *NeuroImage*. https://doi.org/10.1016/j.neuroimage.2011.08.043

Meuli, R., Honey, C. J., Sporns, O., Gigandet, X., Hagmann, P., Cammoun, L., … Hagmann, P. (2009). Predicting human resting-state functional connectivity from structural connectivity. *Proceedings of the National Academy of Sciences*. https://doi.org/10.1073/pnas.0811168106

Middleton, F. A. (2000). Basal ganglia and cerebellar loops: motor and cognitive circuits. *Brain Research Reviews*, *31*(2–3), 236–250. https://doi.org/10.1016/s0165-0173(99)00040-5

Middleton, F. A., & Strick, P. L. (2000). Basal Ganglia Output and Cognition: Evidence from Anatomical, Behavioral, and Clinical Studies. *Brain and Cognition*, *42*(2), 183–200. https://doi.org/10.1006/brcg.1999.1099

Milchenko, M., Norris, S. A., Poston, K., Campbell, M. C., Ushe, M., Perlmutter, J. S., & Snyder, A. Z. (2018). 7T MRI subthalamic nucleus atlas for use with 3T MRI. *Journal of Medical Imaging*, *5*(01), 1. https://doi.org/10.1117/1.jmi.5.1.015002

Milford, D., Rosbach, N., Bendszus, M., & Heiland, S. (2015). Mono-exponential fitting in T2-relaxometry: Relevance of offset and first echo. *PLoS ONE*, *10*(12). https://doi.org/10.1371/journal.pone.0145255

Miller, I. N., & Cronin-Golomb, A. (2010). Gender differences in Parkinson's disease: Clinical characteristics and cognition. *Movement Disorders*. https://doi.org/10.1002/mds.23388

Miller, M. I., Younes, L., Ratnanather, J., Brown, T., Trinh, H., Lee, D. S., … Albert, M. (2015). Amygdalar atrophy in symptomatic Alzheimer's disease based on diffeomorphometry: the BIOCARD cohort. *Neurobiology of Aging*, *36*, S3--S10. https://doi.org/10.1016/j.neurobiolaging.2014.06.032

Minati, L., Grisoli, M., Carella, F., De Simone, T., Bruzzone, M. G., & Savoiardo, M. (2007). Imaging degeneration of the substantia Nigra in Parkinson disease with inversion-recovery MR imaging. *American Journal of Neuroradiology*, *28*(2), 309–313.

Mirzadeh, Z., & Ponce, F. A. (2015). DBS with versus without MER: Clinical equipoise or malpractice? *Movement Disorders*, *30*(3), 439–441. https://doi.org/10.1002/mds.26168

Mirzadeh, Z., Chapple, K., Lambert, M., Dhall, R., & Ponce, F. A. (2014). Validation of CT-MRI fusion for intraoperative assessment of stereotactic accuracy in DBS surgery. *Movement Disorders*, *29*(14), 1788–1795. https://doi.org/10.1002/mds.26056

Mirzadeh, Z., Chapple, K., Lambert, M., Evidente, V. G., Mahant, P., Ospina, M. C., … Ponce, F. A. (2016). Parkinson's disease outcomes after intraoperative CT-guided asleep deep brain stimulation in the globus pallidus internus. *Journal of Neurosurgery*, *124*(4), 902–907. https://doi.org/10.3171/2015.4.JNS1550

Mitew, S., Gobius, I., Fenlon, L. R., McDougall, S. J., Hawkes, D., Xing, Y. L., … Emery, B. (2018). Pharmacogenetic stimulation of neuronal activity increases myelination in an axon-specific manner. *Nature Communications*. https://doi.org/10.1038/s41467-017-02719-2

Mitsumori, F., Watanabe, H., Takaya, N., Garwood, M., Auerbach, E. J., Michaeli, S., & Mangia, S. (2011). Toward understanding transverse relaxation in human brain through its field dependence. *Magnetic Resonance in Medicine*, *68*(3), 947–953. https://doi.org/10.1002/mrm.23301

Miyachi, S., Lu, X., Imanishi, M., Sawada, K., Nambu, A., & Takada, M. (2006). Somatotopically arranged inputs from putamen and subthalamic nucleus to primary motor cortex. *Neuroscience Research*, *56*(3), 300–308. https://doi.org/10.1016/j.neures.2006.07.012

Miyata, M., & Sasaki, K. (1984). Horseradish peroxidase studies on thalamic and striatal connections of the mesial part of area 6 in the monkey. *Neuroscience Letters*, *49*(1–2), 127–133. https://doi.org/10.1016/0304-3940(84)90148-4

Moenninghoff, C., Kraff, O., Schlamann, M., Ladd, M. E., Katsarava, Z., & Gizewski, E. R. (2010). Assessing a Dysplastic Cerebellar Gangliocytoma (Lhermitte-Duclos Disease) with 7T MR Imaging. *Korean Journal of Radiology*, *11*(2), 244. https://doi.org/10.3348/kjr.2010.11.2.244

Moerel, M., de Martino, F., Ugurbil, K., Yacoub, E., & Formisano, E. (2015). Processing of frequency and location in human subcortical auditory structures. *Scientific Reports*, *5*(1). https://doi.org/10.1038/srep17048

Moisan, F., Kab, S., Mohamed, F., Canonico, M., Le Guern, M., Quintin, C., … Elbaz, A. (2016). Parkinson disease male-to-female ratios increase with age: French nationwide study and meta-analysis. *Journal of Neurology, Neurosurgery and Psychiatry*. https://doi.org/10.1136/jnnp-2015-312283

Mole, J. P., Subramanian, L., Bracht, T., Morris, H., Metzler-Baddeley, C., & Linden, D. E. J. (2016). Increased fractional anisotropy in the motor tracts of Parkinson's disease suggests compensatory neuroplasticity or selective neurodegeneration. *European Radiology*. https://doi.org/10.1007/s00330-015-4178-1

Mollink, J., van Baarsen, K. M., Dederen, P. J. W. C., Foxley, S., Miller, K. L., Jbabdi, S., … van Cappellen van Walsum, A. M. (2015). Dentatorubrothalamic tract localization with postmortem MR diffusion tractography compared to histological 3D reconstruction. *Brain Structure and Function*, *221*(7), 3487–3501. https://doi.org/10.1007/s00429-015-1115-7

Molnar-Szakacs, I., Iacoboni, M., Koski, L., & Mazziotta, J. C. (2005). Functional segregation within pars opercularis of the inferior frontal gyrus: Evidence from fMRI studies of imitation and action observation. *Cerebral Cortex*. https://doi.org/10.1093/cercor/bhh199

Monakow, K. H. von, Akert, K., & Künzle, H. (1978). Projections of the precentral motor cortex and other cortical areas of the frontal lobe to the subthalamic nucleus in the monkey. *Experimental Brain Research*, *33*(3–4), 395–403. https://doi.org/10.1007/BF00235561

Morey, R. D. (2014). BayesFactor: Computation of Bayes Factors for Common Designs (version 0.9.12-4.2). Retrieved April 30, 2020, from https://rdrr.io/cran/BayesFactor/

Morey, R. D., & Wagenmakers, E.-J. J. (2014). Simple relation between Bayesian order-restricted and point-null hypothesis tests. *Statistics and Probability Letters*, *92*, 121–124. https://doi.org/10.1016/j.spl.2014.05.010

Moro, E., Esselink, R. J. A., Xie, J., Hommel, M., Benabid, A. L., & Pollak, P. (2002). The impact on Parkinson's disease of electrical parameter settings in STN stimulation. *Neurology*, *59*(5), 706–713. https://doi.org/10.1212/WNL.59.5.706

Moro, E., Esselink, R. J. A., Xie, J., Hommel, M., Benabid, A. L., & Pollak, P. (2002). The impact on Parkinson's disease of electrical parameter settings in STN stimulation. *Neurology*, *59*(5), 706–713. https://doi.org/10.1212/WNL.59.5.706

Morris, L. S., Kundu, P., Dowell, N., Mechelmans, D. J., Favre, P., Irvine, M. A., … Voon, V. (2016). Fronto-striatal organization: Defining functional and microstructural substrates of behavioural flexibility. *Cortex*, *74*, 118–133. https://doi.org/10.1016/j.cortex.2015.11.004

Mortazavi, F., Oblak, A., Morrison, W., Schmahmann, J., Stanley, H., & Rosene, D. (2018). Geometric Navigation of Axons in a Cerebral Pathway: Comparing dMRI with Tract Tracing and Immunohistochemistry. *Cerebral Cortex*. *28*(4), 1219-1232. https://doi.org/10.1093/cercor/bhx034

Moser, E., Stahlberg, F., Ladd, M. E., & Trattnig, S. (2012). 7-T MR-from research to clinical applications? *NMR in Biomedicine*, Vol. 25, pp. 695–716. https://doi.org/10.1002/nbm.1794

Mulder, M. J., Boekel, W., Ratcliff, R., & Forstmann, B. U. (2014). Cortico-subthalamic connection predicts individual differences in value-driven choice bias. *Brain Structure and Function*, *219*(4), 1239–1249. https://doi.org/10.1007/s00429-013-0561-3

Mulder, M. J., Keuken, M. C., Bazin, P.-L., Alkemade, A., & Forstmann, B. U. (2019). Size and shape matter: the impact of voxel geometry on the identification of small nuclei. *PLoS ONE*, *14*(4). https://doi.org/10.1371/journal.pone.0215382

Nachev, P., Kennard, C., & Husain, M. (2008). Functional role of the supplementary and pre-supplementary motor areas. *Nature Reviews Neuroscience*. https://doi.org/10.1038/nrn2478

Nagy, A. M., & Tolleson, C. M. (2016). Rescue procedures after suboptimal deep brain stimulation outcomes in common movement disorders. *Brain Sciences*, *6*(4). https://doi.org/10.3390/brainsci6040046

Nakajima, T., Zrinzo, L., Foltynie, T., Olmos, I. A., Taylor, C., Hariz, M. I., & Limousin, P. (2011). MRI-guided subthalamic nucleus deep brain stimulation without microelectrode recording: Can we dispense with surgery under local anaesthesia? *Stereotactic and Functional Neurosurgery*, *89*(5), 318–325. https://doi.org/10.1159/000330379

Nakano, N., Taneda, M., Watanabe, A., & Kato, A. (2012). Computed Three-Dimensional Atlas of Subthalamic Nucleus and Its Adjacent Structures for Deep Brain Stimulation in Parkinson's Disease. *ISRN Neurology*, *2012*, 1–13. https://doi.org/10.5402/2012/592678

Nambu, A. (2008). Seven problems on the basal ganglia. *Current Opinion in Neurobiology*. https://doi.org/10.1016/j.conb.2008.11.001

Nambu, A., Takada, M., Inase, M., & Tokuno, H. (2018). Dual somatotopical representations in the primate subthalamic nucleus: evidence for ordered but reversed body-map transformations from the primary motor cortex and the supplementary motor area. *The Journal of Neuroscience*, *16*(8), 2671–2683. https://doi.org/10.1523/jneurosci.16-08-02671.1996

Nambu, A., Tokuno, H., & Takada, M. (2002). Functional significance of the cortico-subthalamo-pallidal "hyperdirect" pathway. *Neuroscience Research*, *43*(2), 111–117. https://doi.org/10.1016/S0168-0102(02)00027-5

Nambu, A., Tokuno, H., Inase, M., & Takada, M. (1997). Corticosubthalamic input zones from forelimb representations of the dorsal and ventral divisions of the premotor cortex in the macaque monkey: Comparison with the input zones from the primary motor cortex and the supplementary motor area. *Neuroscience Letters*, *239*(1), 13–16. https://doi.org/10.1016/S0304-3940(97)00877-X

Nandish, S., Prabhu, G., & Rajagopal, K. V. (2017). Multiresolution image registration for multimodal brain images and fusion for better neurosurgical planning. *Biomedical Journal*, *40*(6), 329–338. https://doi.org/10.1016/j.bj.2017.09.002

Neto, L. L., Oliveira, E., Correia, F., & Ferreira, A. G. (2008). The human nucleus accumbens: Where is it? A stereotactic, anatomical and magnetic resonance imaging study. *Neuromodulation*, *11*(1), 13–22. https://doi.org/10.1111/j.1525-1403.2007.00138.x

Neubert, F., Mars, R. B. B., Buch, E. R. R., Olivier, E., & Rushworth, M. F. S. F. S. (2010). Cortical and subcortical interactions during action reprogramming and their related white matter pathways. *Proceedings of the National Academy of Sciences*, *107*(30), 13240–13245. https://doi.org/10.1073/pnas.1000674107

Neubert, F., Mars, R. B., Sallet, J., & Rushworth, M. F. S. (2015). Connectivity reveals relationship of brain areas for reward-guided learning and decision making in human and monkey frontal cortex. *Proceedings of the National Academy of Sciences of the United States of America*, *112*(20), E2695-704. https://doi.org/10.1073/pnas.1410767112

Neubert, F., Mars, R. B., Thomas, A. G., Sallet, J., & Rushworth, M. F. S. S. (2014). Comparison of Human Ventral Frontal Cortex Areas for Cognitive Control and Language with Areas in Monkey Frontal Cortex. *Neuron*, *81*(3), 700–713. https://doi.org/10.1016/j.neuron.2013.11.012

Ng, B., Varoquaux, G., Poline, J. B., Thirion, B., Greicius, M. D., & Poston, K. L. (2017). Distinct alterations in Parkinson's medication-state and disease-state connectivity. *NeuroImage: Clinical*. https://doi.org/10.1016/j.nicl.2017.09.004

Nichols, T. E., Das, S., Eickhoff, S. B., Evans, A. C., Glatard, T., Hanke, M., … Yeo, B. T. T. (2017). Best practices in data analysis and sharing in neuroimaging using MRI. *Nature Neuroscience*, *20*(3), 299–303. https://doi.org/10.1038/nn.4500

Nieuwenhuys, R. (2012). The myeloarchitectonic studies on the human cerebral cortex of the Vogt-Vogt school, and their significance for the interpretation of functional neuroimaging data. *Brain Structure and Function*, *218*(2), 303–352. https://doi.org/10.1007/s00429-012-0460-z

Nieuwenhuys, R., Broere, C. A. J., & Cerliani, L. (2014). A new myeloarchitectonic map of the human neocortex based on data from the Vogt–Vogt school. *Brain Structure and Function*, *220*(5), 2551–2573. https://doi.org/10.1007/s00429-014-0806-9

Noël, P., Bammer, R., Reinhold, C., & Haider, M. A. (2009). Parallel imaging artifacts in body magnetic resonance imaging. *Canadian Association of Radiologists Journal*, *60*(2), 91–98. https://doi.org/10.1016/j.carj.2009.02.036

Novak, P., Novak, V. ., Kangarlu, A., Abduljalil, A. M., Chakeres, D. W., & Robitaille, P.-M. L. (2001). High Resolution MR} of the Brainstem at 8 T. *Journal of Computer Assisted Tomography*, *25*(2), 242–246. https://doi.org/10.1097/00004728-200103000-00016

Novak, V., Abduljalil, A., Kangarlu, A., Slivka, A., Bourekas, E., Novak, P., … Robitaille, P.-M. L. (2001). Intracranial ossifications and microangiopathy at 8 Tesla MRI. *Magnetic Resonance Imaging*, *19*(8), 1133–1137. https://doi.org/10.1016/s0730-725x(01)00447-7

Nowacki, A., Debove, I., Fiechter, M., Rossi, F., Oertel, M. F., Wiest, R., … Pollo, C. (2017). Targeting Accuracy of the Subthalamic Nucleus in Deep Brain Stimulation Surgery: Comparison Between 3 T T2-Weighted Magnetic Resonance Imaging and Microelectrode Recording Results. *Operative Neurosurgery*, *15*(1), 66–71. https://doi.org/10.1093/ons/opx175

O'Brien, K. R., Kober, T., Hagmann, P., Maeder, P., Marques, J., Lazeyras, F., … Roche, A. (2014). Robust T1-Weighted Structural Brain Imaging and Morphometry at 7T Using MP2RAGE. *PLoS ONE*, *9*(6), e99676. https://doi.org/10.1371/journal.pone.0099676

O'Gorman, R. L., Jarosz, J. M., Samuel, M., Clough, C., Selway, R. P., & Ashkan, K. (2009). CT/MR image fusion in the postoperative assessment of electrodes implanted for deep brain stimulation. *Stereotactic and Functional Neurosurgery*, *87*(4), 205–210. https://doi.org/10.1159/000225973

O'Gorman, R. L., Shmueli, K., Ashkan, K., Samuel, M., Lythgoe, D. J., Shahidiani, A., … Jarosz, J. (2011). Optimal MRI methods for direct stereotactic targeting of the subthalamic nucleus and globus pallidus. *European Radiology*, *21*(1), 130–136. https://doi.org/10.1007/s00330-010-1885-5

Obeso, J. A., Olanow, C. W., Rodriguez-Oroz, M. C., Krack, P., Kumar, R., & Lang, A. E. (2001). Deep-brain stimulation of the subthalamic nucleus or the pars interna of the globus pallidus in Parkinson's disease. *New England Journal of Medicine*, *345*(13), 956–963. https://doi.org/10.1056/NEJMoa000827

Obeso, J. A., Rodríguez-Oroz, M. C., Benitez-Temino, B., Blesa, F. J., Guridi, J., Marin, C., & Rodriguez, M. (2008). Functional organization of the basal ganglia: Therapeutic implications for Parkinson's disease. *Movement Disorders*, *23*(3), S548-59. https://doi.org/10.1002/mds.22062

Obeso, J. A., Rodriguez-Oroz, M., Rodriguez, M., Lanciego, J. L., Artieda, J., Gonzalo, N., & Olanow, C. W. (2000). Pathophysiology of the basal ganglia in Parkinson' s disease. *Trends in Neurosciences*, *23*(8–19).

Odekerken, V. J. J., Boel, J. A., Geurtsen, G. J., Schmand, B. A., Dekker, I. P., De Haan, R. J., … De Bie, R. M. A. (2015). Neuropsychological outcome after deep brain stimulation for Parkinson disease. *Neurology*, *84*(13), 1355–1361. https://doi.org/10.1212/WNL.0000000000001419

Odekerken, V. J. J., van Laar, T., Staal, M. J., Mosch, A., Hoffmann, C. F. E., Nijssen, P. C. G., … de Bie, R. M. A. (2013). Subthalamic nucleus versus globus pallidus bilateral deep brain stimulation for advanced Parkinson's disease (NSTAPS study): A randomised controlled trial. *The Lancet Neurology*, *12*(1), 37–44. https://doi.org/10.1016/S1474-4422(12)70264-8

Ofori, E., Pasternak, O., Planetta, P. J., Li, H., Burciu, R. G., Snyder, A. F., … Vaillancourt, D. E. (2015). Longitudinal changes in free-water within the substantia nigra of Parkinson's disease. *Brain*. https://doi.org/10.1093/brain/awv136

Olanow, C. W., Obeso, J. A., & Stocchi, F. (2006). Continuous dopamine-receptor treatment of Parkinson's disease: scientific rationale and clinical implications. *Lancet Neurology*, *5*(8), 677–687. https://doi.org/10.1016/S1474-4422(06)70521-X

Oldfield, R. C. (1971). The assessment and analysis of handedness: The Edinburgh inventory. *Neuropsychologia*, *9*(1), 97–113. https://doi.org/10.1016/0028-3932(71)90067-4

Oliveira, I. S., Hedgire, S. S., Li, W., Ganguli, S., & Prabhakar, A. M. (2016). Blood pool contrast agents for venous magnetic resonance imaging. *Cardiovascular Diagnosis and Therapy*, *6*(6), 508–518. https://doi.org/10.21037/cdt.2016.12.05

Ostrem, J. L., Galifianakis, N. B., Markun, L. C., Grace, J. K., Martin, A. J., Starr, P. A., & Larson, P. S. (2013). Clinical outcomes of PD patients having bilateral STN DBS using high-field interventional MR-imaging for lead placement. *Clinical Neurology and Neurosurgery*, *115*(6), 708–712. https://doi.org/10.1016/j.clineuro.2012.08.019

Ostrem, J. L., Ziman, N., Galifianakis, N. B., Starr, P. A., Luciano, M. S., Katz, M., … Larson, P. S. (2016). Clinical outcomes using ClearPoint interventional MRI for deep brain stimulation lead placement in Parkinson's disease. *Journal of Neurosurgery*, *124*(4), 908–916. https://doi.org/10.3171/2015.4.JNS15173

Ou, Y., Sotiras, A., Paragios, N., & Davatzikos, C. (2011). DRAMMS: Deformable registration via attribute matching and mutual-saliency weighting. *Medical Image Analysis*, *15*(4), 622–639. https://doi.org/10.1016/j.media.2010.07.002

Paek, S. H., Lee, J.-Y., Kim, H.-J., Kang, D., Lim, Y. H., Kim, M. R., … Kim, D. G. (2011). Electrode Position and the Clinical Outcome after Bilateral Subthalamic Nucleus Stimulation. *Journal of Korean Medical Science*, *26*(10), 1344. https://doi.org/10.3346/jkms.2011.26.10.1344

Pallavaram, S., D'Haese, P. F., Lake, W., Konrad, P. E., Dawant, B. M., & Neimat, J. S. (2015). Fully automated targeting using nonrigid image registration matches accuracy and exceeds precision of best manual approaches to subthalamic deep brain stimulation targeting in parkinson disease. *Neurosurgery*, *76*(6), 756–763. https://doi.org/10.1227/NEU.0000000000000714

Parent, A., & Hazrati, L. N. (1995a). Functional anatomy of the basal ganglia. I. The cortico-basal ganglia-thalamo-cortical loop. *Brain Research Reviews*, *20*(1), 91–127. https://doi.org/10.1016/0165-0173(94)00007-C

Parent, A., & Hazrati, L. N. (1995b). Functional anatomy of the basal ganglia. II. The place of subthalamic nucleus and external pallidium in basal ganglia circuitry. *Brain Research. Brain Research Reviews*, *20*(1), 128–154. https://doi.org/10.1016/0165-0173(94)00008-D

Park, C. K., Jung, N. Y., Kim, M., & Chang, J. W. (2017). Analysis of Delayed Intracerebral Hemorrhage Associated with Deep Brain Stimulation Surgery. *World Neurosurgery*, *104*, 537–544. https://doi.org/10.1016/j.wneu.2017.05.075

Parthasarathy, H. B., Schall, J. D., & Graybiel, A. M. (1992). Distributed but convergent ordering of corticostriatal projections: Analysis of the frontal eye field and the supplementary eye field in the macaque monkey. *Journal of Neuroscience*, *12*(11), 4468–4488. https://doi.org/10.1523/jneurosci.12-11-04468.1992

Parsons, T. D., Rogers, S. A., Braaten, A. J., Woods, S. P., & Tröster, A. I. (2006). Cognitive sequelae of subthalamic nucleus deep brain stimulation in Parkinson's disease: A meta-analysis. *The Lancet Neurology*, *5*(7), 578–588. https://doi.org/10.1016/S1474-4422(06)70475-6

Patel, N. K., Heywood, P., O'Sullivan, K., Love, S., & Gill, S. S. (2002). MRI-directed subthalamic nucleus surgery for Parkinson's disease. *Stereotactic and Functional Neurosurgery*, *78*(3–4), 132–145. https://doi.org/10.1159/000068964

Patel, N. K., Khan, S., & Gill, S. S. (2008). Comparison of atlas- and magnetic-resonance-imaging-based stereotactic targeting of the subthalamic nucleus in the surgical treatment of Parkinson's disease. *Stereotactic and Functional Neurosurgery*, *86*(3), 153–161. https://doi.org/10.1159/000120427

Peerlings, J., Compter, I., Janssen, F., Wiggins, C. J., Postma, A. A., Mottaghy, F. M., Lambin, P., & Hoffmann, A. L. (2019). Characterizing geometrical accuracy in clinically optimised 7T and 3T magnetic resonance images for high-precision radiation treatment of brain tumours. *Physics and Imaging in Radiation Oncology*, *9*, 35–42. https://doi.org/10.1016/j.phro.2018.12.001

Pereira, J. L. B., Furie, S., Sharim, J., Yazdi, D., DeSalles, A. A. F., & Pouratian, N. (2016). Lateralization of the subthalamic nucleus with age in Parkinson's disease. *Basal Ganglia*. https://doi.org/10.1016/j.baga.2016.01.003

Perlmutter, J. S. (2009). Assessment of parkinson disease manifestations. *Current Protocols in Neuroscience*. https://doi.org/10.1002/0471142301.ns1001s49

Perlmutter, J. S., & Mink, J. W. (2006). Deep Brain Stimulation. *Annual Review of Neuroscience*, *29*(1), 229–257. https://doi.org/10.1146/annurev.neuro.29.051605.112824

Peters, A. M., Brookes, M. J., Hoogenraad, F. G., Gowland, P. A., Francis, S. T., Morris, P. G., & Bowtell, R. (2007). T2* measurements in

human brain at 1.5, 3 and 7 T. *Magnetic Resonance Imaging*, *25*(6), 748–753. https://doi.org/10.1016/j.mri.2007.02.014

Petersen, E. A., Holl, E. M., Martinez-Torres, I., Foltynie, T., Limousin, P., Hariz, M. I., & Zrinzo, L. (2010). Minimizing brain shift in stereotactic functional neurosurgery. *Neurosurgery*, *67*(1). https://doi.org/10.1227/01.NEU.0000380991.23444.08

Petras, J. M. (1968). Some Efferent Connections Of The Motor And Somatosensory Cortex Of Simian Primates And Felid, Canid And Procyonid Carnivores. *Annals of the New York Academy of Sciences*, *167*(1), 469–505. https://doi.org/10.1111/j.1749-6632.1969.tb20461.x

Petrides, M., & Pandya, D. N. (1999). Dorsolateral prefrontal cortex: comparative cytoarchitectonic analysis in the human and the macaque brain and corticocortical connection patterns. *European Journal of Neuroscience*, *11*(3), 1011–1036. https://doi.org/10.1046/j.1460-9568.1999.00518.x

Petry-Schmelzer, J. N., Krause, M., Dembek, T. A., Horn, A., Evans, J., Ashkan, K., Rizos, A., Silverdale, M., Schumacher, W., Sack, C., Loehrer, P. A., Fink, G. R., Fonoff, E. T., Martinez-Martin, P., Antonini, A., Barbe, M. T., Visser-Vandewalle, V., Ray-Chaudhuri, K., Timmermann, L., … EUROPAR and the IPMDS Non-Motor PD Study Group. (2019). Non-motor outcomes depend on location of neurostimulation in Parkinson's disease. *Brain: A Journal of Neurology*, *142*(11), 3592–3604. https://doi.org/10.1093/brain/awz285

Petsko, G. A. (2012). The coming epidemic of neurologic disorders: What science is-and should be-doing about it. *Daedalus*, *141*(3), 98–107. https://doi.org/10.1162/DAED_a_00165

Planetta, P. J., Ofori, E., Pasternak, O., Burciu, R. G., Shukla, P., Desimone, J. C., … Vaillancourt, D. E. (2016). Free-water imaging in Parkinson's disease and atypical parkinsonism. *Brain*. https://doi.org/10.1093/brain/awv361

Plantinga, B. R. (2016). A clear view on Parkinson's disease : 7T MRI investigation of the basal ganglia and development of patient-specific deep brain stimulation. Technische Universiteit Eindhoven.

Plantinga, B. R., Roebroeck, A., Kemper, V. G. G., Uludag, K., Melse, M., Mai, J., … Temel, Y. (2016). Ultra-High Field MRI Post Mortem Structural Connectivity of the Human Subthalamic Nucleus, Substantia Nigra, and Globus Pallidus. *Frontiers in Neuroanatomy*, *10*, 66. https://doi.org/10.3389/fnana.2016.00066

Plantinga, B. R., Temel, Y., Duchin, Y., Uludağ, K., Patriat, R., Roebroeck, A., … Harel, N. (2018). Individualized parcellation of the subthalamic nucleus in patients with Parkinson's disease with 7T MRI. *NeuroImage*, *168*, 403–411. https://doi.org/10.1016/j.neuroimage.2016.09.023

Plantinga, B. R., Temel, Y., Roebroeck, A., Uludag, K., Ivanov, D., Kuijf, M., & ter Haar Romenij, B. M. (2014). Ultra-high field magnetic resonance imaging of the basal ganglia and related structures. *Frontiers in Human Neuroscience*, *8*. https://doi.org/10.3389/fnhum.2014.00876

Plewes, D. B., & Kucharczyk, W. (2012). Physics of MRI: A primer. *Journal of Magnetic Resonance Imaging*, (35), 1038–1054. https://doi.org/10.1002/jmri.23642

Pohmann, R., Speck, O., & Scheffler, K. (2015). Signal-to-noise ratio and MR tissue parameters in human brain imaging at 3, 7, and 9.4 tesla using current receive coil arrays. *Magnetic Resonance in Medicine*, *75*(2), 801–809. https://doi.org/10.1002/mrm.25677

Polanski, W. H., Martin, K. D., Engellandt, K., von Kummer, R., Klingelhoefer, L., Fauser, M., … Sobottka, S. B. (2015). Accuracy of subthalamic nucleus targeting by T2, FLAIR and SWI-3-Tesla MRI confirmed by microelectrode recordings. *Acta Neurochirurgica*, *157*(3), 479–486. https://doi.org/10.1007/s00701-014-2328-x

Polders, D. (2012). *Quantitative MRI of the human brain at 7Tesla*. Utrecht University, The Netherlands.

Polders, D., Leemans, A., Luijten, P. R., & Hoogduin, H. (2012). Uncertainty estimations for quantitative in vivo MRI T1 mapping. *Journal of Magnetic Resonance*, *224*, 53–60. https://doi.org/10.1016/j.jmr.2012.08.017

Poldrack, R. A., Fletcher, P. C., Henson, R. N., Worsley, K. J., Brett, M., & Nichols, T. E. (2008). Guidelines for reporting an fMRI study. *NeuroImage*, *40*(2), 409–414. https://doi.org/10.1016/j.neuroimage.2007.11.048

Pollo, C., Meuli, R., Maeder, P., Vingerhoets, F., Ghika, J., & Villemure, J. G. (2003). Subthalamic Nucleus Deep Brain Stimulation for Parkinson's Disease: Magnetic Resonance Imaging Targeting Using Visible Anatomical Landmarks. *Stereotactic and Functional Neurosurgery*, *80*(1–4), 76–81. https://doi.org/10.1159/000075163

Pouratian, N., & Sheth, S. A. (Eds.). (2020). Stereotactic and Functional Neurosurgery: Principles and Applications. Springer Nature.

Priovoulos, N., Jacobs, H. I. L., Ivanov, D., Uludaug, K., Verhey, F. R. J., & Poser, B. A. (2018). High-resolution in vivo imaging of human locus coeruleus by magnetization transfer MRI at 3T and 7T. *NeuroImage*, *168*, 427–436. https://doi.org/10.1016/j.neuroimage.2017.07.045

Pyatigorskaya, N., Gallea, C., Garcia-Lorenzo, D., Vidailhet, M., & Lehericy, S. (2014). A review of the use of magnetic resonance imaging in Parkinson's disease. *Therapeutic Advances in Neurological Disorders*, *7*(4), 206–220. https://doi.org/10.1177/1756285613511507

R Development Core Team. (2011). R: A Language and Environment for Statistical Computing. *The R Foundation for Statistical Computing*. https://doi.org/10.1007/978-3-540-74686-7

Rabie, A., Metman, L. V., & Slavin, K. V. (2016). Using "Functional" target coordinates of the subthalamic nucleus to assess the indirect and direct methods of the preoperative planning: Do the anatomical and functional targets coincide? *Brain Sciences*, *6*(4). https://doi.org/10.3390/brainsci6040065

Ranjan, M., Boutet, A., Xu, D. S., Lozano, C. S., Kumar, R., Fasano, A., … Lozano, A. M. (2018). Subthalamic Nucleus Visualization on Routine Clinical Preoperative MRI Scans: A Retrospective Study of Clinical and Image Characteristics Predicting Its Visualization.

Stereotactic and Functional Neurosurgery, *96*(2), 120–126. https://doi.org/10.1159/000488397

Rauscher, A., Sedlacik, J., Barth, M., Mentzel, H. J., & Reichenbach, J. R. (2005). Magnetic susceptibility-weighted MR phase imaging of the human brain. *American Journal of Neuroradiology*, *26*(4), 736–742.

Raz, N., Lindenberger, U., Rodrigue, K. M., Kennedy, K. M., Head, D., Williamson, A., … Acker, J. D. (2005). Regional Brain Changes in Aging Healthy Adults: General Trends, Individual Differences and Modifiers. *Cerebral Cortex*, *15*(11), 1676–1689. https://doi.org/10.1093/cercor/bhi044

Reck, C., Maarouf, M., Wojtecki, L., Groiss, S. J., Florin, E., Sturm, V., … Timmermann, L. (2012). Clinical outcome of subthalamic stimulation in Parkinson's disease is improved by intraoperative multiple trajectories microelectrode recording. *Journal of Neurological Surgery, Part A: Central European Neurosurgery*, *73*(6), 377–386. https://doi.org/10.1055/s-0032-1326957

Renvall, V., Witzel, T., Wald, L. L., & Polimeni, J. R. (2016). Automatic cortical surface reconstruction of high-resolution T1 echo planar imaging data. *NeuroImage*, *134*, 338–354. https://doi.org/10.1016/j.neuroimage.2016.04.004

Reveley, C., Seth, A. K., Pierpaoli, C., Silva, A. C., Yu, D., Saunders, R. C., … Ye, F. Q. (2015). Superficial white matter fiber systems impede detection of long-range cortical connections in diffusion MR tractography. *Proceedings of the National Academy of Sciences of the United States of America*, *112*(21), E2820–E2828. https://doi.org/10.1073/pnas.1418198112

Richter, E. O., Hoque, T., Halliday, W., Lozano, A. M., & Saint-Cyr, J. A. (2004). Determining the position and size of the subthalamic nucleus based on magnetic resonance imaging results in patients with advanced Parkinson disease. *Journal of Neurosurgery*, *100*(3), 541–546. https://doi.org/10.3171/jns.2004.100.3.0541

Rijkers, K., Temel, Y., Visser-Vandewalle, V., Vanormelingen, L., Vandersteen, M., Adriaensens, P., … Beuls, E. A. M. (2007). The microanatomical environment of the subthalamic nucleus. *Journal of Neurosurgery*, *107*(1), 198–201. https://doi.org/10.3171/jns-07/07/0198

Rinck, P. A. (2016). *Magnetic resonance in medicine*. Wiley-Blackwell.

Roberts, R. E., Anderson, E. J., & Husain, M. (2013). White matter microstructure and cognitive function. *Neuroscientist*, *19*(1), 8–15. https://doi.org/10.1177/1073858411421218

Robitaille, P.-M. L. (2007). Ultra High Field Magnetic Resonance Imaging: A Historical Perspective. *Ultra High Field Magnetic Resonance Imaging*, *26*, 1–17. https://doi.org/10.1007/978-0-387-49648-1_1

Robitaille, P.-M. L., Kangarlu, A., & Abduljalil, A. M. (1999). RF Penetration in Ultra High Field MRI: Challenges in Visualizing Details Within the Center of the Human Brain. *Journal of Computer Assisted Tomography*, *23*(6), 845–849. https://doi.org/10.1097/00004728-199911000-00006

Rolston, J. D., Englot, D. J., Starr, P. A., & Larson, P. S. (2016). An unexpectedly high rate of revisions and removals in deep brain stimulation surgery: Analysis of multiple databases. *Parkinsonism and Related Disorders*, *33*, 72–77. https://doi.org/10.1016/j.parkreldis.2016.09.014

Rolston, J. D., Englot, D. J., Starr, P. A., & Larson, P. S. (2016). An unexpectedly high rate of revisions and removals in deep brain stimulation surgery: Analysis of multiple databases. *Parkinsonism and Related Disorders*, *33*, 72–77. https://doi.org/10.1016/j.parkreldis.2016.09.014

Romanelli, P., Esposito, V., Schaal, D. W., & Heit, G. (2005). Somatotopy in the basal ganglia: experimental and clinical evidence for segregated sensorimotor channels. *Brain Research Reviews*, *48*(1), 112–128. https://doi.org/10.1016/j.brainresrev.2004.09.008

Romanzetti, S., Mirkes, C. C., Fiege, D. P., Celik, A., Felder, J., & Shah, N. J. (2014). Mapping tissue sodium concentration in the human brain: A comparison of MR sequences at 9.4Tesla. *NeuroImage*, *96*, 44–53. https://doi.org/10.1016/j.neuroimage.2014.03.079

Roméo, F., & Hoult, D. I. (1984). Magnet field profiling: Analysis and correcting coil design. *Magnetic Resonance in Medicine*, *1*(1), 44–65. https://doi.org/10.1002/mrm.1910010107

Rooney, W. D., Johnson, G., Li, X., Cohen, E. R., Kim, S.-G., Ugurbil, K., & Springer, C. S. (2007). Magnetic field and tissue dependencies of human brain longitudinal1H2O relaxation in vivo. *Magnetic Resonance in Medicine*, *57*(2), 308–318. https://doi.org/10.1002/mrm.21122

Ropele, S., & Langkammer, C. (2016). Iron quantification with susceptibility. *NMR in Biomedicine*, *30*(4), e3534. https://doi.org/10.1002/nbm.3534

Rosenberg, S., Lu, Q., Chong, S., Fancy, S., Zhang, L., Shen, Y., … Hahn, A. (2011). Neurite outgrowth inhibitor Nogo-A establishes spatial segregation and extent of oligodendrocyte myelination. *Proceedings of the National Academy of Sciences*, *109*(4), 1299–1304. https://doi.org/10.1073/pnas.1113540109

Rosenfeld, J. P., & Olson, J. M. (2021). Bayesian Data Analysis: A Fresh Approach to Power Issues and Null Hypothesis Interpretation. *Applied Psychophysiology and Biofeedback*, *46*(2), 135-140.

Rossi, A., Berger, K., Chen, H., Leslie, D., Mailman, R. B., & Huang, X. (2018). Projection of the prevalence of Parkinson's disease in the coming decades: Revisited. *Movement Disorders*, *33*(1), 156–159. https://doi.org/10.1002/mds.27063

Rouder, J. N., Morey, R. D., Speckman, P. L., & Province, J. M. (2012). Default Bayes factors for ANOVA designs. *Journal of Mathematical Psychology*, *56*(5), 356–374. https://doi.org/10.1016/j.jmp.2012.08.001

Rouder, J. N., Morey, R. D., Verhagen, J., Swagman, A. R., & Wagenmakers, E. J. (2017). Bayesian analysis of factorial designs. *Psychological Methods*, *22*(2), 304–321. https://doi.org/10.1037/met0000057

Rowe, J., Stephan, K. E., Friston, K., Frackowiak, R., Lees, A., & Passingham, R. (2002). Attention to action in Parkinson's disease: impaired effective connectivity among frontal cortical regions. *Brain : A Journal of Neurology*, *125*(Pt 2), 276–289.

https://doi.org/10.1093/brain/awf036

Rua, C., Clarke, W. T., Driver, I. D., Mougin, O., Morgan, A. T., Clare, S., … Rodgers, C. T. (2020). Multi-centre, multi-vendor reproducibility of 7T QSM and R2* in the human brain: Results from the UK7T study. *NeuroImage*, *223*, 117358. https://doi.org/10.1016/j.neuroimage.2020.117358

Rubchinsky, L. L., Kopell, N., & Sigvardt, K. A. (2003). Modeling facilitation and inhibition of competing motor programs in basal ganglia subthalamic nucleus-pallidal circuits. *Proceedings of the National Academy of Sciences of the United States of America*, *100*(2), 14427–14432. https://doi.org/10.1073/pnas.2036283100

Rubin, J. E., Mcintyre, C. C., Turner, R. S., & Wichmann, T. (2012). Basal ganglia activity patterns in parkinsonism and computational modeling of their downstream effects. *European Journal of Neuroscience*, *36*(2), 2213–2228. https://doi.org/10.1111/j.1460-9568.2012.08108.x

Rubinov, M., & Sporns, O. (2010). Complex network measures of brain connectivity: Uses and interpretations. *NeuroImage*, *52*(3), 1059–1069. https://doi.org/10.1016/j.neuroimage.2009.10.003

Rudko, D. A., Solovey, I., Gati, J. S., Kremenchutzky, M., & Menon, R. S. (2014). Multiple Sclerosis: Improved Identification of Disease-relevant Changes in Gray and White Matter by Using Susceptibility-based MR Imaging. *Radiology*, *272*(3), 851–864. https://doi.org/10.1148/radiol.14132475

Rutt, B. K., & Lee, D. H. (1996). The impact of field strength on image quality in MRI. *Journal of Magnetic Resonance Imaging*, *6*(1), 57–62. https://doi.org/10.1002/jmri.1880060111

Saikiran, P., & Priyanka. (2020). Effectiveness of QSM over R2∗ in Assessment of Parkinson's Disease - A Systematic Review. *Neurology India*, *68*(2), 278–281. https://doi.org/10.4103/0028-3886.284377

Saint-Cyr, J. a A., Hoque, T., Pereira, L. C. M. C. M. M., Dostrovsky, J. O. O., Hutchison, W. D. D., Mikulis, D. J. J., … Lozano, A. M. M. (2002). Localization of clinically effective stimulating electrodes in the human subthalamic nucleus on magnetic resonance imaging. *Journal of Neurosurgery*, *97*(5), 1152–1166. https://doi.org/10.3171/jns.2002.97.5.1152

Sallet, J., Mars, R. B., Noonan, M. P., Neubert, F., Jbabdi, S., O'Reilly, J. X., … Sallet, J. (2013). The Organization of Dorsal Frontal Cortex in Humans and Macaques. *Journal of Neuroscience*, *33*(30), 12255–12274. https://doi.org/10.1523/jneurosci.5108-12.2013

Sampaio-Baptista, C., & Johansen-Berg, H. (2017). White Matter Plasticity in the Adult Brain. *Neuron*, *96*(6), 1239–1251. https://doi.org/10.1016/j.neuron.2017.11.026

Santangelo, G., Trojano, L., Vitale, C., Ianniciello, M., Amboni, M., Grossi, D., & Barone, P. (2007). A neuropsychological longitudinal study in Parkinson's patients with and without hallucinations. *Movement Disorders*, *22*(16), 2418–2425. https://doi.org/10.1002/mds.21746

Santin, M. D., Didier, M., Valabrègue, R., Yahia Cherif, L., García-Lorenzo, D., Loureiro de Sousa, P., … Lehéricy, S. (2017). Reproducibility of R2* and quantitative susceptibility mapping (QSM) reconstruction methods in the basal ganglia of healthy subjects. *NMR in Biomedicine*, *30*(4). https://doi.org/10.1002/nbm.3491

Saranathan, M., Tourdias, T., Bayram, E., Ghanouni, P., & Rutt, B. K. (2014). Optimization of white-matter-nulled magnetization prepared rapid gradient echo (MP-RAGE) imaging. *Magnetic Resonance in Medicine*, *73*(5), 1786–1794. https://doi.org/10.1002/mrm.25298

Satpute, A. B., Wager, T. D., Cohen-Adad, J., Bianciardi, M., Choi, J.-K., Buhle, J. T., … Barrett, L. F. (2013). Identification of discrete functional subregions of the human periaqueductal gray. *Proceedings of the National Academy of Sciences*, *110*(42), 17101–17106. https://doi.org/10.1073/pnas.1306095110

Schäfer, A., Forstmann, B. U., Neumann, J., Bowtell, R., Turner, R., Wharton, S., & Mietke, A. (2012). Direct visualization of the subthalamic nucleus and its iron distribution using high-resolution susceptibility mapping. *Human Brain Mapping*, *33*(12), 2831–2842. https://doi.org/10.1002/hbm.21404

Schäfer, A., Wharton, S., Gowland, P., & Bowtell, R. (2009). Using magnetic field simulation to study susceptibility-related phase contrast in gradient echo MRI. *NeuroImage*, *48*(1), 126–137. https://doi.org/10.1016/j.neuroimage.2009.05.093

Schafer, R. J., & Moore, T. (2007). Attention Governs Action in the Primate Frontal Eye Field. *Neuron*, *56*(3), 541–551. https://doi.org/10.1016/j.neuron.2007.09.029

Schilling, K., Gao, Y., Janve, V., Stepniewska, I., Landman, B. A., & Anderson, A. W. (2018). Confirmation of a gyral bias in diffusion MRI fiber tractography. *Human Brain Mapping*, *39*(3), 1449–1466. https://doi.org/10.1002/hbm.23936

Schindler, S., Schönknecht, P., Schmidt, L., Anwander, A., Trampel, R., Bazin, P.-L., … Geyer, S. (2013). Development and Evaluation of an Algorithm for the Computer-Assisted Segmentation of the Human Hypothalamus on 7-Tesla Magnetic Resonance Images. *PLoS ONE*, *8*(7), e66394. https://doi.org/10.1371/journal.pone.0066394

Schindler, Stephanie, Schreiber, J., Bazin, P.-L., Trampel, R., Anwander, A., Geyer, S., & Schönknecht, P. (2017). Intensity standardisation of 7T MR images for intensity-based segmentation of the human hypothalamus. *PLoS ONE*, *12*(3), e0173344. https://doi.org/10.1371/journal.pone.0173344

Schlaier, J.R., Habermeyer, C., Warnat, J., Lange, M., Janzen, A., Hochreiter, A., … Fellner, C. (2011). Discrepancies between the MRI- and the electrophysiologically defined subthalamic nucleus. *Acta Neurochirurgica*, *153*(12), 2307–2318. https://doi.org/10.1007/s00701-011-1081-7

Schlaier, Juergen Ralf, Habermeyer, C., Janzen, A., Fellner, C., Hochreiter, A., Proescholdt, M., … Lange, M. (2013). The influence of intraoperative microelectrode recordings and clinical testing on the location of final stimulation sites in deep brain stimulation for

Parkinson's disease. *Acta Neurochirurgica*, *155*(2), 357–366. https://doi.org/10.1007/s00701-012-1592-x

Schmidt, F., Schindler, S., Adamidis, M., Tränkner, M. S. A., Trampel, R., Walter, M., … Schönknecht, P. (2017). Habenula volume increases with disease severity in unmedicated major depressive disorder as revealed by 7T MRI. *European Archives of Psychiatry and Clinical Neuroscience*, *267*(2), 107–115. https://doi.org/10.1007/s00406-016-0675-8

Schmidt, M., Engelhorn, T., Marxreiter, F., Winkler, J., Lang, S., Kloska, S., … Doerfler, A. (2017). Ultra high-field SWI of the substantia nigra at 7T: reliability and consistency of the swallow-tail sign. *BMC Neurology*, *17*(1). https://doi.org/10.1186/s12883-017-0975-2

Schmitz, B. L., Aschoff, A. J., Hoffmann, M. H. K., & Grön, G. (2006). Advantages and pitfalls in 3T MR brain imaging: a pictorial review. *American Journal of Neuroradiology*, *26*(9), 2229-2237.

Schönbrodt, F. D., & Wagenmakers, E.-J. (2018). Bayes factor design analysis: Planning for compelling evidence. *Psychonomic Bulletin & Review*, *25*(1), 128–142. https://doi.org/10.3758/s13423-017-1230-y

Schreiner, S. J., Liu, X., Gietl, A. F., Wyss, M., Steininger, S. C., Gruber, E., … Unschuld, P. G. (2014). Regional Fluid-Attenuated Inversion Recovery (FLAIR) at 7 Tesla correlates with amyloid beta in hippocampus and brainstem of cognitively normal elderly subjects. *Frontiers in Aging Neuroscience*, *6*. https://doi.org/10.3389/fnagi.2014.00240

Schrock, L. E., Patriat, R., Goftari, M., Kim, J., Johnson, M. D., Harel, N., & Vitek, J. L. (2021). 7T MRI and Computational Modeling Supports a Critical Role of Lead Location in Determining Outcomes for Deep Brain Stimulation: A Case Report. *Frontiers in Human Neuroscience*, *15*, 631778. https://doi.org/10.3389/fnhum.2021.631778

Schroeder, U. (2002). Subthalamic nucleus stimulation affects striato-anterior cingulate cortex circuit in a response conflict task: a PET study. *Brain*. https://doi.org/10.1093/brain/awf199

Schweser, F., & Zivadinov, R. (2018). Quantitative susceptibility mapping (QSM) with an extended physical model for MRI frequency contrast in the brain: a proof-of-concept of quantitative susceptibility and residual (QUASAR) mapping. *NMR in Biomedicine*, *31*(12), e3999. https://doi.org/10.1002/nbm.3999

Schweser, F., Deistung, A., & Reichenbach, J. R. (2016). Foundations of MRI phase imaging and processing for Quantitative Susceptibility Mapping (QSM). *Zeitschrift Für Medizinische Physik*, *26*(1), 6–34. https://doi.org/10.1016/j.zemedi.2015.10.002

Schweser, F., Deistung, A., Lehr, B. W., & Reichenbach, J. R. (2010). Differentiation between diamagnetic and paramagnetic cerebral lesions based on magnetic susceptibility mapping. *Medical Physics*, *37*(10), 5165–5178. https://doi.org/10.1118/1.3481505

Schweser, F., Deistung, A., Lehr, B. W., & Reichenbach, J. R. (2011). Quantitative imaging of intrinsic magnetic tissue properties using MRI signal phase: An approach to in vivo brain iron metabolism? *NeuroImage*, *54*(4), 2789–2807. https://doi.org/10.1016/j.neuroimage.2010.10.070

Schweser, F., Sommer, K., Deistung, A., & Reichenbach, J. R. (2012). Quantitative susceptibility mapping for investigating subtle susceptibility variations in the human brain. *NeuroImage*, *62*(3), 2083–2100. https://doi.org/10.1016/j.neuroimage.2012.05.067

Schweser, F., Sommer, K., Deistung, A., Reichenbach, J. R., Schäfer, A., Forstmann, B. U., … Turner, R. (2012). Direct visualization of the subthalamic nucleus and its iron distribution using high-resolution susceptibility mapping. *NeuroImage*, *46*(12), 2831–2842. https://doi.org/10.1002/jmri.25693

Sclocco, R., Beissner, F., Bianciardi, M., Polimeni, J. R., & Napadow, V. (2017). Challenges and opportunities for brainstem neuroimaging with ultrahigh field MRI. *NeuroImage*, *168*, 412–426. https://doi.org/10.1016/j.neuroimage.2017.02.052

Selemon, L. D., & Goldman-Rakic, P. S. (1985). Longitudinal topography and interdigitation of corticostriatal projections in the rhesus monkey. *Journal of Neuroscience*, *5*(3), 776–794. https://doi.org/10.1523/jneurosci.05-03-00776.1985

Selemon, L. D., & Goldman-Rakic, P. S. (1988). Common cortical and subcortical targets of the dorsolateral prefrontal and posterior parietal cortices in the rhesus monkey: evidence for a distributed neural network subserving spatially guided behavior. *Journal of Neuroscience*, *8*(11), 4049–4068. https://doi.org/10.1523/jneurosci.08-11-04049.1988

Seppi, K., & Poewe, W. (2010). Brain Magnetic Resonance Imaging Techniques in the Diagnosis of Parkinsonian Syndromes. *Neuroimaging Clinics of North America*. https://doi.org/10.1016/j.nic.2009.08.016

Setsompop, K., Feinberg, D. A., & Polimeni, J. R. (2016). Rapid brain MRI acquisition techniques at ultra-high fields. *NMR in Biomedicine*, *29*(9), 1198–1221. https://doi.org/10.1002/nbm.3478

Setsompop, K., Gagoski, B. A., Polimeni, J. R., Witzel, T., Wedeen, V. J., & Wald, L. L. (2012). Blipped-Controlled Aliasing in Parallel Imaging for Simultaneous Multislice Echo Planar Imaging With Reduced g-Factor Penalty. *Magnetic Resonance in Medicine*, *67*(5), 1210–1224. https://doi.org/10.1002/mrm.23097

Sharott, A., Gulberti, A., Zittel, S., Tudor Jones, A. A., Fickel, U., Munchau, A., … Moll, C. K. E. (2014). Activity Parameters of Subthalamic Nucleus Neurons Selectively Predict Motor Symptom Severity in Parkinson's Disease. *Journal of Neuroscience*, *34*(18), 6273–6285. https://doi.org/10.1523/JNEUROSCI.1803-13.2014

Shima, K., & Tanji, J. (1998). Role for cingulate motor area cells in voluntary movement selection based on reward. *Science*, *282*(5392), 1335–1338. https://doi.org/10.1126/science.282.5392.1335

Shin, W., Shin, T., Oh, S. H., & Lowe, M. J. (2016). CNR improvement of MP2RAGE from slice encoding directional acceleration. *Magnetic Resonance Imaging*, *34*(6), 779–784. https://doi.org/10.1016/j.mri.2016.03.014

Shmueli, K., de Zwart, J. A., van Gelderen, P., Li, T.-Q., Dodd, S. J., & Duyn, J. H. (2009). Magnetic susceptibility mapping of brain tissue in vivo using MRI phase data. *Magnetic Resonance in Medicine*, *62*(6), 1510–1522. https://doi.org/10.1002/mrm.22135

Sidiropoulos, C., Rammo, R., Merker, B., Mahajan, A., LeWitt, P., Kaminski, P., … Schwalb, J. M. (2016). Intraoperative MRI for deep brain stimulation lead placement in Parkinson's disease: 1 year motor and neuropsychological outcomes. *Journal of Neurology*, *263*(6), 1226–1231. https://doi.org/10.1007/s00415-016-8125-0

Sladky, R., Baldinger, P., Kranz, G. S., Tröstl, J., Höflich, A., Lanzenberger, R., … Windischberger, C. (2013). High-resolution functional MRI of the human amygdala at 7T. *European Journal of Radiology*, *82*(5), 728–733. https://doi.org/10.1016/j.ejrad.2011.09.025

Slavin, K. V., Thulborn, K. R., Wess, C., & Nersesyan, H. (2006). Direct visualization of the human subthalamic nucleus with 3T MR imaging. *American Journal of Neuroradiology*, *27*(1), 80–84.

Sled, J. G., Zijdenbos, A. P., & Evans, A. C. (1998). A Nonparametric Method for Automatic Correction of Intensity Nonuniformity in MRI Data. *IEEE Transactions On Medical Imaging*, *17*(1).

Slotty, P. J., Wille, C., Kinfe, T. M., & Vesper, J. (2014). Continuous perioperative apomorphine in deep brain stimulation surgery for Parkinson's disease. *British Journal of Neurosurgery*, *28*(3), 378–382. https://doi.org/10.3109/02688697.2013.841859

Smith, K. M., & Dahodwala, N. (2014). Sex differences in Parkinson's disease and other movement disorders. *Experimental Neurology*. https://doi.org/10.1016/j.expneurol.2014.03.010

Smith, S. M. (2002). Fast robust automated brain extraction. *Human Brain Mapping*, *17*(3), 143–155. https://doi.org/10.1002/hbm.10062

Solano-Castiella, E., Schäfer, A., Reimer, E., Türke, E., Pröger, T., Lohmann, G., … Turner, R. (2011). Parcellation of human amygdala in vivo using ultra high field structural MRI. *NeuroImage*, *58*(3), 741–748. https://doi.org/10.1016/j.neuroimage.2011.06.047

Solbach, K., Kraff, O., Minnerop, M., Beck, A., Schöls, L., Gizewski, E. R., … Timmann, D. (2014). Cerebellar pathology in Friedreich's ataxia: Atrophied dentate nuclei with normal iron content. *NeuroImage} Clinical*, *6*, 93–99. https://doi.org/10.1016/j.nicl.2014.08.018

Somasundaram, K., & Kalavathi, P. (2012). Analysis of imaging artifacts in MR brain images. *Oriental J Comput Sci Technol*, *5*(1), 135-141.

Soria, G., Notaris, M. De, Tudela, R., Blasco, G., Puig, J., Planas, A. M., … Prats-Galino, A. (2011). Improved Assessment of Ex Vivo Brainstem Neuroanatomy With High-Resolution MRI and DTI at 7 Tesla. *The Anatomical Record: Advances in Integrative Anatomy and Evolutionary Biology*, *294*(6), 1035–1044. https://doi.org/10.1002/ar.21383

Springer, E., Dymerska, B., Cardoso, P. L., Robinson, S. D., Weisstanner, C., Wiest, R., … Trattnig, S. (2016). Comparison of Routine Brain Imaging at 3 T and 7 T. *Investigative Radiology*, *51*(8), 469–482. https://doi.org/10.1097/RLI.0000000000000256

Stanton, G. B., Goldberg, M. E., & Bruce, C. J. (1988). Frontal eye field efferents in the macaque monkey: I. Subcortical pathways and topography of striatal and thalamic terminal fields. *Journal of Comparative Neurology*, *271*(4), 473–492. https://doi.org/10.1002/cne.902710402

Starr, P. A. (2002). Placement of deep brain stimulators into the subthalamic nucleus or Globus pallidus internus: technical approach. *Stereotactic and Functional Neurosurgery*, *79*(3–4), 118–145. https://doi.org/70828

Stefanescu, M. R., Dohnalek, M., Maderwald, S., Thürling, M., Minnerop, M., Beck, A., … Timmann, D. (2015). Structural and functional MRI abnormalities of cerebellar cortex and nuclei in SCA3, SCA6 and Friedreich's ataxia. *Brain*, *138*(5), 1182–1197. https://doi.org/10.1093/brain/awv064

Stefanescu, M. R., Thürling, M., Maderwald, S., Wiestler, T., Ladd, M. E., Diedrichsen, J., & Timmann, D. (2013). A 7T fMRI study of cerebellar activation in sequential finger movement tasks. *Experimental Brain Research*, *228*(2), 243–254. https://doi.org/10.1007/s00221-013-3558-5

Stefani, A., Cerroni, R., Mazzone, P., Liguori, C., Di Giovanni, G., Pierantozzi, M., & Galati, S. (2019). Mechanisms of action underlying the efficacy of deep brain stimulation of the subthalamic nucleus in Parkinson's disease: central role of disease severity. *European Journal of Neuroscience*, *49*, 805–816. https://doi.org/10.1111/ejn.14088

Stephan, K. E., Tittgemeyer, M., Knösche, T. R., Moran, R. J., & Friston, K. J. (2009). Tractography-based priors for dynamic causal models. *NeuroImage*. https://doi.org/10.1016/j.neuroimage.2009.05.096

Stockmann, J. P., Witzel, T., Keil, B., Polimeni, J. R., Mareyam, A., Lapierre, C., … Wald, L. L. (2016). A 32-channel combined RF and B0 shim array for 3T brain imaging. *Magnetic Resonance in Medicine*, *75*(1), 441–451. https://doi.org/10.1002/mrm.25587

Strotmann, B., Heidemann, R. M., Anwander, A., Weiss, M., Trampel, R., Villringer, A., & Turner, R. (2013). High-resolution MRI and diffusion-weighted imaging of the human habenula at 7 tesla. *Journal of Magnetic Resonance Imaging*, *39*(4), 1018–1026. https://doi.org/10.1002/jmri.24252

Strotmann, B., Kögler, C., Bazin, P.-L., Weiss, M., Villringer, A., & Turner, R. (2013). Mapping of the internal structure of human habenula with ex vivo MRI at 7T. *Frontiers in Human Neuroscience*, *7*. https://doi.org/10.3389/fnhum.2013.00878

Stüber, C., Morawski, M., Schäfer, A., Labadie, C., Wähnert, M., Leuze, C., … Turner, R. (2014). Myelin and iron concentration in the human brain: A quantitative study of MRI contrast. *NeuroImage*, *93*(P1), 95–106. https://doi.org/10.1016/j.neuroimage.2014.02.026

Stucht, D., Danishad, K. A., Schulze, P., Godenschweger, F., Zaitsev, M., & Speck, O. (2015). Highest Resolution In Vivo Human Brain MRI Using Prospective Motion Correction. *PLoS ONE*, *10*(7), e0133921. https://doi.org/10.1371/journal.pone.0133921

Sun, H., Cleary, J. O., Glarin, R., Kolbe, S. C., Ordidge, R. J., Moffat, B. A., & Pike, G. B. (2020). Extracting more for less: multi-echo MP2RAGE for simultaneous T1-weighted imaging, T1 mapping, R2* mapping, SWI, and QSM from a single acquisition. *Magnetic Resonance in Medicine*, *83*(4), 1178–1191. https://doi.org/10.1002/mrm.27975

Sveinbjornsdottir, S. (2016). The clinical symptoms of Parkinson's disease. *Journal of Neurochemistry*, *139*, 318–324.

https://doi.org/10.1111/jnc.13691

Swick, D., Ashley, V., & Turken, A. U. (2008). Left inferior frontal gyrus is critical for response inhibition. *BMC Neuroscience*, *9*(1), 102. https://doi.org/10.1186/1471-2202-9-102

Swire, M., & ffrench-Constant, C. (2018). Seeing Is Believing: Myelin Dynamics in the Adult CNS. *Neuron*. https://doi.org/10.1016/j.neuron.2018.05.005

Tachibana, Y., Nambu, A., Hatanaka, N., Miyachi, S., & Takada, M. (2004). Input-output organization of the rostral part of the dorsal premotor cortex, with special reference to its corticostriatal projection. *Neuroscience Research*, *48*(1), 45–57. https://doi.org/10.1016/j.neures.2003.09.006

Takada, M., Tokuno, H., Hamada, I., Inase, M., Ito, Y., Imanishi, M., … Nambu, A. (2001). Organization of inputs from cingulate motor areas to basal ganglia in macaque monkey. *European Journal of Neuroscience*, *14*(10), 1633–1650. https://doi.org/10.1046/j.0953-816X.2001.01789.x

Takada, M., Tokuno, H., Nambu, A., & Inase, M. (1998). Corticostriatal projections from the somatic motor areas of the frontal cortex in the macaque monkey: segregation versus overlap of input zones from the primary motor cortex, the supplementary motor area, and the premotor cortex. *Experimental Brain Research*, *120*(1), 114–128. https://doi.org/10.1007/s002210050384

Tang, M. Y., Chen, T. W., Zhang, X. M., & Huang, X. H. (2014). GRE T2∗-Weighted MRI: Principles and Clinical Applications. *BioMed Research International*, *2014*. https://doi.org/10.1155/2014/312142

Tang, X., Holland, D., Dale, A. M., Younes, L., & Miller, M. I. (2014). Shape abnormalities of subcortical and ventricular structures in mild cognitive impairment and Alzheimer's disease: Detecting, quantifying, and predicting. *Human Brain Mapping*, *35*(8), 3701–3725. https://doi.org/10.1002/hbm.22431

Team, R. C. (2015). R: A language and Environment for Statistical Computing. *Journal of Computational and Graphical Statistics*, *5*, 299–314.

Temel, Y., Blokland, A., Steinbusch, H. W. M., & Visser-Vandewalle, V. (2005). The functional role of the subthalamic nucleus in cognitive and limbic circuits. *Progress in Neurobiology*, *76*(6), 393–413. https://doi.org/10.1016/j.pneurobio.2005.09.005

Temel, Y., Kessels, A., Tan, S., Topdag, A., Boon, P., & Visser-Vandewalle, V. (2006). Behavioural changes after bilateral subthalamic stimulation in advanced Parkinson disease: A systematic review. *Parkinsonism and Related Disorders*, 12(5), 265–272. https://doi.org/10.1016/j.parkreldis.2006.01.004

Temel, Y., Visser-Vandewalle, V., & Carpenter, R. H. S. (2008). Saccadic latency during electrical stimulation of the human subthalamic nucleus. *Current Biology*, *18*, R412–R414. https://doi.org/10.1016/j.cub.2008.03.008

Temel, Y., Wilbrink, P., Duits, A., Boon, P., Tromp, S., Ackermans, L., … Visser-Vandewalle, V. (2007). Single electrode and multiple electrode guided electrical stimulation of the subthalamic nucleus in advanced Parkinson's disease. *Neurosurgery*, *61*(5.2). https://doi.org/10.1227/01.neu.0000303993.82149.98

Thayyil, S., Cleary, J. O., Sebire, N. J., Scott, R. J., Chong, K., Gunny, R., … Taylor, A. M. (2009). Post-mortem examination of human fetuses: a comparison of whole-body high-field MRI at 9.4 T with conventional MRI and invasive autopsy. *The Lancet*, *374*(9688), 467–475. https://doi.org/10.1016/s0140-6736(09)60913-2

Theilmann, R. J., Reed, J. D., Song, D. D., Huang, M. X., Lee, R. R., Litvan, I., & Harrington, D. L. (2013). White-matter changes correlate with cognitive functioning in Parkinson's disease. *Frontiers in Neurology*. https://doi.org/10.3389/fneur.2013.00037

Thomas, B. P., Welch, E. B., Niederhauser, B. D., Whetsell, W. O., Anderson, A. W., Gore, J. C., … Creasy, J. L. (2008). High-resolution 7T MRI of the human hippocampus in vivo. *Journal of Magnetic Resonance Imaging*, *28*(5), 1266–1272. https://doi.org/10.1002/jmri.21576

Thomas, C., Ye, F. Q., Irfanoglu, M. O., Modi, P., Saleem, K. S., Leopold, D. A., & Pierpaoli, C. (2014). Anatomical accuracy of brain connections derived from diffusion MRI tractography is inherently limited. *Proceedings of the National Academy of Sciences of the United States of America*, *111*(46), 16574–16579. https://doi.org/10.1073/pnas.1405672111

Thompson, P. M., Cannon, T. D., Narr, K. L., van Erp, T., Poutanen, V.-P., Huttunen, M., … Toga, A. W. (2001). Genetic influences on brain structure. *Nature Neuroscience*, *4*(12), 1253–1258. https://doi.org/10.1038/nn758

Thulborn, K., Lui, E., Guntin, J., Jamil, S., Sun, Z., Claiborne, T. C., & Atkinson, I. C. (2015). Quantitative sodium MRI of the human brain at 9.4T provides assessment of tissue sodium concentration and cell volume fraction during normal aging. *NMR in Biomedicine*, *29*(2), 137–143. https://doi.org/10.1002/nbm.3312

Thürling, M., Hautzel, H., Küper, M., Stefanescu, M. R., Maderwald, S., Ladd, M. E., & Timmann, D. (2012). Involvement of the cerebellar cortex and nuclei in verbal and visuospatial working memory: A 7T fMRI study. *NeuroImage*, *62*(3), 1537–1550. https://doi.org/10.1016/j.neuroimage.2012.05.037

Thurling, M., Kahl, F., Maderwald, S., Stefanescu, R. M., Schlamann, M., Boele, H.-J., … Timmann, D. (2015). Cerebellar Cortex and Cerebellar Nuclei Are Concomitantly Activated during Eyeblink Conditioning: A 7T fMRI Study in Humans. *Journal of Neuroscience*, *35*(3), 1228–1239. https://doi.org/10.1523/jneurosci.2492-14.2015

Thürling, M., Küper, M., Stefanescu, R., Maderwald, S., Gizewski, E. R., Ladd, M. E., & Timmann, D. (2011). Activation of the dentate nucleus in a verb generation task: A 7T MRI study. *NeuroImage*, *57*(3), 1184–1191. https://doi.org/10.1016/j.neuroimage.2011.05.045

Tinaz, S., Lauro, P. M., Ghosh, P., Lungu, C., & Horovitz, S. G. (2017). Changes in functional organization and white matter integrity in the connectome in Parkinson's disease. *NeuroImage: Clinical*. https://doi.org/10.1016/j.nicl.2016.12.019

Tinkhauser, G., Pogosyan, A., Debove, I., Nowacki, A., Shah, S. A., Seidel, K., … Schuepbach, M. (2018). Directional local field potentials: A

tool to optimize deep brain stimulation. *Movement Disorders*, *33*(1), 159–164. https://doi.org/10.1002/mds.27215

Tokuno, H., Inase, M., Nambu, A., Akazawa, T., Miyachi, S., & Takada, M. (1999). Corticostriatal projections from distal and proximal forelimb representations of the monkey primary motor cortex. *Neuroscience Letters*, *269*(1), 33–36. https://doi.org/10.1016/S0304-3940(99)00401-2

Tomer, R., Levin, B. E., & Weiner, W. J. (1993). Side of onset of motor symptoms influences cognition in Parkinson's disease. *Annals of Neurology*. https://doi.org/10.1002/ana.410340412

Tona, K.-D., Keuken, M. C., de Rover, M., Lakke, E., Forstmann, B. U., Nieuwenhuis, S., & van Osch, M. J. P. (2017). In vivo visualization of the locus coeruleus in humans: quantifying the test-retest reliability. *Brain Structure and Function*, *222*(9), 4203–4217. https://doi.org/10.1007/s00429-017-1464-5

Tonge, M., Kocabicak, E., Ackermans, L., Kuijf, M., & Temel, Y. (2016). Final electrode position in subthalamic nucleus deep brain stimulation surgery: A comparison of indirect and direct targeting methods. *Turkish Neurosurgery*, *26*(6), 900–903. https://doi.org/10.5137/1019-5149. JTN.13739-14.1

Tourdias, T., Saranathan, M., Levesque, I. R., Su, J., & Rutt, B. K. (2014). Visualization of intra-thalamic nuclei with optimized white-matter-nulled MPRAGE at 7T. *NeuroImage*, *84*, 534–545. https://doi.org/10.1016/j.neuroimage.2013.08.069

Tournier, J. D., Calamante, F., Gadian, D. G., & Connelly, A. (2004). Direct estimation of the fiber orientation density function from diffusion-weighted MRI data using spherical deconvolution. *NeuroImage*, *23*(3), 1176–1185. https://doi.org/10.1016/j.neuroimage.2004.07.037

Trampel, R., Reimer, E., Huber, L., Ivanov, D., Heidemann, R. M., Schäfer, A., & Turner, R. (2013). Anatomical brain imaging at 7T using two-dimensional GRASE. *Magnetic Resonance in Medicine*, *72*(5), 1291–1301. https://doi.org/10.1002/mrm.25047

Trattnig, S., Bogner, W., Gruber, S., Szomolanyi, P., Juras, V., Robinson, S., … Haneder, S. (2015). Clinical applications at ultrahigh field 7T. Where does it make the difference? *NMR in Biomedicine*, *29*(9), 1316–1334. https://doi.org/10.1002/nbm.3272

Trattnig, S., Springer, E., Dymerska, B., Strasser, B., Hangel, G., Cardoso, P. L., … P.L., C. (2018). Key clinical benefits of neuroimaging at 7 T. *NeuroImage*, *168*, 477–489. https://doi.org/http://dx.doi.org/10.1016/j.neuroimage.2016.11.031

Truong, T.-K. K., Chakeres, D. W., Beversdorf, D. Q., Scharre, D. W., & Schmalbrock, P. (2006). Effects of static and radiofrequency magnetic field inhomogeneity in ultra-high field magnetic resonance imaging. *Magnetic Resonance Imaging*, *24*(2), 103–112. https://doi.org/10.1016/j.mri.2005.09.013

Tsialios, P., Thrippleton, M., & Pernet, C. (2017). Evaluation of MRI sequences for quantitative T1 brain mapping. *BioRxiv*, 195859. https://doi.org/10.1101/195859

Tu, P. H., Liu, Z. H., Chen, C. C., Lin, W. L., Bowes, A. L., Lu, C. S., & Lee, S. T. (2018). Indirect targeting of subthalamic deep brain stimulation guided by stereotactic computed tomography and microelectrode recordings in patients with Parkinson's disease. *Frontiers in Human Neuroscience*, *12*. https://doi.org/10.3389/fnhum.2018.00470

Turner, R. (1993). Gradient coil design: A review of methods. *Magnetic Resonance Imaging*, *11*(7), 903–920. https://doi.org/10.1016/0730-725X(93)90209-V

Turner, R. (2011). Neuroscientific Applications of High-Field MRI in Humans. In *High-Field MR Imaging* (pp. 137–149). https://doi.org/10.1007/174_2010_103

Turner, R. (2013). Where Matters: New Approaches to Brain Analysis. In *Microstructural Parcellation of the Human Cerebral Cortex* (pp. 179–196). https://doi.org/10.1007/978-3-662-45766-5_6

Turner, R., & Geyer, S. (2014). Comparing Like with Like: The Power of Knowing Where You Are. *Brain Connectivity*, *4*(7), 547–557. https://doi.org/10.1089/brain.2014.0261

Turner, R., & Haan, D. De. (2017). Bridging the gap between system and cell: The role of ultra-high field MRI in human neuroscience. In *Progress in Brain Research* (pp. 179–220). https://doi.org/10.1016/bs.pbr.2017.05.005

Tustison, N. J., Avants, B. B., Cook, P. A., Zheng, Y., Egan, A., Yushkevich, P. A., & Gee, J. C. (2010). N4ITK: Improved N3 bias correction. *IEEE Transactions on Medical Imaging*, *29*(6), 1310–1320. https://doi.org/10.1109/TMI.2010.2046908

Tykocki, T., Nauman, P., Koziara, H., & Mandat, T. (2013). Microlesion Effect as a Predictor of the Effectiveness of Subthalamic Deep Brain Stimulation for Parkinson's Disease. *Stereotactic and Functional Neurosurgery*, *91*(1), 12–17. https://doi.org/10.1159/000342161

U.S. Food and Drug Administration. (2017). FDA clears first 7T magnetic resonance imaging device. Retrieved February 27, 2020, from FDA News Release website: https://www.fda.gov/news-events/press-announcements/fda-clears-first-7t-magnetic-resonance-imaging-device

Ulla, M., Bonny, J. M., Ouchchane, L., Rieu, I., Claise, B., & Durif, F. (2013). Is R2* a New MRI Biomarker for the Progression of Parkinson's Disease? A Longitudinal Follow-Up. *PLoS ONE*, *8*(3). https://doi.org/10.1371/journal.pone.0057904

Uylings, H. B. M., & Van Eden, C. G. (1990). Qualitative and quantitative comparison of the prefrontal cortex in rat and in primates, including humans. *Progress in Brain Research*, *85*(C), 31–62. https://doi.org/10.1016/S0079-6123(08)62675-8

Uylings, H. B. M., Rajkowska, G., Sanz-Arigita, E., Amunts, K., & Zilles, K. (2005). Consequences of large interindividual variability for human brain atlases: converging macroscopical imaging and microscopical neuroanatomy. *Anatomy and Embryology*, *210*(5–6), 423–431. https://doi.org/10.1007/s00429-005-0042-4

van Beek, E. J. R., Kuhl, C., Anzai, Y., Desmond, P., Ehman, R. L., Gong, Q., … Wang, M. (2019). Value of MRI in medicine: More than just another test? *Journal of Magnetic Resonance Imaging*, *49*, e14–e25. https://doi.org/10.1002/jmri.26211

van Bergen, J., Hua, J., Unschuld, P. G., Lim, I., Jones, C. K., Margolis, R. L., … Li, X. (2015). Quantitative Susceptibility Mapping Suggests Altered Brain Iron in Premanifest Huntington Disease. *American Journal of Neuroradiology*, *37*(5), 789–796. https://doi.org/10.3174/ajnr.a4617

Van Den Bergen, B., Van Den Berg, C. A. T., Bartels, L. ., & Lagendijk, J. J. W. (2007). 7T body MRI: B1 shimming with simultaneous SAR reduction. *Physics in Medicine and Biology*, *52*(17), 5429–5441. https://doi.org/10.1088/0031-9155/52/17/022

van den Bogaard, S. J. A., Dumas, E. M., Teeuwisse, W. M., Kan, H. E., Webb, A., Roos, R. A. C., & Grond, J. (2011). Exploratory 7-Tesla magnetic resonance spectroscopy in Huntington's disease provides in vivo evidence for impaired energy metabolism. *Journal of Neurology*, *258*(12), 2230–2239. https://doi.org/10.1007/s00415-011-6099-5

van den Bos, W., Rodriguez, C. A., Schweitzer, J. B., & McClure, S. M. (2014). Connectivity strength of dissociable striatal tracts predict individual differences in temporal discounting. *Journal of Neuroscience*, *34*(31), 10298–10310. https://doi.org/10.1523/jneurosci.4105-13.2014

Van Der Kolk, A. G., Hendrikse, J., Zwanenburg, J. J. M., Visser, F., & Luijten, P. R. (2013). Clinical applications of 7 T MRI in the brain. *European Journal of Radiology*, *82*(5), 708–718. https://doi.org/10.1016/j.ejrad.2011.07.007

van der Zwaag, W., Schäfer, A., Marques, J. P., Turner, R., & Trampel, R. (2015). Recent applications of UHF-MRI in the study of human brain function and structure: a review. *NMR in Biomedicine*, *29*(9), 1274–1288. https://doi.org/10.1002/nbm.3275

van der Zwaag, W., Schäfer, A., Marques, J. P., Turner, R., & Trampel, R. (2015). Recent applications of UHF-MRI in the study of human brain function and structure: a review. *NMR in Biomedicine*, *29*(9), 1274–1288. https://doi.org/10.1002/nbm.3275

van Laar, P. J., Oterdoom, D. L. M., ter Horst, G. J., van Hulzen, A. L. J., de Graaf, E. K. L., Hoogduin, H., … van Dijk, J. M. C. (2016). Surgical Accuracy of 3-Tesla Versus 7-Tesla Magnetic Resonance Imaging in Deep Brain Stimulation for Parkinson Disease. *World Neurosurgery*, *93*, 410–412. https://doi.org/10.1016/j.wneu.2016.06.084

Van Oostrom, S. H., Gijsen, R., Stirbu, I., Korevaar, J. C., Schellevis, F. G., Susan, H., … Hoeymans, N. (2016). Time Trends in Prevalence of Chronic Diseases and Multimorbidity Not Only due to Aging: Data from General Practices and Health Surveys. *PLoS ONE*, *11*(8). https://doi.org/10.1371/journal.pone.0160264

van Osch, M. J. P. P., & Webb, A. G. (2014). Safety of Ultra-High Field MRI: What are the Specific Risks? *Current Radiology Reports*, *2*(8). https://doi.org/10.1007/s40134-014-0061-0

Van Reeth, E., Tham, I. W. K., Tan, C. H., & Poh, C. L. (2012). Super-resolution in magnetic resonance imaging: A review. *Concepts in Magnetic Resonance Part A*, *40A*(6), 306–325. https://doi.org/10.1002/cmr.a.21249

Vaughan, J. T., & Griffiths, J. R. (Eds.). (2012). *RF coils for MRI*. John Wiley & Sons.

Vaughan, J. T., Garwood, M., Collins, C. M., Liu, W., Delabarre, L., Adriany, G., … Ugurbil, K. (2001). 7T vs. 4T: RF power, homogeneity, and signal-to-noise comparison in head images. *Magnetic Resonance in Medicine*, *46*(1), 24–30. https://doi.org/10.1002/mrm.1156

Vedam-Mai, V., Rodgers, C., Gureck, A., Vincent, M., Ippolito, G., Elkouzi, A., … Okun, M. S. (2018). Deep Brain Stimulation associated gliosis: A post-mortem study. *Parkinsonism and Related Disorders*, *54*, 51–55. https://doi.org/10.1016/j.parkreldis.2018.04.009

Vanegas-Arroyave, N., Lauro, P. M., Huang, L., Hallett, M., Horovitz, S. G., Zaghloul, K. A., & Lungu, C. (2016). Tractography patterns of subthalamic nucleus deep brain stimulation. *Brain: A Journal of Neurology*, *139*(Pt 4), 1200–1210. https://doi.org/10.1093/brain/aww020

Verhagen, R., Schuurman, P. R., Van Den Munckhof, P., Contarino, M. F., De Bie, R. M. A., & Bour, L. J. (2016). Comparative study of microelectrode recording-based STN location and MRI-based STN location in low to ultra-high field (7.0 T) T2-weighted MRI images. *Journal of Neural Engineering*, *13*(6), 066009. https://doi.org/10.1088/1741-2560/13/6/066009

Verma, G., Hariharan, H., Nagarajan, R., Nanga, R. P. R., Delikatny, E. J., Thomas, M. A., & Poptani, H. (2013). Implementation of two-dimensional L-COSY at 7 tesla: An investigation of reproducibility in human brain. *Journal of Magnetic Resonance Imaging*, *40*(6), 1319–1327. https://doi.org/10.1002/jmri.24510

Vertinsky, A. T., Coenen, V. A., Lang, D. J., Kolind, S., Honey, C. R., Li, D., & Rauscher, A. (2009). Localization of the subthalamic nucleus: Optimization with susceptibility-weighted phase MR imaging. *American Journal of Neuroradiology*, *30*(9), 1717–1724. https://doi.org/10.3174/ajnr.A1669

Vidailhet, M., Vercueil, L., Houeto, J.-L., Krystkowiak, P., Benabid, A.-L., Cornu, P., … Pollak, P. (2005). Bilateral Deep-Brain Stimulation of the Globus Pallidus in Primary Generalized Dystonia. *New England Journal of Medicine*, *352*(5), 459–467. https://doi.org/10.1056/nejmoa042187

Visser, E., Douaud, G., Jenkinson, M., Keuken, M. C., Forstmann, B. U., Gaura, V., … Bachoud-Levi, A. (2016). Automatic segmentation of the striatum and globus pallidus using MIST: Multimodal Image Segmentation Tool. *NeuroImage*, *125*, 479–497. https://doi.org/10.1016/j.neuroimage.2015.10.013

Visser, E., Keuken, M. C., Forstmann, B. U., & Jenkinson, M. (2016). Automated segmentation of the substantia nigra, subthalamic nucleus and red nucleus in 7 T data at young and old age. *NeuroImage*, *139*, 324–336. https://doi.org/10.1016/j.neuroimage.2016.06.039

von Monakow, K. H., Akert, K., & Künzle, H. (1979). Projections of precentral and premotor cortex to the red nucleus and other midbrain areas in macaca fascicularis. *Experimental Brain Research*, *34*(1), 91–105. https://doi.org/10.1007/BF00238343

Vymazal, J., Hajek, M., Patronas, N., Giedd, J., Bulte, J., Baumgarner, C., … Brooks, R. (1995). The quantitative Relation Between T1-

Weighted and T2-Weighted MRI of Normal gray Matter and iron concentration. *Journal of Magnetic Resonance Imaging*, *5*(5), 554–560. https://doi.org/10.1002/jmri.1880050514

Wachowicz, K. (2014). Evaluation of active and passive shimming in magnetic resonance imaging. *Research and Reports in Nuclear Medicine*, *4*, 1. https://doi.org/10.2147/rrnm.s46526

Wadghiri, Y. Z., Johnson, G., & Turnbull, D. H. (2001). Sensitivity and performance time in MRI dephasing artifact reduction methods. *Magnetic Resonance in Medicine*, *45*(3), 470–476. https://doi.org/10.1002/1522-2594(200103)45:3<470::AID-MRM1062>3.0.CO;2-E

Waehnert, M. D., Dinse, J., Schäfer, A., Geyer, S., Bazin, P.-L., Turner, R., & Tardif, C. L. (2016). A subject-specific framework for in vivo myeloarchitectonic analysis using high resolution quantitative MRI. *NeuroImage*, *125*, 94–107. https://doi.org/10.1016/j.neuroimage.2015.10.001

Walhovd, K. B., Johansen-Berg, H., & Káradóttir, R. T. (2014). Unraveling the secrets of white matter - Bridging the gap between cellular, animal and human imaging studies. *Neuroscience*. https://doi.org/10.1016/j.neuroscience.2014.06.058

Wang, J. Y., Zhuang, Q. Q., Zhu, L. B., Zhu, H., Li, T., Li, R., … Zhu, J. H. (2016). Meta-analysis of brain iron levels of Parkinson's disease patients determined by postmortem and MRI measurements. *Scientific Reports*, *6*. https://doi.org/10.1038/srep36669

Wang, R., Xie, G., Zhai, M., Zhang, Z., Wu, B., Zheng, D., … Cheng, J. (2017). Stability of R2*and quantitative susceptibility mapping of the brain tissue in a large scale multi-center study. *Scientific Reports*, *7*(1), 1–8. https://doi.org/10.1038/srep45261

Wang, X.-Y., Zhao, L., Yu, T., Qiao, L., Ni, D.-Y., Zhang, G.-J., & Li, Y.-J. (2016). Assessment of Age-Related Morphometric Changes of Subcortical Structures in Healthy People Using Ultra-High Field 7 Tesla Magnetic Resonance Imaging. *Frontiers in Aging Neuroscience*, *8*. https://doi.org/10.3389/fnagi.2016.00224

Wang, Y., & Liu, T. (2015). Quantitative susceptibility mapping (QSM): Decoding MRI data for a tissue magnetic biomarker. *Magnetic Resonance in Medicine*, *73*(1), 82–101. https://doi.org/10.1002/mrm.25358

Wang, Y., Spincemaille, P., Liu, Z., Dimov, A., Deh, K., Li, J., … Prince, M. R. (2017). Clinical quantitative susceptibility mapping (QSM): Biometal imaging and its emerging roles in patient care. *Journal of Magnetic Resonance Imaging*, *46*(4), 951–971. https://doi.org/10.1002/jmri.25693

Wargo, C. J., & Gore, J. C. (2013). Localized high-resolution DTI of the human midbrain using single-shot EPI, parallel imaging, and outer-volume suppression at 7T. *Magnetic Resonance Imaging*, *31*(6), 810–819. https://doi.org/10.1016/j.mri.2013.01.013

Weaver, F. M., Follett, K., Stern, M., Hur, K., Harris, C., Marks, W. J., … Huang, G. D. (2009). Bilateral deep brain stimulation vs best medical therapy for patients with advanced parkinson disease: A randomized controlled trial. *JAMA - Journal of the American Medical Association*, *301*(1), 63–73. https://doi.org/10.1001/jama.2008.929

Weiskopf, N., Mohammadi, S., Lutti, A., & Callaghan, M. F. (2015). Advances in MRI-based computational neuroanatomy: From morphometry to in-vivo histology. *Current Opinion in Neurology*, *28*(4), 313–322. https://doi.org/10.1097/WCO.0000000000000222

Weiss, M., Alkemade, A., Keuken, M. C., MHuller-Axt, C., Geyer, S., Turner, R., & Forstmann, B. U. (2014). Spatial normalization of ultrahigh resolution 7~T magnetic resonance imaging data of the postmortem human subthalamic nucleus: a multistage approach. *Brain Structure and Function*, *220*(3), 1695–1703. https://doi.org/10.1007/s00429-014-0754-4

Welter, M. L., Schüpbach, M., Czernecki, V., Karachi, C., Fernandez-Vidal, S., Golmard, J. L., … Agid, Y. (2014). Optimal target localization for subthalamic stimulation in patients with Parkinson disease. *Neurology*, *82*(15), 1352–1361. https://doi.org/10.1212/WNL.0000000000000315

Wen, J., Cross, A. H., & Yablonskiy, D. A. (2015). On the role of physiological fluctuations in quantitative gradient echo MRI: Implications for GEPCI, QSM, and SWI. *Magnetic Resonance in Medicine*, *73*(1), 195–203. https://doi.org/10.1002/mrm.25114

Wetzels, R., & Wagenmakers, E. J. (2012). A default Bayesian hypothesis test for correlations and partial correlations. *Psychonomic Bulletin and Review*, *19*(6), 1057–1064. https://doi.org/10.3758/s13423-012-0295-x

Wetzels, R., Matzke, D., Lee, M. D., Rouder, J. N., Iverson, G. J., & Wagenmakers, E.-J. (2011). Statistical Evidence in Experimental Psychology. *Perspectives on Psychological Science*, *6*(3), 291–298. https://doi.org/10.1177/1745691611406923

Wharton, S., & Bowtell, R. (2010). Whole-brain susceptibility mapping at high field: A comparison of multiple- and single-orientation methods. *NeuroImage*, *53*(2), 515–525. https://doi.org/10.1016/j.neuroimage.2010.06.070

Wharton, S., & Bowtell, R. (2015). Effects of white matter microstructure on phase and susceptibility maps. *Magnetic Resonance in Medicine*, *73*(3), 1258–1269. https://doi.org/10.1002/mrm.25189

Wharton, S., Schäfer, A., & Bowtell, R. (2010). Susceptibility mapping in the human brain using threshold-based k-space division. *Magnetic Resonance in Medicine*, *63*(5), 1292–1304. https://doi.org/10.1002/mrm.22334

What is GRADE? (2010). *BMJ Best Practice*. Retrieved from https://bestpractice.bmj.com/info/us/toolkit/learn-ebm/what-is-grade/

Whittall, K. P., MacKay, A. L., Graeb, D. A., Nugent, R. A., Li, D. K., & Paty, D. W. (1997). In vivo measurement of T2 distributions and water contents in normal human brain. *Magnetic Resonance in Medicine*, *37*(1), 34–43. https://doi.org/10.1002/mrm.1910370107

Wichmann, T., & DeLong, M. R. (2006). Deep Brain Stimulation for Neurologic and Neuropsychiatric Disorders. *Neuron*, *52*(1), 197–204. https://doi.org/10.1016/j.neuron.2006.09.022

Wiggins, G. C., Polimeni, J. R., Potthast, A., Schmitt, M., Alagappan, V., Wald, L. L., … Wald, L. L. (2009). 96-Channel receive-only head coil for 3 Tesla: Design optimization and evaluation. *Magnetic Resonance in Medicine*, *62*(3), 754–762. https://doi.org/10.1002/mrm.22028

Williams, A., Gill, S., Varma, T., Jenkinson, C., Quinn, N., Mitchell, R., … Wheatley, K. (2010). Deep brain stimulation plus best medical therapy versus best medical therapy alone for advanced Parkinson's disease (PD SURG trial): a randomised, open-label trial. *The Lancet Neurology*, *9*(6), 581–591. https://doi.org/10.1016/S1474-4422(10)70093-4

Wilson, J. L., Jenkinson, M., & Jezzard, P. (2002). Optimization of static field homogeneity in human brain using diamagnetic passive shims. *Magnetic Resonance in Medicine*, *48*(5), 906–914. https://doi.org/10.1002/mrm.10298

Winkler, S. A., Schmitt, F., Landes, H., DeBever, J., Wade, T., Alejski, A., & Rutt, B. K. (2018). Gradient and shim technologies for ultra high field MRI. *NeuroImage*, *168*, 59–70. https://doi.org/10.1016/j.neuroimage.2016.11.033

Wonderlick, J. S., Ziegler, D. A., Hosseini-Varnamkhasti, P., Locascio, J. J., Bakkour, A., Triantafyllou, C., … van der Kouwe, A. (2009). Reliability of MRI-derived cortical and subcortical morphometric measures: Effects of pulse sequence, voxel geometry, and parallel imaging. *NeuroImage*, *44*(4), 1324–1333. https://doi.org/10.1016/j.neuroimage.2008.10.037

Woods, R. P., Grafton, S. T., Holmes, C. J., Cherry, S. R., & Mazziotta, J. C. (1998). Automated image registration: I. General methods and intrasubject, intramodality validation. *Journal of Computer Assisted Tomography*, *22*(1), 139–152. https://doi.org/10.1097/00004728-199801000-00027

Woolrich, M. W., Jbabdi, S., Patenaude, B., Chappell, M., Makni, S., Behrens, T., … Smith, S. M. (2009). Bayesian analysis of neuroimaging data in FSL. *NeuroImage*, *45*(1), S173–S186. https://doi.org/10.1016/j.neuroimage.2008.10.055

Wright, P. J., Mougin, O. E., Totman, J. J., Peters, A. M., Brookes, M. J., Coxon, R., … Gowland, P. A. (2008). Water proton T 1 measurements in brain tissue at 7, 3, and 1.5T using IR-EPI, IR-TSE, and MPRAGE: results and optimization. *Magnetic Resonance Materials in Physics, Biology and Medicine*, *21*(1–2), 121–130. https://doi.org/10.1007/s10334-008-0104-8

Wu, T., Wang, L., Chen, Y., Zhao, C., Li, K., & Chan, P. (2009). Changes of functional connectivity of the motor network in the resting state in Parkinson's disease. *Neuroscience Letters*, *460*(1), 6–10. https://doi.org/10.1016/j.neulet.2009.05.046

Wu, Y., Ragin, A. B., Du, H., Sidharthan, S., Dunkle, E. E., Koktzoglou, I., & Edelman, R. R. (2010). Sub-millimeter isotropic MRI for segmentation of subcortical brain regions and brain visualization. *Journal of Magnetic Resonance Imaging*, *31*(4), 980–986. https://doi.org/10.1002/jmri.22120

Wylie, S. A., Ridderinkhof, K. R., Bashore, T. R., & Van Den Wildenberg, W. P. M. (2010). The effect of Parkinson's disease on the dynamics of on-line and proactive cognitive control during action selection. *Journal of Cognitive Neuroscience*. https://doi.org/10.1162/jocn.2009.21326

Xiao, Y., Jannin, P., D'Albis, T., Guizard, N., Haegelen, C., Lalys, F., … Collins, D. L. (2014). Investigation of morphometric variability of subthalamic nucleus, red nucleus, and substantia nigra in advanced Parkinson's disease patients using automatic segmentation and PCA-based analysis. *Human Brain Mapping*, *35*(9), 4330–4344. https://doi.org/10.1002/hbm.22478

Xiao, Y., Lau, J. C., Hemachandra, D., Gilmore, G., Khan, A. R., & Peters, T. M. (2020). Image guidance in deep brain stimulation surgery to treat Parkinson's disease: a review. *IEEE Transactions on Biomedical Engineering*. https://doi.org/10.1109/TBME.2020.3006765

Xiaowu, H., Xiufeng, J., Xiaoping, Z., Bin, H., Laixing, W., Yiqun, C., … Jianmin, L. (2010). Risks of intracranial hemorrhage in patients with Parkinson's disease receiving deep brain stimulation and ablation. *Parkinsonism and Related Disorders*, *16*(2), 96–100. https://doi.org/10.1016/j.parkreldis.2009.07.013

Yang, S., Yang, Z., Fischer, K., Zhong, K., Stadler, J., Godenschweger, F., … Walter, M. (2013). Integration of ultra-high field MRI and histology for connectome based research of brain disorders. *Frontiers in Neuroanatomy*, *7*. https://doi.org/10.3389/fnana.2013.00031

Yao, B., Li, T., van Gelderen, P., Shmueli, K., de Zwart, J. A., & Duyn, J. H. (2009). Susceptibility contrast in high field MRI of human brain as a function of tissue iron content. *NeuroImage*, *44*(4), 1259–1266. https://doi.org/10.1016/j.neuroimage.2008.10.029

Yarach, U., Luengviriya, C., Stucht, D., Godenschweger, F., Schulze, P., & Speck, O. (2016). Correction of B 0-induced geometric distortion variations in prospective motion correction for 7T MRI. *Magnetic Resonance Materials in Physics, Biology and Medicine*, *29*(3), 319–332. https://doi.org/10.1007/s10334-015-0515-2

Yarnykh, V. L. (2010). Optimal radiofrequency and gradient spoiling for improved accuracy of T1 and B1 measurements using fast steady-state techniques. *Magnetic Resonance in Medicine*, *63*(6), 1610–1626. https://doi.org/10.1002/mrm.22394

Yeterian, E. H., & Van Hoesen, G. W. (1978). Cortico-striate projections in the rhesus monkey: The organization of certain cortico-caudate connections. *Brain Research*, *139*(1), 43–63. https://doi.org/10.1016/0006-8993(78)90059-8

Zaitsev, M., Maclaren, J., & Herbst, M. (2015). Motion artifacts in MRI: A complex problem with many partial solutions. *Journal of Magnetic Resonance Imaging*, *42*(4), 887–901. https://doi.org/10.1002/jmri.24850

Zarzycki, M. Z., & Domitrz, I. (2020). Stimulation-induced side effects after deep brain stimulation – a systematic review. *Acta Neuropsychiatrica*, *32*(2), 57–64. https://doi.org/10.1017/neu.2019.35

Zeineh, M. M., Parekh, M. B., Zaharchuk, G., Su, J. H., Rosenberg, J., Fischbein, N. J., & Rutt, B. K. (2014). Ultrahigh-Resolution Imaging of the Human Brain with Phase-Cycled Balanced Steady-State Free Precession at 7 T. *Investigative Radiology*, *49*(5), 278–289. https://doi.org/10.1097/rli.0000000000000015

Zhang, Y., Brady, M., & Smith, S. (2001). Segmentation of brain MR images through a hidden Markov random field model and the expectation-maximization algorithm. *IEEE Transactions on Medical Imaging*, *20*(1), 45–57. https://doi.org/10.1109/42.906424

Zhang, Z., Liu, S., Lin, X., Teng, G., Yu, T., Fang, G., & Zang, F. (2011). Development of fetal brain of 20 weeks gestational age: Assessment with post-mortem Magnetic Resonance Imaging. *European Journal of Radiology*, *80*(3), e432--e439.

https://doi.org/10.1016/j.ejrad.2010.11.024

Zhao, C., Carass, A., Jog, A., & Prince, J. L. (2016). Effects of Spatial Resolution on Image Registration. *Proceedings of SPIE--the International Society for Optical Engineering*, *9784*. https://doi.org/10.1117/12.2217322

Zhou, D., Liu, T., Spincemaille, P., & Wang, Y. (2014). Background field removal by solving the Laplacian boundary value problem. *NMR in Biomedicine*, *27*(3), 312–319. https://doi.org/10.1002/nbm.3064

Ziegler, E., Rouillard, M., André, E., Coolen, T., Stender, J., Balteau, E., … Garraux, G. (2014). Mapping track density changes in nigrostriatal and extranigral pathways in Parkinson's disease. *NeuroImage*, *99*, 498–508. https://doi.org/10.1016/j.neuroimage.2014.06.033

Zielman, R., Teeuwisse, W. M., Bakels, F., der Grond, J. Van, Webb, A., van Buchem, M. A., … Terwindt, G. M. (2014). Biochemical changes in the brain of hemiplegic migraine patients measured with 7 tesla 1H-MRS. *Cephalalgia*, *34*(12), 959–967. https://doi.org/10.1177/0333102414527016

Zrinzo, L., Hariz, M., Hyam, J. A. J., Foltynie, T., & Limousin, P. (2016). Letter to the Editor: A paradigm shift toward MRI-guided and MRI-verified DBS surgery. *Journal of Neurosurgery*, *124*(4), 1135–1138. https://doi.org/10.3171/2015.9.jns152061

Zrinzo, L., Zrinzo, L. V, Massey, L. A., Thornton, J., Parkes, H. G., White, M., … Holton, J. L. (2011). Targeting of the pedunculopontine nucleus by an MRI-guided approach: a cadaver study. *Journal of Neural Transmission*, *118*(10), 1487–1495. https://doi.org/10.1007/s00702-011-0639-0

Zwanenburg, J. J. M., Hendrikse, J., Takahara, T., Visser, F., & Luijten, P. R. (2008). MR angiography of the cerebral perforating arteries with magnetization prepared anatomical reference at 7T: Comparison with time-of-flight. *Journal of Magnetic Resonance Imaging*, *28*(6), 1519–1526. https://doi.org/10.1002/jmri.21591

Zwanenburg, J. J. M., Hendrikse, J., Visser, F., Takahara, T., & Luijten, P. R. (2009). Fluid attenuated inversion recovery (FLAIR) MRI at 7.0 Tesla: comparison with 1.5 and 3.0~Tesla. *European Radiology*, *20*(4), 915–922. https://doi.org/10.1007/s00330-009-1620-2

Zwirner, J., Möbius, D., Bechmann, I., Arendt, T., Hoffmann, K. T., Jäger, C., … Hammer, N. (2017). Subthalamic nucleus volumes are highly consistent but decrease age-dependently—a combined magnetic resonance imaging and stereology approach in humans. *Human Brain Mapping*, *38*(2), 909–922. https://doi.org/10.1002/hbm.23427

CV

Bethany Rose Isaacs was born in Plymouth, England, on the 25th of January 1992. Between 2010 and 2013 she attended the University of Plymouth, completing a Psychology with Law Bachelor of Science degree. Following this, from autumn 2013 to summer 2014 Bethany completed a Masters in Cognitive Psychology also at the University of Plymouth, producing a thesis on visual processing under the supervision of Prof. Girgio Ganis. Bethany moved to The Netherlands in the summer of 2014 and completed a Research Master of Science in Cognitive Neuroscience at the University of Amsterdam. Here she produced a thesis investigating the neuroanatomical changes occurring in the substantia nigra with MRI, which was completed in 2016 and supervised by Dr. Max C. Keuken at the Integrative Model-based Cognitive Neuroscience Research Unit led by Prof. Birte U. Forstmann. From 2016 to 2020 Bethany completed her PhD in Clinical Neuroscience under the supervision of Prof. Birte U. Forstmann as well as Prof. Yasin Temel at the Department of Experimental Neurosurgery at Maastricht University Medical Centre. She spent the first part in Maastricht, and returned to Amsterdam in 2019. During this time, Bethany conducted the research described in this thesis. Bethany currently works as a clinical data scientist at *Our Future Health*, a world-leading platform for early disease detection and prevention research.

List of Publications

Isaacs, B. R*., Heijmans*, Temel, Y. , Kuijf, M., M., Kubben, P., Ackermanns, L., M. C. Keuklen., & Forstmann, B. U. (2021). Deep brain stimulation MRI-based targeting variability of the subthalamic nucleus. Under review*, Neuroimage Clinical.*

Isaacs, B. R., Keuken, M. C., Alkemade, A., Temel, Y., Bazin, P. L., & Forstmann, B. U. (2020). Methodological considerations for neuroimaging in deep brain stimulation of the subthalamic nucleus in Parkinson's disease patients. *Journal of Clinical Medicine*, *9*(10), 3124.

Isaacs, B. R., Mulder, M. J., Groot, J. M., van Berendonk, N., Lute, N., Bazin, P. L., ... & Alkemade, A. (2020). 3 versus 7 Tesla magnetic resonance imaging for parcellations of subcortical brain structures in clinical settings. *PloS one*, *15*(11), e0236208.

Alkemade, A., Mulder, M. J., Groot, J. M., **Isaacs, B. R**., van Berendonk, N., Lute, N., ... & Forstmann, B. U. (2020). The Amsterdam Ultra-high field adult lifespan database (AHEAD): A freely available multimodal 7 Tesla submillimeter magnetic resonance imaging database. *NeuroImage*, *221*, 117200.

Isaacs, B. R., Trutti, A. C., Pelzer, E., Tittgemeyer, M., Temel, Y., Forstmann, B. U., & Keuken, M. C. (2019). Cortico-basal white matter alterations occurring in Parkinson's disease. *PloS one*, *14*(8), e0214343.

Habets, J*., **Isaacs, B. R***., Vinke, S., & Kubben, P. (2019). Controversies in Deep Brain Stimulation Surgery: Micro-Electrode Recordings. In *Evidence for Neurosurgery* (pp. 97-109). Springer, Cham.

Isaacs, B. R., Forstmann, B. U., Temel, Y., & Keuken, M. C. (2018). The connectivity fingerprint of the human frontal cortex, subthalamic nucleus and striatum. *Frontiers in neuroanatomy*, *12*, 60.

Keuken, M. C*., **Isaacs, B. R***., Trampel, R., van der Zwaag, W., & Forstmann, B. U. (2018). Visualizing the human subcortex using ultra-high field magnetic resonance imaging. *Brain topography*, *31*(4), 513-545. ** Springer Journals 2018 best paper award **

Forstmann, B. U., **Isaacs, B. R**., & Temel, Y. (2017). Ultra-high field MRI-guided deep brain stimulation. *Trends in biotechnology*, *35*(10), 904-907.

Battaglini, L., Casco, C., **Isaacs, B. R**., Bridges, D., & Ganis, G. (2017). Electrophysiological correlates of motion extrapolation: an investigation on the CNV. *Neuropsychologia*, *95*, 86-93.

* joint first authorship

Acknowledgements

First and foremost, I would like to thank my esteemed supervisors, Prof. Birte U. Forstmann and Prof. Yasin Temel, for their continuous support and patience. Their immense knowledge and passion have encouraged me throughout my Ph.D. Additional thanks to Dr. Max C. Keuken and my co-promotors, Dr. Anneke Alkemade and Dr. Pilou Bazin, for their support, guidance and expertise.

A special thank you to Annie (for the wine) and Steven (for the help, and the wine), and to the rest of my friends and office-mates, Scott, Jos and Russ at the UvA. Further acknowledgments go out to colleagues and friends in Maastricht.

My warmest appreciation extends to the patients who took part in our research. Thank you for your dedication and your time.